Lappeenranta
University of Technology

Aleksei Romanenko

TITLE: STUDY OF INVERTER-INDUCED BEARING DAMAGE MONITORING IN VARIABLE-SPEED-DRIVEN MOTOR SYSTEMS

Thesis for the degree of Doctor of Science (Technology) to be presented with
due permission for public examination and criticism in the Auditorium 2303
at Lappeenranta University of Technology, Lappeenranta, Finland on the
13th of December, 2017, at 13:00.

Acta Universitatis
Lappeenrantaensis 781

Supervisors Professor Jero Ahola
LUT School of Energy Systems
Lappeenranta University of Technology
Finland

Professor Annette Muetze
Electric Drives and Machines Institute
Graz University of Technology
Austria

Reviewers Professor Andreas Binder
Institut für Elektrische Energiewandlung
Technische Universität Darmstadt
Germany

Professor Elias Strangas
Department of Electrical and Computer Engineering
Michigan State University
The United States of America

Opponent Dr. Ville Srkimki
Drives Service
ABB Oy
Finland

ISBN 978-952-335-184-4
ISBN 978-952-335-185-1 (PDF)
ISSN-L 1456-4491
ISSN 1456-4491
Lappeenrannan teknillinen yliopisto
Yliopistopaino 2017

Abstract

Aleksei Romanenko
Study of inverter-induced bearing damage monitoring in variable-speed-driven motor systems
Lappeenranta 2017
114 pages
Acta Universitatis Lappeenrantaensis 781
Diss. Lappeenranta University of Technology
ISBN 978-952-335-184-4
ISBN 978-952-335-185-1 (PDF)
ISSN-L 1456-4491
ISSN 1456-4491

Bearing currents are parasitic phenomenon which is commonly present in modern inverter-driven motors. At this date the root causes of this phenomenon can be considered as well identified - mainly occurring due to magnetic flux unbalance and high-frequency components of the common-mode voltage. However, the mitigation techniques, that were developed to reduce the negative effect of this phenomenon on the life time of motors, are not yet at the level, where the problem could be resolved with a standardized method. That is mainly due to the prevalence of various bearing current subtypes in different motor size groups and types, and due to the limited ways to retrofit the machinery, that is already in the exploitation.

This work presents the review of state-of-art in diagnostic methods and insight on the physical processes, that occur in presence of bearing currents and cause deterioration of motor life time. The work further reviews and combines the results of the recent research, that focuses on the aspects of diagnosing defects, caused by bearing current using the vibration and radio-frequency based methods. After that, the work presents analytical model, that is aimed as a way to develop new methods of diagnosing the defects, caused by bearing currents. Finally, the model is used to evaluate the vibration analysis techniques, that are commonly used nowadays and to establish their sensitivity to some of the parameters of motor operation.

Keywords: Ball bearings, converter machine interactions, diagnostics, induction machine, wireless sensors.

Acknowledgements

I would like to express my gratitude to my supervisors Professor Jero Ahola and Professor Annette Muetze for the guidance and assitance in preparation of this dissertation and publications.

Assistance in resolving bureaucratic questions related to my research which was provided by Piipa Virkki was greatly appreciated.

Markku Niemel, Jouni Ryhnen and Kysti Tikkanen provided me with valuable assistance in organizing and assembling of laboratory equipment.

I would like to thank Dr. Liisa Puro and Toni Vkiparta for their invaluable help in the execution and assistance in interpretation of chemical analysis, presented in this work.

I am particularly grateful for the assistance given by personnel of Schaeffler Technologies AG & Co. KG and, personally, by Franziska Berg for in depth laboratory analysis and interpretation of chemical analysis results.

I would like express my appreciation to Dr. Ville Niskanen for his assistance during the early stage of my research and his contribution to the design and assembly of laboratory equipment.

Finally, I would like to offer my special thanks to Oxana Saloshina, my wife, for her assistance in proof reading and support during the preparation of this manuscript.

Aleksei Romanenko
December 2017
Lappeenranta, Finland

Contents

Abstract

Acknowledgements

Contents

List of publications **9**

List of Symbols and Abbreviations **11**

1 Introduction **17**
1.1 Motivation . . . 17
1.2 Research focus . . . 17
1.3 Main question and problems . . . 17
1.4 Main scientific contribution . . . 18
1.5 Limitations . . . 18

2 Background studies **20**
2.1 Bearing currents . . . 20
2.1.1 Bearing-current related issues . . . 20
2.1.2 Bearing-current origins and the electric circuit model of machine . 20
2.1.3 Bearing impedance modelling . . . 23
2.1.4 Other electrical circuit components modelling . . . 26
2.2 Mechanical model of a loaded bearing . . . 27
2.3 Motor operation parameters influencing currents and discharge activity . . 27
2.4 Diagnostic methods . . . 30
2.4.1 Intrusive diagnostics . . . 30
2.4.2 Non-intrusive diagnostics . . . 33
2.5 Models of bearing discharge activity . . . 34
2.6 Damage mitigation techniques . . . 35

3 Materials and methods **39**
3.1 Research plan . . . 39
3.2 Laboratory setup . . . 39
3.2.1 Long-term degradation. . . . 39
3.2.2 Grease degradation . . . 40
3.3 Test procedure . . . 42
3.3.1 Long-term degradation . . . 42
3.3.2 Grease degradation . . . 42
3.4 Lubrication materials . . . 43
3.5 Diagnostic algorithms . . . 45
3.5.1 Time-domain analysis . . . 45

3.5.2 Frequency-domain analysis . . . 45
3.6 Simulation of mechanical degradation during discharges . . . 46
3.6.1 System components . . . 46
3.6.2 Variation of parameters during modelling runs . . . 53
3.6.3 Modelling process . . . 54

4 Results **56**
4.1 Publication I: Study of incipient bearing damage monitoring in variable-speed drive systems . . . 57
4.2 Publication II: Vibration measurement approach to the bearing damage evolution study in the presence of electrostatic discharge machining currents 58
4.3 Publication III: Influence of electric discharge activity on bearing lubricating grease degradation . . . 59
4.4 Publication IV: Effects of electrostatic discharges on bearing grease electric properties . . . 60
4.5 Publication V: Effects of electrostatic discharges on bearing grease dielectric strength and composition . . . 61
4.6 Publication VI: Incipient bearing damage monitoring of 940-hour variable speed drive system operation . . . 62

5 Numerical modelling of bearing degradation process **64**
5.1 Modelling hypotheses . . . 64
5.2 Modelling results . . . 64
5.2.1 Lubricant bearing coefficient sensitivity. . . . 66
5.2.2 Bearing clearance sensitivity. . . . 66
5.2.3 Bearing capacitance sensitivity . . . 70
5.3 Correlation analysis of features obtained through modelling . . . 70

6 Discussion **70**
6.1 Modelling discussion . . . 70
6.1.1 Hypothesis 1. . . . 75
6.1.2 Hypothesis 2. . . . 76
6.1.3 Other observations. . . . 76
6.2 Discussion of results presented in publications. . . . 77
6.3 Interpretation of combined results . . . 78
6.4 Further research . . . 78

References **80**

List of publications

This thesis is based on the following publications.

Publication I

A. Romanenko, J. Ahola, A. Muetze, and V. Niskanen, Study of incipient bearing damage monitoring in variable-speed drive systems, in 2014 16th European Conference on Power Electronics and Applications, EPE-ECCE Europe 2014, 2014, pp. 1-10

Publication II

A. Romanenko, S. Lahdelma, A. Muetze, and J. Ahola, Vibration measurement approach to the bearing damage evolution study in the presence of electrostatic discharge machining currents, in Maintenance, Condition Monitoring and Diagnostics, Maintenance Performance Measurement and Management, Oulu, 2015, pp. 57-62

Publication III

A. Romanenko, J. Ahola, and A. Muetze, Influence of electric discharge activity on bearing lubricating grease degradation, in 2015 IEEE Energy Conversion Congress and Exposition (ECCE), 2015, pp. 4851-4852.

Publication IV

A. Romanenko, A. Mutze, and J. Ahola, Effects of electrostatic discharges on bearing grease electric properties, in 2015 IEEE International Electric Machines Drives Conference (IEMDC), 2015, pp. 254-259.

Publication V

A. Romanenko, A. Muetze, and J. Ahola, Effects of Electrostatic Discharges on Bearing Grease Dielectric Strength and Composition, IEEE Trans. Ind. Appl., vol. 52, no. 6, pp. 4835-4842, 2016.

Publication VI

A. Romanenko, A. Muetze, and J. Ahola, Incipient Bearing Damage Monitoring of 940-Hour Variable Speed Drive System Operation, IEEE Trans. Energy Convers., vol. 32, no. 99, p. 99-110, 2017.

Aleksei Romanenko was the main investigator and author in publications I-VI. The long-term degradation setup used in publications I-III and VI was based on the setup designed and assembled by Prof. Jero Ahola and Dr. Ville Niskanen. In publication II Prof. Emer. Sulo Lahdelma assisted with the analysis of the vibration monitoring results. The experimental work of publication IV was performed by Aleksei Romanenko and Jero Ahola. Publications I-VI were written with major input by Prof. Annette Muetze both in the terms of structuring and wording and interpretation of the results.

List of Symbols and Abbreviations

Roman symbols

A	Surface area, square meters
AV	Vector of acceleration values for modelling iteration
b	Viscosity
BVR	Bearing Voltage Ratio
c	Dampening coefficient
C	Capacitance, Farads
CF	Crest Factor
d	Distance, meters
D	Diameter, millimetres
dT	Time step of modelling
e	Base of natural logarithm
E	Energy, Joules
f	Frequency, Hertz
F	Force, Newton
$FFTmag$	Magnitude Fourier transform spectrum
G	Dimensionless parameter of lubricant properties
GVR	Gear Voltage Ratio
h	Harmonic number
H	Elastohydrodynamic lubrication film thickness
i	Iterator variable
I	Current, Amps
J	Moment of inertia, kilogram·meters
k	Spring stiffness coefficient
K	Experimental correction coefficient
k_{c}	Carter factor
KP	Proportional coefficient of power law model of material viscosity
l	Length, thickness; meters
L	Inductance, Henries
m	Mass, kilogrammes
M	Poisson ratio
n	Power law index
N	Number of objects
Q	Load Force, Newtons
r	Radius, meters
R	Resistance, Ohms
t	Time, seconds
T	Temperature, degrees Celsius or Kelvin scale
U	Voltqage, Volts

v	Velocity, meters per second
VD	Dimensionless parameter of rotation speed
V	Voltage, Volts
VV	Vector of velocity values for modelling iteration
W	Dimensionless parameter of load
x	State space variable of linear model
y	Shear ratio, reciprocal seconds
Y	Young's modulus, Newtons per square meter
Z	Impedance

Greek symbols

α Bearing cage position with respect to outer ring, rad
β Bearing cage position with respect to inner ring, rad
δ Bearing ball position angle in cage frame of coordinates, rad
ε Dielectric constant of the material
μ Dimensionless Hertzian coefficient
ν Dimensionless Hertzian coefficient
ρ Material density, kilograms per cubic meter
σ Standard deviation of normal distribution
ω Rotation frequency, radians per second sort
τ Local error of modelling sort
θ Angle of rotation, radians sort

Abbreviations

-OH	Hydroxy functional group
BLDC	Brushless direct current
BRSC	Bearing race surface component
BVR	Bearing voltage ratio
CH	Carbon-hydrogen
DC	Direct current
DE	Drive end
ECMC	Electrical circuit model component
EDM	Electrostatic discharge machining
EHL	Elastohydrodynamic lubrication
EMF	Electromotive force
ESIM	Electrostatically Shielded Induction Machine
FEM	Finite element modelling/method
FTIR	Fourier transform infrared spectroscopy
GVR	Gear voltage ratio
HF	High frequency
ISO	International standard organisation

NDE	Non-drive end
PCB	Printed Circuit board
PWM	Pulse width modulation
RC	Resistive-Capacitive circuit
RF	Radio frequency
RGC	Rotor to ground current
RL	Resistive-Inductive circuit
RLC	Resistive-Inductive-Capacitive circuit
RMS	Root mean square
SCC	Small capacitive current
SEM	Scanning electron microscope
THD	Total harmonic distortion
TMMC	Transient mechanical modelling component
VSD	Variable speed drive
XRD	X-Ray Diffractometry

Subscripts

a	Axial
ag	Airgap
AS	Air springs
avg	Average
axial	Machine axial length
B	Bearing
bc	Bearing current
bde	Across drive end bearing
bfA	Across bearing A of fast gear
bfB	Across bearing B of fast gear
bnde	Across non-drive end bearing
BRKT-G	Bracket to ground
bsA	Across bearing A of slow gear
bsB	Across bearing B of slow gear
B-SC	Bearing to stator core
BB	Bearing ball
BPI	Ball pass inner
BPO	Ball pass outer
BU	Bushings (dampeners)
c	Bearing cage
cbl	Cable
cd	Conductor depth
center	Center of distribution
cl	Clearance
CM	Center of Mass

const	Constant
corr	Correction rate for step size
cw	Conductor width
D	Centre of mass displacement
dd	Distribution of defects
DE	Drive end
defl	Deflection
disch	Discharge
eff	Effective
ell	Ellipticity
EW	End winding
f	First order fault
F	Machine frame
fl	Filter
gt	Gear teeth
H	Housing
Hertz	Herztian contact
i	I-th element of vector
i+1	I+1-st element of vector
IN	Entrance area of elastohydrodynamic contact
inner	Inner ring of bearing
insul	Insulation and air layer from conductor to slot
j	J-th iteration of modelling
j+1	One step ahead of j-th of modelling
j+2	Two steps ahead of j-th iteration of modelling
L	Load
lubr	Lubricant material
max	Maximal limit
melt	Affected by melting
MG	Magnet
MG-RC	Magnet to rotor core
min	Minimal
MS	Mount system
N	For a sequence of N elements
NDE	Non-drive end
opening	Stator slot opening depth
OUT	Exit area of elastohydrodynamic contact
outer	Outer ring of bearing
pp	Peak to peak
PWM	Pulse width modulation
r	Radial
R	Rotor
RC-G	Rotor core to ground
RC-SC	Rotor core to stator core

rel	Relative
rf	Rotor to frame
RFe	Rotor iron
rotorgrav	Rotor gravitation
rotorunb	Rotor unbalance
RW-RC	Rotor winding to rotor core
sampl	Sampling
SC-MG	Stator core to magnet
SFe	Stator iron
SH	Motor shaft
SH,EXT	Shaft extension
shrot	Shaft rotation
slot	Stator slot
slotwidth	Stator slot opening width
SP	spindle
stat	Stator
SW-BRKT	Stator winding to bracket
SW-MG	Stator winding to magnet
SW-SC	Stator winding to stator core
SW-RW	Stator winding to rotor winding
SW-RC	Stator winding to rotor core
swr	Stator winding to rotor
t	Total
t=0	Value at temperature 0 degrees Celsius
tdep	Temperature dependent
tol	Tolerance
unb	Occurring due to magnetic field unbalance
wedge	Stator slot wedge depth
wf	Stator winding to frame

Units

µH	Microhenry
µm	Micrometre
Ω	Ohm
^{o}C	Degree Celsius grade
A	Ampere
cm	Centimetre
Hz	Hertz
J	Joule
K	Degrees of temperature, Kelvin scale
kΩ	Kiloohm
kg	Kilogram

kHz Kilohertz
kV Kilovolt
kW Kilowatt
m Metre
mΩ Milliohm
mA Milliampere
MHz Megahertz
min Minute
mm Millimetre
MV Megavolt
N Newton
nF Nanofarad
nm Nanometre
ns Nanoseconds
pF Picofarad
rpm Rotations per minute
s Second
V Volt
W Watt

Constants

e Base of natural logarithm
ε_0 Permittivity of vacuum, approximately $8.854187817 \cdot 10^{-12}$ Farads per metre
π Ratio between circumference of a circle and its diameter

1 Introduction

1.1 Motivation

The phenomenon of bearing currents is an almost century old parasitic effect, that may occur in electrical drive due to various side effects of design. With the advances made in power electronics and control engineering in the 21st century new cause for bearing currents became a common reason for motor and drive failures in VSD applications. This cause was identified as high-frequency harmonic components of pulse-width modulated signal that is typically produced by inverters. Previous research indicated several approaches in mitigation of this phenomena and some insight on its nature. Different solutions have been proposed to mitigate and prevent the phenomenon. However, the existing solutions are not universal, and demand for significant modifications to drive on early stages of design process or expensive materials.

At the same time advances in computation facilitates improvements and development of new methods for drive health state monitoring as they allow complex analysis to be performed in real-time. The recent leap in performance also allows multiphysics modelling of processes occurring on the time scale of nanoseconds. Such modelling often improves the ability to understand the whole system.

1.2 Research focus

This research focuses on the nature of bearing degradation, physical and chemical phenomena occurring in the bearings, opportunities to diagnose changes caused by such phenomena and suggestions on how to reduce the degradation during the design stage of the drive. Of different bearing current types this paper mainly investigates the discharge bearing currents.

1.3 Main question and problems

The main question of this research is what changes occur inside the bearings due to electrostatic discharges.

Research Question 1: What diagnostic non-intrusive tools can be used to observe the state of the bearing and detect incipient damage?

Research Question 2: How does discharge activity relate to machine operation and design parameters?

Research Question 3: What changes happen to the physical parameters of the bearing grease due to discharges?

Research Question 4: Is the existing level of understanding of discharging bearing current phenomenon sufficient to simulate the degradation processes?

Research Question 5: How can the modelling of bearing currents improve the design practices?

1.4 Main scientific contribution

The study contributes to the existing knowledge with the following novel insights.

- The study builds up on the insight, provided by previously published works. This work performs the analysis of previously published results. These results are different approaches to tackle the problem of bearing degradation due to EDM. The study combines the results of published works, revisits the important conclusions and provides additional claims on the previously published data, that can only be justified, using all the results in combination.
- The work provides analytical model of bearing degradation process, that provides a depth of insight, that has not yet been achieved by previous attempts to model the system, primarily as those attempts were mainly limited to individual components of the system, whereas this work models the system as a closed loop model.
- The results of numerical modelling contribute to explanation of phenomena observed via vibration monitoring and generation of new hypotheses about the expected behaviour of vibration in the system.

1.5 Limitations

The main limitations of this study are: the limited amount of experimental work, limited amount of types of tested lubrication materials, and the constraints imposed on the mechanical system for the purpose of numerical simulation.

The study is based on the results of three long-term degradation tests, for which the results were published in the peer-reviewed journals and conferences. This amount of experimental work is on its own not sufficient to prove the existence of new correlations. However, that should be sufficient to demonstrate limitations of the existing vibration monitoring methods.

The quality of numerical modelling performed to analytically predict the potential vibration features, that should occur in the system due to the parasitic effects, which are studied in this work, is limited by extremely high non-linearity order of the used EHL model equation. The accuracy of simulation can only be achieved at extremely small modelling time steps while the nature of the studied phenomenon requires long-term analysis of changes, that occur in the vibration. In this study a reasonable, from the author's point of view, trade off — between the total duration of modelling and tolerated mechanical error — has been made.

Finally, the amount of tested lubricating materials is a significant limitation factor. It is not possible to treat the results of the applied lubrication degradation test to define the limited amount of tested samples as representative for their classes. The number of overall tested base oils is limited as well.

2 Background studies

2.1 Bearing currents

2.1.1 Bearing-current related issues

Bearing currents are diverse in their origin and background physics. One type of bearing currents — circulating currents — caused by different side effects of manufacturing and design in the electrical machine design were observed by engineers and researchers as early as of 1907 (Punga and Hess, 1907). Since then, researchers have observed other types of this phenomenon, and the knowledge about bearing currents has been improved over time, but up to this date is far from being perfect.

In previous studies (Zika et al., 2009) one of the recently discovered types of bearing currents — EDM currents — were named as the cause of pitting damage, occurring on the running surfaces. Studies of (Erdman et al., 1996b) also suggest that such damage significantly affects the friction coefficient of bearings leading to mechanical overload. At the same time a survey of causes for motor failures indicated that bearing failure contributes about one third of all the cases (IEEE, 1985), with high speed machines being more vulnerable to this type of failure than the low speed ones. Of those reported failure rates, overloading, overheating, and lubricant degradation were named among the main factors leading to the failure.

Combining this knowledge it is possibly to conclude, that bearing currents in general and EDM currents are dangerous for the lifetime of electrical machines and drive assemblies (Kriese et al., 2012). This statement has recently received additional evidence in the areas, where application of inverter-driven electric machines became common. I.e., study of (Hadden et al., 2016) report observed bearing current problems in electric vehicles.

Besides the threat to the lifetime of drives, bearing currents also cause additional electromagnetic interference: “conducted and radiated noises, ground current escaping to earth through stray capacitors inside a motor (Zare, 2009)”, that may affect the lifetime and cause disruptions in functionality of nearby non-motor equipment.

2.1.2 Bearing-current origins and the electric circuit model of machine

The works on different types of bearing currents commonly tackle the issue of modelling resonance and propagation effects of bearing currents. In this subsection an attempt is made to organise the outcomes of previous studies into a combined electrical model of bearing current circuit.

There are two major known sources of EMF in the circuit of the electrical drive: voltage induced by higher order harmonics of electromagnetic field, and higher order harmonics of PWM voltage input from inverter, that can propagate in common or differential modes of supplied voltage.

These high-order harmonics appear in the magnetic field structure of electrical machines mainly due to non-symmetric spatial distribution of flux paths, variations in the magnetic permittivity of paths as the rotor rotates, and non-linear effects of magnetic materials. These harmonics often loop through the same magnetic paths without producing any useful torque while generating some electromotive force in the loop formed by rotor, stator, windings, bearings and capacitively conductive parts of load on the DE of the shaft.

The second major source of EMF is high order components of PWM voltage applied between stator windings (in case of an induction machine) and rotor. The common mode voltage waveform of supplied PWM usually contains rapid transitions between different voltage levels. In the basic modulation schemes those steps can be as high as the magnitude of DC link voltage, while in converters with more voltage levels it is still typically higher than one sixth of the DC link voltage. The slope of these steps is directly related to the chopping frequency of semiconductor switches used in the inverter. The chopping frequency is in turn one of the limiting factors for the fundamental frequency of inverter output signal. Thus the need for higher fundamental frequencies causes the use of components with high chopping frequency.

In addition, these components, when introduced into sufficiently long power-supply cables, are subject to effects of impedance mismatch, and thus often cause reflections and additional over-voltage up to two times of the rated output value (Persson, 1992), and, in some cases, even more, when the next switching occurs during the still acting voltage reflection of the previous switching.

As the machine is commonly grounded at the stator frame, the induced voltage generates three types of bearing current that go through the stator-to-rotor capacitance and loop back to the ground point (frame of the same machine or another one, connected with common shaft or gearbox) through the bearings. The rapid change in the applied voltage induces:

1) Small capacitive currents (SCC). These currents directly arise from the ability of bearing to conduct alternating current as capacitance. As the capacitive impedance of the bearing itself is often high, these currents have been previously considered of little danger (Muetze and Binder, 2006) to the life expectancy of bearings due to small magnitudes (typically from 5 to 200 mA). Recent developments, however, suggest that, despite the low magnitudes, these high frequency harmonics of currents can pose additional danger to the bearing running surfaces due to skin effect (Liu, 2014).

2) EDM currents, which build up charge across bearings and cause discharges in the lubricating film, when breakdown voltage is reached. Fig. 2.1 presents an equivalent circuit of single-phase of an induction drive with gearbox.

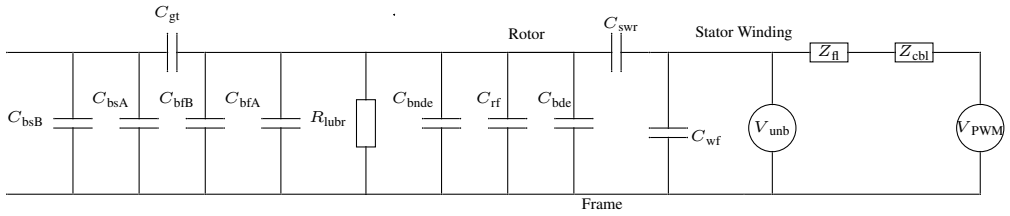

Figure 2.1: Equivalent circuit of a drive-train utilising induction motor. HF equivalent circuit of induction proposed by (Erdman et al., 1996a) and (Tischmacher et al., 2014). The gearbox model as proposed by (Furtmann et al., 2016). In this figure the following symbols are used. V_{unb} - voltage induced due to magnetic flux unbalance, V_{PWM} - common mode voltage, caused due to high-order harmonics of PWM voltage supply, Z_{cbl} - impedance of cable, Z_{fl} - impedance of filter, C_{wf} - stator winding to frame capacitance, C_{swr} - stator winding to rotor capacitance, C_{rf} rotor to frame capacitance, C_{bde} - drive end bearing capacitance, C_{bnde} - non-drive end bearing capacitance, R_{lubr} - resistance of bearing lubricating layer, C_{bsB} - slow gear side B capacitance, C_{bsA} - slow gear side A capacitance, C_{bfB} - fast gear side B capacitance, C_{bfA} - fast gear side A capacitance, C_{gt} - gear fast to slow gear teeth capacitance.

As the loop is mostly capacitive between rotor and stator due to insulating properties of lubricant in bearings, air gap and winding insulation, it only easily conducts high-frequency components of these induced currents while the lower frequencies induce voltage across the capacitances, unless breakdown event happens. The literature commonly refers to the proportion of V_{PWM} applied across to bearing as bearing voltage ratio which is a proportion between stator to rotor capacitance C_{swr} and rotor to frame capacitance C_{rf} (Busse et al., 1997a; Muetze and Binder, 2007c).

$$BVR = \frac{C_{\text{swr}}}{C_{\text{swr}} + C_{\text{rf}} + C_{\text{bde}} + C_{\text{bnde}}}, \tag{2.1}$$

where in a typical case C_{rf} is 10 to 20 times bigger, than drive end bearing capacitance C_{bde} and non-drive end bearing capacitance C_{bnde} (Muetze and Binder, 2007c). According to (Furtmann et al., 2016) for gearbox capacitances a similar gear voltage ration can be defined as

$$GVR = \frac{C_{\text{t}}}{C_{\text{t}} + C_{\text{bsA}} + C_{\text{bsB}}}, \tag{2.2}$$

where C_{t} is total capacitance formed by fast and slow gears, C_{bsA} - capacitance of side A of slow-side gear and C_{bsB} - capacitance of side B of slow-side gears. Two other capacitances: capacitance of side A of fast-side gear C_{bfA} and capacitance of side B of fast-side gearC_{bfB} are connected in parallel to bearing capacitances and would thus additionally contribute to the GVR.

3) Finally, worse grounding of machine frame than that of a load may lead to the lowest impedance path for the common mode voltage to be through the rotor, load coupling, load bearings, and load frame to the grounding of the load itself. In such cases the current flowing is referred to as rotor to ground (RGC) current.

The measured and estimated values of equivalent circuit elements for different induction motors presented in literature are listed in Appendix A. They vary mainly with bearing and machine frame dimensions, and relate well to the corresponding estimates. Further subsections present additional details on models used to predict these values.

2.1.3 Bearing impedance modelling

The bearing impedance consists mainly of capacitive and ohmic components. The latter dominates typically at lower shaft rotation speeds, when the layer of lubricant allows partial metal contact or, at least, quantum-tunnelling effects that, in turn, cause conductivity (Erdman et al., 1996a). As the shaft rotation speed increases the lubrication layer becomes thick enough for the resistance to go up sharply, until it reaches the limits defined by conductivity in grease. According to (Prashad, 2006), the behaviour of grease in the presence of an electrical field is complex and, in a long-term, results in significant variation of resistivity.

Bearing resistance. In the several studies cited by (Prashad, 2006) different grease samples were studied in a laboratory ageing setup. The setup consisted of electrode plates between which the grease samples were placed. The DC voltage field was applied to these plates at different strengths for the duration of up to 250 hours, during which the samples were periodically studied for their resistance. These samples changed their resistivity. For two of four greases, under different electrical field densities, the resistivity increased by up to 23.67 times the initial value. At the same time, two other greases showed less significant increase under some test conditions, and even increase in conductivity under the others. The authors proposed the following effects explaining the changes in grease conductivity:

- Arc discharges in some greases might form impurities and by-products, that would be dissolved in the base oil of the grease, forming ions and, thus, providing conductivity.
- The grease components suffered electrochemical decomposition resulting in decrease of conductivity.
- The electric field caused stretching of the molecules, that resulted in structure transform, that, by opinion stated in (Prashad, 2006), might affect the resistivity.

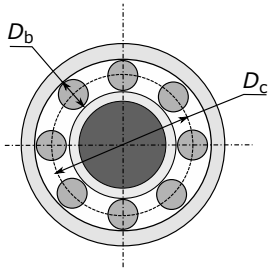

Figure 2.2: Bearing principal dimensions.

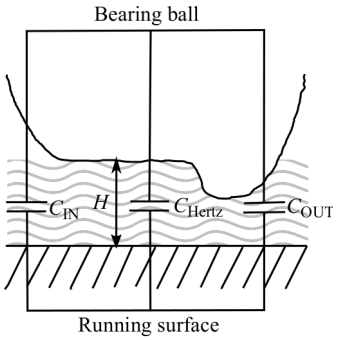

Figure 2.3: Capacitances in a loaded bearing. (Gemeinder et al., 2014; Furtmann et al., 2016). H - elastohydrodynamic lubrication film thickness, C_{IN} - capacitance formed by entrance area, C_{Hertz} - capacitance formed by Hertzian contact area, C_{OUT} - capacitance formed by exit area.

In addition, the authors of (Prashad, 2006) observed a "recouping effect", where the grease resistivity would partially revert to its original state after the removal of the electrical field for a period of several hours.

The impedance of grease mineral oil is also considered to depend on the frequency of the exiting voltage due to losses and inertia of organic charge carriers (Ulrych and Mentlík, 2016).

Bearing capacitance. The capacitance formed by the bearing is considered to be composed by connection of individual capacitances that are formed between each of bearing balls, and inner and outer tracks. In a simplified case, due to bearings being loaded, the capacitance of a single loaded ball or to parallel loaded balls is dominating and the circuit can be reduced. Fig. 2.3 presents an equivalent circuit of a single loaded ball case. Nowadays the common understanding is that the capacitance is formed mostly by the so-called Hertzian contact area, where, due to hydrodynamic pressure and metal properties, a flattened surface is formed with grease being pressed between ball and the track.

Several studies to this date tackled the issue of measuring and developing an analytical approach to estimation of the bearing capacitance values over different ranges of oper-

ating conditions, as the value of bearing capacitance is considered to have effect on the BVR (Magdun et al., 2010b).

First attempts to model the bearing capacitance were undertaken in the study of (Busse and Erdman, 1997), where it was proposed to estimate the bearing capacitance, using equation for a capacitor formed by a radial contact of two spheres. The equation proposed in (Busse and Erdman, 1997) is

$$C_{\mathrm{B}} = \frac{N_{\mathrm{BB}} 4\pi\varepsilon_0\varepsilon_{\mathrm{rel}}}{1/r_{\mathrm{BB}} - 1/(r_{\mathrm{BB}} + l_{\mathrm{cl}})}, \tag{2.3}$$

where r_{BB} is the radius of the bearing ball, N_{BB} - number of balls in the bearing, l_{cl} is the clearance between the bearing ball and the running surface, i.e., due to lubrication and $\varepsilon_{\mathrm{rel}}$ is the relative permittivity of lubricating material.

The work of (Naik et al., 2003) suggested the impedance fitting approach to measurements of bearing capacitance and resistance. The study used a lumped RC circuit to model the impedance behaviour of a bearing at different frequencies. The results of comparison indicated, that a lumped parameter model can be adequate for the representation of a bearing at frequencies above 100 kHz.

In (Muetze and Binder, 2007c) a new approach to bearing capacitance estimation was proposed. This approach assumed, that most of the bearing capacitance is due to a flat area between the rolling element and the race. According to (Muetze and Binder, 2007c), the surface of this Hertzian contact area A_{Hertz} is related to the bearing total capacitance as follows.

$$C_{\mathrm{B}} = 0.5\frac{\varepsilon_0\varepsilon_{\mathrm{rel}} A_{\mathrm{Hertz}}}{l_{\mathrm{cl}}}, \tag{2.4}$$

However, it was noted, that computation of A_{Hertz} based on the elasticity theory was too difficult for practical purposes. Later a simplified equation for A_{Hertz} has been formulated and validated in the study of (Gemeinder et al., 2014) as

$$A_{\mathrm{Hertz}} = \pi\mu_{\mathrm{Hertz}}\nu_{\mathrm{Hertz}}\left[\frac{3\cdot\left(1-\frac{1}{M^2}\right)}{Y\cdot\sum d_{\mathrm{defl}}}Q\right]^{2/3}, \tag{2.5}$$

where μ_{Hertz} and ν_{Hertz} are dimensionless Hertzian coefficients, M is Poisson's ratio, Y is Young's modulus, d_{defl} is deflection distance and Q is load force.

2.1.4 Other electrical circuit components modelling

In (Busse and Erdman, 1997) an initial approach to analytical representation of electrical circuit elements was made. The study proposed modelling of elements as follows.

- Stator to frame capacitance C_{wf} as N_{slot} parallel capacitors in a rectangular conduit. The corresponding relation of capacitance to the physical dimensions of wires and the conduit is

$$C_{\text{wf}} = K_{\text{wf}} N_{\text{slot}} \varepsilon_0 \varepsilon_{\text{rel}} (l_{\text{cd}} + l_{\text{cw}}) \cdot l_{\text{opening}} / l_{\text{insul}}, \tag{2.6}$$

  where l_{cd} is the depth of conductor, l_{cw} - width of the conductor, l_{opening} is thickness of air layer in the slot opening and l_{insul} is the thickness of insulation and air layer from conductor to slot and K_{wf} is experimental correction factor.

- Stator to rotor capacitance C_{swr} as N_{slot} parallel plate capacitors formed by the winding and the underlying rotor segment,

$$C_{\text{swr}} = K_{\text{swr}} N_{\text{slot}} \varepsilon_0 l_{\text{slotwidth}} \cdot l_{\text{axial}} / l_{\text{ag}}, \tag{2.7}$$

  where $l_{\text{slotwidth}}$ is stator slot width, l_{axial} - stator stack axial length, l_{ag} - air gap width, and K_{swr} is experimental correction factor.

- Rotor to frame capacitance C_{rf} as N_{slot} two co-axial cylindrical parallel capacitors with stator inner radius r_{stat} and rotor outer radius r_{R}:

$$C_{\text{rf}} = K_{\text{rf}} \varepsilon_0 l_{\text{axial}} / \ln(r_{\text{stat}} / r_{\text{R}}), \tag{2.8}$$

  where K_{rf} is experimental correction factor.

The study (Muetze and Binder, 2007c) proposed further improvements to analytical formulations of values for C_{swr} and C_{rf}, as they seem to be the ones causing most influence on BVR.

The equation for C_{rf}, proposed in (Muetze and Binder, 2007c), is derived by analogy with the established technique for B-field correction factors. The derivation was done with the assumption of parallel plate capacitor with area equal to the area of rotor surface due to low estimated error of linearisation. Another important addition was the introduction of the Carter factor k_{c}, that should correct the capacitance value for the fact that the outer side has gaps for winding slots. The resulting proposed model is as follows.

$$C_{\text{rf}} = \varepsilon_0 l_{\text{axial}} \frac{\pi l_{\text{axial}}}{k_{\text{c}} l_{\text{ag}}}, \tag{2.9}$$

Additionally, (Muetze and Binder, 2007c) proposed to compute C_{swr} as a series connection of two capacitances with different relative permittivities. With substitutions and simplifications the final equation would look like

$$C_{\text{swr}} = N_{\text{slot}}\varepsilon_0 l_{\text{slotwidth}} \frac{l_{\text{axial}}}{l_{\text{ag}} + l_{\text{opening}} + (l_{\text{wedge}} + l_{\text{insul}})/\varepsilon_{\text{rel}}}, \tag{2.10}$$

where l_{wedge} - thickness of wedging layer.

Another approach to modelling of bearing current circuits had been undertaken by studies (Naik et al., 2003; Magdun et al., 2011; Magdun and Binder, 2014). The main idea of the method is to perform fitting of measured impedance curves with a lumped parameter RLC circuit model. This approach was utilized in (Magdun et al., 2011) to model the HF behaviour of the stator winding via an RL ladder model, and in (Magdun and Binder, 2014) to estimate also the values of the capacitive elements of the bearing current circuit. In addition, (Magdun and Binder, 2014) provides an insight on the variation between the values of these elements and the stator outer diameter dimension of the machine.

2.2 Mechanical model of a loaded bearing

The mechanical parameters of the shaft-bearing-frame system are of significant importance to the insulating properties of the grease. I.e., oscillating variations in the thickness of the lubricant film would affect the breakdown voltage and potentially cause discharges.

In a study of (Jacobs et al., 2014) an identified parametrised model of a mechanical subsystem of a bearing is described. Fig. 2.4 presents the model of the proposed identification rig.

The work identified the dependency of stiffness and dampening parameters of the bearing with respect to different rotation speed. Additionally, the researchers have suggested that these parameters vary during the rotation period as the position of balls in the bearing affects the distribution of the load between the balls. The example of two extreme scenarios (as proposed by (Jacobs et al., 2014)) are presented in Fig. 2.5.

2.3 Motor operation parameters influencing currents and discharge activity

The amount of existing literature on the subject of motor operation parameters is rather limited to this date. Multiple factors have been named as affecting the intensity of elec-

trostatic discharges and EDM bearing currents. Among them the most notable are the ones, that directly affect the thickness of the separating lubrication layer, i.e., mechanical load and bearing surfaces manufacturing quality (Erdman et al., 1996a), motor rotation speed and temperature (Muetze and Binder, 2007a). The thickness of lubrication layer, in its turn, directly affects the breakdown voltage of this lubricating film, for which the breakdown field strength is typically considered to be 10 to 15 V/ µm (Busse et al., 1997c).

The ground work in qualitative assessment of the aforementioned factors was laid in year 2010 by (Magdun et al., 2010a). The paper describes results of a laboratory investigation on a test setup with regulated radial load and bearing temperature. The findings are compared to theoretical models of bearing capacitance variation at different rotation speeds with controlled bearing temperature. The main measure of bearing currents used in this study is EDM current. The authors of the aforementioned study also suggested that bearing load and temperature affect EDM current values.

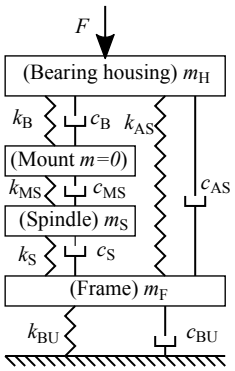

Figure 2.4: The mechanical model of bearing identification rig proposed by (Jacobs et al., 2014). Here F is the sum of radial forces applied on the tested bearing, k_{B} - spring stiffness coefficient of tested bearing, c_{B} - damping coefficient of tested bearing, k_{MS} - spring stiffness coefficient of mount system, c_{MS} - damping coefficient of mount system, k_{SP} - spring stiffness coefficient of spindle (equivalent of shaft in a real drive), c_{SP} - damping coefficient of spindle, k_{AS} - spring stiffness coefficient of air springs, c_{AS} - damping coefficient of air springs, k_{BU} - spring stiffness coefficient of bushings(dampeners), c_{BU} - damping coefficient of bushings, m_{H} - mass of bearing housing, m_{F} - mass of test rig frame, m_{SP} - mass of spindle.

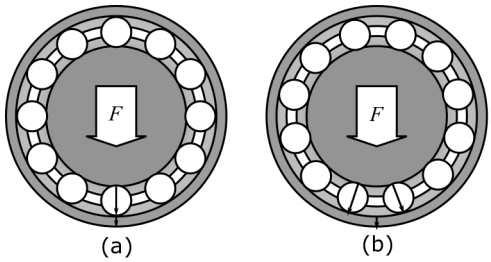

Figure 2.5: Two extreme scenarios of loading force distribution in a loaded bearing (Jacobs et al., 2014)

The work of (Muetze et al., 2011) continues the acquisition of data on relation between the discharge activity and motor operation point. The study successfully used a novel method of wireless detection of individual discharges to monitor medium/long-term variation of discharge activity. The findings, with respect to relation between bearing currents and motor operation parameters, confirm results, presented in (Magdun et al., 2010a) and specify behaviour of discharge activity as having a peak "at certain motor speed, ..., depending on the total time of operation (Muetze et al., 2011)". This study also noted over-time discharge activity variation with, however, no suggestion on the nature of such changes.

Another study (Maetani et al., 2012) concluded that the breakdown voltage of bearing lubricating film changes as the thickness of the film increases or decreases with changes in rotational speed of machine. In addition, the results presented in this study indicate dependency between motor rotation frequency and discharge activity similar to one proposed in (Muetze et al., 2011).

The research carried out in (Niskanen et al., 2014) lead authors to define different operation modes for bearing. The authors claim that at different rotation speeds the bearing can be in either resistive or capacitive mode depending on which part of bearing impedance is dominating. This finding could explain the existence of the peak discharge activity at certain rotation speed observed in (Muetze et al., 2011). The authors of that study suggest that the rate of bearing currents can be judged from the number of transitions between these resistive and capacitive states, effectively spark discharge events and capacitance recharging.

Summarising the outcomes of previous research on this topic, the following assumptions can be formulated:

- Capacitive and resistive components of the bearing impedance are affected by the lubricating film thickness, both being directly proportional. The resistive component, according to the Ohm law, is

$$R_{\text{lubr}} = \frac{\rho_{\text{lubr}} l_{\text{lubr}}}{A_{\text{Hertz}}}, \tag{2.11}$$

  where ρ_{lubr} is resistivity parameter of lubricating material, l_{lubr} - thickness of lubricating material. The capacitive component can be computed from

$$Z_{\text{lubr}} = \frac{1}{i\omega_{\text{bc}} C_{\text{lubr}}}, \tag{2.12}$$

  where ω_{bc} is frequency of current flowing through the bearing and capacitance formed by bearing lubricating layer C_{lubr} can be defined as

$$C_{\text{lubr}} = \frac{\varepsilon_0 \varepsilon_{\text{rel}} A_{\text{Hertz}}}{l_{\text{lubr}}} \tag{2.13}$$

which, when substituted into eq. 2.12, yields

$$Z_{\text{lubr}} = \frac{l_{\text{lubr}}}{i\omega_{\text{bc}}\varepsilon_0\varepsilon_{\text{rel}}A_{\text{Hertz}}}. \tag{2.14}$$

- The motor rotation speed affects the bearing impedance and the resulting discharge activity by causing variation in film thickness, affecting the effective contact area and grease resistivity. The change in resistivity is due to the bearing temperature changes, that are proportional to friction losses, that happen in a bearing and is thus proportional to both radial load and rotation speed.
- The changes in grease resistivity and breakdown voltage of lubricating layer are the main factors affecting variation in discharge activity.

2.4 Diagnostic methods

Diagnosis and prognosis are important applications of the models and techniques, that were developed to describe different types of bearing currents and their effects. The diagnostic methods are commonly divided into intrusive and non-intrusive groups, based on whether the investigation will permanently damage or even destroy the integrity of the bearing.

2.4.1 Intrusive diagnostics

Typical examples of intrusive diagnostic methods are: visual inspection, and SEM imaging of the bearing surfaces. Both methods require cutting the bearing traces.

The so-called trace pitting (Alger and Samson, 1924) and fluting (Lawson, 1993) patterns are typically visually observed defects in the cases where the occurrence of bearing currents is known or suspected. The optical spectrum images of such defects are presented in Fig. 2.6. While this method was initially used to identify the bearing currents as phenomenon (Alger and Samson, 1924), the insight provided was rather limited, and thus advanced methods of inspection were applied to study the phenomenon.

According to (McMullan, 1995), the development of SEM imaging has begun in the 1930s by Ruska (1933), Ruska and Mueller (1940) and Von Borries (1940). The method was developed with the main goal of imaging of surfaces of solid samples. (McMullan, 1995). The SEM imaging is achieved by illuminating the surface of the material with the beam of electrons from the electron tube at some small angle while having a detection device at the same angle on the other hand with respect to the normal vector of the scanned object. The electrons reflected from the surface are detected and counted as the beam is

shifted along two horizontal axes of the sample with deflecting magnetic field in a scanning pattern. Modern SEM devices allow picturing with magnification factor of several thousands. Such big magnification provides a valuable insight into the damage patterns caused by the bearing currents.

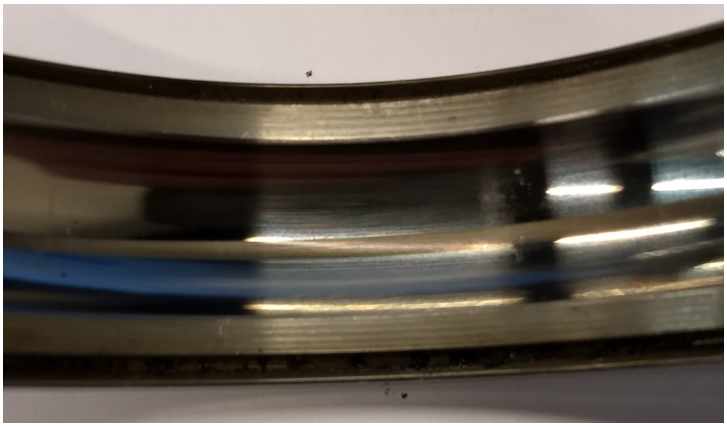

(a) Pitting damage on bearing outer race.

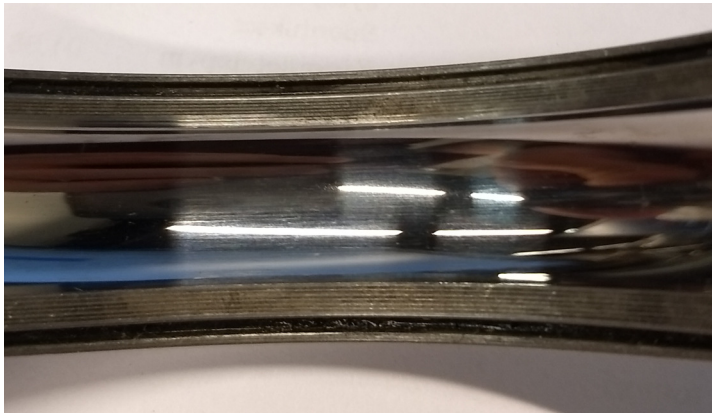

(b) Clear bearing outer race.

(c) Pitting damage on bearing inner race.

Figure 2.6: The photographies of bearing inner and outer surfaces in different conditions.

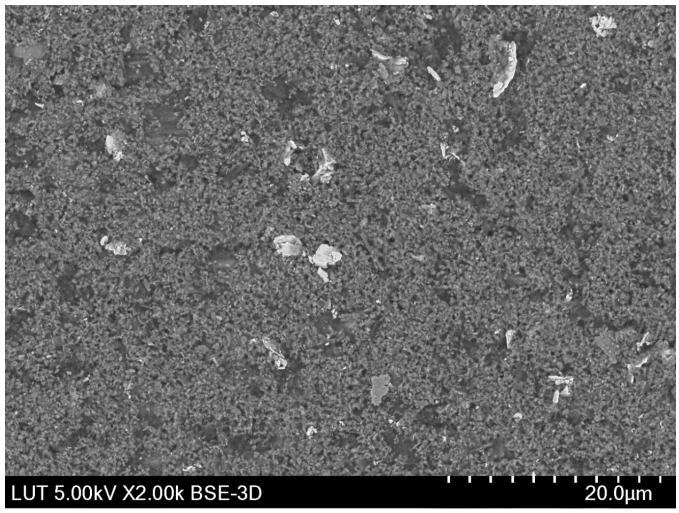

Figure 2.7: The results of SEM imaging of pitting trace.

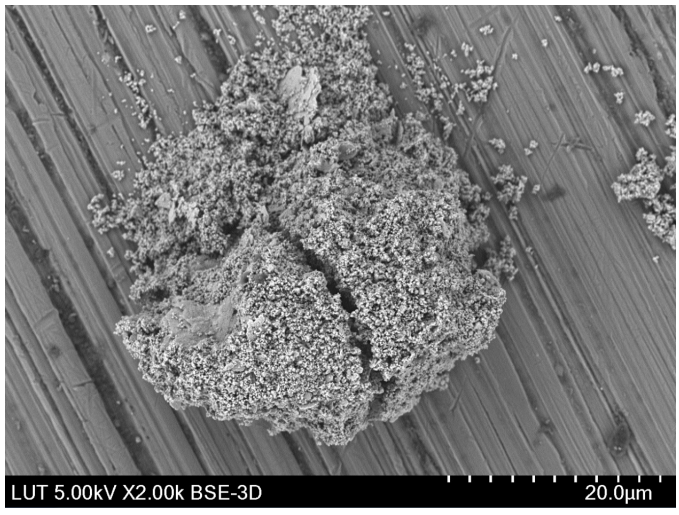

Figure 2.8: The results of SEM imaging featuring a Teflon additive particle on an undamaged race segment.

The examples of different SEM imaging results are presented in Fig. 2.7 and 2.8. Fig. 2.7 has been taken from the pitting area of a bearing after it has been subjected to continuous EDM for more than a thousand hours. There are two major features of this image: big unevenly shaped elements that have high metal contents with low oxidation levels, and small pits, less than one micrometer in size, filled with elements, that can be characterized as organic, and are probably from lubricant base oil. The pattern of these small features is the one, which is characteristic to pitting damage, and the size of these features is directly related to the energy of single discharge (Tischmacher and Gattermann, 2010), which is proportional to the bearing capacitance and breakdown voltage squared. In comparison to this "frosted pattern" a normal state of bearing raceway is characterised by the visibility of polishing traces. The example of such polishing traces can be seen in Fig. 2.8: there is a single Teflon additive particle surrounded by the healthy bearing surface.

2.4.2 Non-intrusive diagnostics

As of 1989, different studies (i.e., (Soediono, 1989)) case-by-case advocate the use of on-line non-intrusive diagnostics in order to decrease the maintenance costs. The recent developments in the field of electronics made it possible to use computers and embedded micro-controllers to process significant amounts of data on-line. This change enabled the development of non-intrusive diagnostics.

The approaches to non-intrusive diagnostics are mainly based on the analysis of measured operational parameters of the electrical drive such as torque, phase current, and stator frame vibration. The methods of signal analysis can be divided into two main categories: time-domain and frequency-domain methods.

Time-domain methods operate with magnitude and energy-related parameters of measured waveform or one of its derivatives. As an example — in case of shaft position — monitoring can provide the position itself, velocity, acceleration, and jerk measurements of which each can be a useful metric for certain defects. A typical use-case includes obtaining such derivative and then filtering it in a certain bandwidth with a band-pass filter. Then, either a peak value of the waveform or an energy-metric, such as the RMS value of the sample, is obtained. The resulting measurement is called feature and used by a diagnostic system to determine the state of the machine. Current industrial standards (ISO 20816: Measurement and evaluation of machine vibration and ISO 10816: Evaluation of machine vibration by measurements on non-rotating parts) for vibration and current-based diagnostics mostly rely on time-domain analysis of signals filtered in certain frequency bands. The same standards, however, briefly propose frequency-domain analysis, offline shock wave study, and even grease residue analysis as methods to perform diagnostics in such cases when time-domain study is unable to separate fault-specific frequencies of vibration and variations occurring during the normal operation.

In the frequency-domain approach either a Fourier or a wavelet transform is first per-

formed. The resulting curve is then analysed, using the a priori knowledge of machine shaft rotation frequency and bearing dimensions. Due to the non-linear effects of steel compression the vibrations in a machine always occur with a significant number of harmonics, occurring on both, odd and even, multiples of the first-order harmonic. It is also common to see harmonic side bands around the main rotation frequency f_{shrot} with frequency of $f_{\text{shrot}} \pm (n \cdot f_{\text{f}})$, where f_{f} is the first-order fault frequency and n is a non-zero integer. The following equations to compute first-order harmonic frequencies for damage occurring in bearings are commonly used (i.e., (Li et al., 2000)):

- Outer ring pass frequency

$$f_{\text{BPO}} = \frac{N_{\text{BB}}}{2} f_{\text{shrot}} (1 - \frac{D_{\text{BB}}}{D_{\text{c}}}) \tag{2.15}$$

- Inner ring pass frequency

$$f_{\text{BPI}} = \frac{N_{\text{BB}}}{2} f_{\text{shrot}} (1 + \frac{D_{\text{BB}}}{D_{\text{c}}}) \tag{2.16}$$

- Ball rotation frequency

$$f_{\text{B}} = \frac{D_{\text{c}}}{2D_{\text{BB}}} f_{\text{shrot}} (1 - \frac{{D_{\text{BB}}}^2}{{D_{\text{c}}}^2}) \tag{2.17}$$

In these equations D_{BB} is bearing ball diameter and D_{c} - cage diameter (Fig. 2.2).

2.5 Models of bearing discharge activity

Bearing current during discharge. In the study (Chen et al., 1996) an attempt to model the currents flowing in the frame-bearing-rotor circuit is made. The study uses a simplified electrical circuit and transmission line approach to model the applied bearing voltage, charging behaviour of the rotor to frame capacitance and bearing currents after the occurrence of discharge. The study (Muetze and Binder, 2007b) proposes a set of models for behaviour of bearing currents during the discharge that are suitable for indirect estimation of bearing currents from external measurements and knowledge of system's physical dimensions. The work of (Magdun et al., 2011) continues this approach and expands it with more experimental results for a larger motor.

Probability discharge model. The works of (Tischmacher et al., 2014) and (Tischmacher et al., 2015) describe the probabilistic model of discharge activity.The authors of the paper suggest approximating by regression the variables that affect bearing capacitance from

measurements performed on a bearing identification rig described in (Wittek et al., 2010) and (Wittek et al., 2012).

FEM simulation. The research published in (Kolbe et al., 2012) proposes FEM simulation of a bearing ball to race contact area with a lubricant intermediate layer. The study considers the thermal conductivity of steel and lubricant to create a transient heat model. The results suggest a localised short-term heat rise up to 3500 K. The authors argue that this is a sufficient temperature rise to cause localized melting and vaporisation of the surface material.

2.6 Damage mitigation techniques

One of the primary focuses for many studies had been the search for efficient damage mitigation techniques.

Electrostatic insulating cage. In the work of (Busse et al., 1997b) the capacitive nature of EDM currents has been targeted with a proposed ESIM design. The electrostatic insulation in such design is achieved with a Faraday cage installed in the air gap of the machine. Three different design approaches were proposed: conductive tape or spray in the gap, and copper-plated slot sticks. These methods were experimentally proven to reduce the BVR by up to 90%. However, a full enclosure of the stator winding in a Faraday cage is not an economically viable option for already existing machines, and a rather expensive protection method. It is also not a solution for machines that have power supplied externally to the rotor. A later experimental study (Magdun et al., 2010b) concluded that for short-rotor machines, where the end-winding significantly contributes to the winding to rotor capacitance, the electrostatic shielding, applied between that overhang and the rotor of the machine is an effective (with up to 80% reduction) solution. FEM computation of a wire to rotor capacitance has been carried out in a study by (Ferreira et al., 2012). The modelling and corresponding experimental results suggest a two times decrease in the overall winding to rotor capacitance due to slot-embedded partial electrostatic shield. Based on the modelling results the residual capacitance is an end-winding capacitance, that was not modelled in the FEM problem. In the study of (Heidler et al., 2016) further improvements to this mitigation method are proposed, such as counter-measures to eddy currents — a side effect, which is induced in the shield.

Grounding. Poor grounding of a machine is commonly recognized as a source for rotor-to-ground currents, if the rotor is grounded, too. In addition, improper grounding can undermine the efforts to mitigate bearing currents with electrostatic insulation and shunt the bearings with a rotor to frame liquid metal or brush contact (Schiferl and Melfi,

2004). (Link, 1999) provides an extensive list of issues that should be considered in the design of the grounding system. Such issues listed in (Link, 1999) include:

- The impedance of grounding path at high frequencies. The study notes that the selection of material is important due to the different behaviour of material impedance with frequencies.
- The influence of inductive coupling between the grounding path and the supply voltage should be assessed and utilized to minimize the impedance.
- Use of 360 degree connectors for cabling system is highly recommended to prevent HF propagation.

Bearing insulation. The idea to insulate the bearings to prevent damage from circulating and EDM currents has been proposed to standards for electrical machinery design in the work of (Daugherty and Wennerstrom, 1991). The typical implementation consists of an insulated layer between NDE bearing and frame. However, in mitigation of EDM and rotor-to-ground currents, this method has been proven to be insufficient (Link, 1999). This is mainly due to EDM and rotor-to-ground currents being of higher frequency ("typically in the range of 50 kHz - 1 MHz (Link, 1999)") whereas circulating currents due to magnetic asymmetries are typically in the order of hundreds of Hertz (Alger and Samson, 1924). A notable exception to that inefficiency is suggested in the study of (Muetze, 2004): the research indicated that a single side insulation can be helpful in the case of circulating bearing currents due to high-frequency components of the PWM signal. The improvements to this method were proposed as hybrid bearings (with ceramic ball elements (Ebert, 1990)) and improved insulating coatings (50 - 250 µm thick oxidized layers) for bearing balls were introduced. With such big insulating thickness it is not possible for breakdown to occur. However, this method of insulation is more expensive than conventional bearings and has some side-effects. First, the high-frequency components of voltage tend to propagate through motor to load coupling and induce extra voltage on the load shaft. If such load does not have its own ceramic bearing balls, the discharges start to occur in the load bearings the same way as in scenario with rotor-to-ground currents (Schiferl and Melfi, 2004). Second, the insulation layer also affects thermal conductivity of bearings resulting in lower heat transfer capacity from the rotor shaft to motor frame (Link, 1999). Finally, to this date, there is no clear understanding on the waveforms of currents, that occur during discharge and flow through the RC circuit, formed by the breakdown channel in lubricant. This is mainly due to lack of measurement techniques, that would be able to detect these currents in non-invasive way. A detailed assessment of mitigation effectiveness of bearing insulation and rotor grounding for AC machinery of up to 500 kW is presented in (Muetze and Binder, 2007a).

Bearing shunting. An opposite to the idea of insulating the bearing is the idea to shunt bearing with a low-impedance path, i.e. carbon brushes (Boyanton and Hodges, 2002).

Such shunting should prevent bearing currents from flowing through the bearing, and thus prevent discharges and degradation. The main drawback of this method is that, while it is effective in dealing with EDM currents, it could subject other bearings in the same drive train to circulating or rotor-to-ground currents (Schiferl and Melfi, 2004). The proper shunting may require installation of both shunting brush and bearing insulation on most or all bearings of the drive train while considering the issues of the proper grounding itself. In addition to that, the type of grounding brush should be considered carefully. In the study of (Boyanton and Hodges, 2002) an observation has been made, that carbon brushes leave carbon on the rotating shaft, resulting in increased impedance, that compromises grounding efficiency.

Supply voltage filtering is a mitigation method directed specifically against the root cause of EDM currents - high order harmonics of PWM signal. The idea is to filter those harmonics before they enter the inverter-machine connection cable, or at least before they enter the machine. This can be achieved with passive RLC circuits, that are configured as low-pass filter. In (von Jouanne et al., 1996) a first-order shunting scheme is presented and compared to other filtering methods, that add serial inductance to cable. The results of this experimental work and simulations indicate, that the proposed shunting method is efficient, and has an advantage of not inducing extra losses to the circuit. Further studies on filtering techniques proposed and evaluated other topologies: RL-Plus-C (Yuen and Chung, 2015), RL-Plus-Cm (Wu et al., 2016), capacitively coupled shunting (Ludois and Reed, 2015)

Modifications to inverter operation. One of the potential solutions to the problem of EDM currents is to prevent high-appearance frequency harmonics in the spectra of supplied voltage waveform through the design of inverter. These proposals can be separated in three categories: reduction of switching frequency, increasing the amount of voltage levels used by inverter, and topology designs, that focus on common mode voltage compensation.

The reduction of switching frequency of inverters has been proposed to mitigate harmonic composition in (Tran et al., 2016). The study suggests use of advanced control design to reduce switching frequency during some parts of the switching cycle that allows to reduce THD down to 4.8 %.

The concept of multilevel switching in inverter design has been inspired by (Nabae et al., 1981). The work proposed use of 5-level switching topology to mitigate harmonics with numbers 17 and 19, and completely eliminate harmonics below the 13-th. Later works proposed multilevel switching concpets with seven, nine, and even more levels of switching, reducing the harmonic distortion of the supplied voltage even further. The study (Rodríguez et al., 2002) features a review on these topologies and claim of less than one percent of THD for an 11-level switching topology.

First attempts to modify the circuit design of a standard 6-switch 3-phase inverter was undertaken in (Zhang et al., 2001). The study proposes a reduced-switch double bridge inverter, that aims at mitigation of common mode voltage and claims the 10-times decrease in voltage variation in comparison to conventional B4 inverter topology. Further study of (Han et al., 2017) proposes balanced inverter topology with 20 dB attenuation in the frequency range of up to 10 MHz. The study, however, points out, that higher frequency ranges cannot be effectively cancelled due to imperfections of switching transitions.

3 Materials and methods

3.1 Research plan

The research had two distinctive types of experimental work: a long-term bearing degradation setup and a scale model of bearing grease degradation processes due to electrostatic discharges. The initial literature survey suggested the long-term bearing degradation approach as one of the well-established methods of investigation in the field of studying of the bearing degradation. The studies (Tischmacher and Gattermann, 2012; Singleton et al., 2017) successfully utilised this approach to get insight into the physics of the degradation process. Later in the research a scaled setup approach was chosen to verify the proposed hypothesis of grease being destroyed and causing the conductivity of the bearing under the discharge. Another aim of the setup was to establish quantitative measures of grease degradation. Different experiments on scale models were successfully performed in the field of Tribology by (Prashad, 2006), which was considered sufficient proof efficiency of the scaled modelling for this phenomenon.

3.2 Laboratory setup

This subsection describes the technical equipment and interconnections used in different versions of each of the two test rigs used in this study and reasoning behind the choices made for the study.

3.2.1 Long-term degradation.

The long-term bearing degradation setup was designed in accordance with the results of previous studies by (Niskanen et al., 2014). The structure of the test rig is presented in Fig. 3.1. The studies suggested the two-motor composition with one of the motors being a driving motor, and the other — a load (tested) one. Unless specified otherwise, this text further refers to the bearings of the load motor, while the bearings of the driving motor are not considered of interest, as they were not subjected to artificial discharging.

Motor and bearing dimensions. During all iterations and versions of the test setup, both motors were serially produced 15 kW, 3-phase, 4-pole induction machines. The bearings used in both motors were 6309 deep grove ball bearings with C3 class of clearance. The lubricating material used in the tested bearings varied during the different iterations of the experimental work, as described in the results section.

Motor coupling. The motors were coupled with an insulating coupler, and the laser alignment procedure was performed to reduce vibrations possibly arising from the shaft misalignment. The purpose of the insulating coupler, as opposed to a rigid metal coupling, was to prevent bearing currents of a driving motor reaching the tested bearings. The bearing currents in the driving motor could have been caused by inverter used as voltage source.

Insulation. All bearings were electrically insulated from the stator frame with polyethylene sleeve in order to avoid the influence of circulating and HF bearing currents, possibly produced by normal machine operation. However, the insulation of the DE bearing of the tested motor was shortened by the current-measurement probe thus forming the complete current loop through the bearing, shaft, voltage source transformer and stator frame. This allowed measuring the actual bearing current, and confirmed the origin of the electromagnetic discharges and verification of impedance state (capacitive or resistive) in which the bearing was at the moment of measurements.

External voltage application system. In order to perform the degradation of bearing in a controlled manner, the natural bearing currents were suppressed to the best achievable degree. On the contrary, an alternating voltage was applied between the shaft and the stator frame of the tested motor from an external voltage generator. As the discharging bearing currents are known to arise mainly from high-frequency components of PWM voltage due to capacitive properties of the circuit (as described in subsection 2.1.2 of this book), the voltage was applied as a narrow-band sine waveform. The centre frequency of the band (300 kHz) was selected in accordance with existing research for the motors of similar geometry (Niskanen et al., 2014).

3.2.2 Grease degradation

General description The schematic of the scaled model of grease degradation is presented in Fig. 3.2. The test setup was designed to imitate the geometry of the contact between the bearing ball and running race. The large scale factor was selected, in order to obtain damaged material in such quantities that would be sufficient to definitive testing, using the FTIR and XRD methods. However, the upper bound was imposed on the distance between the ball and the plate by the requirement to have enough voltage to cause the initial breakdown of the lubricating material. The voltage levels, that were achieved by the discharge generators, allowed to cause initial breakdowns of all tested samples with ball to plate distances of up to $D = 200\,\mu\text{m}$ (Fig. 3.2).

Components of test rig The experimental setup has been produced from an industrially manufactured micrometric screw by welding a ball from 6309 ball bearings to the inner

end of a corkscrew and glueing a square segment of a copper-plated PCB to the inner side of a micrometer's frame. The DC voltage has been supplied through a variable rate transformer, constant 1:10 transformer and an H-bridge rectifier. The rectifier had 4.7 nF ceramic capacitors used for input and output filtering and 5 kΩ current limiting resistors.

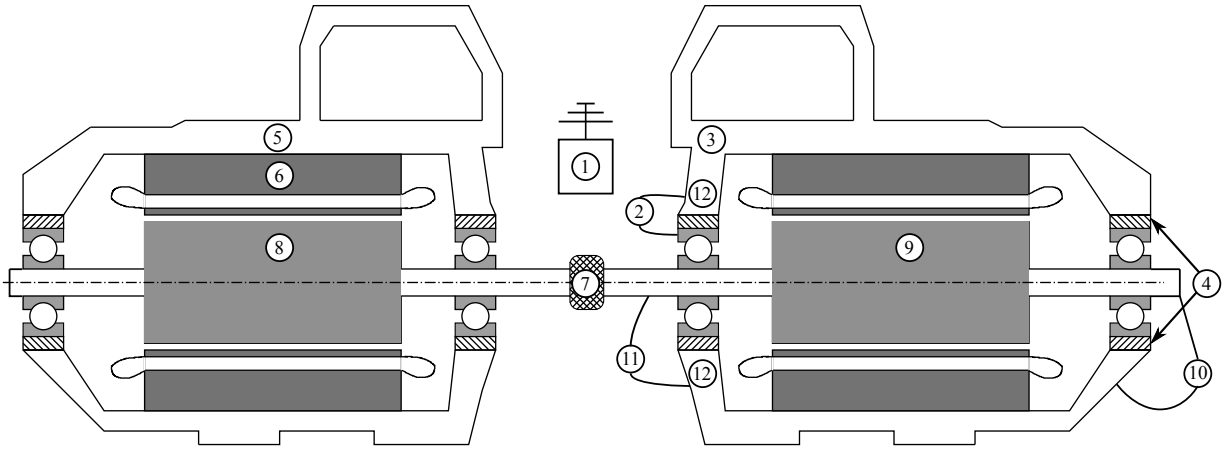

Figure 3.1: Schematic of long-term degradation laboratory test setup. 1) RF measurement equipment; 2) Current measurements; 3) Piezo-electric accelerometer installed in the same plane as DE bearing; 4) Bearing insulation; 5) Frame; 6) Stator; 7) Insulating coupler; 8) Driving motor; 9) Test motor; 10) Adjustable voltage source; 11) Measurements of voltage applied to bearing; 12) Bearing temperature probes.

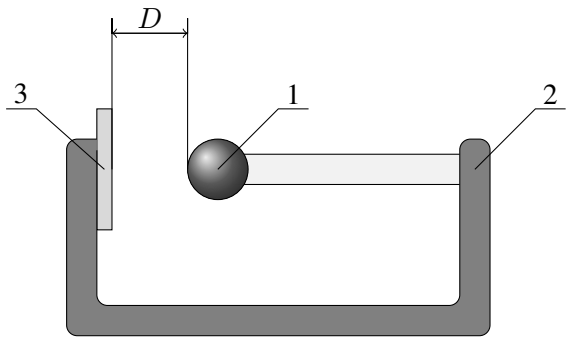

Figure 3.2: Schematic of grease degradation scale model test rig. 1) 17.5 mm diameter bearing ball. 2) Modified 1-axis micrometric screw for exposure of bearing grease to electric discharges. 3) Printed circuit board fragment made of FR4 insulating material.

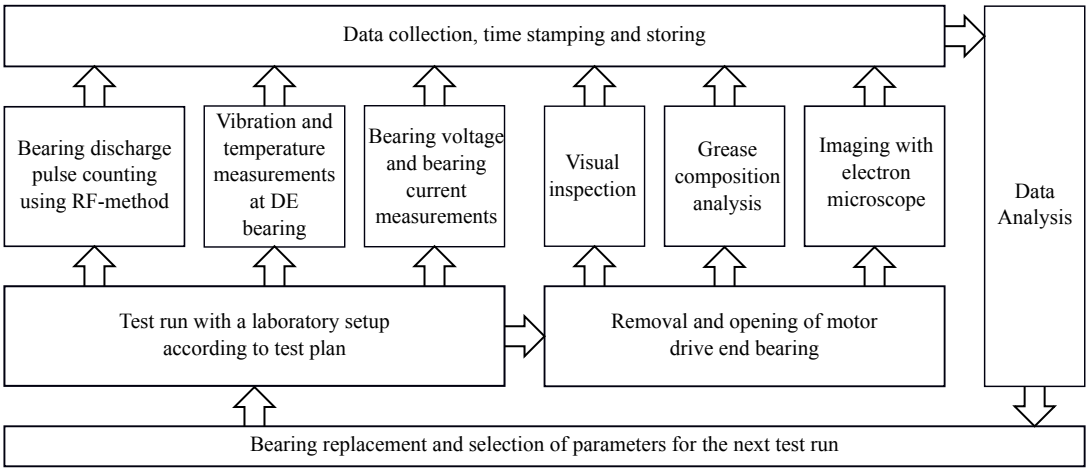

Figure 3.3: The generalised structure of long-term degradation study.

3.3 Test procedure

3.3.1 Long-term degradation

The long-term bearing degradation was performed, using the general structure, presented in Fig. 3.3. Each iteration of experimental work began with the analysis of existing literature and results obtained from previous iterations. Then, the test parameters, such as the estimate of the desired experiment duration, motor rotation speed during the experiment, external voltage parameters (magnitude, frequency and time intervals for application) were corrected to achieve maximal damage to the affected bearing in the shortest possible time frame.

3.3.2 Grease degradation

The scaled grease degradation experiment has been conducted as follows. For each lubricating materials six samples had been taken from the storage container after thorough mixing - 24 samples in total. Each of these 24 samples has been subjected to degradation process for the duration of about one hour.

At the beginning of iteration for each of samples the test area between the copper plate and ball has been cleaned with dry paper towel. Then the distance between the ball and plate was set to 3 mm, and a sample was introduced into the gap with metal stylus. After that, the voltage was applied to the system. The magnitude of DC voltage was maintained at 1350 V during the period of discharging, using the feedback voltage measurement provided by a multimeter. After the initial application of voltage, the ball to plate distance was gradually decreased until the initial discharge occurred. After all initial discharges, bearing immediately became conductive, hence, in order to facilitate discharges, the dis-

tance was increased until the discharge activity became stable. During tests, the discharge activity varied significantly, and samples often became either fully conductive or formed air and lubrication layer that was able to prevent discharges completely. In such cases, the ball to plate distance was adjusted to restore the discharging activity: the distance was increased, when the sample became conductive, and decreased, when it began to isolate discharges completely. At the end of each one hour long iteration, the sample was removed and added to the corresponding damaged sample storage container. At the end of all six iterations for each of the lubricating materials, the damaged samples of that material were mixed together.

3.4 Lubrication materials

A total of four lubrication materials were used in the process of grease degradation under high voltage discharging. In the table 3.1 basic information on grease components is presented. Mineral oil base for lubricants is typically produced from the fossil oils and consists of mixture alkanes. The length of the carbon chains for these alkanes is the defining factor for lubricant's thickness and temperature properties. Synthetic poly-alphaolefines oil base are polymers of alkenes. Usually, only poly-alphaolefines with low molecular weight (low length of carbon chain) are used for lubrication purposes. Synthetic silicone oil base are polymers of siloxanes, of which the most typically used as lubricating material is polydimethylsiloxane. Thickener additives for non-silicon lubricants are soaps of corresponding metal.

The materials feature different mechanical properties and different rate of dependency on the temperature of the environment. The results of rheometry were fitted into the model

Table 3.1: BASE OIL AND THICKENER TYPES OF INVESTIGATED GREASES

Grease	Base oil type	Thickener type	Additive
A	mineral oil	multi-soap complex	–
B	mineral oil	aluminium complex	–
C	synthetic silicone	silicone based	–
D	synthetic poly-alphaolefines	lithium complex	extreme pressure and poly-tetrafluoro-ethylene (PTFE)

Table 3.2: OVERVIEW OF VISCOSITY MEASUREMENTS

Grease	Temperature [°C]	Power law index n	Proportional coefficient KP	Proportional coefficient $KP_{\text{t=0}}$ at 0 °C[Pas^n]	Temperature dependent coefficient KP_{tdep} [Pas^n/°C]
A	25	0.1443	966.4326		
A	40	0.1289	767.5365	1230.2	-11.036
A	60	0.1109	577.1500		
B	25	0.1270	384.0011		
B	40	0.0564	312.5129	457.7	-3.272
B	60	0.0124	267.4456		
C	25	0.0913	1007.8		
C	40	0.1064	964.4926	1145	-5.024
C	60	0.0789	834.8803		
D	25	0.01303	591.2107		
D	40	0.1157	516.3991	731.0	-5.483
D	60	0.1210	399.9867		

of power-law fluid for which the following holds.

$$b = KP(T_{\text{lubr}})y^n, \tag{3.1}$$

where y is shear ratio, n - power law index and $KP(T_{\text{lubr}})$ is proportional coefficient, that depends on the lubricant temperature T_{lubr} as

$$KP(T_{\text{lubr}}) = KP_{\text{t=0}} + KP_{\text{tdep}}T_{\text{lubr}}, \tag{3.2}$$

where $KP_{\text{t=0}}$ is the value of temperature

In the table 3.2 the measured mechanical properties of lubricating materials are provided. The measurements were performed with Anton Paar MCR 302 rheometer.

3.5 Diagnostic algorithms

After considering the commonly used methods of non-intrusive diagnostics presented in 2.4.2, the following methods were selected and applied for the purpose of incipient damage monitoring during the experiments.

3.5.1 Time-domain analysis

The vibration signal has been sampled at intervals of 5 min with the sampling duration of 20 s and the frequency of 20 kHz. The resulting samples were analysed in time-domain, using peak-to-peak value of sample, RMS value of sample, and crest factor — ratio of peak value to RMS value. The first and second order derivatives of signals were also computed to apply the same methods to the derived signals. It is important to keep in mind that time-domain derivation is equivalent to application of a high pass filter, that has gain growing continuously with frequency. In that aspect, multiple application of derivation results in amplification of features, that can be otherwise seen in high frequency bands.

Additionally, peak counting algorithm was applied to time-domain measurements. The algorithm was counting rising edges for vibration pulses with magnitude above one, two, and three times greater than the RMS value of sample.

3.5.2 Frequency-domain analysis

In the frequency domain the samples were scrutinised, using by analysis of frequency bands around the characteristic frequencies, related to bearing dimensions f_{BPO} (eq. 2.15), f_{BPI} (eq. 2.16), and f_{B} (eq. 2.17), and first ten multiples of those frequencies.

After considering those individual frequencies, a wide frequency range analysis was performed, using waterfall plot representations of changes in vibration spectra over time. The low frequency range from 1 to 1000 Hz and low frequency range from 1 to 10 kHz were studied individually, as the behaviour of individual frequencies is more significant at low frequencies, while at high frequency range the vibration characteristics are typically wide band.

As the final approach, the behaviour of components of the so-called envelope spectra were considered. In order to produce such spectra, a wide band of high frequency components was selected. Bands from 1 to 3 kHz, 2 to 5 kHz and 2 to 3 kHz were studied closely. For each of such bands the signal was first filtered in frequency domain by zeroing out the components outside of this range, thus performing ideal digital filtering of signal. The filtered signal was converted to the time domain, and the absolute value envelope of time-domain waveform was computed. The resulting envelope was finally converted back to

the frequency domain and analysed in the low frequency range (1 to 1000 Hz), and for the narrow bands related to individual components of bearing.

3.6 Simulation of mechanical degradation during discharges

The design of automated fault detection algorithms in general requires big amounts of input data. However, in the case of a system like bearings, it is hard to obtain precise information on the internal states of the system (i.e., the state of race track). A detailed commented listing of the proram, that was used to perform this numerical simulation, is presented in Appendix B. The aim of this system is to replace the need of a real system measurements with physics-based simulation of the degradation process. In this chapter the principal components of the model are described.

3.6.1 System components

The system is modelled on the edge of several fields. Each field is represented by a single model component.

Transient mechanical modelling component. TMMC performs a 1-dimensional simulation (along the x-axis) of the position of mechanical components of the system, such as machine frame, rotor and shaft positions. The system is modelled, using the spring-dampener linear model, described in subsection 2.2. Using this approach, it is possible to perform similar parametrisation of a typical shaft-bearing-frame system with a rigid load to the DE connection and rigid body model of a rotor shaft.

The linear model is presented in Fig. 3.4, and the forces and masses of the rigid body model of the rotor shaft are presented in Fig. 3.5. State-space variables of the model are:

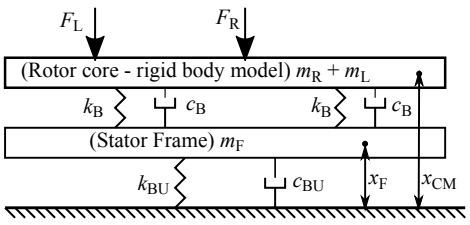

Figure 3.4: The mechanical model of a loaded motor. Here F_L is force exerted on the rigid rotor by the load, F_R - force exerted on the rotor due to rotor unbalance, k_B - spring stiffness coefficient of bearing, c_B - damping coefficient of bearing, k_{BU} - spring stiffness coefficient of bushings, c_{BU} - damping coefficient of bushings, m_F - mass of frame, m_R - mass of rotor and m_L - mass of load.

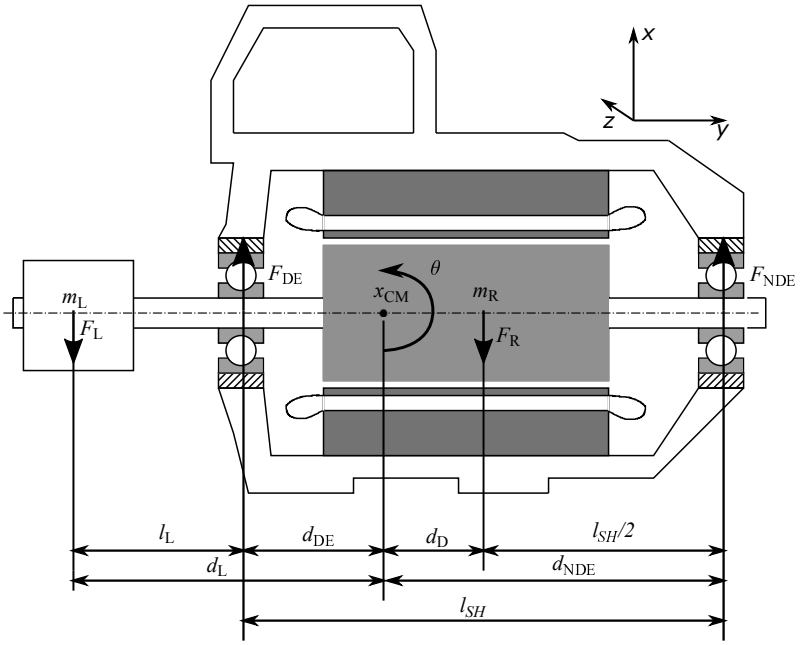

Figure 3.5: Forces and masses of the rigid rotor model.

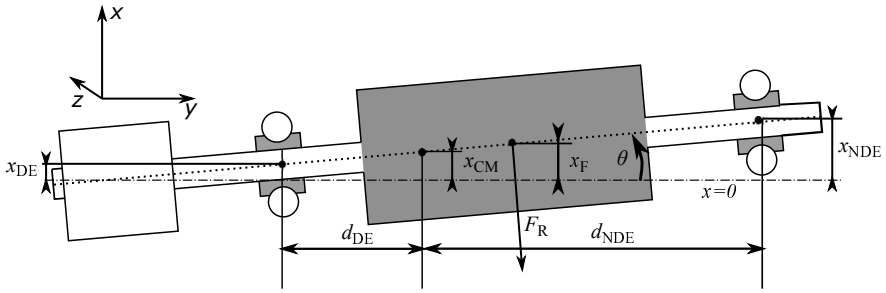

Figure 3.6: Example of used coordinate system in the case of small shaft centre line offset with respect to $x = 0$ coordinate and small rotation around z-axis.

- x_{F} - x-axis coordinate of machine frame and its first derivative.
- x_{CM} - x-axis coordinate of centre of mass for the rotor-shaft-load system and its first derivative.
- θ - angle of rigid rotor body movement in the elastic bearing suspension around its centre of mass and its first derivative.

The characteristic distances of load centre of mass d_{L}, rotor centre of mass d_{R}, DE bearing plane of rotation d_{DE}, d_{D} - displacement of common center of mass and NDE bearing plane of rotation d_{NDE} are defined according to Fig. 3.5.

The dynamics of the machine frame are described by

$$\frac{d^2x_{\mathrm{F}}}{dt^2} = \frac{-k_{\mathrm{BU}} \cdot x_{\mathrm{F}} - c_{\mathrm{BU}} \cdot \frac{dx_{\mathrm{F}}}{dt} - F_{\mathrm{DE}} - F_{\mathrm{NDE}}}{m_{\mathrm{F}}}, \tag{3.3}$$

where m_{F} is mass of frame, k_{BU} - spring stiffness coefficient of bushings and c_{BU} - linear dampening coefficient of bushings, F_{DE} - force, produced by DE bearing, F_{NDE} - force, produced by NDE bearing. The kinematic equations binding this rigid rotor model are as follows. The acceleration of centre of mass point

$$\frac{d^2x_{\mathrm{CM}}}{dt^2} = \frac{F_{\mathrm{t}}}{m_{\mathrm{R}} + m_{\mathrm{L}}} = \frac{F_{\mathrm{DE}} + F_{\mathrm{NDE}} + F_{\mathrm{R}} + F_{\mathrm{L}}}{m_{\mathrm{R}} + m_{\mathrm{L}}}, \tag{3.4}$$

where m_{R} is mass of rotor and shaft, m_{L} - mass of load, F_{t} is total force acting on center of mass of the system, F_{R} - forces occurring in rotor due to mechanical unbalance and gravitation and F_{L} - force occurring in load due to mechanical unbalance and gravitation. Then, the angular acceleration with respect to the centre mass point

$$\frac{d^2\theta}{dt^2} = \frac{-F_{\mathrm{DE}} \cdot d_{\mathrm{DE}} + F_{\mathrm{NDE}} \cdot d_{\mathrm{NDE}} - F_{\mathrm{R}} \cdot d_{\mathrm{D}} + F_{\mathrm{L}} \cdot d_{\mathrm{L}}}{J_{\mathrm{eff}}}. \tag{3.5}$$

Using Huygens-Steiner theorem, the effective moment of inertia for the whole system can be computed as

$$J_{\mathrm{eff}} = J_{\mathrm{R}} + J_{\mathrm{L}} + m_{\mathrm{R}} \cdot d_{\mathrm{D}}^2 + m_{\mathrm{L}} \cdot d_{\mathrm{L}}^2, \tag{3.6}$$

where rotor moment of inertia J_{R}, is roughly estimated according to rod model, which is a valid estimate for rotors with longer stack ($l_{\mathrm{axial}} > 3 \cdot r_{\mathrm{R}}$). In addition, in computation of J_{R}, l_{SH} was used instead of l_{axial} to combine moment of inertia of the whole shaft into a single model. A numerical example, demonstrating validity of this approach is given in Appendix E.

$$J_{\mathrm{R}} = \frac{m_{\mathrm{R}} l_{\mathrm{SH}}^2}{12}, \tag{3.7}$$

where l_{SH} is length of rotor shaft and J_{L} is taken as 0, due to load moment of inertia J_{L} being negligible in comparison to $m_{\mathrm{L}} \cdot d_{\mathrm{L}}^2$.

An example of displaced rotor with position variables marked is presented in Fig. 3.6. The resulting coordinates for the drive end and the non-drive end location of the bearings can be computed, using the aforementioned state variables as follows.

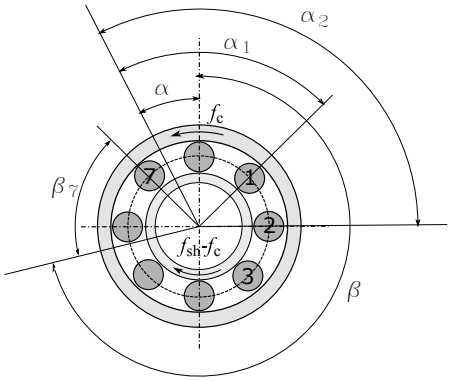

Figure 3.7: Rotary coordinate system used to define position of bearing balls with respect to inner and outer races of the bearing.

$$x_{\mathrm{DE}} = x_{\mathrm{CM}} - \sin(\theta) \cdot d_{\mathrm{DE}}, \tag{3.8}$$

$$x_{\mathrm{NDE}} = x_{\mathrm{CM}} + \sin(\theta) \cdot d_{\mathrm{NDE}}, \tag{3.9}$$

or, under the assumption of small values of θ,

$$x_{\mathrm{DE}} = x_{\mathrm{CM}} - \theta \cdot d_{\mathrm{DE}}, \tag{3.10}$$

$$x_{\mathrm{NDE}} = x_{\mathrm{CM}} + \theta \cdot d_{\mathrm{NDE}}. \tag{3.11}$$

The coordinate system was defined to track bearing ball positions with respect to inner and outer race surface (Fig. 3.7). The coordinate system was fixed to the rotation frame of bearing cage. Thus, each of 8 balls has it's own fixed position defined by the angle δ_{i} from $2\pi/N_{\mathrm{BB}}$ to 2π. In addition to that two angles were defined. Angle α, that describes angle of rotation between the outer ring of the bearing and the cage.

$$\alpha = f_{\mathrm{c}} \cdot 2\pi \cdot t, \tag{3.12}$$

where f_{c} is rotation frequency of bearing cage

$$f_{\mathrm{c}} = f_{\mathrm{shrot}} \cdot (r_{\mathrm{inner}})/(r_{\mathrm{inner}} + r_{\mathrm{outer}}), \tag{3.13}$$

where r_{inner} is radius of bearing inner ring and r_{outer} is radius of bearing outer ring.

And angle β describes angle of rotation between the inner ring of the bearing and the

cage.

$$\beta = (f_{\text{shrot}} - f_{\text{c}}) \cdot 2\pi \cdot t \tag{3.14}$$

Together with δ_{i} equations (3.12) to (3.14) define position of individual bearing with respect to the surface of rings

$$\alpha_{\text{i}} = \delta_{\text{i}} + \alpha \tag{3.15}$$

and

$$\beta_{\text{i}} = \delta_{\text{i}} - \beta \tag{3.16}$$

Linear damping coefficients for bearings are estimated as $c_{\text{B}} = 1200\,\text{N}\,\text{m}/\,\text{s}$, according to the measurements performed in (Jacobs et al., 2014). Instead of using the linear stiffness coefficients, the actual force produced by bearing is a vector sum of all forces, produced by individual balls of the bearing in accordance with the empirical EHL lubrication equation for minimal thickness of lubrication layer. The thickness of lubrication layer is estimated as the displacement of drive end and non-drive end shaft segments with respect to the frame and bearing manufacturing clearance l_{cl} of 5 µm as per class 3 of standard.

$$H_{\text{min}} = l_{\text{cl}} - (x_{\text{B}} - x_{\text{F}})\text{sin}(\alpha) - l_{\text{outer}}(\alpha) - l_{\text{inner}}(\beta), \tag{3.17}$$

where x_{B} is position of corresponding bearing of rotor mechanical model, $l_{\text{outer}}(\alpha)$ and $l_{\text{inner}}(\beta)$ are heights of inner and outer running surface at the angular locations of bearing ball.

The lubrication film versus load force equation (Hamrock and Dowson, 1977) is as follows

$$H_{\text{min}} = 3.63VD^{0.68}G^{0.49}W^{-0.073}(1 - e^{0.68k_{\text{ell}}}), \tag{3.18}$$

where VD - dimensionless speed factor, G - dimensionless material factor, W - dimensionless load factor, k_{ell} - ellipticity parameter.

This equation was modified by grouping constant factors into a single k_{const} parameter and solving the equation with respect to force, produced by the lubricant from the value of lubricant minimal thickness

$$k_{\text{const}} = 3.63G^{0.49}(1 - e^{0.68k}), \tag{3.19}$$

$$W = \frac{{k_{\text{const}}}^{13.70} V D^{9.32}}{{H_{\text{min}}}^{13.70}}. \tag{3.20}$$

For the purpose of proof of concept modelling run, the k_{const} was parametrised, using the estimated load of 15 kW drive, used in experimental setups, and typical value for lubricant thickness H_{min}, that was derived from the observed bearing voltages before the break down of lubricant occurred, and known dielectric strength of the lubricant.

The motor motion was excited through:

1) Shaft rotation around its own axis with f_{SH} = 25 Hz causing change in α and β and producing force due to elastohydrodynamic contact, when running surface height changes.

2) Gravitational pull on motor ($F_{\text{rotorgrav}}$) and load (F_{L})

$$\{F_{\text{L}}\}_{\text{N}} = 9.8 \cdot \{m_{\text{L}}\}_{\text{kg}} \tag{3.21}$$

$$\{F_{\text{rotorgrav}}\}_{\text{N}} = 9.8 \cdot \{m_{\text{R}}\}_{\text{kg}} \tag{3.22}$$

3) Unbalance force of 50 N, acting on rotor with frequency of f_{SH}.

$$\{F_{\text{rotorunb}}\}_{\text{N}} = 50 \cdot \sin(\{f_{\text{SH}}\}_{\text{Hz}} \cdot 2\pi\{t\}_{\text{s}}) \tag{3.23}$$

Hence, total external force acting on rotor is

$$F_{\text{R}} = F_{\text{rotorgrav}} + F_{\text{rotorunb}} \tag{3.24}$$

Bearing race surface component. BRSC is important to simulate the effects of EDM pitting damage on the measured vibration signal and activity of discharges. The tracking of both inner and outer race condition was performed, using a height map with the resolution of 0.1 µm in xy-plane and 0.1 nm in z-axis. Each of the tracked surfaces was modelled as a 10 µm wide strip covering the whole circumference of the corresponding ring.

The surfaces were initialized to have a roughness of 0.02 µm. The algorithm to generate pitting damage, based on the energy of the discharge, and location of the discharge was as follows.

1) In the first step, the radius r_{melt} of area, molten by single discharge, was computed, based on the estimated dependency between melted volume of material and energy E_{disch} of a single discharge by (Tischmacher and Gattermann, 2010)

$$\{r_{\text{melt}}\}_{\text{m}} = (\frac{2\{E_{\text{disch}}\}_{\text{J}}}{2.2 \cdot 10^{10}})^{\frac{1}{3}}. \tag{3.25}$$

Here, the energy is doubled, as the discharge has to have at least two times higher volume, than the one predicted by this equation, to melt the predicted amount of the material, as the computation of material removed happens against a plane, rather than a completely filled volume.

2) In the second step, the actual volume of material in the affected area is computed, and the material is removed by reducing the height of the corresponding material columns.

3) In the third step, the material is refilled into the affected area, according to the equation of a perfect sphere with the radius proportional to the volume of removed material.

Electrical circuit model component. The ECMC was designed to predict the timing and energy of electrostatic discharges in accordance with the breakdown voltage of the lubricating layer and rotor to frame capacitance. The circuit consists of a constant current supply, a chargeable capacitance, and a breakdown switch. The capacitance is assumed to be of a typical value for bearing capacitance, that was measured for a reference 15 kW machine and has the value of 100 pF. The influence of rotor to frame capacitance on the charging process was neglected, as the existing knowledge of the process is not sufficient to model its influence on discharge. The voltage rises on the capacitance over time, as it is charged according to the capacitance equation

$$\frac{dU_{\text{rf}}}{dt} = \frac{I}{C_{\text{B}}}. \tag{3.26}$$

At each step of the modelling of the mechanical system, this voltage is compared with the thickness of the lubricating material between all balls and corresponding contact points. If the resulting field strength is greater than 15 MV/ m (according to (Busse et al., 1997c)), it is considered that the breakdown occurred. At that point, the energy of the discharge is computed as the total energy of the capacitor

$$E_{\text{disch}} = \frac{U^2 C_{\text{B}}}{2}. \tag{3.27}$$

3.6.2 Variation of parameters during modelling runs

The modelling has been performed in three separate sensitivity tests. The modelling runs were performed, using the initial condition of the running surfaces with normally distributed heights. The values of height were distributed with the standard deviation of 0.2 µm and average value of 0 µm. For each of the tests, eight steps of variation have been performed for the variable, which was used for the sensitivity analysis. The rest of parameters were kept at nominal values. The nominal parameters of model are as presented in table 3.3.

Table 3.3: Nominal model parameters

Model parameter	Nominal value	Unit
k_{const}	$3 \cdot 10^{-6}$	
l_{cl}	$5 \cdot 10^{-6}$	m
C_{B}	100	pF
VD	1	-
l_{SH}	1	m
d_{L}	0.2	m
m_{R}	40	kg
m_{F}	50	kg
m_{L}	20	kg
k_{BU}	$2 \cdot 10^{5}$	N/ m
I	$1 \cdot 10^{-7}$	A
c_{B}	1200	N m/ s
c_{BU}	$6 \cdot 10^{3}$	N m/ s
J_{R}	$1/12 \cdot m_{\text{R}} \cdot l_{\text{SH}}^2$	
f_{shrot}	25	Hz
r_{inner}	27.5	mm
r_{outer}	45	mm

Lubricant bearing coefficient sensitivity analysis was performed for k_{const} from $2 \cdot 10^{-6}$ to $6.2 \cdot 10^{-6}$ with step size of $0.6 \cdot 10^{-6}$.

Bearing clearance sensitivity analysis was performed for l_{cl} from 4 µm to 10.3 µm with step size of 0.9 µm.

Bearing capacitance sensitivity analysis was performed for C_{B} from 20 pF to 209 pF with step size of 27 pF.

3.6.3 Modelling process

The system modelling has been performed, using first order Euler method with variable time step. This method was selected as it requires the least amount of system states recorded, which is important, considering the amount of memory, that is required to store the full height map of damaged bearing with reasonable precision. The computation time step has been selected according to the following commonly used algorithm:

1) Preserve initial state space variables $x(t_{\mathrm{j}})$ and derivative $\dot{x}(t_{\mathrm{j}})$ at the t_{j}.

2) Compute two steps of Euler modelling with current time step dT_{j}, starting with

$$x(t_{\mathrm{j+1}}) = x(t_{\mathrm{j}}) + dT_{\mathrm{j}} \cdot \dot{x}(t_{\mathrm{j}}). \tag{3.28}$$

Then compute new derivative $\dot{x}(t_{\mathrm{j+1}})$ at system state $t_{\mathrm{j+1}}$, according to the model equations above and finally

$$x(t_{\mathrm{j+2}}) = x(t_{\mathrm{j+1}}) + dT_{\mathrm{j}} \cdot \dot{x}(t_{\mathrm{j+1}}), \tag{3.29}$$

3) Compute one step of Euler modelling with double current time step $2dT$ from the preserved state space

$$x'(t_{\mathrm{j+2}}) = x(t_{\mathrm{j}}) + 2dT_{\mathrm{j}} \cdot x(t_{\mathrm{j}}). \tag{3.30}$$

4) Estimate local error of modelling $\tau(t_{\mathrm{j}})$ based on difference between $x(t_{\mathrm{j+2}})$ and $x'(t_{\mathrm{j+2}})$ as

$$\tau(t_{\mathrm{j}}) = \frac{2 \cdot |x(t_{\mathrm{j+2}}) - x'(t_{\mathrm{j+1}})|}{|x(t_{\mathrm{j+2}})| + |x'(t_{\mathrm{j+2}})|}. \tag{3.31}$$

5) Using the known local error, upper dT_{max} and lower dT_{min} bounds on time step, and given tolerance value τ_{tol}, compute the $dT_{\mathrm{j+2}}$ as

$$dT_{\mathrm{j+2}} = \max(dT_{\mathrm{min}}, \min(dT_{\mathrm{max}}, k_{\mathrm{corr}} \cdot dT_{\mathrm{j}})), \tag{3.32}$$

where correction factor $k_{\mathrm{corr}} = 0.5$ if $\tau(t_{\mathrm{j}}) > \tau_{\mathrm{tol}}$ and $k_{\mathrm{corr}} = 1.05$ otherwise.

6) Repeat from step one for $t_{\mathrm{j+2}}$

According to (Gear, 1971), this approach ensures local error of modelling to stay below the specified bound of τ_{tol}. For the purpose of modelling for the current study, τ_{tol} has been chosen as 0.01. dT_{min} has been selected as 0.1 femtosecond. In order to let system detect and react on the surface roughness bumps, dT_{max} has been selected based on the average thickness of lubricating layer for the DE bearing:

- For lubricating layer thickness less than 1 µm, dT_{max} was equal to 5 ns.
- For lubricating layer thickness more than 1 µm,

$$\{dT_{\text{max}}\}_{\text{s}} = 5 \cdot 10^{-9} + 10 \cdot (\{l_{\text{lubr}}\}_{\text{m}} - 10^{-6}). \tag{3.33}$$

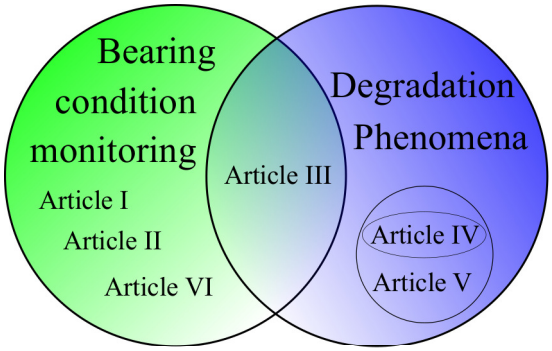

Figure 4.1: The allocation of published publications between topics.

4 Results

Each of the publications, comprising the bulk of this work, is structured as a scientific report on the experiment or experiments, that have been performed to obtain additional knowledge about the phenomena of bearing currents. The reports begin with a brief introduction to the underlying problem of the experiment and review of relevant publications, describing the state-of-the-art situation. Each introduction is followed by detailed description of laboratory setup, measurement procedure and, where applicable, the methods of laboratory analysis. After that, each paper presents the significant results of measurements with graphical or tabular representation. The results section is followed by the analysis of obtained measurements and discussion of these results in the scope of existing state-of-the-art situation. The papers are finalised by a condensed summary of conclusions drawn from the results.

The experiments carried out focus on two main aspects of the degradation process: the underlying physical and chemical phenomena, and on the aspects of bearing state diagnosis. The studies can be, respectively, separated as ones studying the bearing degradation and o focusing on the diagnostic aspects. The separation of publications between these two focuses is presented in Fig. 4.1. The study presented in Publication I approaches the problem of diagnosing the bearing degradation, using a combination of radio-frequency based counting of discharge events in combination with the vibration measurements. Publication II follows the results of Publication I with an attempt to get an insight into the degradation of grease chemistry over the runtime of bearing degradation test. Publications III and V follow up on the observed changes of grease properties with an artificially scaled discharging setup. Publications IV and VI continue the study of different diagnostic approaches with respect to the bearing discharge degradation. The detailed review of these publications and important results is presented further in this chapter.

4.1 Publication I: Study of incipient bearing damage monitoring in variable-speed drive systems

Motivation The study described in the publication was aimed at studying the outcomes of vibration and radio-frequency monitoring in the context of a long-term degradation of bearings under discharging bearing currents.

Method The paper describes the measurements performed, using the long-term degradation test setup. The test setup consisted of a driving 3-phase, 15 kW, 4 pole, squirrel cage motor and a similar motor, disconnected from the power supply as a load and test motor. The machines were coupled, using flexible non-conductive coupler, and aligned with laser positioning to prevent vibrations, caused by coupler flexing.

In this setup configuration, the bearings of load motor were electrically insulated from the stator of load machine, and an external voltage source has been applied to the NDE bearing in order to facilitate the discharges. The supplied voltage had sine waveform with the frequency of 300 kHz and the magnitude of 20 V peak-to-peak. The tested bearings were deep groove 6309 ball bearings with the standard lubricant, as provided by the manufacturer. The lubricant was based on mineral oil with lithium-soap as thickening additive.

The test run was started with a pre-run preparation for two days. After that period, the external voltage was applied. Since the application of voltage, the test run lasted for a total of 1184 hours. After that, the system was stopped in order to verify, that the degradation process has begun, and to check, if there are visible changes on the running traces. This was done by cutting the bearing and submitting it to the SEM imaging.

Results The visual inspection of the bearing indicated the presence of narrow (about 2 mm wide) pitting area on the bottom of the NDE bearing, which was submitted to the discharging. Both the drive and NDE bearings appeared healthy. The results of SEM imaging of the pitted area showed pattern full of what was at that point assumed to be craters up to 0.6 µm in diameter. Imaging of other parts of the cut segments indicated no significant changes with respect to the reference new bearing of the same type.

The paper then analyses how much energy was introduced into the system, during the experiment, using the results of radio-frequency monitoring and estimates of bearing capacitance. This analysis is followed by the basic narrow frequency band inspection of vibration intensities that occurred in the bands, related to bearing inner race, outer race, and ball rotation frequencies. The study concluded that it is sufficient to have bearing degradation with even small amounts of energy introduced to the system.

4.2 Publication II: Vibration measurement approach to the bearing damage evolution study in the presence of electrostatic discharge machining currents

Motivation and method Following the results of Publication I on the detection of discharges, using radio-frequency based method and analysis of damage, the Publication II performs a second iteration test in the similar conditions. The major differences between these test were:

- Increased external voltage magnitude, using both much powerful signal generator and a 1:2 ratio high-frequency transformer. The resulting confirmed voltage magnitude on the shaft was 55 V peak-to-peak at the same, as in previous experiment, frequency of 300 kHz. This change was theorised to increase the damage on the bearing surface, as it was expected to see higher voltage levels on the discharged capacitance.
- Switch to variable shaft rotation frequency between 22.5 and 25 Hz from constant 25 Hz operation. This change was aimed to confirm the claims of previous studies and observations, that variable operation significantly increases the discharge currents. This change was also intended as a way to increase the observable damage.
- The duration of the experiment have been increased up to 2500 hours, in order to see further steps of degradation progression.

Results The results of visual inspection of the bearing surface indicated fully formed 3 mm wide pitting tracks on both the outer and inner ring of the bearing subjected to the external voltage. The SEM analysis of tracks indicated similar melted pattern, as in the case of experiment in Publication I. Temperature monitoring indicated 2-3 degrees temperature increase, during the same time periods, as the increase in vibration suggesting mechanical heating of bearing due to friction.

In this publication the frequency composition analysis of vibration signal has also been performed. The analysis resulted in clear indication that increase in vibration occurs mainly due to high-frequency components. This suggested that main source of additional vibration is the short-term sharp peaks, appearing in the time-domain representation of the signal. The metric of discharge activity, defined in the paper as minimal envelope, showed significant correlation with the intensity of jerk signal (first derivative of acceleration signal, that was measured directly from the accelerometer attached to stator frame in yz-plane).

4.3 Publication III: Influence of electric discharge activity on bearing lubricating grease degradation

Motivation The study described in the third publication focuses on the grease degradation phenomena. The degradation of grease components occurs due to both the high electrical field density, occurring in the gap between bearing races and balls, and high temperature bursts that happen during the arcing discharge in the same gaps.

Method In order to facilitate grease destruction and allow better understanding of the process, the standard grease was removed from the bearing and replaced with a mineral-oil based grease with multi-soap complex thickener and no additional additives. In addition to that, the study program was modified to include multiple intervals. Each interval had a different shaft rotation speed, that was selected on the basis of tuning the rotation speed until the maximal discharge activity was observed. Also, the supplied voltage has been further improved to 60 V peak-to-peak, although the results of previous research indicated that it would not directly affect the energy of a single discharge, but rather the magnitude of current that flows through the bearing, during the direct conductivity state.

After 940 hours of ageing the grease, the system has been stopped, and bearings removed. In order to perform the analysis of running surface, they were cut after the grease samples were taken.

Results Visual inspection of sampled grease indicated that the grease, washed out of the bearing, had changed to darker colour than the brand new grease.

The comparative composition of DE (subjected to electrical and mechanical wear), NDE bearing (subjected only to mechanical wear) and fresh grease sample, taken from the container supplied by manufacturer, was performed. This comparison indicated the appearance of hydroxy group in the DE sample and decrease in Calcite composition of both worn grease samples with respect to the fresh grease.

The patterns of discharge activity, observed in this study, additionally support the hypothesis, that constant speed operation modes are much safer for the motors, that are susceptible to bearing current issues, than cyclic usage. In the study, the discharge activity pattern, during each of the operation intervals, was that of exponential decay over time.

4.4 Publication IV: Effects of electrostatic discharges on bearing grease electric properties

Motivation Following the findings of previous publications, it was decided to perform an experiment to determine how electrostatic discharges affect lubricating materials typically used in rolling bearings.

Method A 100:1 scale model of a bearing ball to outer race junction was assembled. The setup used micrometric screw with 10 µm precision to control the distance between the ball of a 6309 bearing and a copper plate. The space between two was filled with the tested material. The terminals of an electrostatic discharge generator were attached to the plate and ball together with the terminals of a portable oscilloscope.

The oscilloscope was set to trigger on a falling edge of voltage discharge. After the application of discharge generator voltage, the voltage built up on the capacitor formed by the ball and the plate until a breakdown voltage was reached, and the discharge happened. The experiment was performed for multiple samples of each of four grease types.

Results The results of the experiment featured the significant degradation of sample breakdown voltage after the initial discharge. In some cases, series of breakdowns ended with the grease being in a conducting, resistive state, and no further testing was possible. The others featured the process of restoration of sample's insulating properties after the initial degradation. It was noted, that different types of lubricants behave in different ways, while samples of the same lubrication type were consistent in their behaviour.

The study also featured the results of rheological measurements of studied materials and suggested the possible relation of observed behaviour pattern under serial electrostatic discharges to the rheological properties of the greases. The study further indicated that resistive behaviour of bearings, under the effect of bearing currents, can happen without metal-to-metal contact between ball and running races or metal particles in the lubricant.

4.5 Publication V: Effects of electrostatic discharges on bearing grease dielectric strength and composition

Motivation In order to expand the initial results, presented in Publication IV, the experimental grease degradation setup was modified to allow for continuous discharging over significant volumes of the grease sample for longer periods of time. In order to do that, the setup was equipped with wirelessly controlled stepper motor, allowing safe remote control of energized system. Additionally, the discharging generator was replaced with the circuit capable of generating DC voltage of up to 2.5 kV with continuous output power rating of up to 3 W.

Method The grease samples were subjected to continuous discharging under the supplied DC voltage of 1350 V. During the discharge process, the voltage was kept constant, while the distance varied in order to keep the discharging activity going. I.e., to prevent the system to go into the DC mode, the ball to plate distance was increased by 280 µm steps and, in cases, when the discharge activity would stop due to insufficient voltage to cause breakdown, the distance was decreased until the point, when the discharge activity was restored. Each sample was treated in the discharging setup for one hour. Then samples of similar grease type were combined, thoroughly mixed, and their chemical composition was studied.

Results The resulting samples were subject to comparison using the FTIR spectrometry and X-Ray crystallography. The analyses featured a decline in the absorption of infra-red waves in the so-called fingerprint band (400-2000 cm^{-1}), that relate to components used as additives in these greases. The changes in proportion of absorbed light between the fingerprint band and the CH bending band (2600-2900 cm^{-1}) suggest changes of thickener to oil proportion in composition of the grease samples.

4.6 Publication VI: Incipient bearing damage monitoring of 940-hour variable speed drive system operation

Motivation The study focuses on the analysis of the vibration and radio-frequency monitoring results, that were obtained during the 940-hour long test run, described in the Publication III, in order to deduce, which frequencies in the observed vibration spectra can be used for the purpose of incipient monitoring of bearing failure.

Method The study carried out the long-term degradation test run, using the methodology described in subsection 3.2.1. Discharge activity was defined as amount of RF pulses above 5 mV threshold, which were counted, using the antennae and oscilloscope. Such discharges were previously proven to originate from discharge currents, that happen during lubricant breakdown (Niskanen et al., 2014). The bearing was cut, in order for the surface to be visually examined, and SEM imaging to be performed. Finally, the estimation of the energy introduced into the system was performed, using the discharges, that were counted using the radio-frequency detection.

The results of vibration and radio-frequency based monitoring were analysed, using different approaches:

- Time-domain intensity of narrow bands around frequencies, specific to bearing dimensions and shaft rotation speed (f_{BPO}, f_{BPI}, f_{B}).
- Frequency-domain analysis of high frequency spectra evolution during the experiment.
- Spectral analysis of envelope of high-frequency components of the 3-5 kHz band.

The study performed the sensitivity analysis of vibration signal spectral composition for a 2-dimensional bearing defect model for a bearing damage being normally distributed around single point with the number of damage points varying. Note, that the model presented in this publication has nothing in common with the model presented in subsection 3.6 of this book. The applicability and validity of the model, presented in Publication VI, was rather limited in comparison to the one, presented here. The core difference between the model of Publication VI and the model presented in subsection 3.6 is, that the former uses a dry contact model with force computation from simplified Hertzian contact equation, while the latter uses the EHL model, which is more realistic scenario for bearing current modelling. In the model of Publication VI the force was computed as if the bearing had no clearance, the shaft was fixed in place and the force was coming from all 8 bearings at the same time, so that the magnitude of defect would define the dominant force direction. Another significant difference is the way the damage distribution was simulated and not resulted from modelling of electrostatic discharges. The model, described Publication VI, used normal distribution of defect parameters. I.e., the center angles of defects

belonged to normal distribution with standard deviation of σ_{dd} and mean value of α_{center}, that was set to the value, corresponding to a point at the bottom of simulated bearing.

Results Visual inspection indicated presence of grey traces on the bearing that was subject to discharges, while no such traces were observed on the bearing subjected to only mechanical wear. The SEM imaging of traces confirmed the presence of pitting pattern on the surface of grey traces. The pattern of damage suggested formation of elevated areas of sizes up to 1.5 µm due to the surface melting and bigger (2-10 µm) damaged areas with complex shapes that do not resemble pitting patterns or initial polishing.

The analysis of vibration data indicated significant increase in vibration intensity in time domain over the duration of experiment. The composition of added vibration is mainly of the high-frequency components. The vibration samples, taken in the latest hours of the experiment, featured short term, high magnitude spikes. The analysis also indicated gradual increase in the intensity of the vibration in the 1 Hz band around the f_{B} frequency over the duration of the experiment.

5 Numerical modelling of bearing degradation process

5.1 Modelling hypotheses

After analysing the results presented in Publications I-VI, the following hypotheses were formulated to be tested in modelling process:

Hypothesis 1. Detectable variations in vibration, which are due to pitting and fluting damage, do not occur on the characteristic frequencies f_{BPO}, f_{BPI} and f_{B}, that are related to bearing dimensions, and described in subsection 2.4.2. The main reasoning behind this hypothesis is that, despite the detectable pitting damage during the long-term degradation runs, no detectable changes were observed on these frequencies.

Hypothesis 2. Pitting damage causes vibrations in the range from 1 to 5 kHz. Such changes were observed during long-term degradation tests. However, at that time it was understood, that there might be other factors causing such vibrations.

5.2 Modelling results

The results of numerical simulation of bearing degradation process are presented in this subsection. The vibration analysis was performed on the first derivative of frame velocity state variable. The results include:

- Progression of the vibration spectra over the duration of simulation. The progression is presented in the form of vibration spectra for lower and upper bounds of variation for parameter variable of each of the three sensitivity tests: k_{const}, l_{cl}, C_{B}. Every iteration of simulation spans one second of modelled time.

- Variation of the vibration metrics in time and with the variable, for which the sensitivity analysis was performed. The metrics analysed were the frequencies related to the rotation speed of shaft during the model f_{SH} = 25 Hz and computed from the modelled values of frame velocity as follows.

  First, the value of velocity of frame v_{F} state coordinate was obtained from the model output. The obtained data was then down-sampled to the frequency of 20 kHz or dT_{sampl}, using first-order hold. For each iteration of modelling this action resulted in velocity vector VV with 20000 elements. Then, the acceleration vector AV was computed for the frame by performing numerical derivation of the velocity signal.

$$AV_{\mathrm{i}} = (VV_{\mathrm{i+1}} - VV_{\mathrm{i}})/dT_{\mathrm{sampl}}, \tag{5.1}$$

where i is from 1 to 19999. Then, magnitude of discrete Fourier transform was computed using

$$\begin{aligned} FFT(VV,h) &= \sum_{k=1}^{N} VV_{\mathrm{i}}\omega_{\mathrm{N}}^{(i-1)(h-1)}, & (5.2)\\ \omega_{\mathrm{N}} &= e^{(-2\pi i)/N}, & (5.3) \end{aligned}$$

where h is from 0 to 9999, and for each of $FFT(VV,h)$ the magnitude of complex number was computed using

$$FFTmag(VV,h) = \sqrt{Re(FFT(VV,h))^2 + Im(FFT(VV,h))^2}, \tag{5.4}$$

Then, the individual metrics were computed.

1) RMS value of 2 Hz wide bands around frequencies, characteristic to bearing dimensions and shaft rotation speed f_{shrot} = 25 Hz (f_{BPO} = 75.86 Hz, f_{BPI} = 124.14 Hz, and f_{B} = 48.77 Hz):

$$RMS(f_{\mathrm{BPO}}) = \sqrt{\sum_{h=75}^{76} FFTmag(VV,h)^2/2} \tag{5.5}$$

$$RMS(f_{\mathrm{BPI}}) = \sqrt{\sum_{h=124}^{125} FFTmag(VV,h)^2/2} \tag{5.6}$$

$$RMS(f_{\mathrm{B}}) = \sqrt{\sum_{h=48}^{49} FFTmag(VV,h)^2/2} \tag{5.7}$$

2) RMS value of signal in the band from 1 to 5 kHz,

$$RMS(f_{\mathrm{B}}) = \sqrt{\sum_{h=1000}^{4999} FFTmag(VV,h)^2/4000} \tag{5.8}$$

3) Crest factor of sample was computed as

$$CF = \frac{max(AV)}{\sqrt{\sum_{i=0}^{19999} AV_{\mathrm{i}}^2/20000}} \tag{5.9}$$

5.2.1 Lubricant bearing coefficient sensitivity.

The spectra of vibration signal during the modelling for bearing coefficient sensitivity is presented in Fig. 5.1a and Fig. 5.1b. The individual spectra at the beginning and the end of the sensitivity analysis for the highest and the lowest values of parameter are presented in (Fig. 5.3 and 5.4). The main difference, that can be observed between the model runs with low (Fig. 5.1a) and high (Fig. 5.1b) load constant of lubricant, is the location of peak in the high frequency region from 1 to 5 kHz.

The evolution of vibration features during the modelling for bearing coefficient sensitivity is presented in Fig. 5.2. f_{BPO} features strong dependency on the bearing constant of lubricant and very low variations due to damage progression. f_{BPI} and f_{B} don't feature notable variations due to damage progression. Crest factor and RMS vibrations in the 1 to 5 kHz band grow steadily with the progression of damage. The crest factor, however, tends to saturate after 50 samples and has high magnitude spikes at some of early samples.

5.2.2 Bearing clearance sensitivity.

The spectra of vibration signal during the modelling for bearing clearance sensitivity is presented in Fig. 5.1c and Fig. 5.1d. The individual spectra at the beginning and the end of the sensitivity analysis for the highest and the lowest values of parameter are presented in (Fig. 5.6 and 5.7). The vibration signal of model with high clearance (Fig. 5.7) value has an abundance of 75 Hz harmonics (value of f_{BPO} at 1500 rpm). Despite being on the frequency of f_{BPO} and its multiples, these harmonics don't seem to vary with the operation and are present in the samples with very low amount of energy introduced into the system.

The evolution of vibration features during the modelling for bearing clearance sensitivity is presented in Fig. 5.5. f_{BPO}, f_{BPI}, and f_{B} feature strong dependency on the bearing constant of lubricant and very low variations due to damage progression. Crest factor slightly increases with more energy introduced in the process of degradation, but is not consistent within several samples, that have close amounts of energy introduced. RMS value of vibrations in the 1 to 5 kHz band grow steadily with the progression of damage. Fig. 5.5c shows a strong periodicity with a period of 8 iterations or frequency of approximately 0.12 Hz. The cause seems to be the situation, when bearing will exert high force upwards due to numerical computation artefacts, which would cause extreme shaft vibrations, which are not constrained by bearing from upper side due to high clearance

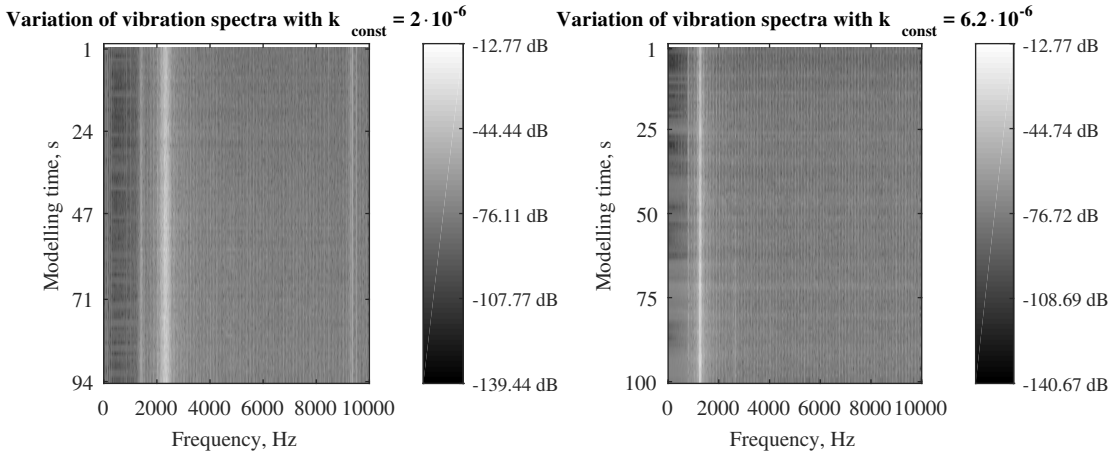

(a) Low lubrication bearing ability

(b) High lubrication bearing ability

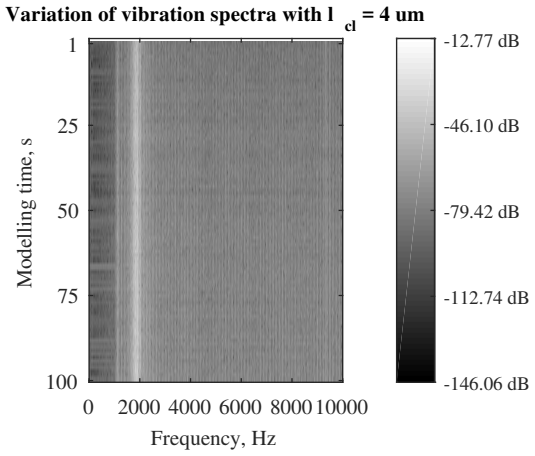

(c) Low bearing clearance

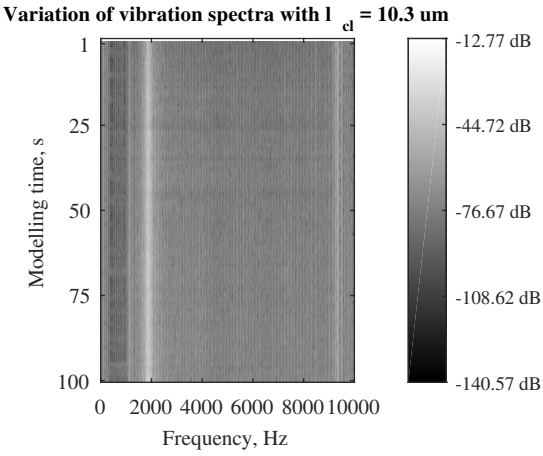

(d) High bearing clearance

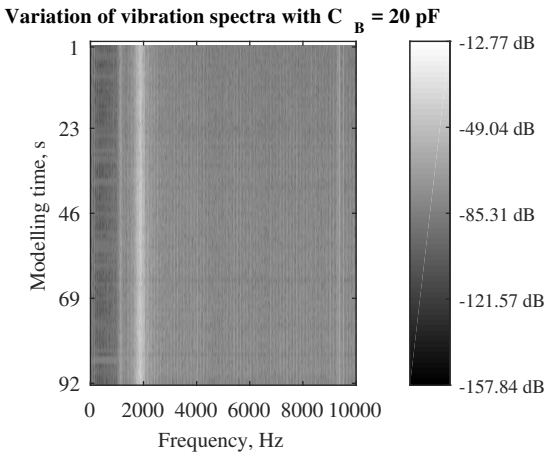

(e) Low bearing capacitance

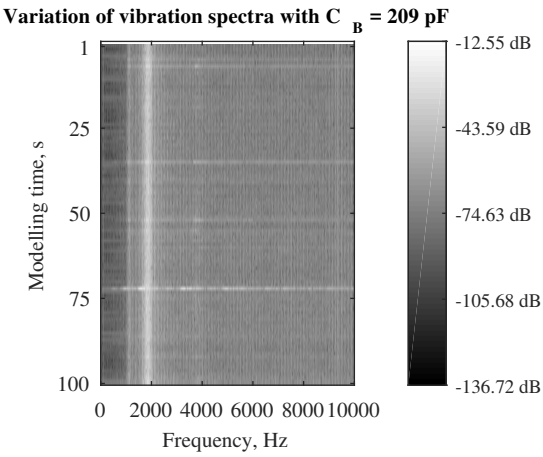

(f) High bearing capacitance

Figure 5.1: Spectra of frame acceleration signal for sensitivity analysis: a,b - lubricant bearing constant sensitivity; c,d - bearing clearance sensitivity, e,f - bearing capacitance sensitivity. Reference value for signal amplitude is 1 m/s^2.

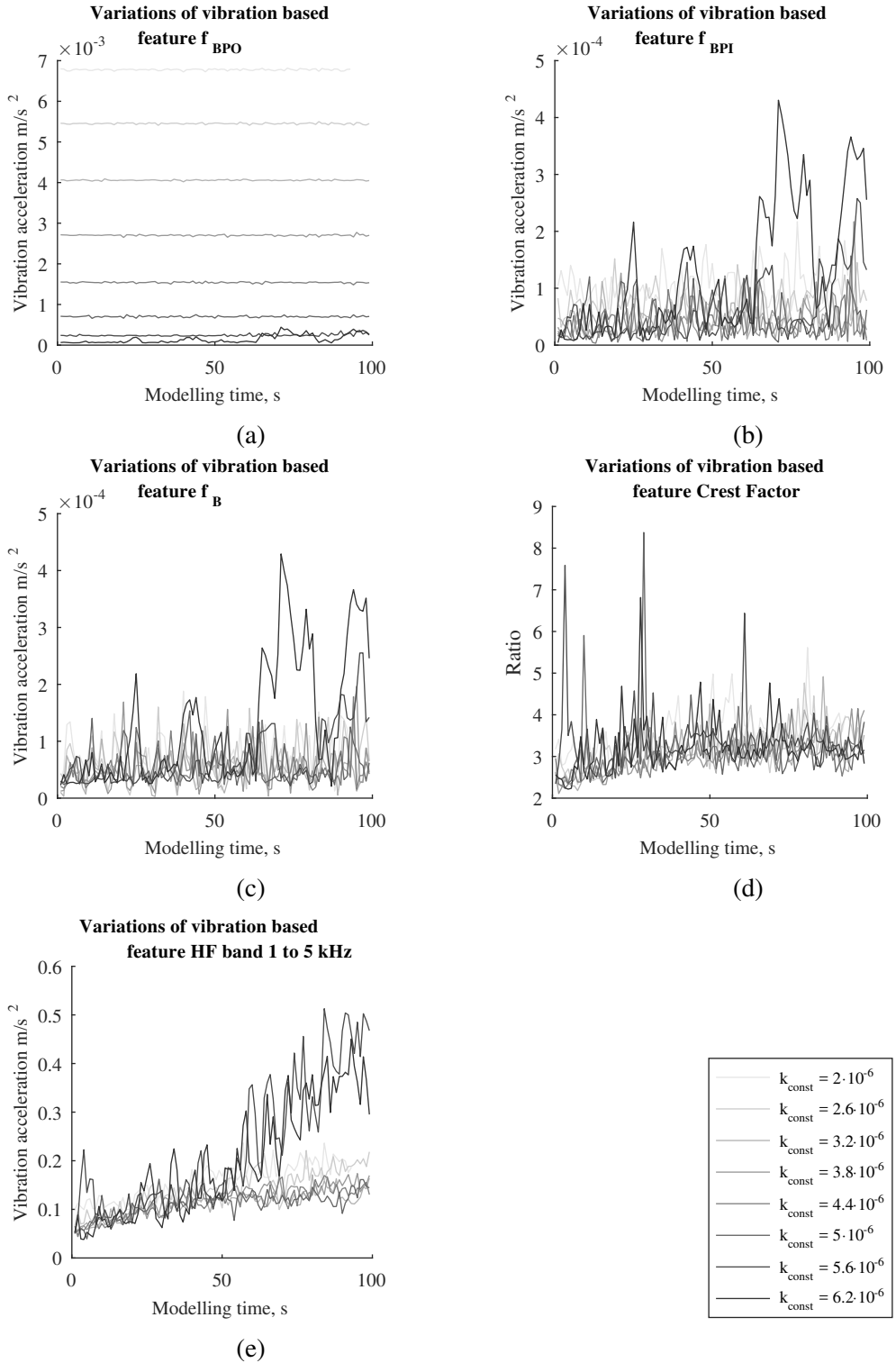

Figure 5.2: Development of vibration features over the duration of bearing coefficient sensitivity analysis.

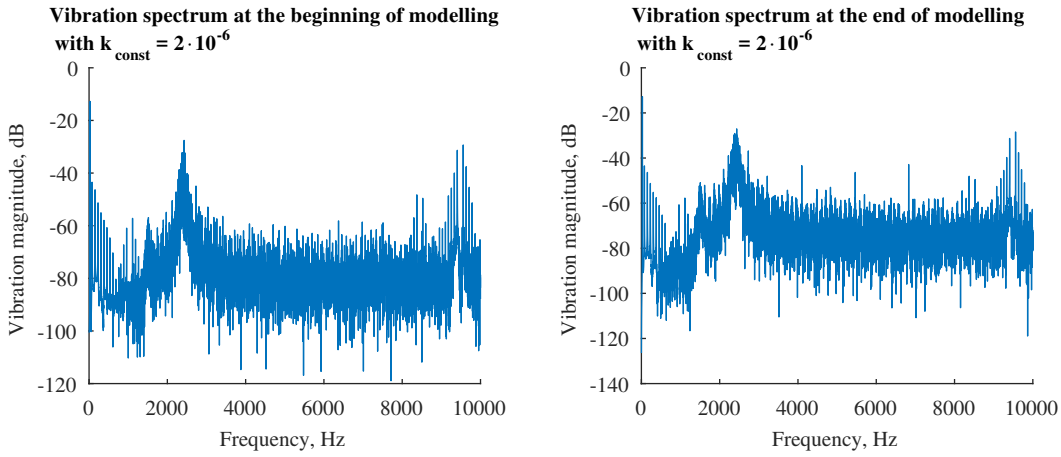

(a) (b)

Figure 5.3: Comparison of vibration spectra at the beginning (left) and at the end (right) of the sensitivity analysis with $k_{\text{const}} = 2 \cdot 10^{-6}$.

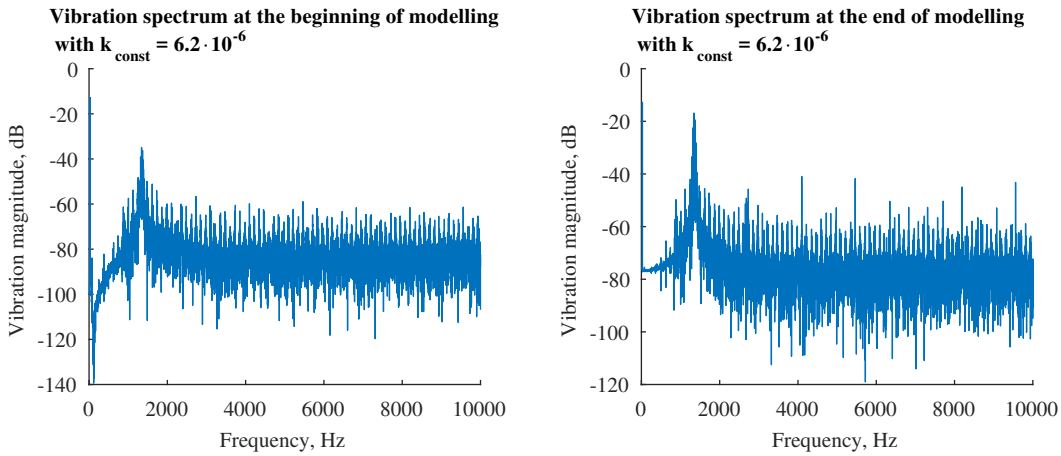

(a) (b)

Figure 5.4: Comparison of vibration spectra at the beginning (left) and at the end (right) of the sensitivity analysis with $k_{\text{const}} = 6.2 \cdot 10^{-6}$.

parameter.

5.2.3 Bearing capacitance sensitivity

The spectra of vibration signal during the modelling for bearing capacitance sensitivity is presented in Fig. 5.1e and Fig. 5.1f. The individual spectra at the beginning and the end of the sensitivity analysis for the highest and the lowest values of parameter are presented in (Fig. 5.9 and 5.10). The vibration signal spectra of modelling with high bearing capacitance have sharp wide band vibration pulses that are not observed for the spectra of low bearing capacitance. This is likely because the sizes of the corresponding pitting defects are proportional to the energy of a single discharge, and bigger size of defects means more intensive acceleration pulses when the ball passes above such defects.

The evolution of vibration features during the modelling for bearing capacitance sensitivity is presented in Fig. 5.8. f_{BPO}, f_{BPI}, and f_{B} do not indicate dependency with either the capacitance nor with the amount of energy introduced into the system. The strong peaks in Fig. 5.8a to Fig. 5.8d are most likely numerical artefacts that occurred with large values of bearing capacitance and, therefore, larger defects, which may be on the boundary of violating assumptions, required for use of EHL equation.

5.3 Correlation analysis of features obtained through modelling

The behaviour of f_{BPO}, f_{BPI}, f_{B}, crest factor, and RMS vibration of 1 to 5 kHz band was analysed, using correlation analysis against the total energy introduced into the system with electrostatic discharges from the beginning of the corresponding modelling iteration. The results of this comparison are presented in the Table 5.1. The plots of accumulated energy of discharges is presented in Appendix C. The scatter diagrams, corresponding to the correlation values presented in the Table 5.1 are presented in Appendix D.

6 Discussion

6.1 Modelling discussion

In this subsection the interpretation of modelling results and correlation analysis is done with respect to the hypotheses that were presented in subsection 5.1. The interpretation is followed by additional observations on the results.

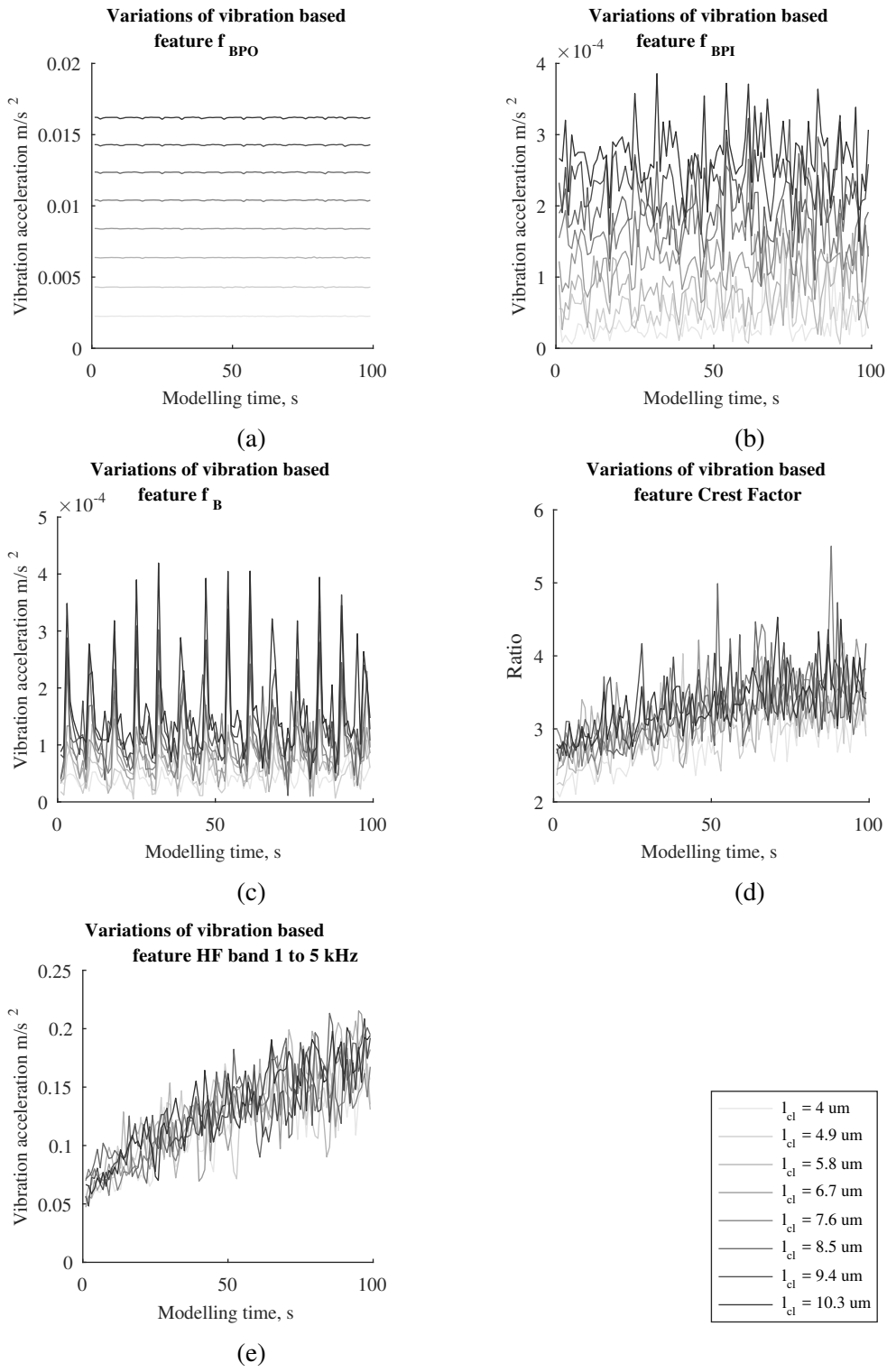

Figure 5.5: Development of vibration features over the duration of bearing clearance sensitivity analysis.

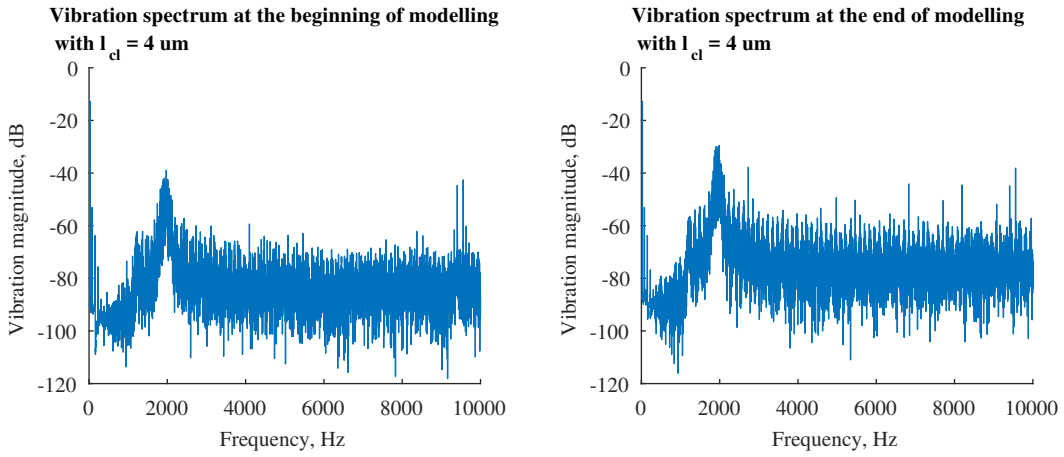

(a) (b)

Figure 5.6: Comparison of vibration spectra at the beginning (left) and at the end (right) of the sensitivity analysis with $l_{\mathrm{cl}} = 4\,\mu\mathrm{m}$.

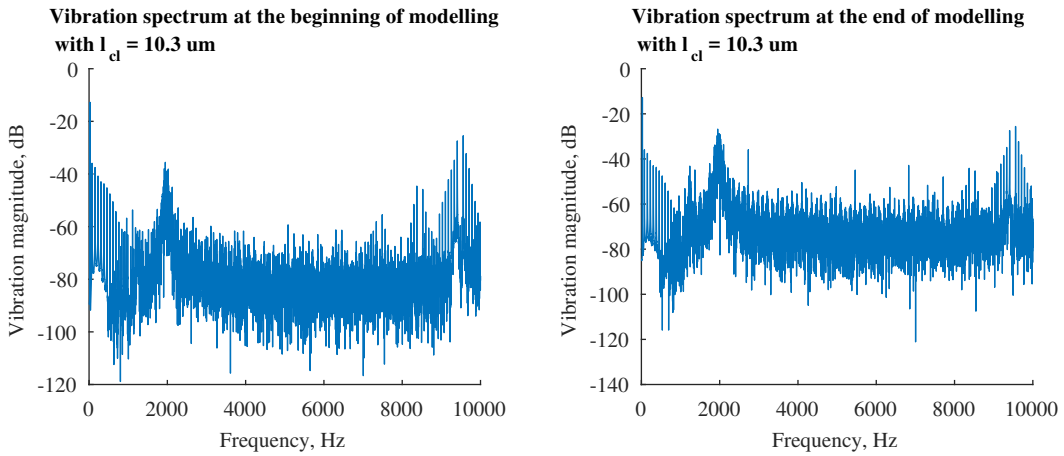

(a) (b)

Figure 5.7: Comparison of vibration spectra at the beginning (left) and at the end (right) of the sensitivity analysis with $l_{\mathrm{cl}} = 10.3\,\mu\mathrm{m}$.

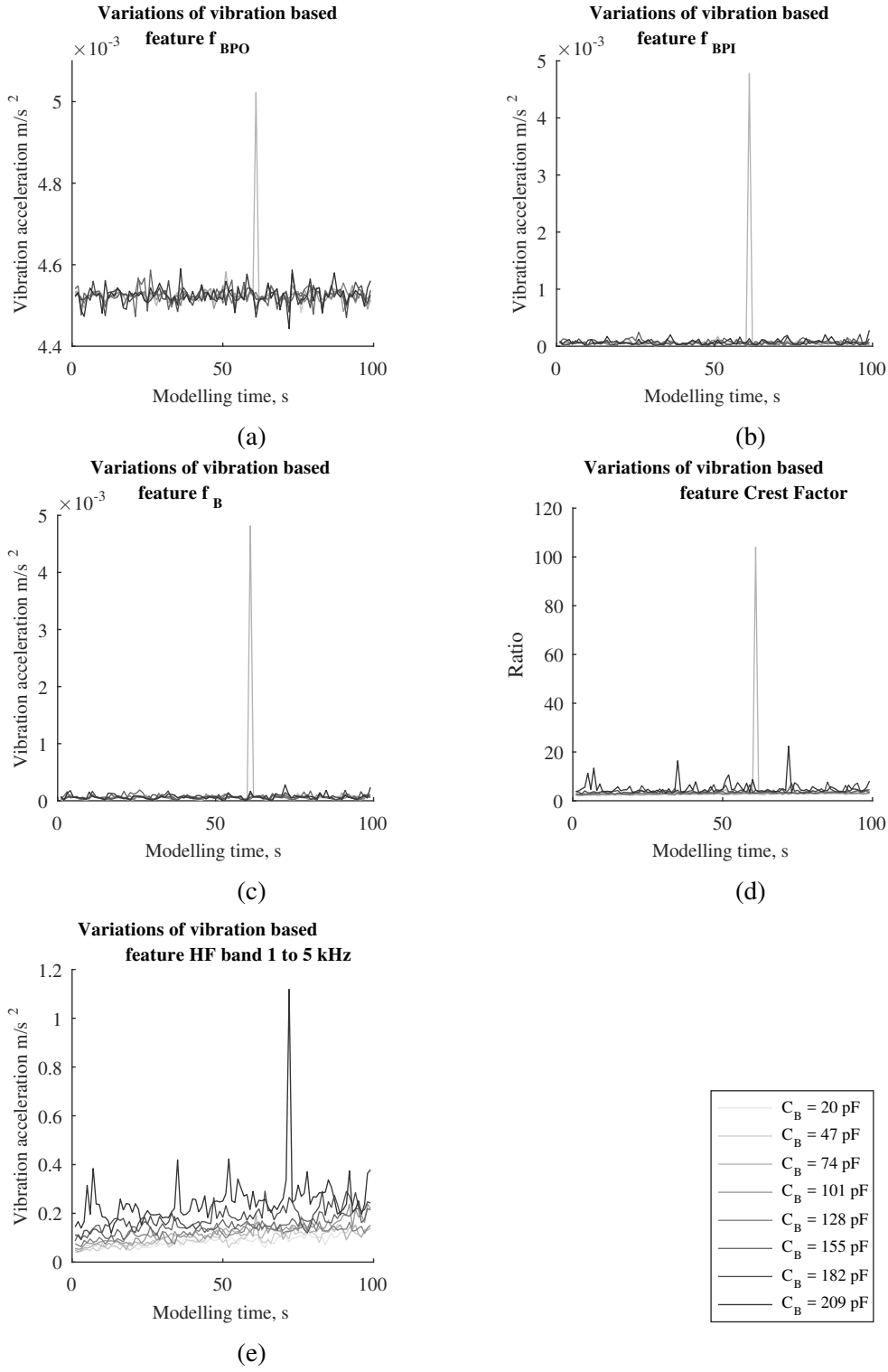

Figure 5.8: Development of vibration features over the duration of bearing capacitance sensitivity analysis.

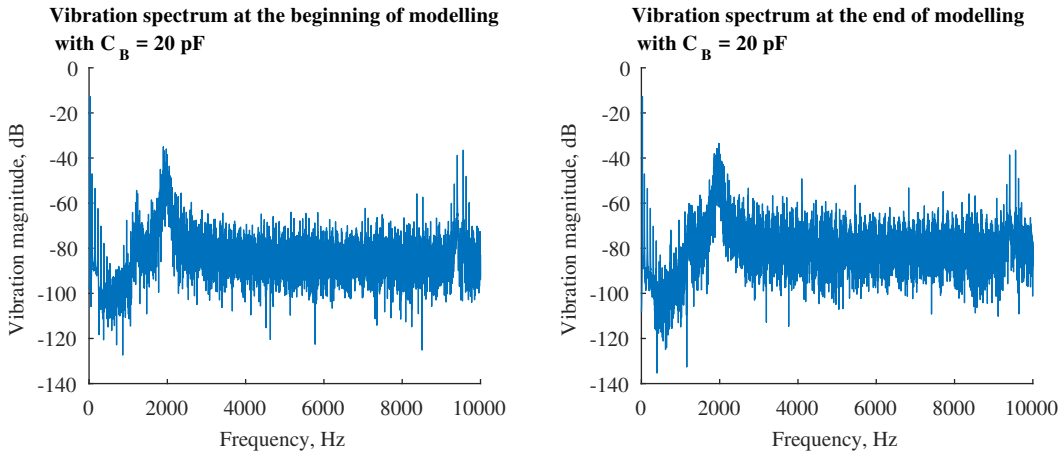

(a) (b)

Figure 5.9: Comparison of vibration spectra at the beginning (left) and at the end (right) of the sensitivity analysis with $C_{\mathrm{B}} = 20\,\mathrm{pF}$.

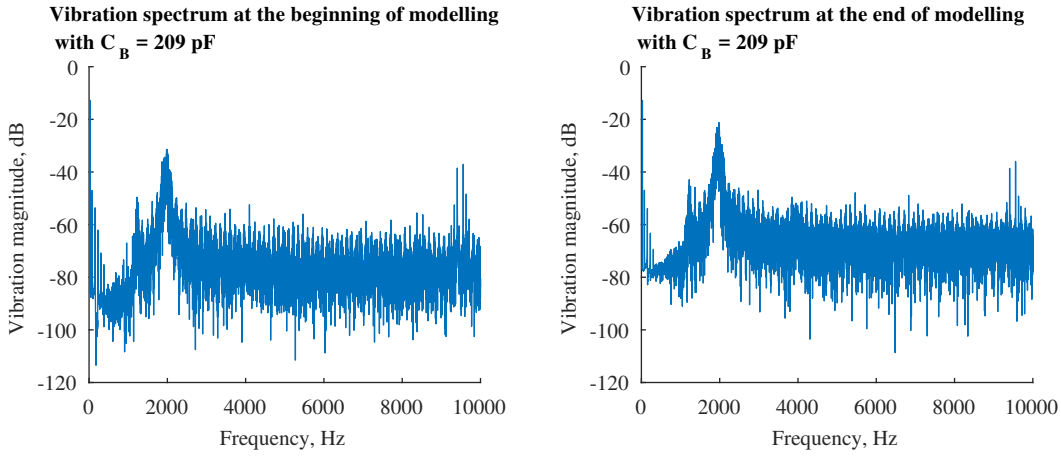

(a) (b)

Figure 5.10: Comparison of vibration spectra at the beginning (left) and at the end (right) of the sensitivity analysis with $C_{\mathrm{B}} = 209\,\mathrm{pF}$.

Table 5.1: Correlation coefficients of f_{BPO}, f_{BPI}, and f_{B} with respect to total energy of discharge during sensitivity analysis.

Analysed variable	Value of variable	Correlation of energy vs f_{BPO}	f_{BPI}	f_{B}	RMS of 1 to 5 kHz band	Crest factor
k_{const}	$2 \cdot 10^{-6}$	-0.17663	0.081441	0.097575	0.70208	0.30042
k_{const}	$2.6 \cdot 10^{-6}$	-0.036175	0.12595	0.2001	0.86937	0.6391
k_{const}	$3.2 \cdot 10^{-6}$	0.036751	-0.014222	0.073849	0.80793	0.5329
k_{const}	$3.8 \cdot 10^{-6}$	-0.0095683	0.29301	0.25371	0.88599	0.66182
k_{const}	$4.4 \cdot 10^{-6}$	-0.1527	0.066745	0.12566	0.86898	0.63429
k_{const}	$5 \cdot 10^{-6}$	-0.013866	0.0066329	0.0021556	0.63657	0.083329
k_{const}	$5.6 \cdot 10^{-6}$	0.43072	0.67219	0.65669	0.87419	0.0086737
k_{const}	$6.2 \cdot 10^{-6}$	0.66789	0.69547	0.67725	0.90975	0.11031
l_{cl}	4 µm	-0.057552	0.32063	0.31132	0.89127	0.73403
l_{cl}	4.9 µm	-0.057552	0.32063	0.31132	0.89127	0.73403
l_{cl}	5.8 µm	-0.0021747	0.20331	0.2163	0.82674	0.62158
l_{cl}	6.7 µm	-0.023627	0.062444	0.10063	0.85965	0.69211
l_{cl}	7.6 µm	-0.010791	-0.01129	0.051941	0.86729	0.61906
l_{cl}	8.5 µm	0.010141	0.048596	0.039335	0.82557	0.56744
l_{cl}	9.4 µm	-0.026484	0.021947	0.042221	0.86686	0.65635
l_{cl}	10.3 µm	0.0013644	0.011926	0.025283	0.90102	0.66136
C_{B}	20 pF	-0.1789	0.13037	0.072112	0.65447	0.31935
C_{B}	47 pF	-0.17478	-0.0068263	0.065427	0.75751	0.46613
C_{B}	74 pF	0.032952	0.038861	0.042201	0.80706	0.05909
C_{B}	101 pF	-0.069564	0.14777	0.21471	0.90036	0.74949
C_{B}	128 pF	0.060328	0.013451	-0.03992	0.73961	0.50613
C_{B}	155 pF	-0.033629	-0.098528	-0.052109	0.80065	0.35448
C_{B}	182 pF	0.065305	0.1816	0.075425	0.73172	0.36143
C_{B}	209 pF	0.091215	0.1231	0.080635	0.31153	0.00023799

6.1.1 Hypothesis 1.

The results of correlation analysis indicate low, and inconsistent among different parameters of the system, correlation between the values of total energy introduced into the system and values of vibration for the frequencies related to f_{BPO}, f_{BPI}, f_{B}, and to crest factor. In addition to that, these vibration features change significantly with changes in parameters of sensitivity analysis — bearing clearance and lubricant loading coefficient. This evidence supports the hypothesis 1.

The difference between the amount of vibrations on frequencies of f_{BPO} and its multiples was observed in the modelling results for sensitivity analyses of lubricant bearing constant and bearing clearance. The variations don't have significant correlation with the amount

of energies introduced into the system.

6.1.2 Hypothesis 2.

The results of modelling indicate that in most of modelled conditions there is correlation between the value of RMS of frame acceleration for frequency band from 1 to 5 kHz and the total amount of energy introduced into the system in the form of electrostatic discharges. The exceptional cases are: 1) model run with low value of C_{B} and 2) model run with low value of lubricant loading constant k_{const}. The lack of correlation for the first case can be explained by extremely low values of energy introduced into the surface during single discharge and, thus, low sizes of defects that would not cause significant vibrations. For the second case, the possible explanation could be that, with such low loading constant, the influence of vibrations, which were caused by the initial discharges, was already high enough to saturate the sensitivity of this metric.

6.1.3 Other observations.

The results of lubricant bearing capacitance sensitivity analysis suggest, that there is significant influence of lubricant's loading constant on the frequency of peak in the range from 1 to 5 kHz, that is present in all vibration samples. The probable explanation of the origin of such vibrations is, that they occur because of the non-linearity of the lubricant force. Similar vibrations were observed in the acceleration samples recorded during the long-term degradation experiment.

Based on this observation, additional analysis of median frequency of vibrations have been performed for the 920 hour long degradation test. The average frequency of vibrations was defined as

$$f_{\mathrm{avg}} = \frac{\sum_{f=1000\,\mathrm{Hz}}^{5000\,\mathrm{Hz}} FFTmag(VV, f) \cdot f}{\sum_{f=1000\,\mathrm{Hz}}^{5000\,\mathrm{Hz}} FFTmag(VV, f)}. \tag{6.1}$$

The results of computation for average frequency for the 920 hour long degradation run is presented in Fig. 6.1. The analysis indicates that this metric mostly grows over the duration of experiment. This suggests the progressing degradation of the lubricant that reduces its loading capacity. The behaviour also features significant variability, as the lubricant has the ability to restore its properties, if the vibrations introduce fresh material into the running area.

6.2 Discussion of results presented in publications.

Similar damage patterns were observed, using SEM on the running surfaces of all DE bearings, during long-term degradation test runs (Publications I, II, III and VI). The patterns, however, were missing from most of the NDE bearings. This suggests that during all test runs surface degradation occurred because of the applied artificial voltage. This suggests, that changes observed in the vibration spectra are due to these pitting defects. On the other hand, the vibration spectra did not feature significant changes on the frequencies of f_{BPO}, f_{BPI}, and f_{B}, which suggests, that these frequencies are not suitable for detection of this type of damage.

It was observed during the long-term degradation test (Publication III), that after changes in the rotational speed of motor, the EDM activity rises sharply and then decays, while the speed of operation is constant. This suggests, that variable driving conditions are more likely to cause extra EDM activity and additional damage to the running surface than constant operation speed. The possible explanation of this behaviour is that the lubricant film tends to either isolate the discharge voltage without breakdowns or become conductive and prevent voltage build up at all. During the grease breakdown field strength testing on a scaled setup (Publications IV and V), similar behaviour was observed supporting this behaviour as the root cause of conductive state of the bearings under EDM. The results of XRD of grease samples, presented in Publication III, indicated absence of notable quantities of metal compounds, that were predicted by previous studies in the field as the result of melting and mechanical extraction of material of running surfaces. The absence of such metal particles disproves the hypothesis, that the nature of the direct conductivity of the grease after some extended in time degradation is caused by electrostatic machining currents.

The appearance in the FTIR spectra of damaged grease of absorption band, that is re-

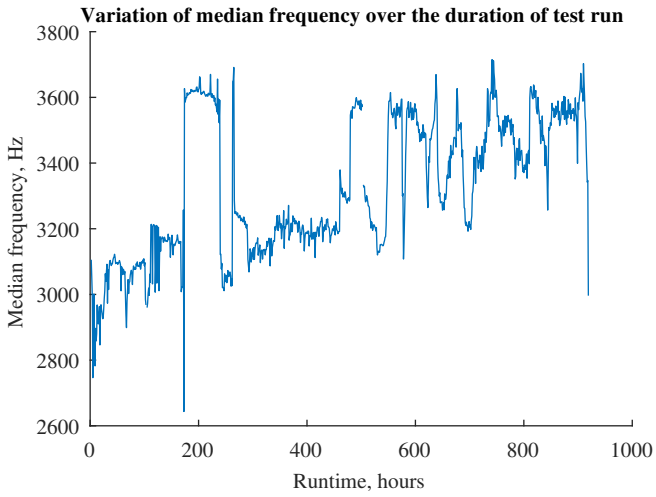

Figure 6.1: Weighted average frequency of vibration in the band from 1 to 5 kHz.

lated to -OH group (Publication III), supports the hypothesis of chemical degradation of some grease compounds under electric currents proposed by (Prashad, 2006) and further investigated in (Muetze et al., 2006).

6.3 Interpretation of combined results

Considering the results of long-term degradation tests, accelerated lubricant degradation tests, and numerical simulation together, the following conclusions may be drawn.

- In addition to already studied phenomenon of surface pitting damage, EDM currents seem to affect the insulating and loading properties of lubricant. The increased conductivity and low ability to resist consequent breakdowns results in bearing becoming conductive, which, in its turn, may increase the magnitudes of other types of bearing currents. The decrease in loading constant of lubricant, on the other hand, directly affects the lifetime expectation of bearing.

- The existing diagnostic methods, that rely on detection of single frequency harmonics, such as f_{BPO}, f_{BPI}, and f_{B}, are not well suited to detect incipient damage due to pitting, or degradation of lubricant (Publications I, II, III and VI).

- RMS of vibrations in high frequency band from 1 to 5 kHz (Publications III and VI) seems to be correlated with appearance of pitting damage, at least for the studied machine frame sizes under given lubrication and temperature conditions. A broader study should attempt to disprove the feasibility of this metric for other operating conditions to establish the applicability boundaries.

- Numerical simulations suggest that the frequency of vibration peak in the 1 to 5 kHz region are correlated to the value of lubricant loading constant. This observation was confirmed for a real life experiment, that had this metric growing through the duration of experiment and indicated lubricant degradation at the end of the experiment.

6.4 Further research

Further research is required to improve our understanding of what is the actual relation between the vibrations in the high frequency region and lubricant load constant. Despite the probability, that this relation is non-linear and it is possible, that other factors, like lubricant degradation, are involved, it should be possible to formulate a proportionality law through the extensive experimental work and analysis of real motor vibration data under different operating temperatures.

Additionally, it is important to undertake further steps to implement monitoring system, that could be based on the state of the lubricant detected with either vibration measurements, measurements of lubricant breakdown voltage, or both at the same time. Such monitoring system could be used to determine the state of lubricant and define the timing for preventive maintenance with either re-greasing of bearings or replacing them.

Another direction, that could be interesting for further investigation, is the analysis of lubricant mechanical properties under the energy controlled degradation process with electrostatic discharges.

References

Alger, P.L. and Samson, H.W. (1924). Shaft Currents in Electric Machines. *Transactions of the American Institute of Electrical Engineers*, XLIII, pp. 235–245. ISSN 0096-3860, doi:10.1109/T-AIEE.1924.5060981.

Boyanton, H.E. and Hodges, G. (2002). Bearing fluting [motors]. *IEEE Industry Applications Magazine*, 8(5), pp. 53–57. ISSN 1077-2618, doi:10.1109/MIA.2002.1028391.

Busse, D., Erdman, J., Kerkman, R.J., Schlegel, D., and Skibinski, G. (1997a). Bearing currents and their relationship to PWM drives. *IEEE Transactions on Power Electronics*, 12(2), pp. 243–252. ISSN 0885-8993, doi:10.1109/63.558735.

Busse, D.F., Erdman, J.M., Kerkman, R.J., Schlegel, D.W., and Skibinski, G.L. (1997b). An evaluation of the electrostatic shielded induction motor: a solution for rotor shaft voltage buildup and bearing current. *IEEE Transactions on Industry Applications*, 33(6), pp. 1563–1570. ISSN 0093-9994, doi:10.1109/28.649969.

Busse, D. and Erdman, J. (1997). System electrical parameters and their effects on bearing currents. *IEEE Transactions on Industry Applications*, 33(2), pp. 577–584. ISSN 00939994, doi:10.1109/28.568025.

Busse, D.F., Erdman, J.M., Kerkman, R.J., and Schlegel, D.W. (1997c). The effects of PWM voltage source inverters on the mechanical performance of rolling bearings. *IEEE Transactions on Industry Applications*, 33(2), pp. 567–576. ISSN 00939994, doi:10.1109/28.568024.

Chen, S., Lipo, T.A., and Fitzgerald, D. (1996). Modeling of motor bearing currents in PWM inverter drives. *IEEE Transactions on Industry Applications*, 32(6), pp. 1365–1370. ISSN 00939994, doi:10.1109/28.556640.

Daugherty, R.H. and Wennerstrom, C.H. (1991). Need for industry standards for AC induction motors intended for use with adjustable-frequency controllers. *IEEE Transactions on Industry Applications*, 27(6), pp. 1175–1185. ISSN 0093-9994, doi:10.1109/28.108471.

Ebert, F.J. (1990). Performance of silicon nitride (Si 3N4) components in aerospace bearing applications. In: *Proceedings of the ASME Turbo Expo*, vol. 5. American Society of Mechanical Engineers (ASME). ISBN 9780791879085.

Erdman, J.M., Kerkman, R.J., Schlegel, D.W., and Skibinski, G.L. (1996a). Effect of PWM inverters on AC motor bearing currents and shaft voltages. *IEEE Transactions on Industry Applications*, 32(2), pp. 250–259. ISSN 0093-9994, doi:10.1109/28.491472.

Erdman, J.M., Kerkman, R.J., Schlegel, D.W., and Skibinski, G.L. (1996b). Effect of PWM inverters on ac motor bearing currents and shaft voltages. *IEEE Transactions on Industry Applications*, 32(2), pp. 250–259. ISSN 00939994, doi:10.1109/28.491472.

Ferreira, F.J.T.E., Cistelecan, M.V., and de Almeida, A.T. (2012). Evaluation of Slot-Embedded Partial Electrostatic Shield for High-Frequency Bearing Current Mitigation in Inverter-Fed Induction Motors. *IEEE Transactions on Energy Conversion*, 27(2), pp. 382–390. ISSN 0885-8969, doi:10.1109/TEC.2012.2187452.

Furtmann, A., Tischmacher, H., and Poll, G. (2016). Extended HF equivalent model of a drive train. In: *2016 XXII International Conference on Electrical Machines (ICEM)*, pp. 2244–2250.

Gear, C.W. (1971). *Numerical Initial Value Problems in Ordinary Differential Equations*. Upper Saddle River, NJ, USA: Prentice Hall PTR. ISBN 0136266061.

Gemeinder, Y., Schuster, M., Radnai, B., Sauer, B., and Binder, A. (2014). Calculation and validation of a bearing impedance model for ball bearings and the influence on EDM-currents. *Proceedings - 2014 International Conference on Electrical Machines, ICEM 2014*, (1), pp. 1804–1810. doi:10.1109/ICELMACH.2014.6960428.

Hadden, T., Jiang, J.W., Bilgin, B., Yang, Y., Sathyan, A., Dadkhah, H., and Emadi, A. (2016). A Review of Shaft Voltages and Bearing Currents in EV and HEV Motors. In: *IECON 2016 - 42nd Annual Conference of the IEEE Industrial Electronics Society*, pp. 1578–1583.

Hamrock, B.J. and Dowson, D. (1977). Isothermal elastohydrodynamic lubrication of point contacts. III - Fully flooded results. *Journal of Tribology*, 99(2), pp. 264–275. ISSN 04021215, doi:10.1115/1.3453074.

Han, D., Morris, C.T., and Sarlioglu, B. (2017). Common-Mode Voltage Cancellation in PWM Motor Drives With Balanced Inverter Topology. *IEEE Transactions on Industrial Electronics*, 64(4), pp. 2683–2688. ISSN 02780046, doi:10.1109/TIE.2016.2633234.

Heidler, B., Brune, K., and Doppelbauer, M. (2016). Design aspects of an electrostatic shield in an electric machine for hybrid electric vehicles. In: *8th IET International Conference on Power Electronics, Machines and Drives (PEMD 2016)*, pp. 1–6.

IEEE (1985). Report of Large Motor Reliability Survey of Industrial and Commercial Installations, Part II. *IEEE Transactions on Industry Applications*, IA-21(4), pp. 865–872. ISSN 0093-9994, doi:10.1109/TIA.1985.349533.

Jacobs, W., Boonen, R., Sas, P., and Moens, D. (2014). The influence of the lubricant film on the stiffness and damping characteristics of a deep groove ball bearing. *Mechanical Systems and Signal Processing*, 42(1-2), pp. 335–350. ISSN 08883270, doi: 10.1016/j.ymssp.2013.07.018.

Jaeger, C., Grinbaum, I., and Smajic, J. (2016). Numerical simulation and measurement of common-mode and circulating bearing currents. In: *Proceedings - 2016 22nd International Conference on Electrical Machines, ICEM 2016*, pp. 486–491.

von Jouanne, A., Rendusara, D.A., Enjeti, P.N., and Gray, J.W. (1996). Filtering techniques to minimize the effect of long motor leads on PWM inverter-fed AC motor drive systems. *IEEE Transactions on Industry Applications*, 32(4), pp. 919–926. ISSN 0093-9994, doi:10.1109/28.511650.

Kolbe, H., Muetze, A., and Hameyer, K. (2012). Modelling of impulse currents in mechanical rolling element bearings. *COMPEL - The international journal for computation and mathematics in electrical and electronic engineering*, 31(6), pp. 1575–1589. doi:10.1108/03321641211267001.

Kriese, M., Wittek, E., Gattermann, S., Tischmacher, H., Poll, G., and Ponick, B. (2012). Influence of bearing currents on the bearing lifetime for converter driven machines. In: *Proceedings - 2012 20th International Conference on Electrical Machines, ICEM 2012*, pp. 1735–1739. ISBN 9781467301428.

Lawson, J.A. (1993). Motor bearing fluting. In: *Conference Record of 1993 Annual Pulp and Paper Industry Technical Conference*, pp. 32–35.

Li, B., Chow, M.Y., Tipsuwan, Y., and Hung, J.C. (2000). Neural-network-based motor rolling bearing fault diagnosis. *IEEE Transactions on Industrial Electronics*, 47, pp. 1060–1069. ISSN 02780046.

Link, P.J. (1999). Minimizing electric bearing currents in ASD systems. *IEEE Industry Applications Magazine*, 5(4), pp. 55–66. ISSN 1077-2618, doi:10.1109/2943.771367.

Liu, W. (2014). The prevalent motor bearing premature failures due to the high frequency electric current passage. *Engineering Failure Analysis*, 45, pp. 118–127.

Ludois, D.C. and Reed, J.K. (2015). Brushless Mitigation of Bearing Currents in Electric Machines Via Capacitively Coupled Shunting. *IEEE Transactions on Industry Applications*, 51(5), pp. 3783–3790. ISSN 0093-9994, doi:10.1109/TIA.2015.2434795.

Maetani, T., Morimoto, S., Yamamoto, K., Isomura, Y., and Watanabe, A. (2012). Influence of motor rotating speed on shaft voltage of brushless DC motor with insulated rotor driven by PWM inverters. In: *International Symposium on Power Electronics Power Electronics, Electrical Drives, Automation and Motion*, pp. 730–735.

Magdun, O., Gemeinder, Y., and Binder, A. (2010a). Investigation of influence of bearing load and bearing temperature on EDM bearing currents. In: *2010 IEEE Energy Conversion Congress and Exposition*, pp. 2733–2738. ISSN 2329-3721.

Magdun, O., Gemeinder, Y., and Binder, A. (2010b). Prevention of harmful EDM currents in inverter-fed AC machines by use of electrostatic shields in the stator winding overhang. In: *IECON 2010 - 36th Annual Conference on IEEE Industrial Electronics Society*, pp. 962–967. ISSN 1553-572X.

Magdun, O. and Binder, A. (2014). High-frequency induction machine modeling for common mode current and bearing voltage calculation. *IEEE Transactions on Industry Applications*, 50(3), pp. 1780–1790. ISSN 00939994, doi:10.1109/TIA.2013.2284301.

Magdun, O., Gemeinder, Y., Binder, A., and Reis, K. (2011). Calculation of bearing and common-mode voltages for the prediction of bearing failures caused by EDM currents. *SDEMPED 2011 - 8th IEEE Symposium on Diagnostics for Electrical Machines, Power Electronics and Drives*, pp. 462–467. doi:10.1109/DEMPED.2011.6063664.

McMullan, D. (1995). Scanning electron microscopy 19281965. *Scanning*, 17(3), pp. 175–185. ISSN 01610457, doi:10.1002/sca.4950170309.

Muetze, A. and Binder, A. (2006). Don't lose your bearings. *IEEE Industry Applications Magazine*, 12(4), pp. 22–31. ISSN 10772618, doi:10.1109/MIA.2006.1678327.

Muetze, A. and Binder, A. (2007a). Practical Rules for Assessment of Inverter-Induced Bearing Currents in Inverter-Fed AC Motors up to 500 kW. *IEEE Transactions on Industrial Electronics*, 54(3), pp. 1614–1622. ISSN 0278-0046, doi: 10.1109/TIE.2007.894698.

Muetze, A. and Binder, A. (2007b). Techniques for Measurement of Parameters Related to Inverter-Induced Bearing Currents. *IEEE Transactions on Industry Applications*, 43(5), pp. 1274–1283. ISSN 0093-9994, doi:10.1109/TIA.2007.904413.

Muetze, A., Binder, A., Vogel, H., and Hering, J. (2006). What can bearings bear? *IEEE Industry Applications Magazine*, 12(6), pp. 57–64. ISSN 1077-2618, doi:10.1109/IAM.2006.248014.

Muetze, A., Tamminen, J., and Ahola, J. (2011). Influence of Motor Operating Parameters on Discharge Bearing Current Activity. *IEEE Transactions on Industry Applications*, 47(4), pp. 1767–1777. ISSN 0093-9994, doi:10.1109/TIA.2011.2154353.

Muetze, A. (2004). *Bearing Currents in Inverter-Fed AC Motors*.

Muetze, A. and Binder, A. (2007c). Calculation of motor capacitances for prediction of the voltage across the bearings in machines of inverter-based drive systems. *IEEE Transactions on Industry Applications*, 43(3), pp. 665–672. ISSN 00939994, doi: 10.1109/TIA.2007.895734.

Muetze, A., Niskanen, V., and Ahola, J. (2014). On radio-frequency-based detection of high-frequency circulating bearing current flow. *IEEE Transactions on Industry Applications*, 50, pp. 2592–2601. ISSN 00939994, doi:10.1109/TIA.2013.2296626.

Nabae, A., Takahashi, I., and Akagi, H. (1981). A New Neutral-Point-Clamped PWM Inverter. *IEEE Transactions on Industry Applications*, IA-17(5), pp. 518–523. ISSN 0093-9994, doi:10.1109/TIA.1981.4503992.

Naik, R., Nondahl, T.A., Melfi, M.J., Schiferl, R., and Wang, J.S. (2003). Circuit model for shaft voltage prediction in induction motors fed by PWM-based AC drives. *IEEE Transactions on Industry Applications*, 39(5), pp. 1294–1299. ISSN 00939994, doi: 10.1109/TIA.2003.816504.

Niskanen, V., Muetze, A., and Ahola, J. (2014). Study on Bearing Impedance Properties at Several Hundred Kilohertz for Different Electric Machine Operating Parameters. *IEEE Transactions on Industry Applications*, 50(5), pp. 3438–3447. ISSN 0093-9994, doi:10.1109/TIA.2014.2308392.

Persson, E. (1992). Transient effects in application of PWM inverters to induction motors. *IEEE Transactions on Industry Applications*, 28(5), pp. 1095–1101. ISSN 0093-9994, doi:10.1109/28.158834.

Prashad, H. (2006). Behavior of lubricants in rolling-element bearings under the influence of electric current. In: Prashad, H., ed., *Tribology in Electrical Environments*, vol. 49, pp. 25–69. Tribology and Interface Engineering Series. Elsevier. ISSN 1572-3364.

Punga, F. and Hess, W. (1907). Eine Erscheinung an Wechsel- und Drehstromgeneratoren. *Elektrotechnik und Maschinenbau*, (25), pp. 615–618. ISSN 0367-0627.

Rodríguez, J., Lai, J.S., and Peng, F.Z. (2002). Multilevel inverters: A survey of topologies, controls, and applications. *IEEE Transactions on Industrial Electronics*, 49(4), pp. 724–738. ISSN 02780046, doi:10.1109/TIE.2002.801052.

Schiferl, R.F. and Melfi, M.J. (2004). Bearing current remediation options: Sources, investigative measurements, and installation modifications to reduce damage as a result of bearing currents. *IEEE Industry Applications Magazine*, 10(4), pp. 40–50. ISSN 1077-2618, doi:10.1109/mia.2004.1311162.

Singleton, R.K., Strangas, E.G., and Aviyente, S. (2017). The Use of Bearing Currents and Vibrations in Lifetime Estimation of Bearings. *IEEE Transactions on Industrial Informatics*, 13(3), pp. 1301–1309. ISSN 1551-3203, doi:10.1109/TII.2016.2643693.

Soediono, B. (1989). Reliability Improvement and Economic Benefits of on-Line Monitoring Systems for Large Induction Machines. *Journal of Chemical Information and Modeling*, 53, p. 160. ISSN 1098-6596, doi:10.1017/CBO9781107415324.004.

Tischmacher, H. and Gattermann, S. (2010). Bearing currents in converter operation. In: *The XIX International Conference on Electrical Machines - ICEM 2010*, pp. 1–8.

Tischmacher, H. and Gattermann, S. (2012). Multiple signature analysis for the detection of bearing currents and the assessment of the resulting bearing wear. In: *International Symposium on Power Electronics Power Electronics, Electrical Drives, Automation and Motion*, pp. 1354–1359.

Tischmacher, H., Tsoumas, I.P., and Furtmann, A. (2015). Extended probability model for discharge activities in the drive train of converter-fed electric motors. *2015 17th European Conference on Power Electronics and Applications, EPE-ECCE Europe 2015*. doi:10.1109/EPE.2015.7309392.

Tischmacher, H., Tsoumas, I.P., and Gattermann, S. (2014). Probability model for discharge activities in bearings of converter-fed electric motors. In: *2014 International Conference on Electrical Machines (ICEM)*, pp. 1818–1824.

Tran, Q.T., Truong, A.V., and Le, P.M. (2016). Reduction of harmonics in grid-connected inverters using variable switching frequency. *International Journal of Electrical Power and Energy Systems*, 82, pp. 242–251. ISSN 01420615, doi: 10.1016/j.ijepes.2016.03.027.

Ulrych, J.. and Mentlík, V. (2016). Dielectric properties of sunflower, rapeseed and commonly used mineral oil. In: *2016 17th International Scientific Conference on Electric Power Engineering (EPE)*, 5, pp. 1–4. ISBN 9781509009084.

Wittek, E., Kriese, M., Tischmacher, H., Gattermann, S., Ponick, B., and Poll, G. (2010). Capacitances and lubricant film thicknesses of motor bearings under different operating conditions. In: *The XIX International Conference on Electrical Machines - ICEM 2010*, pp. 1–6.

Wittek, E., Kriese, M., Tischmacher, H., Gattermann, S., Ponick, B., and Poll, G. (2012). Capacitance of bearings for electric motors at variable mechanical loads. In: *2012 XXth International Conference on Electrical Machines*, pp. 1602–1607.

Wu, W., Jiang, Y., Liu, Y., Huang, M., He, Y., and Chung, S.H. (2016). A new passive filter design method for overvoltage suppression and bearing currents mitigation in a long cable based PWM inverter-fed motor drive system. In: *2016 IEEE 8th International Power Electronics and Motion Control Conference (IPEMC-ECCE Asia)*, pp. 3103–3110.

Yuen, K.K.F. and Chung, H.S.H. (2015). A Low-Loss #x201C;RL-Plus-C #x201D; Filter for Overvoltage Suppression in Inverter-Fed Drive System With Long Motor Cable. *IEEE Transactions on Power Electronics*, 30(4), pp. 2167–2181. ISSN 0885-8993, doi: 10.1109/TPEL.2014.2325824.

Zare, F. (2009). EMI in modern AC motor drive systems. *IEEE EMC Society Newsletters*, (222), pp. 53–58.

Zhang, H., Von Jouanne, A., and Dai, S. (2001). A reduced-switch dual-bridge inverter topology for the mitigation of bearing currents, EMI, and DC-link voltage variations. *IEEE Transactions on Industry Applications*, 37(5), pp. 1365–1372. ISSN 00939994, doi:10.1109/28.952512.

Zika, T., Gebeshuber, I.C., Buschbeck, F., Preisinger, G., and Gröschl, M. (2009). Surface analysis on rolling bearings after exposure to defined electric stress. *Proceedings of the Institution of Mechanical Engineers, Part J: Journal of Engineering Tribology*, 223, pp. 787–797. ISSN 1350-6501, doi:10.1243/13506501JET538.

Appendix A. Estimated values of equivalent circuit elements.

Table A1: Estimates of equivalent circuit elements.

Element name	Meaning	Measured value	Estimated Value	Machine and bearing dimensions	Source	Notes
Z_{B}	bearing impedance	78.8 kΩ	81.8 kΩ	1.5 kW motor, 6205 C3 bearing 1000 rpm , 60 ^{o}C, F_{r} = 400 N, F_{a} = 350 N	(Gemeinder et al., 2014)	at 11 kHz
Z_{B}		9.09 kΩ	9 kΩ			at 100 kHz
Z_{B}		0.927 kΩ	0.9 kΩ			at 1 MHz
Z_{B}		76.8 kΩ	90 Ω			at 10 MHz
$C_{\mathrm{SW\text{-}RC}}$	capacitance stator winding to rotor core		19.5 pF	5 kW motor	(Jaeger et al., 2016)	FEM Electrostatic
$C_{\mathrm{SW\text{-}RW}}$	capacitance stator winding to rotor winding		16.84 pF			
$C_{\mathrm{SW\text{-}SC}}$	capacitance stator winding to stator core		2860 pF			
$C_{\mathrm{RW\text{-}RC}}$	capacitance rotor winding to rotor core		210.4 pF			
$C_{\mathrm{RC\text{-}SC}}$	capacitance rotor core to stator core		417.8 pF			
$C_{\mathrm{B\text{-}SC}}$	capacitance bearing to stator core		654 pF			

Continued on next page

Table A1 – continued from previous page

Element name	Meaning	Measured value	Estimated Value	Machine and bearing dimensions	Source	Notes
R_{EW}	capacitance bearing to stator core		4.58 mΩ	5 kW motor 10 kHz	(Jaeger et al., 2016)	FEM Eddy
L_{EW}	capacitance bearing to stator core		0.0554 µH			FEM Eddy
R_{SFe}	capacitance bearing to stator core		9.826 mΩ			Analytical
L_{SFe}	capacitance bearing to stator core		0.234 µH			Analytical
R_{RFe}	capacitance bearing to stator core		43.599 mΩ			Analytical
L_{RFe}	capacitance bearing to stator core		1.041 µH			Analytical
R_{EW}	capacitance bearing to stator core		10.3 mΩ	5 kW motor 30 kHz	(Jaeger et al., 2016)	FEM Eddy
L_{EW}	capacitance bearing to stator core		0.0437 µH			FEM Eddy

Continued on next page

Table A1 – continued from previous page

Element name	Meaning	Measured value	Estimated Value	Machine and bearing dimensions	Source	Notes
R_{SFe}	capacitance bearing to stator core		17.020 mΩ	(Jaeger et al., 2016)	(Jaeger et al., 2016)	Analytical
L_{SFe}	capacitance bearing to stator core		0.135 µH			Analytical
R_{RFe}	capacitance bearing to stator core		75.516 mΩ			Analytical
L_{RFe}	capacitance bearing to stator core		0.601 µH			Analytical
C_{B}	bearing capacitance	210 pF		6309 C3, 15 kW motor (160 mm frame) 5 V_{pp}, 300 kHz, external voltage, 30 ^{o}C	(Muetze et al., 2014)	210 rpm
C_{B}		380 pF				300 rpm
C_{B}		1700 pF		6316 C3, 75 kW motor (280 mm frame) 5 V_{pp}, 300 kHz, external voltage, 30 ^{o}C	(Muetze et al., 2014)	210 rpm
C_{B}		8500 pF				300 rpm
C_{B}	bearing capacitance	360 pF		15 kW motor (160 mm frame) 6309 C3 5 V_{pp}, 300 kHz, external voltage	(Niskanen et al., 2014)	240 rpm , 23 ^{o}C
C_{B}		890 pF				240 rpm, 37 ^{o}C
C_{B}		360 pF				450 rpm, 28 ^{o}C
C_{B}		900 pF				450 rpm, 48 ^{o}C
C_{B}		620 pF				1500 rpm, 30 ^{o}C

Continued on next page

Table A1 – continued from previous page

Element name	Meaning	Measured value	Estimated Value	Machine and bearing dimensions	Source	Notes
C_{B}	bearing capacitance	120 pF		15 kW motor (160 mm frame) 6309 C3 5 V_{pp}, 300 kHz, external voltage	(Niskanen et al., 2014)	2000 rpm, 24 ^{o}C
C_{B}		310 pF				2000 rpm, 41 ^{o}C
C_{B}		120 pF				3000 rpm, 24 ^{o}C
C_{B}		350 pF				3000 rpm, 44 ^{o}C
C_{B}	bearing capacitance	310 pF		15 kW motor (160 mm frame) 6309 C3 5 V_{pp}, 1500 kHz, external voltage	(Niskanen et al., 2014)	200 rpm , 28 ^{o}C
C_{B}		240 pF				400 rpm, 26 ^{o}C
C_{B}		150 pF				1500 rpm, 27 ^{o}C
C_{B}		240 pF				1500 rpm, 48 ^{o}C
C_{B}		140 pF				2000 rpm, 29 ^{o}C
C_{B}		220 pF				2000 rpm, 47 ^{o}C
C_{B}		140 pF				3000 rpm, 28 ^{o}C
C_{B}		260 pF				3000 rpm, 48 ^{o}C
C_{B}	bearing capacitance	510 pF		75 kW motor (280 mm frame) 6316 C3 5 V_{pp}, 300 kHz, external voltage	(Niskanen et al., 2014)	240 rpm , 24 ^{o}C
C_{B}		670 pF				240 rpm, 37 ^{o}C
C_{B}		360 pF				450 rpm, 24 ^{o}C
C_{B}		620 pF				450 rpm, 37 ^{o}C
C_{B}		970 pF				450 rpm, 46 ^{o}C
C_{B}		260 pF				1500 rpm, 24 ^{o}C
C_{B}		510 pF				1500 rpm, 37 ^{o}C
C_{B}		920 pF				1500 rpm, 57 ^{o}C
C_{B}		250 pF				2000 rpm, 27 ^{o}C
C_{B}		320 pF				2000 rpm, 36 ^{o}C
C_{B}		360 pF				2000 rpm, 47 ^{o}C
C_{B}		180 pF				3000 rpm, 28 ^{o}C

Continued on next page

Table A1 – continued from previous page

Element name	Meaning	Measured value	Estimated Value	Machine and bearing dimensions	Source	Notes
C_{B}		230 pF				3000 rpm, 36 ^{o}C
C_{B}		400 pF				3000 rpm, 50 ^{o}C
C_{B}	bearing capacitance	220 pF		75 kW motor (280 mm frame) 6316 C3 5 V_{pp}, 1500 kHz, external voltage	(Niskanen et al., 2014)	200 rpm , 25 ^{o}C
C_{B}		180 pF				400 rpm, 25 ^{o}C
C_{B}		390 pF				400 rpm, 39 ^{o}C
C_{B}		180 pF				1500 rpm, 26 ^{o}C
C_{B}		250 pF				1500 rpm, 39 ^{o}C
C_{B}		540 pF				1500 rpm, 48 ^{o}C
C_{B}		160 pF				2000 rpm, 27 ^{o}C
C_{B}		550 pF				2000 rpm, 50 ^{o}C
C_{B}		1100 pF				2000 rpm, 64 ^{o}C
C_{B}		200 pF				3000 rpm, 28 ^{o}C
C_{B}		260 pF				3000 rpm, 38 ^{o}C
C_{B}		400 pF				3000 rpm, 50 ^{o}C
C_{B}	bearing capacitance	100 pF		60 BLDC motor 608 ZZ	(Maetani et al., 2012)	1000 rpm , total capacitance of both bearings
$C_{\mathrm{SW\text{-}SC}}$	capacitance stator winding to stator core	400 pF		60 BLDC motor 608 ZZ	(Maetani et al., 2012)	
$C_{\mathrm{SC\text{-}MG}}$	capacitance stator core to magnet	70 pF				

Continued on next page

Table A1 – continued from previous page

Element name	Meaning	Measured value	Estimated Value	Machine and bearing dimensions	Source	Notes
$C_{\text{SW-MG}}$	capacitance stator winding to magnet	8 pF		60 BLDC motor 608 ZZ	(Maetani et al., 2012)	
C_{MG}	capacitance magnet	69 pF				
$C_{\text{MG-RC}}$	capacitance magnet to rotor core	4.5 pF				
$C_{\text{RC-G}}$	capacitance rotor core to ground	7.7 pF				
$C_{\text{BRKT-G}}$	capacitance bracket to ground	20 pF				
$C_{\text{SW-BRKT}}$	capacitance stator winding to bracket	19 pF				

Appendix B. Pseudo-code of functions used in modelling and processing of results. Matalb-like syntax

```
1
2  % MAIN ROUTINE
3
4  % 1. Define global physical parameters of the system.
5  global mr = 40; % Mass of rotor + shaft, kg
6  global mf = 50; % Mass of frame, kg
7  global ml = 20; % Mass of load, kg
8  global kbu = 2e5; % Spring coefficient of bushings
9  global Capacitance = 0.02e-9; % Capacitance of bearing, F
10 global Q=0; % Initial charge on bearing, C
11 global Ich=1e-7; % Charging current, A
12 global cb = 1200 ; % Bearing damping coefficient
13 global cbu = 6e3; % Bushings damping coefficient
14 global Lsh=1; % Shaft length
15 global Ll=0.2; % Load center of mass location
16 global bearingclearance = (5e-6); % Bearing clearance, m
17 global kbear = 3e-6; % Lubricant bearing constant
18 global Fshaft = 25; % Shaft rotation speed, Hz
19 global Bearing_inner_radius = 27.5; % mm
20 global Bearing_outer_radius = 45; % mm
21
22 % 2. Compute sine lookup table.
23 global sinlookup=sin((1:1:2002)/1000*2*pi);
24
25 % 3. Reset count of discharges.
26 dischcount = 0; %
27
28 % 4. Define output sampling rate.
29 outsamplerate = 20000; % Sampling rate
30
31 % 5. Compute common center of mass displacement d_displ and
       combined moment of inertia Jeff.
32 global Jr=1/12 * mr * Lsh^2;
33 global d_displ = (Ll*ml/mr);
34 global d_de = Lsh/2-d_displ;
35 global d_nde = Lsh/2+d_displ;
36 global d_l= (Ll+Lsh/2)-d_displ;
37 global Jeff=Jr+mr*d_displ^2+ml*d_l^2;
38
39 % 6. Define system matrix for linear components.
```

```
40
41 A=[0 0 0 1 0 0 ; % Shaft Center of Mass position
42     0 0 0 0 1 0 ; % Shaft tilt
43     0 0 0 0 0 1 ; % Frame reference position
44     0 0 0 0 0 0; % Shaft Center of Mass velocity
45     0 0 0 0 0 0; % Shaft angular velocity
46     0 0 0 0 0 0] % Frame velocity
47
48 % shaft Center of Mass acceleration dependence on
49 % Shaft Center of Mass velocity
50 A(4,4) = -2*cb/(mr+ml);
51 % Shaft angular velocity
52 A(4,5) = -cb*(d_de-d_nde)/(mr+ml);
53 % Frame velocity
54 A(4,6) = (2*cb)/(mr+ml);
55 % shaft angular acceleration dependence on
56 % Shaft Center of Mass velocity
57 A(5,4) = (-cb*d_nde+cb*d_de)/Jeff;
58 % Shaft angular velocity
59 A(5,5) = -cb*(d_de*d_de+d_nde*d_nde)/Jeff ;
60 % Frame velocity
61 A(5,6) = (-cb*d_de+cb*d_nde)/Jeff;
62 % Frame acceleration dependence on
63 % Frame reference position
64 A(6,3) = (-kbu)/mf;
65 % Shaft Center of Mass velocity
66 A(6,4) = 2*cb/mf ;
67 % Shaft angular velocity
68 A(6,5) = cb*(d_de-d_nde)/mf ;
69 % Frame velocity
70 A(6,6) = (-cbu-2*cb)/mf;
71
72 % 7. Define initial time step
73 dT = 1e-12;
74
75
76 % 8. Define arbitrary roughness vector for NDE bearing.
77 roughness_standard_deviation = 2e-9 % Roughness Standard
     Deviation, m
78 roughnesssteps = 1e7
                                % Amount of roughness steps per
     1 iteration
79 rough = roughness_standard_deviation*abs(randn(
     roughnesssteps+1,2));
```

```
80
81 % 9. Compute cage frequency using bearing inner and outer
       radii.
82 Fcage = Fshaft * Bearing_inner_radius/(Bearing_inner_radius
       +Bearing_outer_radius);
83
84
85 % 10. Allocate memory for inner and outer race tracks.
86 track_width = 10e-6; % m
87 initial_roughness_level = 20; % nm
88 trackouter=TrackHndl(Bearing_outer_radius,track_width,
       initial_roughness_level*10);
89 trackinner=TrackHndl(Bearing_inner_radius,track_width,
       initial_roughness_level*10);
90 trlenouter = length(trackouter.Track);
91 trleninner = length(trackinner.Track);
92
93 % 11. Initialize track position angles aleph and bet.
94 aleph=0;
95 bet=0;
96
97 % 12. Initialize state-space variables at perfect alignment
       with no velocity.
98 x = [0 0 0 0 0 0]';
99 xbackup = [0 0 0 0 0 0]';
100 Ubackup = [0 0 0 0 0 0]';
101
102 % 13. Initialize discharge energy tracking.
103 totdisch =[];
104 totenerg =[];
105 energ=0;
106
107 % 14. Define initial axial drift for bearing positions. The
       centre of bearing ball shifts from 2 um to 8 um.
108 axial_drift_um = 5; % um centre point
109 axial_drift_offset_um = 2; % um
110 axial_drift_max_um = 3; % um
111 axial_drift = axial_drift_um*10;
112 positionupdaterate=1e5; % Rate at which shaft shifts
       axially
113
114 % 15. Define lubricant force lookup table for lubricant
       thickness from 0.00001 nm to 5 um with step of 0.00001
       nm.
```

```
115 Forcelookup=(kbear ./((1:1:5e7)/1e13)).^(1/0.078);
116
117 % 16. Loop through iterations from 1 to 200 for steps from
    17 to 49 with iterator variable 'iteration'.
118
119 % 17. Save discharge count and energy at the beginning of
    the iteration.
120 totdisch(iteration)=dischcount
121 totenerg(iteration)=energ
122
123 % 18. Update new target location for axial movement.
124 balldrifttarget = rand(1)*axial_drift_max_um*20  +
    axial_drift_offset_um*10;
125
126 % 19. Reset local timer of iteration.
127 T = 0;
            % Time of computaton
128 lastT = 0;                                          %
    Time on previous step of computaton
129 posupdateTrack = 0;              % Time to track updates if
    ball position
130
131 % 20. Reset subiteration counter, that is used for Euler
    step changes.
132 subiter = 0;
133
134 % 21. Prefetch averaged height values from main height
    arrays. Convert them to double to speed up following
    computations.
135 prefetch_width_um = 2 ; % Width of averaging, um. This
    simulates some narrow Herzian contact area for which the
     force is proportional to some averaged height value
136
137 prefetchinner=double(sum(trackinner.Track(:,round(
    axial_drift)-(prefetch_width_um/2*10)+(1:(
    prefetch_width_um*10))),2)/20);
138 prefetchouter=double(sum(trackouter.Track(:,round(
    axial_drift)-(prefetch_width_um/2*10)+(1:(
    prefetch_width_um*10))),2)/20);
139
140 % 22. Reset last stored output sample and timestamp.
141
142 lastoutsample = zeros(6,1);
143 lastouttime = 0;
```

```
144
145 % 23. Prepare output index.
146 outindex = 1;
147
148 % 24. Preallocate output array.
149 out=zeros(6,outsamplerate);
150
151 % 25. Iterate through steps 26 to 48 while T < 1.
152
153 % 26. Increment subiter counter.
154 subiter = subiter+1;
155
156 % 27. If posupdateTrack < 1/positionupdaterate goto 30.
157
158 % 28. Shift shaft axial position 1 step into the direction
      of balldrifttarget using exponential decay.
159 axial_drift = (1/positionupdaterate)*(balldrifttarget-
      axial_drift)+axial_drift;
160 roundeddrift = round(axial_drift);
161
162 % 29. Decrement time counter for next position update
      happen at least in 1/positionupdaterate.
163 posupdateTrack = posupdateTrack-1/positionupdaterate;
164
165 % 30. Compute current voltage of bearing capacitance.
166 Ubr=Q/Capacitance;
167
168 % 31. Compute discharge event occurances and update track
      arrays.
169 [track,track2, Q, Ubr] = TrackDischargeOccurences(x, aleph,
      bet, Q, Ubr, roundeddrift, prefetchinner, prefetchouter
      , trackleninner, tracklenouter, track, track2 )
170
171 % 32. Compute forces produced by non-linear component of
      bearing model
172 [Fde,Fnde] = ForceComputationNonLinear(x, aleph, bet,
      roundeddrift, prefetchinner, prefetchouter,
      trackleninner, tracklenouter)
173
174
175 % 33. Compute exciting and non-linear force vector.
176 U = [0;
177       0;
178       0;
```

```
179         ((-(mr+ml)*9.8)+50*sin(2*pi*Fshaft*T)+Fde+Fnde)/(mr+ml
                );
180         (((-mr*d_displ+ml*d_l)*9.8)-50*sin(2*pi*Fshaft*T)*
                d_displ-Fde*d_de+Fnde*d_nde)/(Jeff);
181         (-Fde-Fnde)/mf];
182
183
184 % 34. Compute state-space derivative.
185 der = (A*x + U );
186
187 % 35. Compute limit on time step due to thin lubrication
        layerdTcl.
188 dTcl=1e-8; % Default value s
189 if ((bearingclearance-abs(x(1)-x(2)*d_de-x(3)))>1e-6)    %
        If actual layer is less than 1 um scale down time step
190       dTcl=1e-8+(bearingclearance-abs(x(1)-x(2)*d_de-x(3))-1e
              -6)*10;
191 end
192
193 % 36. Every odd step of subiter perform steps from 37 to 40
        otherwise goto 41
194 %if mod(subiter, 2) == 1
195
196 % 37. Compute 2-times larger step of Euler method using
        saved variables xbackup and Ubackup, that are saved
        every odd step.
197 xfast=xbackup + dT*2*(A*xbackup + Ubackup);
198
199 % 38. Compute local error.
200 error=2*abs(x-xfast)./(abs(x)+abs(xfast));
201
202 % 39. If maximal error among states is greater than 1% -
        decrease time step dT by a factor of 2, otherwise
        increase time step dT  by 5%.
203       if ((max(error(1:6)) > 1e-2))
204           dT = dT*0.5;
205           dT = max(dT,1e-16);
206       else
207           dT = dT*1.05;
208           dT = min(dT,dTcl);
209       end
210 % 40. Save new start points for fast Euler computation.
211       Ubackup = U;
212       xbackup = x;
```

```
213
214 % 41. Update state-space variables.
215 x = x + dT*der;
216
217 % 42. Update charge on the bearing.
218 Q=Q+Ich*dT;
219
220 % 43. Update angles of rotation for bearing inner and outer
        rings. Loop if greater than 1 and update pre fetch
       array.
221 aleph = aleph + dT*Fcage;
222 if aleph > 1
223      aleph = aleph - 1;
224      prefetchouter=double(sum(trackouter.Track(:,
           roundeddrift-10+(1:20)),2)/20);
225 end
226 bet = bet + dT*(Fshaft - Fcage);
227 if bet > 1
228      bet = bet - 1;
229       prefetchinner=double(sum(trackinner.Track(:,
            roundeddrift-10+(1:20)),2)/20);
230 end
231
232 % 44. Update counter for shaft axial position update.
233 posupdateTrack = posupdateTrack+dT;
234
235 % 45. Update iteration time.
236 T = T+dT;
237
238 % 46. Update last output time track.
239 lastouttime = lastouttime + dT;
240
241 % 47. If it is time to take new sample - compute one using
        first order hold (linear interpolation).
242 if lastouttime > 1/outsamplerate
243          lastouttime = lastouttime - 1/outsamplerate;
244          out(1:6,outindex) = (1-lastouttime/dT).*
               lastoutsample+(lastouttime/dT).*x;
245          outindex=outindex+1;
246 end
247
248 % 48. Update last preserved sample for linear interpolation
       .
249 lastoutsample = x;
```

```
250
251 % 49. Save output data.
252
253 % 50. End of program.
```

```
1
2  % SUBROUTINE [Fde,Fnde] = ForceComputationNonLinear(x,
       aleph, bet, roundeddrift, prefetchinner, prefetchouter,
       trackleninner, tracklenouter)
3
4  % 1. Define computed forces as 0.
5  Fde = 0;
6  Fnde = 0;
7
8  % 2. For each of bearings numbered i from 1 to 8 do steps
       from 3 to 12.
9  for i = 1:8
10
11 % 3. Compute position of the ball (number from 0 to 1,
       where 0 corresponds to 0 degrees turn 1 is 360 degrees
       turn) with respect to the outer ring, using rotation
       angle aleph and an offset from reference bearing of i/8.
12 balllocouter = i/8 + aleph;
13 balllocinner = i/8 - bet;
14
15 % 4. Wrap positions if they are greater than 1.
16 if balllocouter > 1
17         balllocouter = balllocouter -1;
18 end
19 if balllocinner > 1
20         balllocinner = balllocinner -1;
21 end
22
23 % 5. Compute sine of ball location to be used for
       computation of force vector direction.
24 s=sinlookup(round(balllocouter*1000)+1);
25
26 % 6. Get local height of inner and outer rings at ball
       location angles, sum up and convert to meters.
27 trackoffs = 1e-10*double(prefetchinner(ceil(balllocinner*
       trackleninner))+prefetchouter(ceil(balllocouter*
       tracklenouter))); % Scaled in m
28
29 % 7. Compute lubricant layer thickness and convert it to
       index in force lookup table.
30 idx=floor((bearingclearance-trackoffs-s*(x(1)-x(3)-x(2)*
       d_de))*10000000000000);% 1 unit of index is 1e-13 m
31
32 % 8. Force saturation, when lubricant is too thin, to avoid
```

```
    physiucally impossible forces.
if (idx < 100000)
        idx = 100000;
end

% 9. Force saturation, when lubricant is too thick, then it
    produces negligibly small force.
if (idx > length(Forcelookup))
        idx = length(Forcelookup);
end

% 10. Add force from this ball to vector sum of DE bearing
    forces, using sine of ball's position.
Fde = Fde - s*Forcelookup(idx);

% 11. Obtain track offset for NDE bearing from static
    roughness look up table
trackoff = rough(floor(T*length(rough))+1,2);

% 12. Perform similar computations as steps 7 to 10 for NDE
    bearing.
idx=floor((bearingclearance-trackoff-s*(x(1)-x(3)+x(2)*
    d_nde))*10000000000000);
if (idx < 100000)
        idx = 100000;
end

if (idx > length(Forcelookup))
        idx = length(Forcelookup);
end
Fnde = Fnde - s*Forcelookup(idx);

% 13. End subroutine, return Fde, Fnde.
```

```
% SUBROUTINE [track,track2, Q, Ubr] =
    TrackDischargeOccurences(x, aleph, bet, Q, Ubr,
    roundeddrift, prefetchinner, prefetchouter,
    trackleninner, tracklenouter, track, track2 )

% 1. For each of bearings numbered i from 1 to 8 do steps
    from 2 to 12.
for i2 = 1:8

% 2. Compute position of the ball (number from 0 to 1,
    where 0 corresponds to 0 degrees turn 1 is 360 degrees
    turn) with respect to the outer ring, using rotation
    angle aleph and an offset from reference bearing of i/8.
balllocouter = i/8 + aleph;
balllocinner = i/8 - bet;

% 3. Wrap positions if they are greater than 1.
if balllocouter > 1
        balllocouter = balllocouter -1;
end
if balllocinner > 1
        balllocinner = balllocinner -1;
end

% 4. Compute sine of ball location to be used for
    computation of force vector direction.
s=sinlookup(round(balllocouter*1000)+1);

% 5. Get local height of inner and outer rings at ball
    location angles, sum up and convert to meters.
trackoffs = 1e-10*double(prefetchinner(ceil(balllocinner*
    trackleninner))+prefetchouter(ceil(balllocouter*
    tracklenouter))); % Scaled in m

% 6. Compute breakdown threshold thickness, using breakdown
     strength limit of 15 MV/m.
threshold_thickness =(Ubr/15e6)

% 7. Compute actual thickness of lubricant layer under the
    contact point of given ball.
actual_thickness = (bearingclearance-trackoffs+(s*(x(1)-x
    (2)*d_de-x(3))))

% 8. If actual thickness is less than threshold value
```

```
    process breakdown, otherwise goto 1.
31 if  threshold_thickness > actual_thickness
32
33 % 9. Compute discharge energy.
34 dener = ((Capacitance*Ubr*Ubr/2))/2;
35
36 % 10. Modify inner and outer race height maps according to
    the melting procedure at given point with given energy
    of a discharge.
37 TrackDischargeOccurences(track,ceil(ballloc*trlen),(
    roundeddrift),dener);
38 TrackDischargeOccurences(track2,ceil(ballloc2*trlen2),(
    roundeddrift),dener);
39
40 % 11. Count discharges and energy.
41 dischcount = dischcount + 1;
42 energ = energ + dener;
43
44 % 12. Reset charge and voltage of capacitance.
45 Q = 0;
46 Ubr = 0;
47
48 % 13. End subroutine.
```

```
% SUBROUTINE [track] = TrackDischargeOccurences(trk,x,y,
    energy)

% 1. Get reference height of discharge
zinit = trk.Track(x,y);

% 2. Compute melted radius
% Double the volume because we expect to melt only half a
    sphere
radmelt = ((2* energy / (2.2e10))^(1/3)*1e7); % Unit of
    grid is 0.1 um

% 3. Square value for optimization
rmsq = radmelt*radmelt;


% 4. Initialize counter for total volume melted
melted = double(0);


% 5. Iterate over x around the point of discharge from x
    discharge - radmelt to x discharge + radmelt do steps 6
    to 13
for i = (x-ceil(radmelt)):(x+ceil(radmelt))

% 6. Compute square of distance from current coordinate to
    center of discharge
isq = (i-x)*(i-x);

% 7. Iterate over y around the point of discharge from y
    discharge - radmelt to y discharge + radmelt do steps 8
    to 13
for j = (y-ceil(radmelt)):(y+ceil(radmelt))

% 8. Compute squared affected radius minus squared distance
     to the center of discharge. If greater than 0 we are
    inside the radius and have to reduce current point of
    height map, otherwise goto 7
test = rmsq-isq-(j-y)*(j-y);
if test > 0

% 9. Compute target depth using sphere equation for sphere
    with center in (x,y,zinit) and radius radmelt
depth = round(sqrt(rmsq-isq-(j-y)*(j-y))*1000*(0.6+0.4*
```

```
    randn(1)));
33
34 % 10. Wrap coordinates of track to form continuos space
35 ie = i;
36 je = j;
37 if j < 1
38         je = 1;
39 end
40 if j > length(trk.Track(1,:));
41         je = length(trk.Track(1,:));
42 end
43 if i < 1
44         ie = i + length(trk.Track);
45 end
46 if i > length(trk.Track);
47         ie = i - length(trk.Track);
48 end
49
50 % 11. If the depth of track higher than what it should
    become after the discharge do steps 12 and 13, otherwise
     goto 7
51 if (trk.Track(ie,je)) > zinit-depth
52
53 % 12. Add all material above the level of melting to melted
     quantity.
54 melted = melted + double(trk.Track(ie,je)-zinit+depth);
55
56 % 13. Set new height map level
57 trk.Track(ie,je) = zinit-depth;
58
59 % 14. Compute radius of a new sphere to be formed from the
    melted material and its squared value
60 raddraw = ((melted/1000 * 3 /4/pi)^(1/3));
61 rmsq = raddraw*raddraw;
62
63 % 15. Iterate over x around the point of discharge from x
    discharge - raddraw to x discharge + raddraw do steps 16
     to 21
64 for i = (x-ceil(raddraw)):(x+ceil(raddraw))
65
66 % 16. Compute square of distance from current coordinate to
     center of discharge
67 isq = (i-x)*(i-x);
68
```

```
69 % 17. Iterate over y around the point of discharge from y
       discharge - raddraw to y discharge + raddraw do steps 18
        to 21
70 for j = (y-ceil(raddraw)):(y+ceil(raddraw))
71
72 % 18. Compute squared affected radius minus squared
       distance to the center of discharge. If greater than 0
       we are inside the radius and have to increase current
       point of height map, otherwise goto 17
73 test = rmsq-isq-(j-y)*(j-y);
74 if test > 0
75
76 % 19. Compute the added value to the height map using
       sphere equation
77 depth = round(sqrt(rmsq-isq-(j-y)*(j-y)));
78
79 % 20. Wrap coordinates of track to form continuos space
80 ie = i;
81 je = j;
82 if j < 1
83         je = 1;
84 end
85 if j > length(trk.Track(1,:));
86         je = length(trk.Track(1,:));
87 end
88 if i < 1
89         ie = i + length(trk.Track);
90 end
91 if i > length(trk.Track);
92         ie = i - length(trk.Track);
93 end
94
95 % 21. If thereis something to add, add to the height map
96 if (depth) > 0
97         trk.Track(ie,je) = trk.Track(ie,je) + 2*depth;
98 end
99
100 % 22. End of subroutine
```

Appendix C. Total energy of discharges observed during modelling.

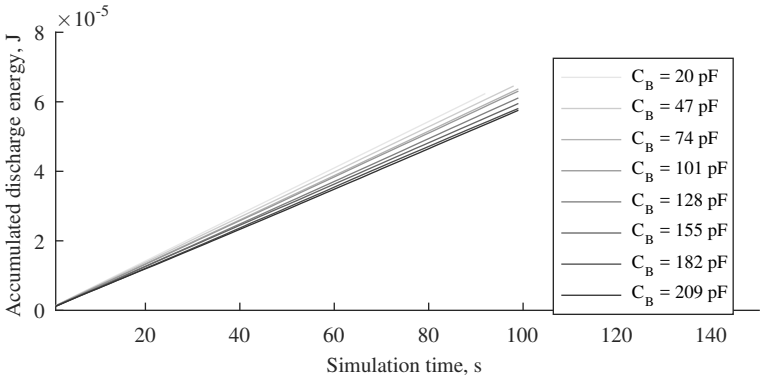

Figure C.1: Total energy of discharges observed during sensitivity analysis to C_{B}.

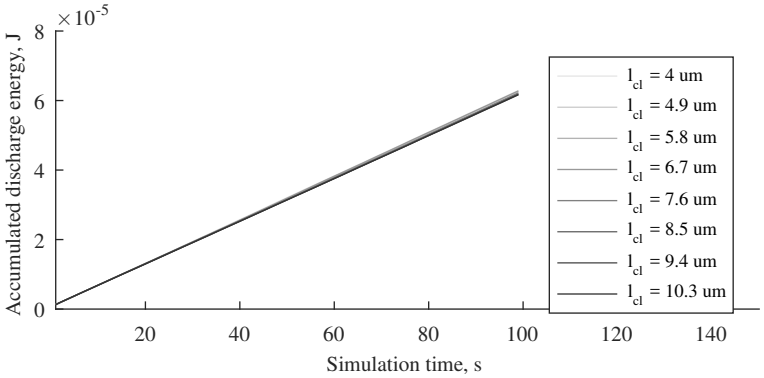

Figure C.2: Total energy of discharges observed during sensitivity analysis to l_{cl}.

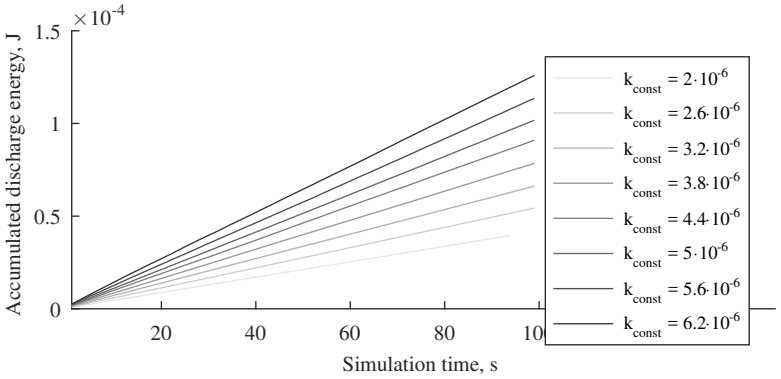

Figure C.3: Total energy of discharges observed during sensitivity analysis to k_{const}.

Appendix D. Scatter diagrams for total energy of discharges

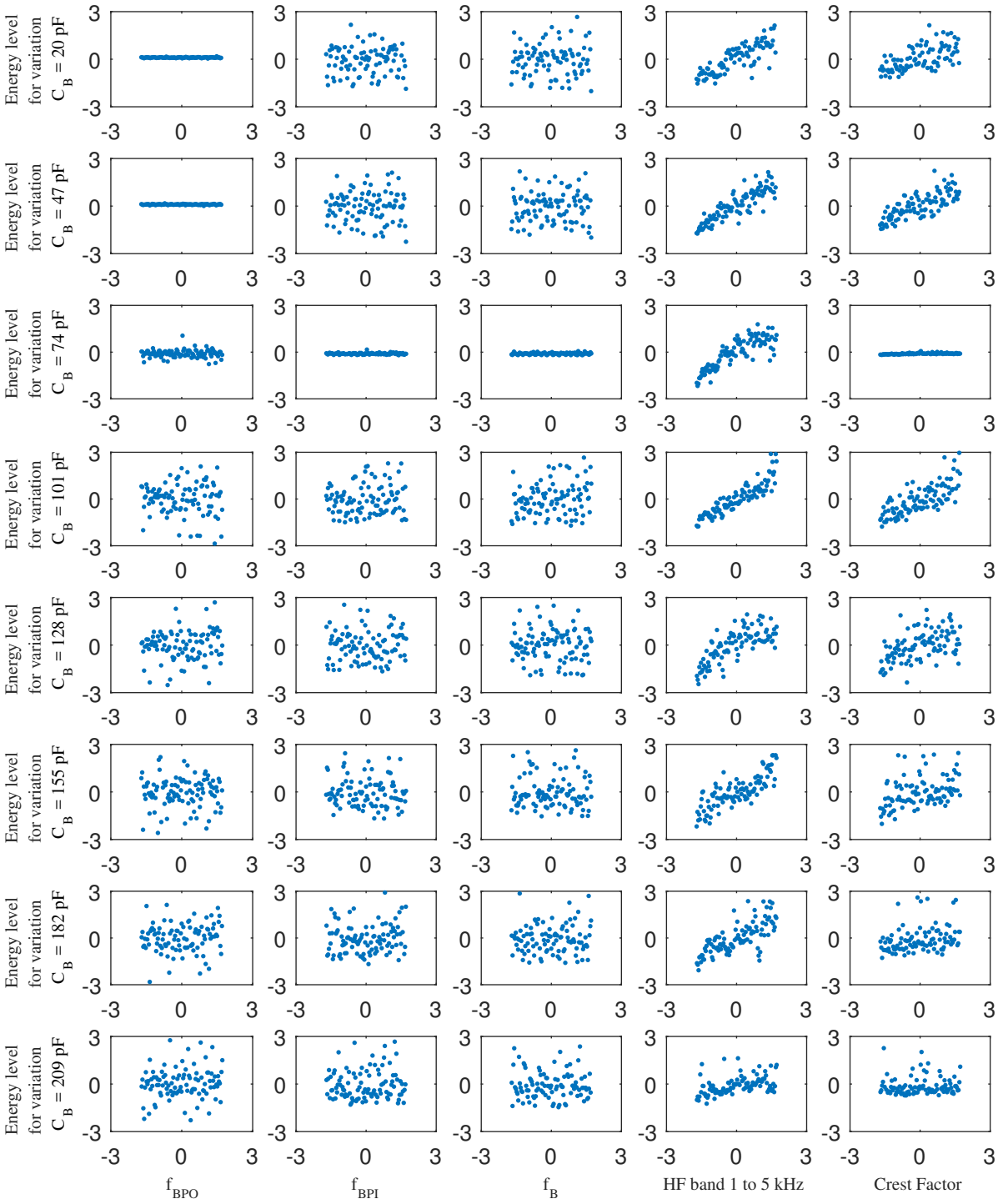

Figure D.1: Scatter diagrams for total energy of discharges versus vibration features for sensitivity analysis to C_{B}.

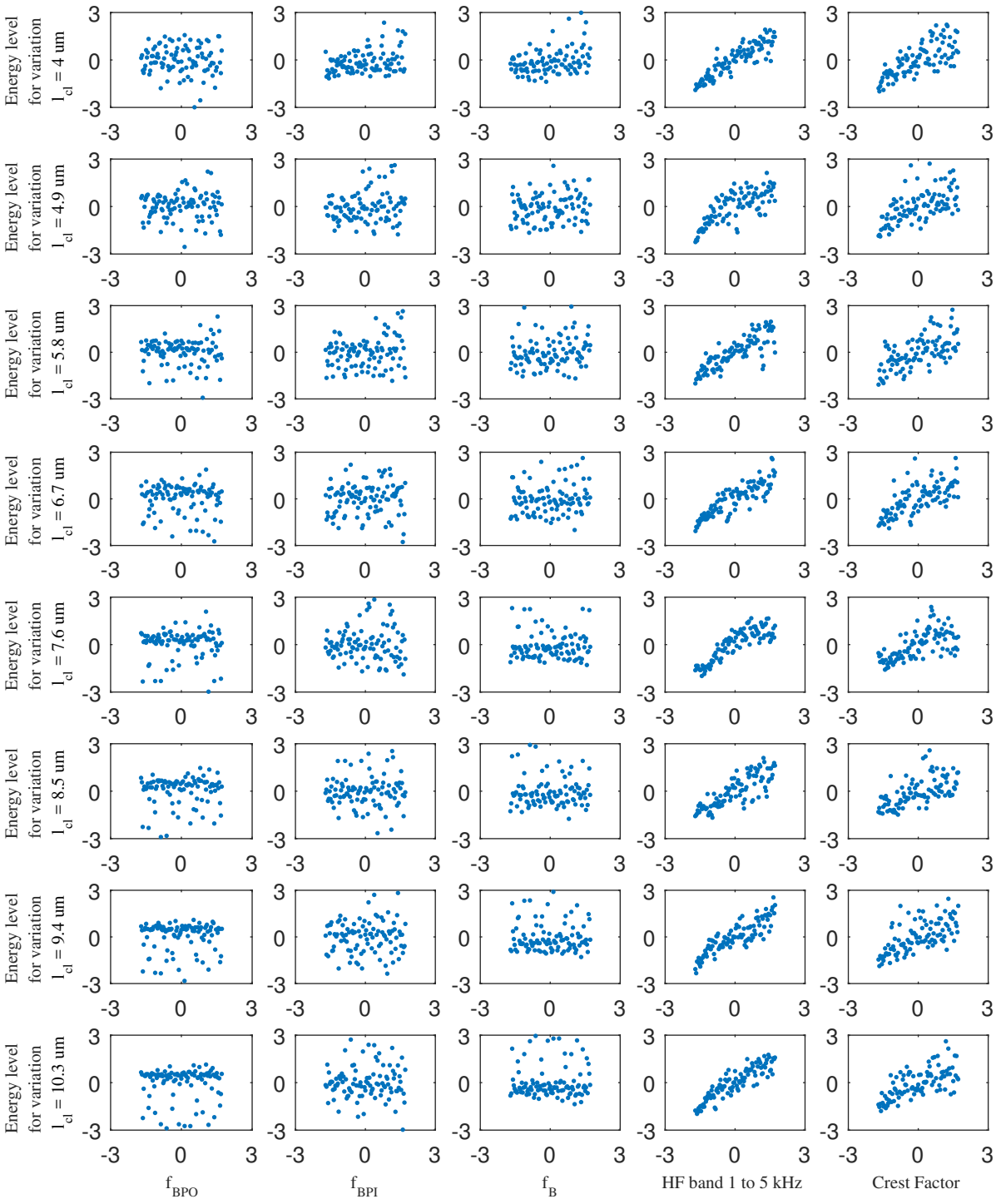

Figure D.2: Scatter diagrams for total energy of discharges versus vibration features for sensitivity analysis to l_{cl}.

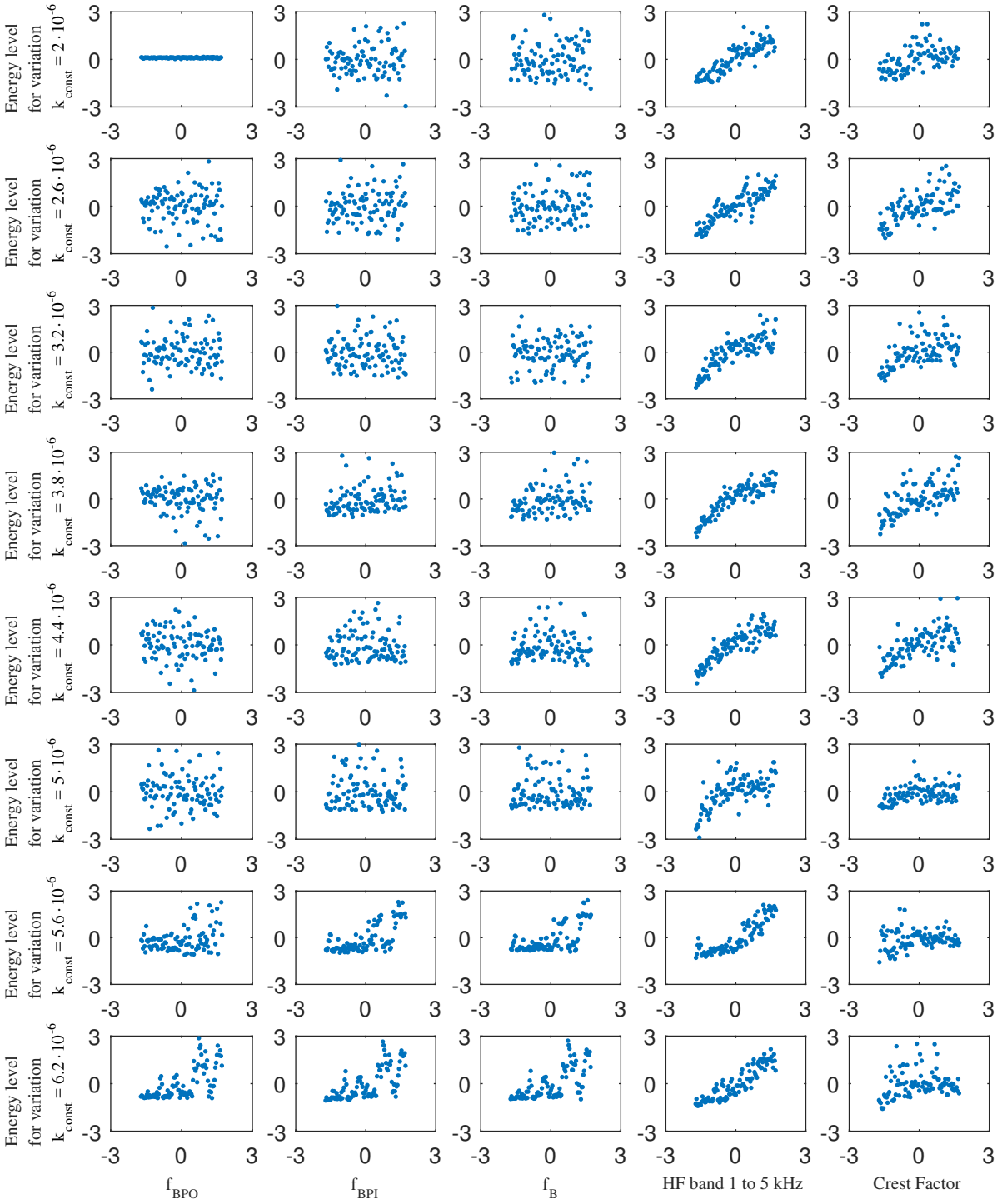

Figure D.3: Scatter diagrams for total energy of discharges versus vibration features for sensitivity analysis to k_{const}.

Appendix E. Proof of validity for rotor shaft estimate.

Let's assume computation of total moment of inertial of rotor stack and rotor shaft for a solid rotor induction motor with the dimensions as defined in Fig. E.4: rotor stack outer radius r_{R}, rotor shaft outer radius r_{SH}, rotor stack axial length l_{axial}, length of shaft extension outside of rotor stack $l_{\mathrm{SH,EXT}}$. In addition, let's assume that density of materials used in rotor stack and shaft are the same ρ.

Then, the total moment of inertia, using the Huygens-Steiner theorem and solid cylinder model can be computed as

$$J_{\mathrm{t}} = J_{\mathrm{R}} + 2 \cdot J_{\mathrm{SH,EXT}} + 2 \cdot m_{\mathrm{SH,EXT}} \cdot ((l_{\mathrm{axial}} + l_{\mathrm{SH,EXT}})/2)^2, \tag{E.2}$$

where rotor moment of inertia J_{R} is

$$J_{\mathrm{R}} = \frac{m_{\mathrm{R}}}{12}(3 \cdot r_{\mathrm{R}}^2 + l_{\mathrm{axial}}^2), \tag{E.3}$$

shaft end piece moment of inertia J_{R} is

$$J_{\mathrm{SH,EXT}} = \frac{m_{\mathrm{SH,EXT}}}{12}(3 \cdot r_{\mathrm{SH}}^2 + l_{\mathrm{SH,EXT}}^2), \tag{E.4}$$

mass of rotor is

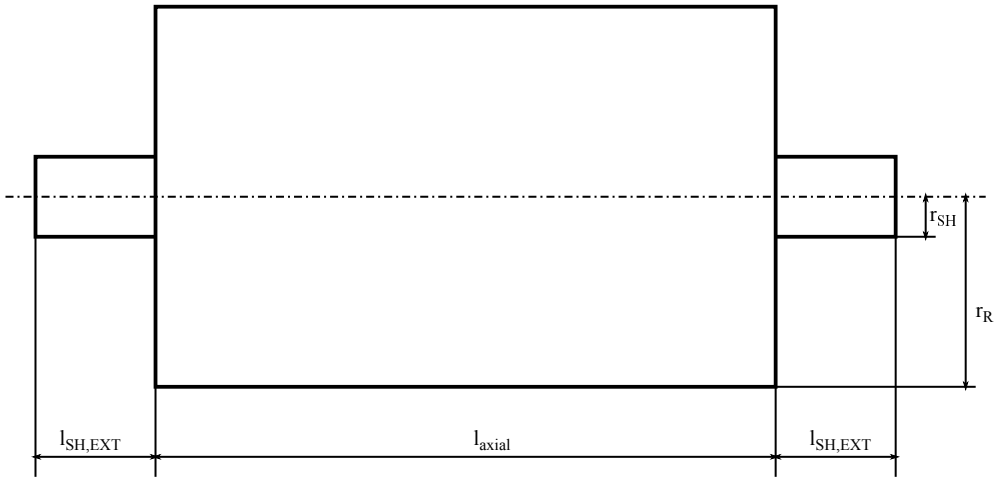

Figure E.4: Sketch of motor dimensions, used in proof.

$$m_{\mathrm{R}} = \rho\pi r_{\mathrm{R}}^2 \cdot l_{\mathrm{axial}}, \tag{E.5}$$

and mass of shaft end piece is

$$m_{\mathrm{SH,EXT}} = \rho\pi r_{\mathrm{SH}}^2 \cdot l_{\mathrm{SH,EXT}}. \tag{E.6}$$

Which yields after substitution:

$$\begin{aligned} J_{\mathrm{t}} = 2\big(&\frac{l_{\mathrm{SH,EXT}}\pi\rho {r_{\mathrm{SH}}}^2 \left(3{r_{\mathrm{SH}}}^2 + {l_{\mathrm{SH,EXT}}}^2\right)}{12} + \\ &+ \frac{l_{\mathrm{SH,EXT}} \left(l_{\mathrm{SH,EXT}} + l_{\mathrm{axial}}\right)^2 \pi\rho {r_{\mathrm{SH}}}^2}{4}\big) + \\ &+ \frac{l_{\mathrm{axial}}\pi {r_{\mathrm{R}}}^2 \left(3{r_{\mathrm{R}}}^2 + {l_{\mathrm{axial}}}^2\right)\rho}{12} \end{aligned} \tag{E.7}$$

Assuming the ratio between $l_{\mathrm{SH,EXT}}$ and l_{axial} as $l_{\mathrm{SH,EXT}} = 0.1 \cdot l_{\mathrm{axial}}$ and ratio between r_{R} and r_{SH} as $r_{\mathrm{SH}} = 0.33 \cdot r_{\mathrm{R}}$ we can simplify (E.7) to

$$\begin{aligned} J_{\mathrm{t}} = 2 \cdot (&\frac{1}{120} \cdot l_{\mathrm{axial}}\pi\rho {r_{\mathrm{SH}}}^2 \left(3{r_{\mathrm{SH}}}^2 + 0.01{l_{\mathrm{axial}}}^2\right) + \\ &+ 0.03025{l_{\mathrm{axial}}}^3\pi\rho {r_{\mathrm{SH}}}^2) + \\ &+ \frac{l_{\mathrm{axial}}\pi {r_{\mathrm{R}}}^2 \left(3{r_{\mathrm{R}}}^2 + {l_{\mathrm{axial}}}^2\right)\rho}{12} \end{aligned} \tag{E.8}$$

$$\begin{aligned} J_{\mathrm{t}} = 2 \cdot (&0.00121 \cdot {l_{\mathrm{axial}}}^3\pi {r_{\mathrm{R}}}^2\rho + \\ &+ \frac{10}{3} \cdot 10^{-4}\, l_{\mathrm{axial}}\pi {r_{\mathrm{R}}}^2 \left(0.12{r_{\mathrm{R}}}^2 + 0.01{l_{\mathrm{axial}}}^2\right)\rho) + \\ &+ \frac{l_{\mathrm{axial}}\pi {r_{\mathrm{R}}}^2 \left(3{r_{\mathrm{R}}}^2 + {l_{\mathrm{axial}}}^2\right)\rho}{12} \end{aligned} \tag{E.9}$$

$$J_{\mathrm{t}} = 0.0123050152368 \cdot l_{\mathrm{axial}}^5\pi\rho \tag{E.10}$$

Let's now compute J_{R} using the simplified rod model (eq. 3.7) and computing l_{SH} as

$$l_{\mathrm{SH}} = l_{\mathrm{axial}} + 2 \cdot l_{\mathrm{SH,EXT}}. \tag{E.11}$$

Using the same assumptions on drive proportions as in (E.8) to (E.10) we obtain

$$J_{\mathrm{R}} = 0.013068 \cdot l_{\mathrm{axial}}^{5} \pi \rho. \tag{E.12}$$

From this it can be concluded, that, for these assumed drive proportions, the simplified equation provides the value for moment of inertia which is overestimated by 6.2%. This level of precision was deemed sufficient for the modeling of bearing degradation process.

Publication I

Romanenko A., Ahola J., Muetze A., and Niskanen V.
Study of incipient bearing damage monitoring in variable-speed drive systems

Reprinted from
16th European Conference on Power Electronics and Applications, EPE-ECCE Europe 2014,
EPE-ECCE Europe 2014, 2014, pp. 1-10

Study of incipient bearing damage monitoring in variable-speed drive systems

Aleksei Romanenko, Jero Ahola
LAPPEENRANTA UNIVERSITY OF TECHNOLOGY
P.O. Box 20
FI-53851 Lappeenranta, Finland
Tel.: +358 40 5168237
Fax: +358 5 621 6799
E-mail: aleksei.romanenko@lut.fi, jero.ahola@lut.fi

Annette Muetze
GRAZ UNIVERSITY OF TECHNOLOGY
Inffeldgasse 18/I
A-8010 Graz, Austria
Tel.: +43 316 873 7240
Fax: +43 664 60 873 107240
E-mail: muetze@tugraz.at

Ville Niskanen
LAPPEENRANTA UNIVERSITY OF TECHNOLOGY
P.O. Box 20
FI-53851 Lappeenranta, Finland
Tel.: +358 40 5168237
Fax: +358 5 621 6799
E-mail: ville.niskanen@lut.fi

Keywords

«Measurements», «Induction motor», «Converter machine interactions», «Diagnostics», «Wireless sensors»

Abstract

Inverter-induced high-frequency bearing currents are a common root cause of bearing failures in frequency converter-fed motors and generators. Bearing faults are typically identified by vibration measurements. In our work, we experimentally submit bearings to electric discharge machining (EDM) bearing currents, use different means to measure the electrical stress placed on the bearings, measure the resulting vibration signal, and apply signal processing for feature extraction. All this is done 1184 hours of operation, so as to study the incipient bearing failure behavior.

Introduction

Today, it is well recognized that modern variable-speed drives that use fast-switching inverters may bring forth a variety of parasitic phenomena. Inverter-induced EDM bearing currents are one of these phenomena and may significantly harm the drive and eventually lead to the failure of the electric machine's bearings. Different authors have described the cause-and-effect chains, allowing the selection of appropriate mitigation techniques (e.g. in [1]–[13]). Several types of inverter-induced bearing currents are distinguished, EDM bearing currents, circulating bearing currents and rotor-to-ground currents. For example, with EDM bearing currents, electric discharges occur statistically distributed between the raceways of the inner and outer ring and the rolling elements of a bearing (leading, for example, to pitting and grey traces, as can be seen in Fig. 4 below). While the exact mechanism of bearing failure due to such bearing currents has not been understood today, it has been well established that such currents can be a starting point for a bearing damage. The bearing damage (fluting pattern) resulting from the bearing currents can be detected with vibration-measurement based methods [12]-[14]. According to [14], EDM currents first lead to pitting of the outer or inner ring and in later stages to an increase of wideband vibration. In [19] Kriese et al. explain that, the usability of vibration monitoring for the predictive maintenance of inverter-induced bearing failures is rather limited. This is mainly due to the lack of knowledge on the damage evolution within the bearing from the incipient damage at which stage counter-measures could be applied and operation continued up to severe damage that does not allow any further operation. The main objective of this paper is to show results of a test run in the laboratory with a specially modified motor setup, and to link the propagation of inverter-induced bearing damage to the features extracted from the vibration analysis.

Laboratory test setup

The test rig comprises a low-voltage off-the shelf squirrel cage induction motor (3-phase, 15 kW, 4-pole) and a load machine of similar type coupled with an insulating coupler (Fig. 1 and Fig. 2). The test motor has 6309 deep groove ball bearings with a clearance of C3, greased with an off-the shelf lithium-soap-based grease. Both bearings of the test motor are electrically insulated towards the frame by using polyethylene sleeves. The drive-end (DE) bearing insulation is short-circuited by a short wire, enabling intrusive bearing current measurement (R&S ZC-20 (DC-100MHz)). Thereby, the bearing current will always flow through the DE bearing of the motor. To generate the discharge currents, voltage is supplied to the motor non-drive end (NDE) between the motor shaft and the frame with a signal generator (Hameg HM-8131-2) connected to a buffer amplifier circuit. The signal is supplied to the rotor by the means of an electric slip ring (Mercotac 110, contact resistance $R_{contact} < 1$ mΩ, max. current $I_{max} = 10$ A, max. frequency $F_{max} = 200$ MHz).

The bearing voltage is measured with a high impedance differential probe (R&S ZT-01 DC-100MHz)) from the terminals of the coupler. The measurement equipment further comprises a piezoelectric vibration measurement sensor (Kistler 8712A5M1, ±5g, BW = 0.5-8000 Hz) with related amplifier and filters, three temperature sensors (EPCOS - B57560G104F 100 kOhm thermistors) for the measurement of bearing outer ring temperature, as well as a radio-frequency (RF) measurement setup for the counting of pulses originating from the bearing discharges [15], [16], [17]. The RF measurement equipment includes an antenna (EMCO 93148), an oscilloscope

(R&S RTO1014), and a digital pulse counter. The antenna is directed to the DE of the test motor, having distance approximately of 1 m (Fig. 2). The RF pulses are measured over 50 ohms termination. The triggering voltage to detect RF pulses is adjusted to 5 mV, detecting the rising edge. The so-called discharge activity (DA) is determined from the number of counted discharges sampled over time windows of 30 s [21]. Test motor is rotated by the load machine which enables the adjustment of the DE bearing operating temperature. The vibration signal from the motor DE (20 kSamples/s, 400 kSamples record length), the bearing temperature, and the detected RF signals are measured and periodically stored by using a general purpose data acquisition system. (Period times of 30 seconds for the temperature and RF signal, 5 minutes for the vibration measurements respectively.)

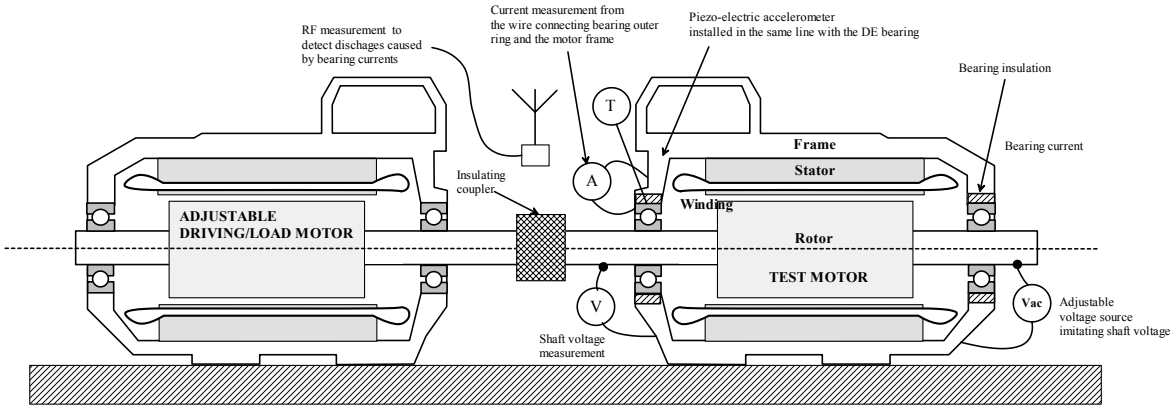

Fig. 1 Schematic of laboratory test setup for the testing of vibration measurement based detection of incipient inverter induced bearing failures.

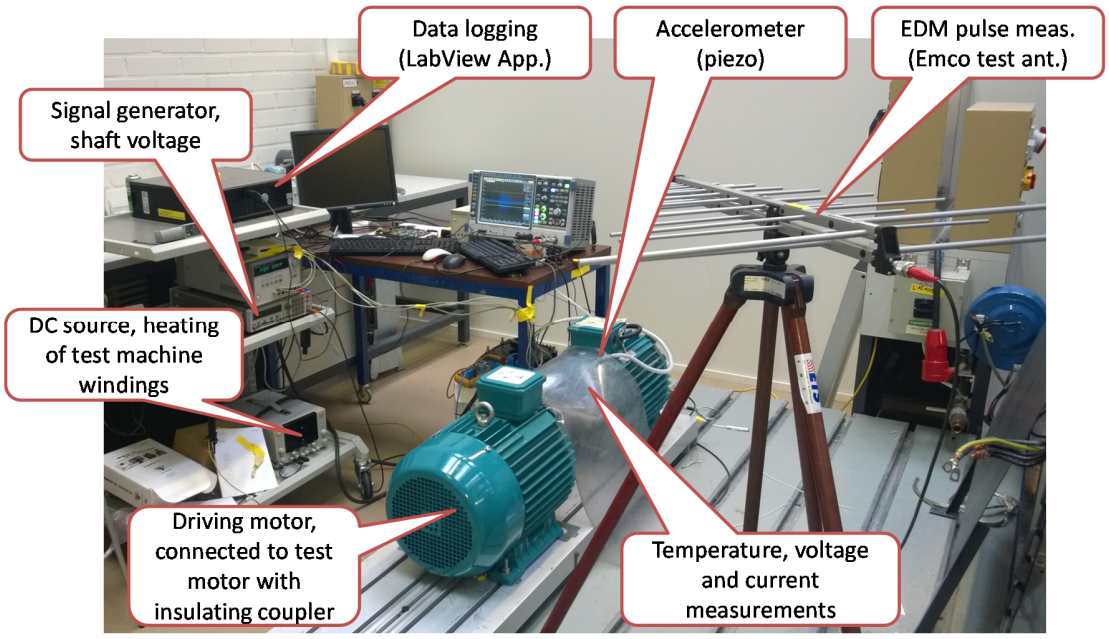

Fig. 2 Photo of the laboratory test setup.

Test program

Methodology

Fig. 3 illustrates the approach used to analyse the DA. The bearings are submitted to electric stress of a predefined level, controlled to the extent possible through a predefined operating speed and voltage signal. The EDM DA is monitored with the non-intrusive RF-based bearing current detection method and additional recording of the bearing temperature. The state of health of the bearing is monitored by vibration measurement, so that any possible incipient failure within the bearing can be related to the electric stress the bearing had been subjected to. Once the predefined running time of the bearing has been completed, the bearing is inspected both visually and with an electron microscope to understand its state of health and correlate it with the condition determined with the vibration-based measurement approach.

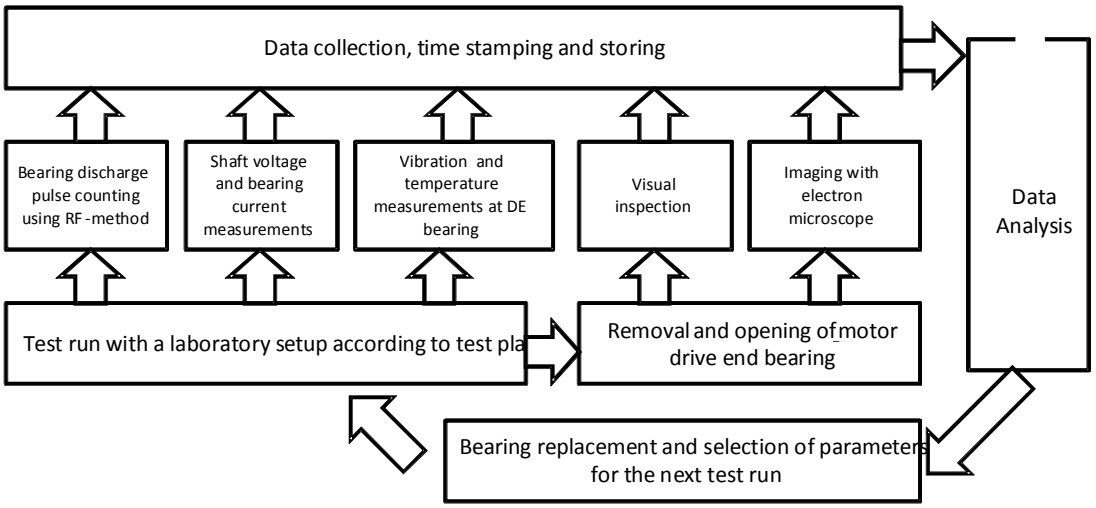

Fig. 3 Principle of test run with the laboratory test setup and its evaluation.

Selected electric bearing load

The test motor was supplied with new bearings and first was operated directly from the mains for about two days, without any external voltage supplied to the shaft. Then, the shaft was supplied with the external sinusoidal voltage with 20 V_{pp} and 300 kHz frequency, as described above. The sampling of bearing temperatures, vibration and discharges was started and the motor let to run for 1184 hours. Then, the bearings were analyzed following the previously explained approach.

Results of experimental investigations

Visual inspection and imaging with a scanning electron microscope

For the visual inspection and analysis with the electron microscope the DE bearing was removed, opened, and cut into smaller sections. Visually, the bearing balls and inner ring look like brand new. The raceway of the outer rings shows a grey trace with darker and lighter areas (Fig. 4, left).

Next, the two bearing rings were studied with an electron microscope (imaging voltage of 20 kV). A picture of the bearing outer ring is shown in Fig. 4: the traces of surface polishing (Fig. 4, right) have almost entirely disappeared. In addition, the raceway shows many craters with diameters of up to 0.6 µm and a single larger crater with of 1 µm diameter. Fig. 5 shows the electron microscope images of the raceways of the used DE bearing inner ring and of the outer ring of a new bearing: In both cases, the traces due to polishing are still visible, and there are no craters due to EDM currents.

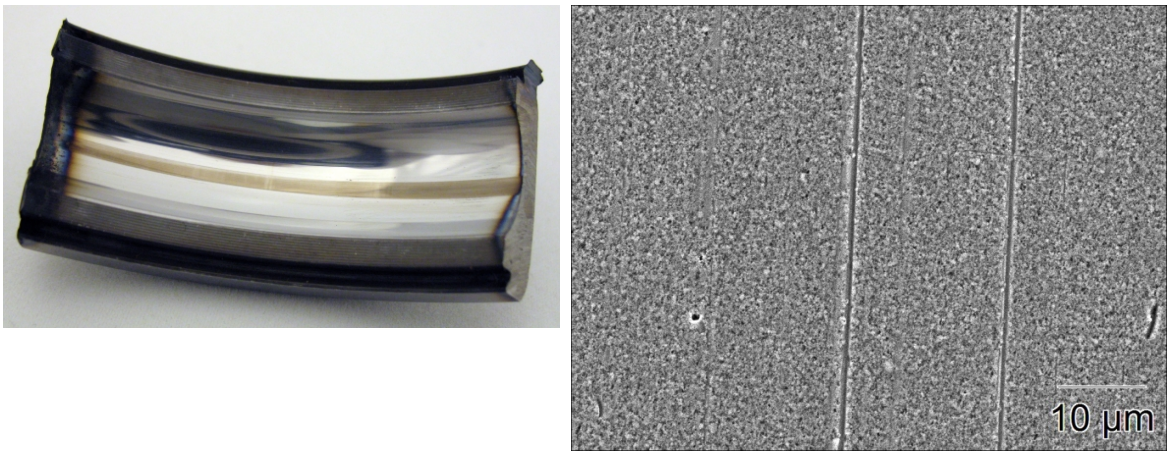

Fig. 4 Visual inspection of outer race of DE bearing (left): the grey trace caused by EDM bearing currents is clearly visible. Electron microscope picture of grey trace on bearing outer ring (right).

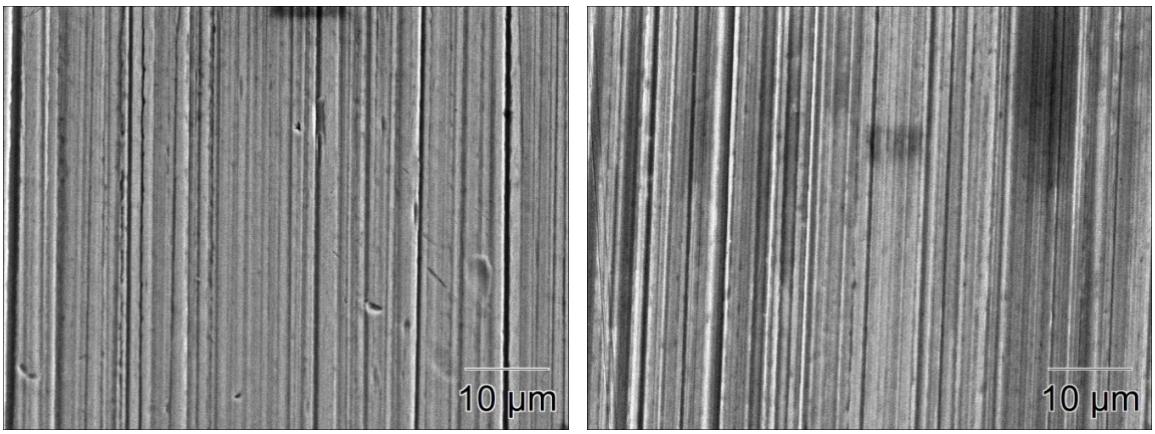

Fig. 5 Electron microscope images of the used DE bearing's inner ring (left) and of the new bearing's outer ring (right).

Preliminary results: Bearing temperature during running time

Fig. 6 shows the recorded hourly averages of the measured bearing temperature averaged from the three temperature sensors.

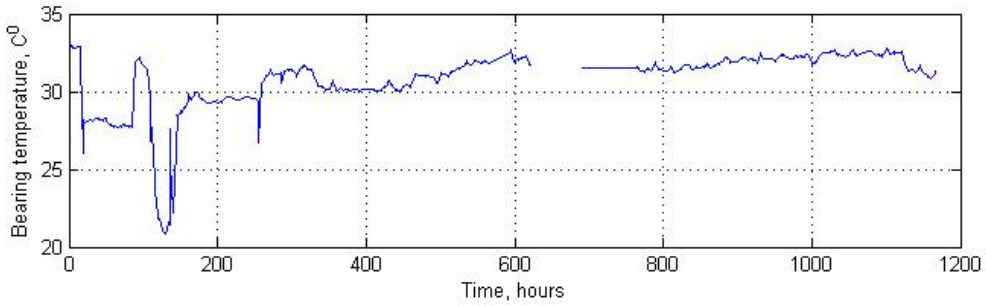

Fig. 6 Measured bearing temperature over time; temperatures averaged over one hour.

Apart from some changes of some tens of K within a few hours running time occurring within the initial period of the test run, the temperature increased slowly but steadily during the time of operation. One possible explanation might be the increase due to a minor increase in friction caused by the small craters. Such behaviour would indeed provide a means for incipient bearing failure detection, provided all other reasons for a change in bearing temperature are excluded, such as change of operating point, or of ambient temperature.

No significant change in bearing temperature that might have been caused by significant discharge activity occurred: As expected, the energy discharged into the bearing was effectively dissipated within the bearing. The bearing did not reach a condition in which fault propagation would have resulted in continuous increase of the bearing temperature, what, in turn, would have further worsened the state of health the bearing.

Single discharge energy analysis

In [20] Niskanen et al. performed capacitance measurements for the same machine and bearing type as in this experiment. The capacitance values computed in that research were 0.36 nF at 23 C° and 0.89 nF at 37 C°. Assuming a linear interpolation, the bearing capacitance as a function of temperature is given by

$$C_b = 0.0379\ (T - 23) + 0.36\ \text{[nF]}, \quad (1)$$

where T is the bearing temperature in degree C°. The average temperature during the experiment varied between 21 and 33 degrees C°. From this, the bearing capacitance is estimated to vary between 0.28 nF (21 C° value) and 0.74 nF (33 C° value). Note that the order of magnitude of these values is in agreement with published bearing capacitance values, such as those presented in [22].

The larger value (at 33 C°) is used to estimate the upper bound of energy released from within the bearing onto the bearing surface during a discharge,

$$E = \frac{C_b U^2}{2}, \quad (2)$$

where C_b is the estimated worst-case bearing capacitance and U is the maximal shaft voltage. For the chosen supply voltage level of 20 Vpp, the energy of a single discharge is E = 38 nJ. Note that the true upper bound of energy released into the bearing would be even higher, as additional energy

might be released from the rotor-to-frame capacitance. However, according to [19], such energy level would be sufficient to vaporize craters with radii up to 0.64 µm and melt craters with radii up to 1.2 µm while the electron microscope analysis demonstrates craters with the diameters of up to 0.6 µm which is twice as small. This corresponds to the discharges happening in a 0.74 nF capacitance (computed C_b value at 33 C°) at 3.23 V. It was observed that the discharges might as well happen before the shaft voltage had reached the peak value of the applied shaft voltage. This can prevent the shaft voltage from reaching higher values as the bearing temporarily goes into resistive mode [20]. Furthermore, it is understood that some of the energy dissipated during the discharge is dissipated into the grease film, contributing to its degeneration.

Analysis of counted RF pulses

The measurement of discharge activity has been carried out using the methodology presented in [21]. The trigger level was selected to be 5 mV. Fig. 7 shows the measured discharge activity over the duration of the experiment, which changes over time, as reported in [21], and the total number of accumulated discharges that has been computed from the measured discharge activity.

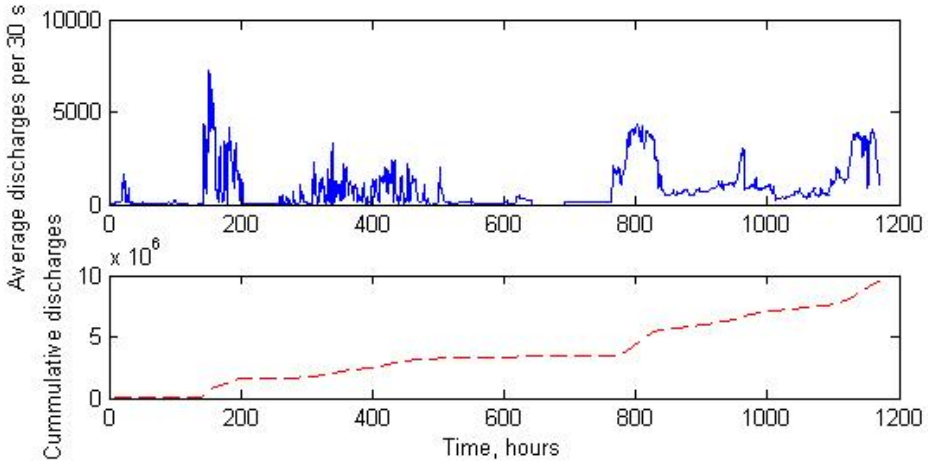

Fig. 7 Discharge activity and cumulative discharge count.

The total number of observed discharges over the duration of experiment was approximately 10 million. This means that the total amount of energy released into the bearing was 0.38 J. While this is a small number for the machine in general it was applied to a small surface. However, the average intensity of the discharges was only 89.15 nW. We consider such a low power level to be unable to cause additional heating to bearings due to heat conduction. The measured discharge activity varies significantly over time. This is caused by the bearing going into resistive mode for current conductance preventing any further discharges until the bearing state changes significantly.

Analysis of vibration measurements

Spectral analysis and Fourier transformation had been selected to analyze the measured vibrations, as they allow a good tradeoff between computational effort (allowing processing of significant amounts of data) and insight into the degradation process.

The envelope carrier band of the spectral analysis was set to 1-5 kHz. For electric machines operating with rolling element bearings, changes in vibration levels are mainly expected at three different frequencies [18]:

Outer ring pass frequency: $F_{\mathrm{BPO}} = \frac{N_{\mathrm{B}}}{2} F_{\mathrm{S}}(1 - \frac{D_{\mathrm{b}}}{D_{\mathrm{c}}})$ (3)

Inner ring pass frequency: $F_{BPI} = \frac{N_{\mathrm{B}}}{2} F_{\mathrm{S}}(1 + \frac{D_{\mathrm{b}}}{D_{\mathrm{c}}})$ (4)

Ball rotation frequency: $F_B = \frac{D_{\mathrm{c}}}{2D_{\mathrm{b}}} F_{\mathrm{S}}(1 - \frac{D_{\mathrm{b}}^2}{D_{\mathrm{c}}^2})$ (5)

where D_{b} and D_{c} are the bearing ball and cage diameters respectively, and F_{S} is the shaft rotational frequency. For the test setup, the corresponding values are D_{b} = 17.5 mm, D_{c} = 72.5 mm and F_{S} = 50 Hz, giving F_{BPO} = 151.7 Hz, and F_{B} = 74 Hz, F_{BPI} = 248 Hz. To eliminate noise, the measurements were smoothed using a moving average filters with windows of 20-50 samples. The results for the outer ring pass and for the ball rotation frequencies are shown in Fig. 8. The frequency components related to F_{BPI} contained no significant signal and thus are not presented.

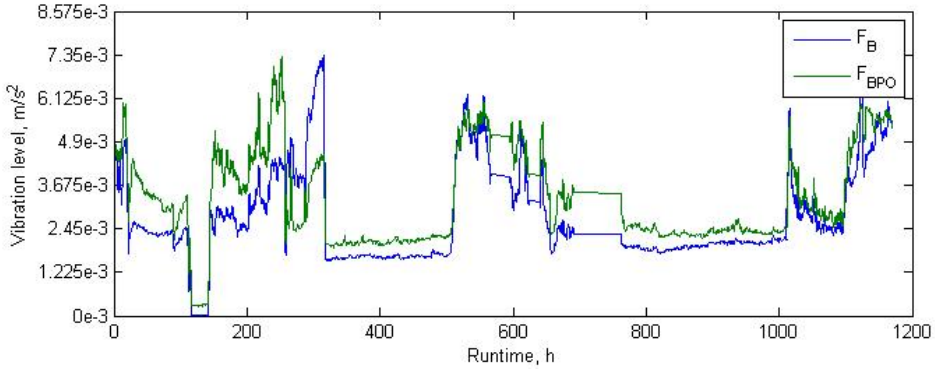

Fig. 8 Envelope spectrum analysis; 20 samples moving average.

The Fourier analysis was applied to the same frequencies, F_{BPO} and F_{B}. The results are shown in Fig. 9.

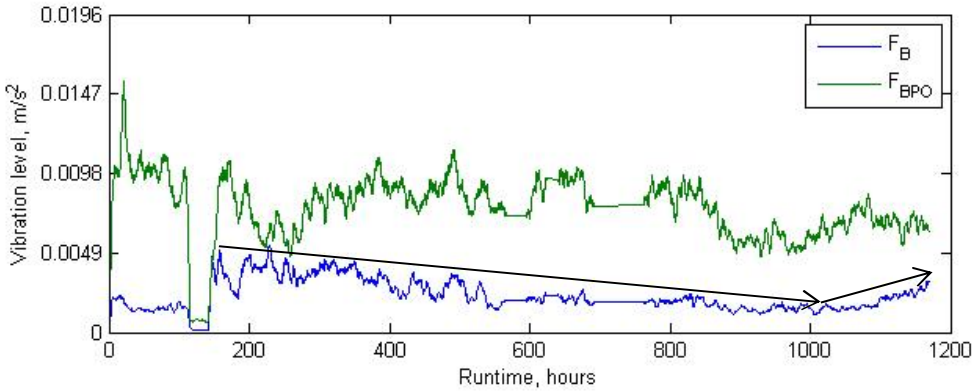

Fig. 9 FFT analysis of vibration bands; 50 samples moving average.

The conventional FFT markers demonstrate almost no correlation with the envelope spectrum. This is explained by the rather high level of noise caused by the shaft rotation frequency harmonics.

However, the latter part of F_B plot starts to go into positive trend after a very long and slow continuous decrease which might provide another indicator for an incipient bearing failure and thus the beginning of a bearing wear process that might eventually lead to bearing failure.

Fig. 10 shows the vibration level RMS value analysis, applied to the source envelope signal of 1-5 kHz band.

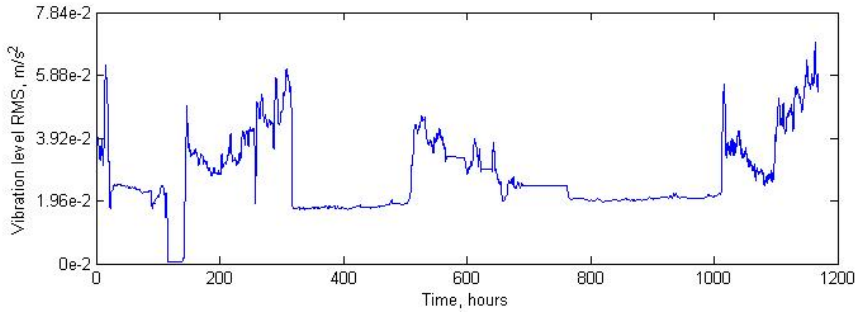

Fig. 10 RMS vibration level of 1-5 kHz band; 30 samples moving average.

This marker follows the same pattern of increased and decreased magnitudes as the selected vibration bands of F_B and F_{BPO} over the duration of experiment.

Summary

The results obtained from different means to measure the electric stress placed on the bearings complement each other very well and lead to a comprehensive picture: The electron microscope analysis of the bearing showed that the outer ring suffered wear in the form of micro-craters on its surface from the electric discharges the bearing had been subjected to. From the recorded discharge activity, a total of 0.38 J was determined to have been dissipated over the 1184 hours of machine runtime. This comparatively low energy intensity can be easily dissipated by the bearing without causing additional bearing heat that can provoke dramatic change in capacitance causing self-amplifying degradation process. The vibration level of the bearing was found to increase only very slowly over the bearing time of operation and can barely be detected by conventional vibration analysis.

References

[1] CHEN S., LIPO T.A.., FITZGERALD D., 'Modelling of bearing currents in inverter drives,' *IEEE Trans. Ind. App*., 1996, 32, (6), pp. 1365-1370.

[2] ERDMAN J., KERKMAN R., SCHLEGEL D., 'Effect of PWM inverters on AC motor bearing currents and shaft voltages,' *IEEE Trans. Ind. Appl*., 1996, 32, (2), pp. 250-259.

[3] BUSSE D., ERDMAN J., KERKMAN R., SCHLEGEL D., 'Bearing currents and their relationship to PWM drives,' *IEEE Trans. Power Electron*., 1997, 12, (2), pp. 243-252.

[4] BUSSE D., ERDMAN J., KERKMAN R., SCHLEGEL D., SKIBINSKI G., 'System electrical parameters and their effect on bearing currents,' *IEEE Trans. Ind. Appl*., 1997, 33, (2), pp. 577-584.

[5] BUSSE D., ERDMAN J., KERKMAN R., SCHLEGEL D., SKIBINSKI G., 'Characteristics of shaft voltage and bearing currents,' *IEEE Ind. Appl. Mag*., 1997, 3, pp. 21-32.

[6] LINK P., 'Minimizing electric bearing currents in ASD systems', *IEEE Ind. Appl. Mag*., 1999, 5, pp. 55-66.
[7] BOYANTON H.E., HODGES G., 'Bearing fluting,' *IEEE Ind. Appl. Mag.*, 2002, 8, pp. 53-57.
[8] SCHIFERL R.F., MELFI M.J., 'Bearing current remediation options,' *IEEE Ind. Appl. Mag.*, 2004, 10, pp. 40-50.
[9] AKAGI H., DOUMOTO T., 'An approach to eliminating high-frequency shaft voltage and leakage current from an inverter-driven motor,' *IEEE Trans. Ind. Appl.*, 2004, 40, (4), pp. 1162-1169.
[10] MUETZE A., BINDER A., 'Don't lose your bearings – mitigation techniques for bearing currents in inverter-supplied drive systems,' *IEEE Mag. Ind. Appl.*, 2006, 12, (4), pp. 22-31.
[11] MUETZE A., BINDER A., 'Practical rules for assessment of inverter-induced bearing currents in inverter-fed AC motors up to 500 kW,' *IEEE Trans. Ind. Appl., 2007*, 54, (3), pp. 1614-1622.
[12] TISCHMACHER H., GATTERMANN S., 'Bearing Currents in Converter Operation', *Proc. ICEM 2010*, 6-8th Sep. 2012, pp. 1-8.
[13] ZIKA T., GEBESHUBER I.C., BUSCHBEK F., PREISINGER G., GRÖSCHL M., 'Surface analysis on rolling bearings after exposure to defined electric stress', *Proc. IMechE 2009*, 2009, Vol. 223, Part J, pp. 787-797.
[14] TISCHMACHER H., GATTERMANN S., 'Multiple Signature Analysis for the Detection of Bearing Currents and the Assessment of the Resulting Bearing Wear', *Proc. SPEEDAM 2012,* 20-22 June, 2012, pp. 1354-1359.
[15] SÄRKIMÄKI V., Radio frequency method for detecting bearing currents in induction motors, PhD Thesis, Lappeenranta University of Technology, Finland, 2009.
[16] AHOLA J., SÄRKIMÄKI V., MUETZE A., 'Radio-frequency-based detection of electrical discharge machining bearing currents', *IET Electric Power App*., 5, (4), Apr. 2011, pp. 386-392.
[17] NISKANEN V., MUETZE A., AHOLA J., 'On the role of the shaft end in the radio-frequency emission of discharge bearing currents in induction motors', *EPE Journal*, pp. 42-50, vol. 23, no. 4, Dec. 2013.
[18] LI, B., MO-YUEN CHOW, TIPSUWAN, Y., HUNG, J.C., 'Neural-network-based motor rolling bearing fault diagnosis', *Industrial Electronics, IEEE Transactions on* , 47, (5), Oct 2000, pp.1060-1069.
[19] KRIESE, M.; WITTEK, E.; GATTERMANN, S.; TISCHMACHER, H.; POLL, G.; PONICK, B., 'Influence of bearing currents on the bearing lifetime for converter driven machines', *Electrical Machines (ICEM), 2012 20th International Conference on* , 2-5 Sept. 2012, pp.1735-1739.
[20] NISKANEN, V.; MUETZE, A.; AHOLA, J., 'Study on bearing impedance properties at several hundred kilohertz for different electric machine operating parameters', *Industry Applications, IEEE Transactions on* , vol.PP, no.99, pp.1-1.
[21] MUETZE, A.; TAMMINEN, J.; AHOLA, J., 'Influence of motor operating parameters on discharge bearing current activity', *Industry Applications, IEEE Transactions on*, 47, (4), pp.1767-1777, July-Aug. 2011.
[22] WITTEK, E.; KRIESE, M.; TISCHMACHER, H.; GATTERMANN, S.; PONICK, B.; POLL, G., 'Capacitance of bearings for electric motors at variable mechanical loads, ' *Electrical Machines (ICEM), 2012 20th International Conference on* , vol., no., pp.1602,1607, 2-5 Sept. 2012.

Publication II

Romanenko A., Lahdelma S., Muetze A., and Ahola J.
Vibration Measurement Approach to the Bearing Damage Evolution Study in the Presence of Electrostatic Discharge Machining Currents

Reprinted from
Maintenance, Condition Monitoring and Diagnostics, Maintenance Performance Measurement and Management,
Oulu, 2015, pp. 57-62

Vibration measurement approach to the bearing damage evolution study in the presence of electrostatic discharge machining currents

Aleksei Romanenko* Sulo Lahdelma**
Annette Mütze* Jero Ahola***

** Control Engineering and Digital Systems, School of Energy Systems, P.O.Box 20, 53850, Lappeenranta University of Technology, Finland (e-mail: {aleksei.romanenko|jero.ahola}@lut.fi)*
***Engineering Office Mitsol Oy, Tirriäisentie 11, 90540 Oulu, Finland (e-mail: sulo.lahdelma@mitsol.inet.fi)*
**** Electric Drives and Machines Institute, Graz University of Technology, Inffeldgasse 18/1, A-8010, Graz, Austria (e-mail: muetze@TUGraz.at)*

Abstract: The high-frequency components inherent in frequency converter operation can cause additional high-frequency currents to flow within an electric machine. Such currents can cause electrical discharges within the bearings that may damage the bearing surfaces and eventually lead to mechanical overload and bearing faults. Multiple mitigation approaches have been recently suggested by different researchers. However, neither of them provides a universal and complete solution nor gives a deep explanation of the damage evolution mechanism. This paper studies the vibration data observed during an accelerated life testing using excessive high-frequency voltage applied between the rotor shaft and the bearing house. The purpose of the analysis is to define the criteria suitable for the detection of damage patterns resulting from electrostatic discharge machining (EDM) currents.

Keywords: Rolling element bearing, diagnosis, condition monitoring, variable speed drive, EDM current

1. INTRODUCTION

The high-frequency components inherent in frequency converter operation can cause additional high-frequency currents to flow within an electric machine (Von Jouanne et al., 1996; Chen et al. 1996). Such currents can cause electrical discharges within the bearings that may damage the bearing surfaces (Boyanton and Hodges, 2002; Tischmacher and Gattermann, 2010) and eventually lead to mechanical overload and bearing faults. Multiple mitigation approaches were suggested by different researchers (Link, 1999; Schiferl and Melfi, 2004; Muetze and Binder, 2006). However, neither of them provides a universal and complete solution nor gives an exhaustive explanation of the damage evolution mechanism. This paper studies the vibration data observed during an accelerated life testing using excessive high-frequency voltage applied between the rotor shaft and the bearing housing. The purpose of the analysis is to define the criteria suitable for the detection of damage patterns on the rolling element bearing resulting from electrostatic discharge machining (EDM) currents.

2. METHOD

2.1 Vibration sampling and equipment

The test setup comprises of two 3-phase 4-pole 50 Hz 15 kW squirrel cage induction motors on the same shaft, fitted with 2 new type 6309ZZ bearings, powered by an ABB ACS 400 frequency converter, function generator Hameg HM-8131-2, 4 EPCOS - B57560G104F 100 $\mathrm{k}\Omega$ thermistors, a piezo-electric vibration measurement sensor (Kistler 8712A5M1, sensitivity 1V/g, ±5g, BW(±5%) = 0.5-8000 Hz) attached with a screw to the end-shield of the test motor (Figure 1) and a computer with LabVIEW logging application. The acceleration and temperature signals were sampled using 16-bit National Instruments digital acquisition units NI USB-6211.

Fig. 1. Accelerometer attachment view.

The sampling of the acceleration signal was performed at sampling frequency (f_s) of 20 kHz with 20 second long samples, every 5 minutes during the constant speed rotation mode (25 Hz). The temperature was measured at 3 vertices of equilateral triangle around the shaft opening 3 cm away from the shaft surface on the end-shield using EPCOS B57560G104F NTC thermistors. All calculations were performed using MATLAB.

2.2 Test run description

The first test run was performed according to the methodology presented in (Romanenko, 2014). In this test run, the machine was line-fed from a 3-phase 50 Hz power grid for 1280 hours after a pre-run period of approximately 3 days. The shaft was

rotating at a constant speed of 1500 rpm. This test run showed significant variation in electrostatic discharge intensity over the duration of the run, suggesting significant changes in the grease's electrical properties resulting in its direct current conductivity which might have prevented further discharges.

After the bearing was replaced for the second test run the setup was pre-run for 4 days at 1500 rpm without any additional voltage applied to the shaft. Then, the drive was set to variable speed mode ($n(t) = [1425 + 75 \cdot \sin(0.05\ t)]$ rpm) to improve the stability of the grease's electric properties by facilitating variation in grease thickness and thus improving its mixing in the bearing. The machine was driven by the frequency converter to provide variable rotational speed, while an additional voltage (sine 20 V peak to peak, 300 kHz) was applied to the shaft. This point is considered t = 0 for the rest of the experiment. After 240 hours of operation, the voltage supplied to the shaft was increased to 55 Vpp. At t = 509 h the drive speed control from the PC was added. Since then the drive operated in iterative cycles of the following two modes of operation:

- 4 minutes. $n(t) = [1425 + 75 \cdot \sin(0.05\ t)]$ rpm
- 1 minute. $n(t) = 1500$ rpm.

At around 580 total hours of runtime a power failure occurred that caused the system to stop for 5 days (t = 578 - 696 h). Later on the system suffered 2 more power failures at t = 1870 - 1897 h and t = 2090 - 2109 h.

3. RESULTS AND ANALYSIS

3.1 Visual inspection

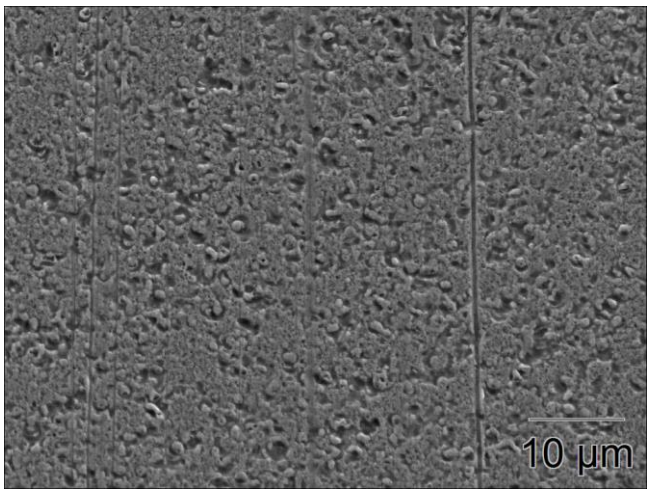

Fig. 2. Scanning electron microscope picturing of a part of the dark trace area on the outer ring surface of the drive-end bearing.

The surface of the bearing was examined after a 2500 hours long test run. Both the outer and inner ring had a visible dark trace, approximately 3 mm wide, in the area where the contact with rolling elements is expected to occur. The surface of the trace was pictured using a scanning electron microscope. The scan result is presented in Figure 2.

3.2 Temperature monitoring

The average of the measured bearing temperatures is presented in Figures 3 and 4. During both the runs the bearing temperature varied between 28 and 34 degrees Celsius. The main difference in the bearing temperature between these two test runs is due to the variable speed mode of operation. This setting resulted in changes in friction and frictional loss in the bearings. This variation in dissipated energy was sufficient to cause temperature oscillations with the same frequency as the speed reference was changing. Another notable oscillation appears in the second test run and has a period of 24 hours. This oscillation might be caused by laboratory room temperature variations which were not monitored.

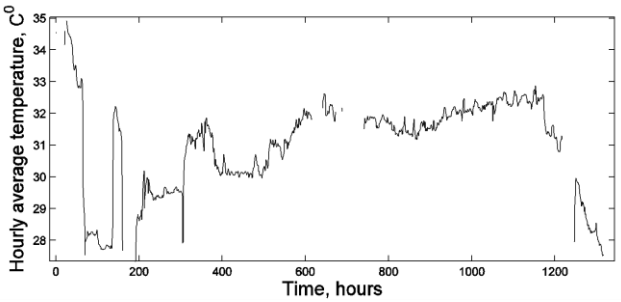

Fig. 3. The hourly average temperature of the drive-end bearing during the first test run, which was 1280 hours long (Romanenko, 2014).

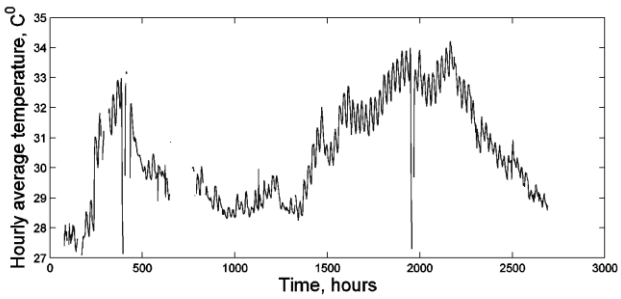

Fig. 4. The hourly average temperature of the drive-end bearing during the second test run, which was 2500 hours long.

3.3 Discharge activity

The discharge activity plots are presented in Figures 5 and 6. The highest discharge activity observed during the first run was $4.4 \cdot 10^5$ discharges per hour. The total number of discharges recorded over the duration of the experiment (1280 hours) was $3.8 \cdot 10^7$. The highest activity for the second run (2500 hours) was $1.49 \cdot 10^6$ discharges per hour while the total number of discharges was $5.28 \cdot 10^8$. It can be noted that the discharge activity during the first test run increased rapidly and then declined to low levels after every stop of the system. In contrast, the discharge activity during the second run increased over time as the rotational speed was constantly changing between a constant and varying speed. To analyse the observed pattern, the lowest detected discharge activities over 20 consecutive measurements (10 minutes) were computed (Figure 7). The discharge activity grew continuously from 1000 to 2200 hours and decreased at the end of the monitored period.

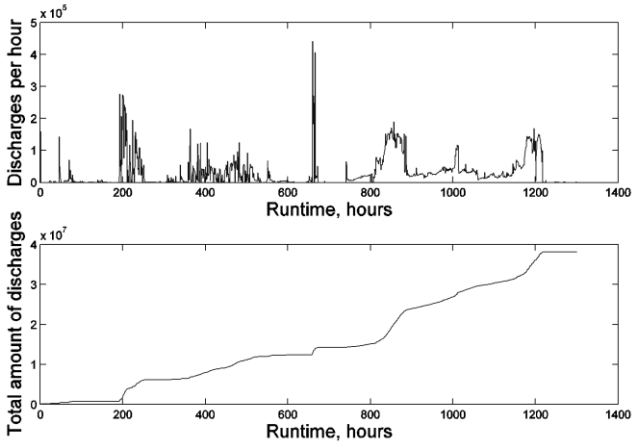

Fig. 5. Discharge activity plot for the first test run over 1280 hours (Romanenko, 2014).

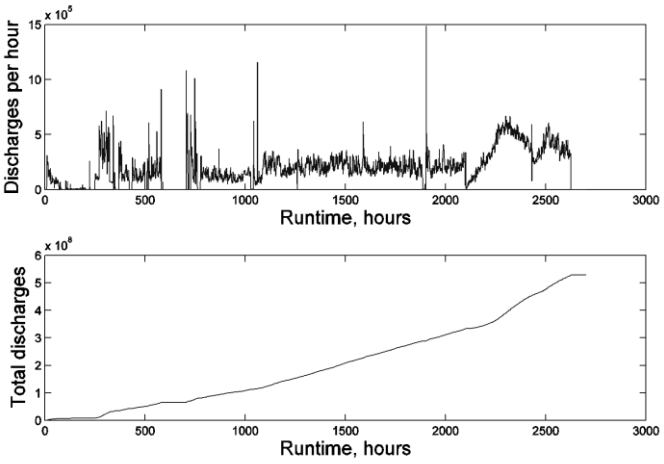

Fig. 6. Discharge activity plot for the second test run over 2500 hours.

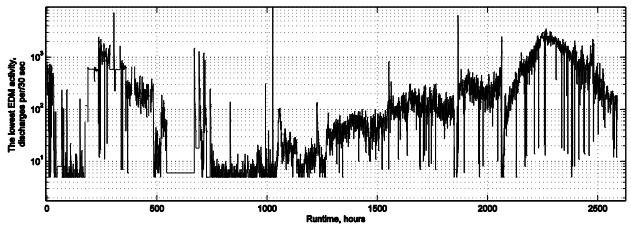

Fig. 7. The lowest detected level of the observed discharge activity in a 10-minute window.

3.4 Measurement range and fault frequencies

The linearity of the accelerometer allows performing measurements up to 8 kHz. The sampling frequency f_s = 20 kHz limits the upper cut-off frequency as follows: 20 kHz / 2.56 = 7.81 kHz. The factor 2.56 is commonly used in FFT-analyzers. Based on these facts, the upper cut-off frequency of 7.8 kHz was chosen. A Butterworth anti-aliasing filter with the order n = 8 was used when calculating the spectra. The number of samples N was 4096.

3.5 Time-domain vibration analysis

The most common time-domain quantities used in modern bearing diagnostics are the peak and root-mean-square (rms) values of the acceleration signal ($x^{(2)}$) and its first (jerk) and second (snap) time derivatives. The third useful quantity is the maximum absolute value of the signal divided by the rms value. It is known as the crest factor. These features were computed for the vibration samples. The jerk signal was obtained from the acceleration signal by computing the difference between consecutive samples without scaling for the time interval size. The snap signal was computed from the jerk signal in the same manner. The resulting rms values that were obtained using downsampling to 500 minutes are presented in Figure 8. When the acceleration signal is used, the changes of rms in the frequency range 1 - 7800 Hz are not as clear as in the case of jerk or snap (Figure 8).

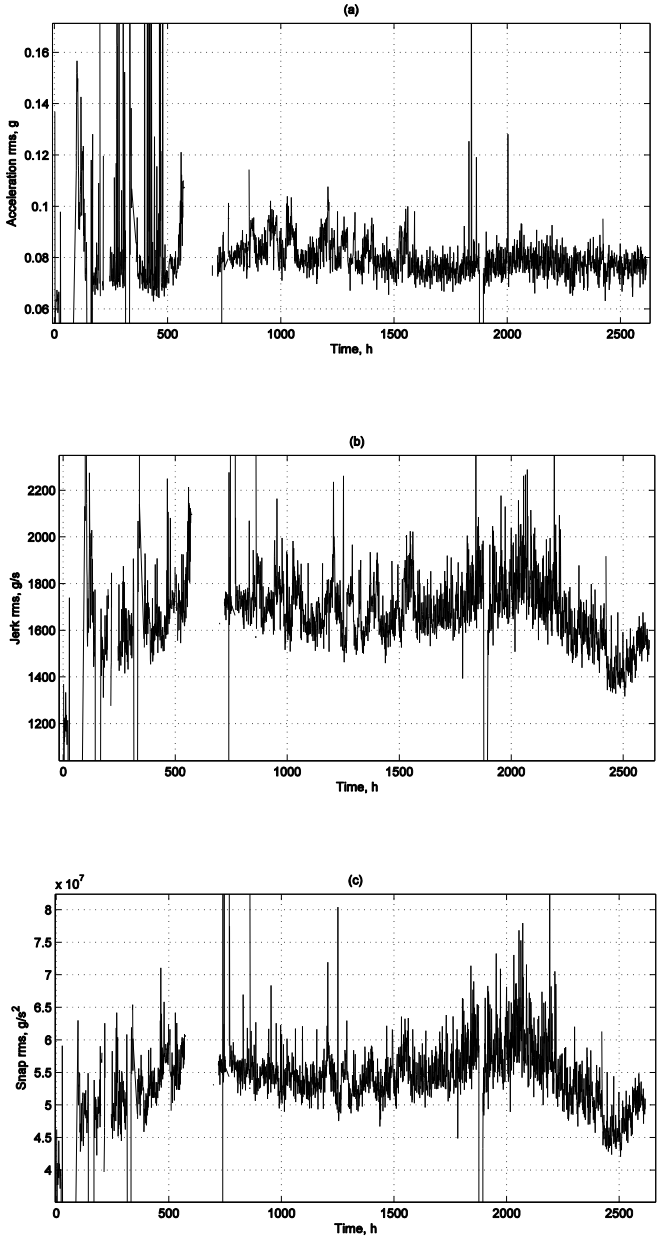

Fig. 8. The rms trends of (a) acceleration, (b) jerk and (c) snap in the frequency range 1 - 7800 Hz.

The curve in Figure 4 has quite a similar shape with the curves in Figures 8b and 8c. This is to be expected because mechanical vibration transforms into thermal energy in the bearing. Figures 7 and 8 have some similarities as well.

The time domain signals in the frequency range of 1 - 7500 Hz (Figure 9) show that there can be high peaks in the acceleration signal. The peak values of the signals 9a and 9b are 0.2008 g and 0.608 g, respectively.

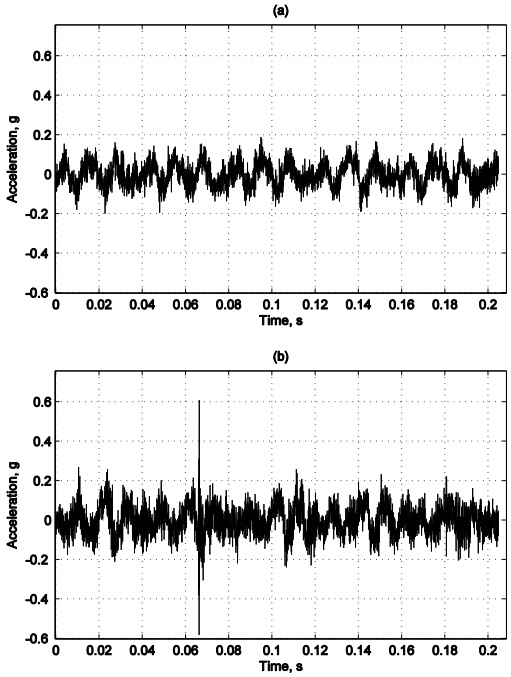

Fig. 9. Acceleration signals in the frequency range of 1 - 7500 Hz, when (a) t = 9.4 h and (b) t = 2188 h.

3.6 Frequency-domain vibration analysis

The most important fault frequencies in the low frequency range for the test rig are:

Rotational frequency, n	Line frequency, f_l	Ball spin frequency, BSF
1 x n = 25.0 Hz	1 x f_l = 50 Hz	1 x BSF = 48.77 Hz
2 x n = 50.0 Hz	2 x f_l = 100 Hz	2 x BSF = 97.54 Hz
3 x n = 75.0 Hz	3 x f_l = 150 Hz	3 x BSF = 146.31 Hz
4 x n = 100.0 Hz	4 x f_l = 200 Hz	4 x BSF = 195.08 Hz
5 x n = 125.0 Hz	5 x f_l = 250 Hz	6 x BSF = 292.62 Hz

Ball pass frequency of outer ring, BPFO	Ball pass frequency of inner ring, BPFI
1 x BPFO = 75.86 Hz	1 x BPFI = 124.14 Hz
2 x BPFO = 151.72 Hz	2 x BPFI = 248.28 Hz
3 x BPFO = 227.58 Hz	3 x BPFI = 372.42 Hz
4 x BPFO = 303.44 Hz	4 x BPFI = 496.56 Hz

The Fast Fourier Transform (FFT) was applied to each sample to separate the frequency components from the vibration signal, resulting in a frequency spectrum from 1 Hz to 7.5 kHz. These spectra were downsampled by averaging to steps of 5 Hz and 500 minutes (8 hours 20 minutes). The magnitudes of the resulting spectra are represented as a spectrogram against frequency and runtime in Figure 10.

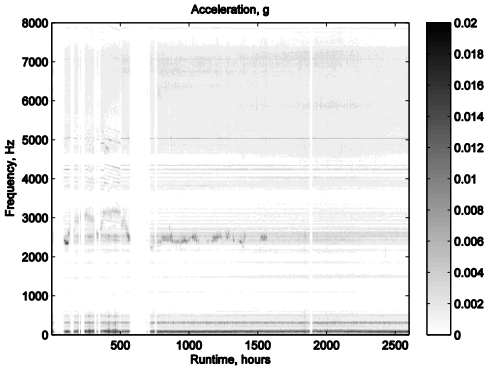

Fig. 10. Spectrogram of acceleration (g) over the whole frequency range.

It can be seen from Figure 10 that the interesting frequency ranges are around 2.5 kHz and in the low frequencies. Based on the spectrogram in Figure 11, the components below 400 Hz should be examined more closely.

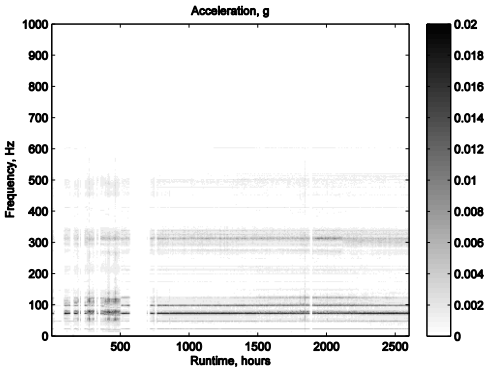

Fig. 11. Spectrogram of acceleration (g) up to 1000 Hz.

An interesting fact is that frequencies 2 x n and 1 x BSF are close to each other. Similar is the case with 3 x n and 1 x BPFO as well as with 5 x n and 1 x BPFI. Vibrations in the frequencies of 25 Hz, 75 Hz, 100 Hz and 125 Hz can be seen in the high resolution spectrum in Figure 12b.

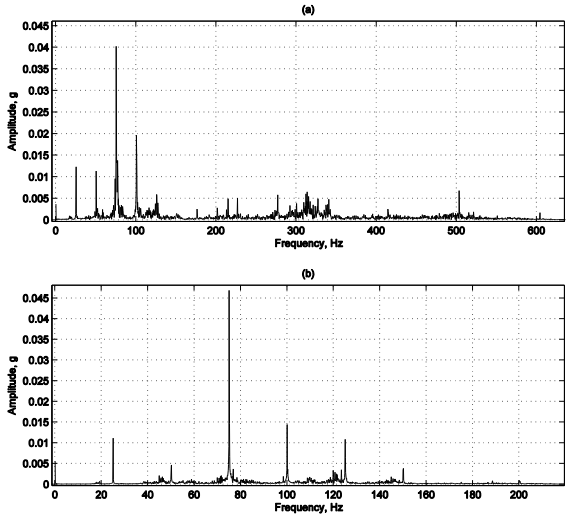

Fig. 12. The amplitude spectrum of acceleration (a) up to 600 Hz, when t = 1488 h and (b) up to 200 Hz, when t = 9.4 h.

The frequency analysis reveals that the vibrations around 2.5 kHz vary. This is apparent from the spectra in Figure 13. Furthermore, changes of its second harmonic (5kHz) can be noticed. Figure 14 shows the trends of the components at 75 Hz, 125 Hz and 2.5 kHz.

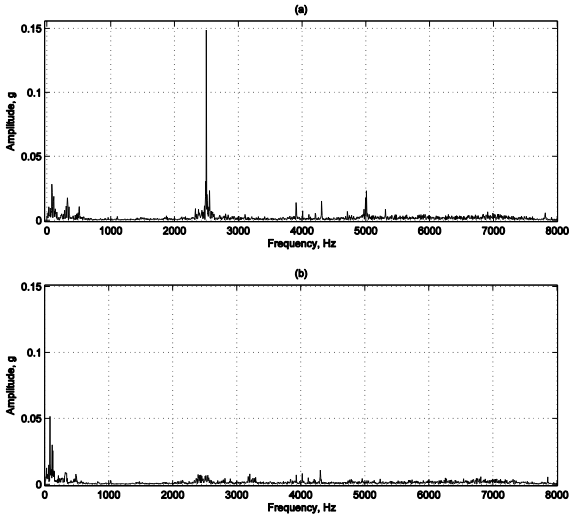

Fig. 13. The amplitude spectra of acceleration up to 7500 Hz, when (a) t = 339.8 h and (b) t = 456.8 h.

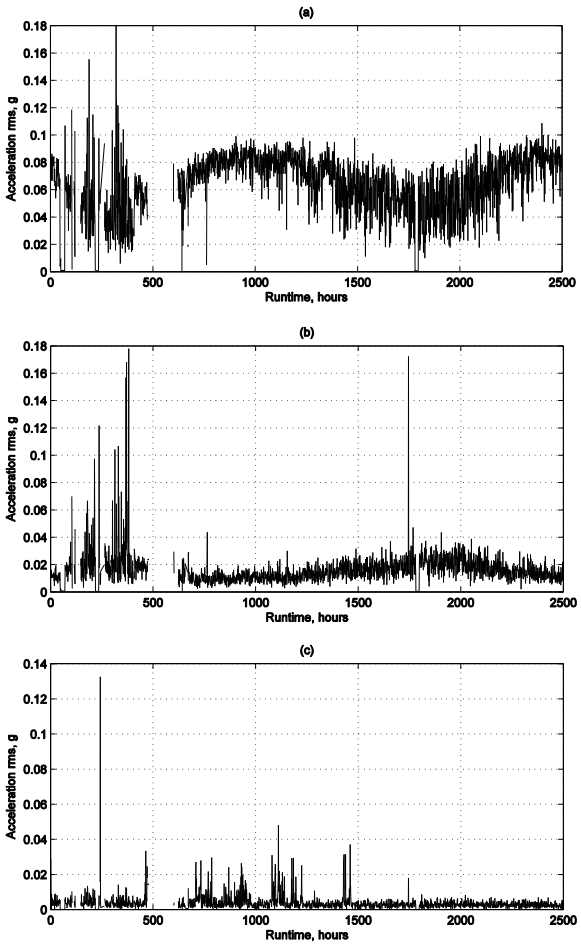

Fig. 14. The trend of rms acceleration in the range of (a) 70.8 - 80.6 Hz, (b) 119.6 - 129.4 Hz and (c) 2495.1 - 2504.9 Hz.

Practical experience has shown that bearing faults cause vibrations in the high frequency range of 2 - 4 kHz (Kowal, 1999). Sidebands of either BPFO, BPFI or a combination of both can also occur. From this perspective the spectrum in the Figure 15 is interesting, because it has a peak at the frequency of 2500 Hz - 2 x BPFI.

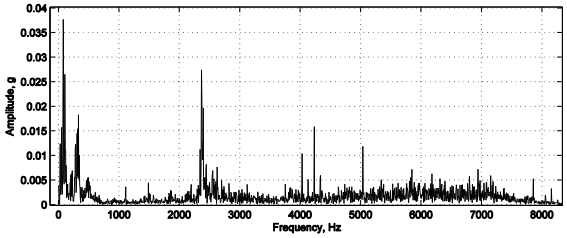

Fig. 15. The amplitude spectrum of acceleration up to 7500 Hz, when t = 1380 h.

Based on the obtained results, we decided to make an envelope analysis using a band-pass filtering over the frequency range of 2 - 5 kHz. The envelope spectra were down-sampled by averaging to steps of 5 Hz and 500 minutes. The spectrogram is presented in Figure 16. The main harmonics are multiples of 25 Hz and 100 Hz. The spectrum in Figure 12 reveals that there is vibration around 300 Hz at the sideband frequencies of 300 Hz - n, 300 Hz + n and also at the frequency of 315 Hz.

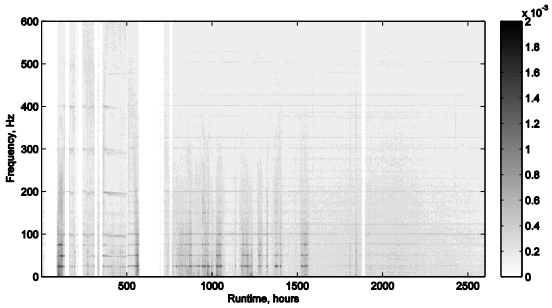

Fig. 16. Spectrogram of enveloped acceleration (g) using a band-pass filter from 2 to 5 kHz.

4. DISCUSSION

The visual representation of these spectra as a spectrogram provides a convenient representation of the frequency composition changes in the vibration signal as the bearing damage evolves. Among these frequencies and bands several criteria can be selected for the quantitative evaluation of the bearing damage. While most of them provide some insight into the bearings' state of health, they do not allow predicting the failure reliably as a standalone criterion. Such criteria are usually implemented as part of a neural networks based, fuzzy decision-making or some other artificial intelligence system (Lahdelma and Juuso, 2011).

New criteria can be added to the system by the implementation of monitoring for other physical processes apart from vibration and electrical current monitoring. One of such processes is the monitoring of electromagnetic pulses emitted by the discharges taking place in the bearings. The discharge activity under certain conditions seems to have some correlation with the vibrations occurring during machine operation. This effect might be caused by electromagnetic coupling between the vibration measurement system and discharge sparks. However, such disruptions are expected to be wide-band and unlikely to

have the same characteristic frequencies as the mechanical parts of the system. On the one hand, the discharges are expected to depend on vibration and shaft rotational speed as both affect the thickness of the grease layer (Muetze et al., 2011). On the other hand, the process of discharging is also affected by the chemistry of the grease (Romanenko et al., 2015). Therefore, a universal relationship between the instantaneous discharge activity of a bearing and its state of health might be very difficult, if not impossible, to derive, given the current state of knowledge of the discharge and damage processes. The absence of such would make this method a good addition to other diagnosis criteria but not a complete replacement.

Comparing the two test runs it seems that the change in the rotational speed of the electrical machine is likely to affect the bearing health degradation process, which is in line with the influence of the shaft rotational speed on the discharge activity and the occurrence of high discharge activity during the "start-up test" observed by Muetze et al. (2011). The variable speed and load conditions promote the intensity of the discharging activity, which in some cases (i.e. in lifetime greased bearings) reduces the lifetime of the bearing.

The observed changes at some characteristic frequencies can be explained by the presence of melted trace areas in the bearing. A single area at the bottom of the bearing where the melted race starts to appear in first place should result in increased vibrations at the ball pass outer ring frequency in the same way it happens for a single damage point (Lindh, 2003). However, as the trace becomes larger it would probably disappear from this frequency as the track becomes sufficiently uniform and it is unclear what would be the characteristic frequencies for such complex damage pattern. Thus, further theoretical research and modelling is necessary to analyse the possible effects of fluting patterns and the presence of local melting areas on the vibration spectra.

The analysis showed that the levels of the vibration component at 2.5 kHz vary. Around this frequency there were also sidebands which correspond to the fault frequencies BPFI and BPFO. These observations support the results (Kowal, 1999) according to which EDM causes vibrations in the high frequency range of 2 - 4 kHz. There was also some variation in the vibration at the second harmonic of 2.5 kHz. The vibration level trend showed that the 2.5 kHz vibration was mostly low, but at times the levels were high. The vibrations at the rotational frequency were quite stable. The acceleration component of 75 Hz varied and was mainly higher than the 125 Hz component, although the latter had high values at times as well.

Some short time domain signals showed strong impacts. The connection between these impacts and the electric discharges is worth to be examined closer. There were similarities between the rms values of the vibrations and the temperature values, especially when jerk and snap were used. It is also worth paying attention to the connection between the logarithm of the lowest observed discharge activity and the rms values of vibrations, because there were similarities between these trends as well (Figure 7 and 8).

5. CONCLUSIONS

The initial studies in detecting the occurrence of the electrostatic discharge machine (EDM) currents have been encouraging. The rms of the first and second time derivatives of acceleration respond well to the changes in the high frequency vibrations. There are similarities between their rms values and the logarithm of the lowest detected level of observed discharge activity. Similarity was also quite clear between the temperature and the vibrations. In the future, more long-term tests could be performed, and real and complex order time derivatives and l_p norms could be used.

REFERENCES

Boyanton, H.E. and Hodges, G. (2002). Bearing fluting [motors]. IEEE Industry Applications Magazine, 8(5), 53-57. doi: 10.1109/MIA.2002.1028391.

Chen, S., Lipo, T.A. and Fitzgerald, D. (1996). Source of induction motor bearing currents caused by PWM inverters. IEEE Transactions on Energy Conversion, 11(1), 25-32. doi: 10.1109/60.486572.

Kowal, D. (1999). Bearing Damage Resulting from Shaft Voltages and Currents. Application Note. Computational Systems Incorporated. 7p.

Lahdelma, S. and Juuso, E. (2011). Signal processing and feature extraction by using real order derivatives and generalised norms. Part 1: Methodology. International Journal of Condition Monitoring, 1(2), 46-53.

Lindh, T. (2003). On the Condition Monitoring of Induction Machines. Ph.D. thesis, Lappeenranta University of Technology. 146 p. URL doria.fi/handle/10024/29786.

Link, P.J. (1999). Minimizing electric bearing currents in ASD systems. IEEE Industry Applications Magazine, 5(4), 55-66. doi: 10.1109/2943.771367.

Muetze, A. and Binder, A. (2006). Don't lose your bearings. IEEE Industry Applications Magazine, 12(4), 22-31. doi: 10.1109/MIA.2006.1678327.

Muetze, A., Tamminen, J. and Ahola, J. (2011). Influence of motor operating parameters on discharge bearing current activity. IEEE Transactions on Industry Applications, 47(4), 1767–1777. doi: 10.1109/TIA.2011.2154353.

Romanenko, A., Ahola, J., Muetze, A. and Niskanen, V. (2014). Study of incipient bearing damage monitoring in variable-speed drive systems. In 16th European Conference on Power Electronics and Applications, 2014, 1-10. doi: 10.1109/EPE.2014.6910992.

Romanenko, A., Muetze, A. and Ahola, J. (2015). Effects of Electrostatic Discharges on Bearing Grease Electric Properties. In IEEE International Electric Machines and Drives Conference, 2015, IEMDC 2015.

Schiferl, R.F. and Melfi, M.J. (2004). Bearing current remediation options. IEEE Industry Applications Magazine, 10(4), 40-50. doi: 10.1109/MIA.2004.1311162.

Tischmacher, H. and Gattermann, S. (2010). Bearing currents in converter operation. International Conference on Electrical Machines (ICEM), 2010 XIX, 1-8. doi:10.1109/ICELMACH.2010.5608126.

Von Jouanne, A., Enjeti, P. and Gray, W. (1996). Application issues for PWM adjustable speed AC motor drives. IEEE Industry Applications Magazine, 2(5), 10-18. doi:10.1109/2943.532149.

Publication III

Romanenko A., Ahola J., and Muetze A.
Influence of Electric Discharge Activity on Bearing Lubricating Grease Degradation

Reprinted from
2015 IEEE Energy Conversion Congress and Exposition (ECCE)
2015, pp. 4851-4852

Influence of electric discharge activity on bearing lubricating grease degradation

Aleksei Romanenko, Jero Ahola
Laboratory of Control Engineering and Digital Systems
Lappeenranta University of Technology
Lappeenranta, Finland
{aleksei.romanenko,jero.ahola}@lut.fi

Annette Muetze
Electric Drives and Machines Institute
Graz University of Technology
Graz, Austria
muetze@tugraz.at

***Abstract*—The emergence of high-frequency converters has introduced additional stress on the bearings of the systems they are used in: the high-frequency components of the converter output voltage may lead to building up of voltage across the bearings. If it exceeds the voltage that the bearing can withstand these voltages may cause a discharge leading to so-called "discharge bearing currents". This paper studies the influence of such discharges on the grease chemical composition, a parameter that is considered key for the further understanding of the bearing damage mechanism itself. The composition is analysed using Fourier Transform Infrared spectroscopy and X-Ray crystallography.**

Keywords—ball bearings, lubricants, discharges (electric), degradation, condition monitoring, variable speed drives.

I. Introduction

Electric machines are frequently used in industrial applications. Modern frequency controlled power systems allow precise speed control at frequencies ranging from zero to several hundreds of revolutions per second. However, this application of frequency controlled power supplies poses additional problems to the reliability of these machines.

One of the problems arises from the presence of high-frequency harmonics in the spectrum of the pulse-width modulated (PWM) signal the electric machine is supplied with. The high-frequency components may lead to parasitic effects within the system. Notably, voltage may build up through capacitive coupling between the shaft and the stator of the machine [1-3]. Such voltages may cause electrostatic discharges to occur within the bearings, resulting in localized high temperatures and leading to bearing damage (pitting at the bearing surfaces) [4, 5] and grease chemical degradation [6]. This damage can decrease lubrication capability, and increase vibrations and friction as well as overall bearing temperature, which, in turn, may result in bearing overloading and failure [7]. While different mitigation techniques for such bearing currents have been proposed by different authors [8-11] the bearing damage mechanism itself has still not been fully understood today.

In this paper we focus on the grease degradation processes by quantifying the discharge activity via a radio-frequency detection methods and comparing the changes of the chemical composition of the grease of two bearings: one subjected only to mechanical wear during the test run and another, subjected to high-frequency electrical field and discharges as well. The authors of [12] suggest that discharge activity can degrade the grease film leading to increased local friction heating of the grease-metal contact. The thermal aging on the other hand is known to affect the grease lubrication properties due to oxidation reactions [13]. Such oxidation changes the composition of the grease, i.e. the ratio between the oil base and additional thickeners. This change can be detected using Fourier Transform Infrared spectroscopy (FTIR), which is sensitive to the carbon-oxygen bonds in organic components of the grease, and by X-Ray crystallography (XRD) analysis that allows detecting the presence of crystalline structures formed i.e. by silicate compounds [14].

II. Method

A. Equipment

The wear setup consisted of two 3-phase, 15 kW, 4-pole squirrel cage induction motors, coupled with an electrically insulated coupling, an antenna EMCO 93148 connected to an R&S RTO1014 oscilloscope, an ABB ACS 400 frequency converter, a sine voltage generator Hameg HM-8131-2, and a PC. The test bearings were of type 6309 C3 lubricated with mineral oil-based grease with multi soap thickener. The voltage was supplied to the shaft using a mercurial contact Mercotac 110. The grease chemical composition analysis was performed using a Perkin Elmer Spotlight 200 FTIR imaging system and a Brucker D8 advance X-ray diffractometer.

B. Runtime sampled parameters

The electrostatic discharge machining activity was recorded by a Rhode Schwartz oscilloscope. The discharge activity was monitored by counting the falling edges at the level of 5 mV of the antenna output. Each event corresponds to 10000 falling edges. For each trigger event the oscilloscope produced a pulse to signal the counting field-programming gate array (FPGA). Every 30 seconds, the FPGA sent the counted discharges to the PC via the COM-link. The measurements were sampled every 30 seconds. At the same time the temperature at the end-shield close to the drive end bearing was sampled. Every five minutes the vibration was measured

by an accelerometer attached to the stator of the machine to detect possible indicators of bearing degradation.

C. Test programm

For the experimental test run the driving motor was rotating the load motor at a specified rotation speed. The bearings of the load motor were electrically insulated with a polyethylene sleeve from the stator frame while the drive end bearing's insulation was short circuited by the external voltage generator. The generator provided the shaft to stator frame excitation voltage at 60 V peak to peak with 300 kHz frequency. For further details, we refer to [15]. The prerun period of the new bearings lasted for 126.5 hours. The bearings were prerun at nominal speed without any external voltage applied. The fundamental frequency of the supply voltage F_F ranged from 13 to 50 Hz and was changed several times throughout the test program as detailed in Table I. Interval no. 2 corresponds to a dead stop of the motor due to a power failure in the frequency converter supply circuit. Because the motor came to stop, no discharge activity occurred during this interval. Interval no. 7 had a variable speed setting resulting in a change of shaft rotation speed as described by

$$n_1(t) = 1425 + 75 \sin(0.05\, t) \text{ rpm}, \quad (1)$$

for $0 \text{ s} \le t \le 240$ s, and

$$n_2(t) = 1500 \text{ rpm} \quad (2)$$

for $240 \text{ s} \le t \le 300$ s. This pattern was repeated every five minutes.

TABLE I. MOTOR SPEED SETTINGS DURING THE EXPERIMENT

Interval	t_{start} [hours]	Duration [hours]	F_F [Hz]
0	0	126.5	50
1	126.5	40.2	50
2	166.7	28.8	0
3	195.5	67.3	13
4	262.8	23	30
5	285.8	27.8	13
6	313.6	3.8	20
7	317.4	114	varying, eqs. (1), (2)
8	431.4	52.4	50
9	483.8	66.9	20
10	550.7	389.5	50

The experiment was stopped when the detected discharge activity stayed low (below 1 event per 30 seconds) for a prolonged period of time (500 hours) despite the efforts to increase it by changing the speed of motor.

D. Grease sampling and analysis

The samples were obtained from the area, formed by the ball and the cage (Fig. 1), where the grease that was washed from the bearing-cage pocket formed clusters. Sampling was performed for three grease samples: one from new grease from the manufacturer package and two from: the non-drive end and the drive end bearings that were subjected to the wear runs described above, out of which only the drive end bearing had been subjected to electrical wear through electric discharges.

The FTIR is based on the phenomenon of photons with certain wavelengths in the IR spectrum being consumed by the atoms of molecules due to resonant frequencies in the chemical bonds of those molecules. The method is frequently

Fig. 1. Used bearings: non drive-end(left) and drive-end (right) with the sampled areas marked by white circles.

used to detect groups and specific types of chemical bonds in organic chemistry.

The XRD scan is performed by measuring the amount of photons reflected under certain angles due to elastic scattering in regular crystal structures. This method allows detecting the presence of crystals and other regular structures in material analysis. The relationship between the angle between the falling and reflected particle 2θ, distance d between the consecutive planes of crystal structure, and the wavelength of the falling particle λ was initially discovered by William Lawrence and William Henry Bragg [16].

III. Results and Analysis

A. Temperature monitoring

The recorded bearing temperatures are presented in Fig. 2 below. The temperatures measured with three probes embedded into the end-shield of the drive located in the vertices of equilateral triangles around the shaft 3 cm away from the surface of the shaft varied between 31 and 34 degrees Celsius when the motor was run at speeds greater than 1200 rpm and between 29 and 32 degrees at other speeds.

B. Discharge activity monitoring

The log scale discharge activity plot is presented in Fig. 3. During the prerun period (126.5 hours) the discharge activity stayed below the ambient noise level (0.0022 events per second). When the shaft voltage was applied, noteworthy discharges started to occur. At constant speed, the discharge activity decayed until the speed was changed. The new speed was selected as follows: the speed was varied to identify the operating point of maximum discharge activity. The state of the bearing was monitored with the oscilloscope using the shaft to frame voltage. At $t = 317.4$ hours the speed reference was set to the varying speed mode. During this mode of operation the discharge activity first started to rise, reached a maximum of 197 events per second, before it started to decay. Then, two more cycles of constant speed operation were set, resulting in the bearing going into resistive mode of operation. At this point, the discharge activity no longer grew significantly after changes in speed setting, in contrast to the previously observed increases. So the speed was set to 50 Hz constant so as to minimize the interference and observe the discharge activity variation during what was expected to be the final stage of bearing degradation. When the discharge activity dropped below 0.16 events per second, the sensitivity of the scope was changed to output pulses every 100 instead of every 10000 edges. The discharge activity varied significantly despite the fact that the speed was kept constant. One possible explanation may be given by short time and very small variations of the local speed in the contact area, due to the instantaneous discharge events and their effects on the local material interfaces caused sufficient vibration to partially restore the grease in the contact areas of the bearing.

C. Infrared spectroscopy of grease samples

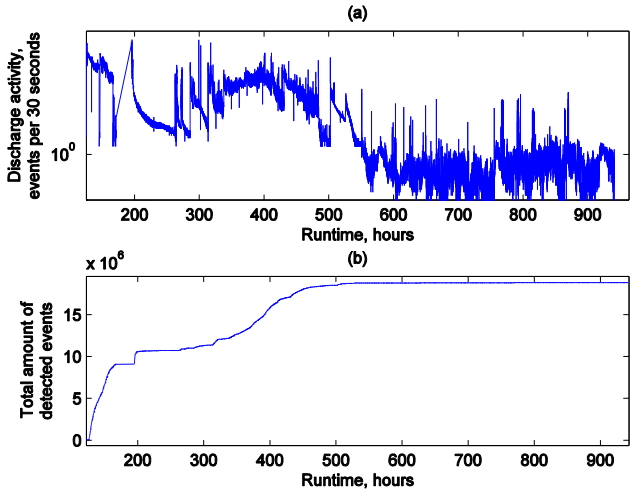

Fig. 3. Discharge activity plot for the test run over 940 hours.

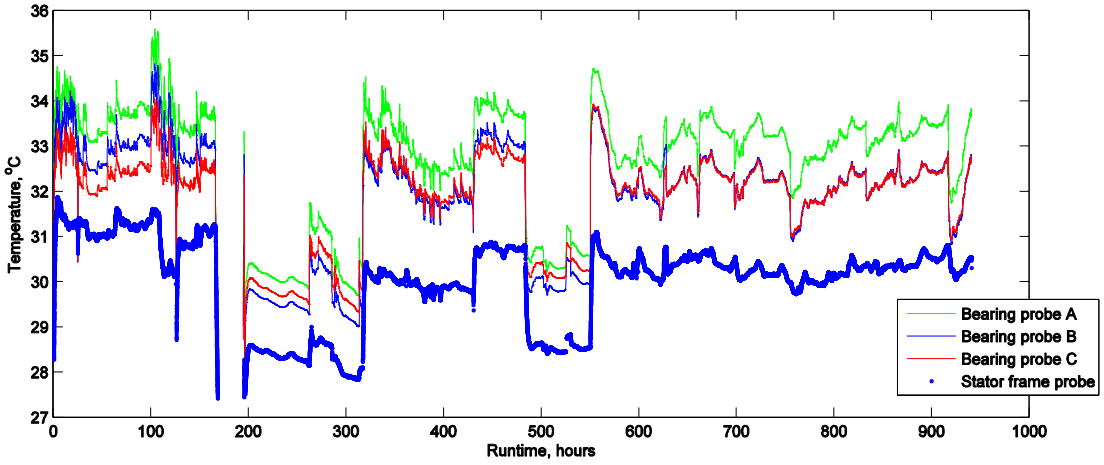

Fig. 2. Temperature measurements during the test run.

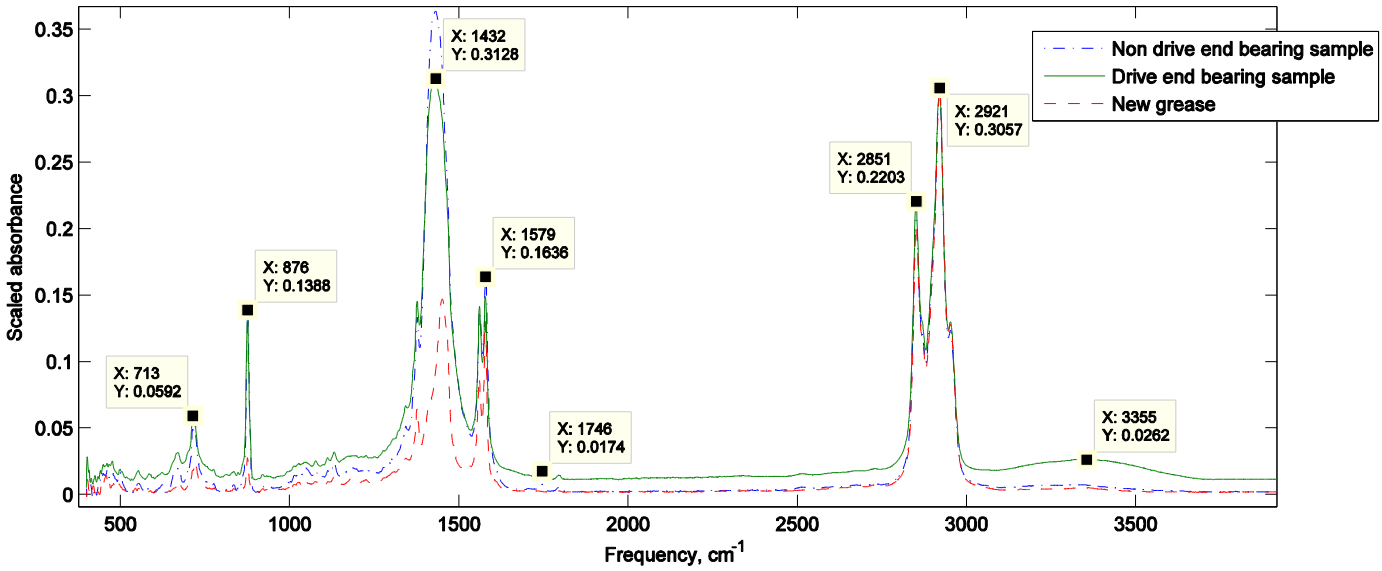

Fig. 4. Fourier transform infrared spectrometry of test samples.

The overall absorption rate of a sample can vary depending on the amount of material sampled. Therefore, some scaling is required. One possibility is to scale the whole plot against one of the strong spikes. This scaling was performed against the value of the absorption at 2920 cm^{-1}. The results of the scaled FTIR spectrometry are presented in Fig. 4. The samples show absorption spikes at several wave numbers with the strongest ones occurring at 720, 876, 1377, 1451, 1561, 1579, 2851, 2954, 2920, and 3365 cm^{-1}. In order to quantify the relative changes in the grease composition the weighting of peak absorption rates was performed according to

$$\overline{w_i} = \frac{w_i}{\sum_{j=1}^{10} w_j} 100\% , \quad (3)$$

where w_i is the spike absorption rate maximal value. Both absolute and relative rates are presented in Table II. The analysis of the FTIR spectra of the grease samples shows the following significant features:

- Minor changes in the C-H stretch region 2800-3000 cm^{-1} are present. The strength ratio between the absorption of 2921 cm^{-1} and 2851 cm^{-1} bands changed from 1.51 in the new grease sample to 1.41 and 1.39 for the non-drive end and the drive end-bearing samples correspondingly. According to [17] a tendency to such changes is present in alkanes as their main carbon chains get shorter which is expected as base oil suffers mechanical and thermal (electrical discharges) wear.
- The bands 710-715, 1440-1470 cm^{-1} and 1570-1590 cm^{-1} are related to the spectrum consumption of lithium soap thickeners. An IR spectrum of lithium soap of stearic acid is presented in Fig. 5. The amount of thickener in the grease sampled from the "wash-out" grease pocket is lower than the one of a new grease which can be explained by the sample point selection: the washed out grease is unlikely to contain the same or more thickener than the new grease because it was pushed out from between the rolling surfaces and because the base oil is more liquid than the thickener.
- The bands 850-890 cm^{-1} and 1420-1440 cm^{-1} demonstrate the presence of additional components in the grease composition. These bands may be related to

TABLE II. ABSORPTION SPIKES' PEAK VALUES

Wave number	Non drive end bearing sample		Drive end bearing sample		New grease	
	Absolute	Relative	Absolute	Relative	Absolute	Relative
3365	0.0067	0.4 %	0.0261	1.6 %	0.0038	0.4 %
2954	0.1229	7.7 %	0.1292	8.1 %	0.1004	11.4 %
2920	0.3054	19.1 %	0.3057	19.2 %	0.2397	27.3 %
2851	0.2168	13.6 %	0.2203	13.9 %	0.1587	18.1 %
1579	0.1636	10.3 %	0.1481	9.3 %	0.1019	11.6 %
1561	0.1383	8.7 %	0.1413	8.9 %	0.0678	7.7 %
1451	0.3173	19.9 %	0.2808	17.7 %	0.1156	13.2 %
1377	0.1335	8.4 %	0.1453	9.1 %	0.0507	5.8 %
876	0.1388	8.7 %	0.135	8.5 %	0.0213	2.4 %
720	0.0525	3.3 %	0.0566	3.6 %	0.0186	2.1 %

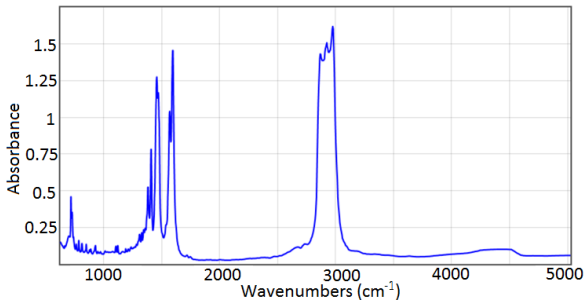

Fig. 5. IR spectrum of lithium stearate [18].

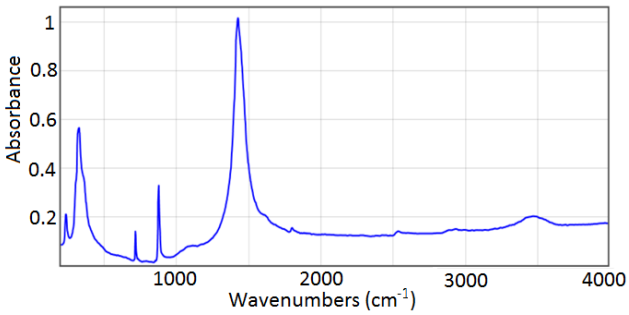

Fig. 6. IR spectrum of calcium carbonide (calcite) [18].

calcium carbonate (calcite) which seems be used as an additive in this grease's composition. The IR spectrum of calcite is presented in Fig. 6. The significant increase in calcite content can be explained similarly as the increase of the base oil – it can be easier washed out. The grease sample that was subject of discharging features lesser relative absorption of calcite related bands suggesting that calcite has somehow participated in the chemical reactions.

- A new wide absorption band has appeared in the IR spectra of the drive-end bearing grease sample. The band spans 3200 to 3600 cm^{-1}. According to [12, 19] this band indicates the presence of a hydroxyl groups. The appearance of such groups can be explained by hydration (breaking of the double oxygen bond) of the ketone group of lithium soap. Such reaction would turn the soap into alcohol or carboxylic acid affecting the mixture's chemical properties.

D. X-Ray difractometry of grease samples

A wide-angle XRD scan was performed on the samples using CuKa X-rays. The detection angle span covered the "2θ" angles (with a "2θ" angle corresponding to the angle between the falling and the reflected ray) from 10 to 90 degrees. To decrease the influence of the sample's volume on the final result each of the measured data set was scaled by its maximum value which for all sets occurred at the incidence angle of 2θ = 29.47 deg.

The scaled results are presented in Fig. 7. The analysis shows a number of narrow sharp spikes at phase angles corresponding to those of calcite. The relative intensities of these spikes suggest that this material is present in the grease composition which corresponds to the presence of certain frequencies in the FTIR spectra as well. The main differences between the new grease sample and those that suffered from mechanical and electrical wear is increased noisiness of the sample and appearance of new wide band spikes. This can be explained by a shift of resonant frequencies of different organic compounds as their intermolecular distances vary as decomposition or chemical alteration of molecules occurs.

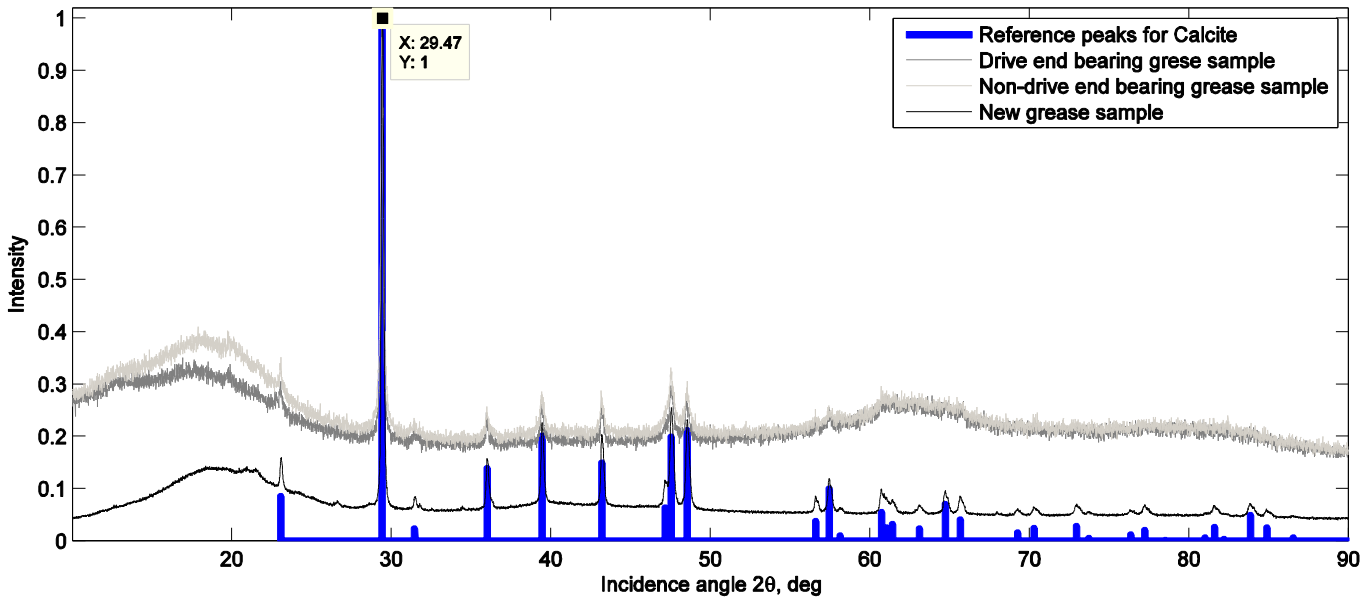

Fig. 7. The scaled X-ray diffractometry results. Caclite reference phases are provided by Crystallography Open Database [20,21,22].

IV. Summary and Discussion

The detailed analysis of the grease composition shows significant changes between the samples of new grease and greases from bearings that were subjected to pure mechanical and a combination of mechanical and electrical wear. While both worn samples seem to have significant changes of the proportions between thickener, base oil and additives, these do not seem to be critical on their own. However, the base oils suffered chemical reactions that led to a larger variety of organic compounds and number of reflection spikes in the diffraction joined together into wide reflection angular bands. Such changes in composition can affect the viscosity as hydrocarbons become more liquid when the length of their carbon chains is reduced. In addition, the appearance of a hydroxyl group in the grease subjected to electrical discharges may further liquefy the solution by forming alcohols or carboxylic acids. This change is arguably dangerous for a bearing's health as the load capacity varies and the grease may lose its chemical neutrality.

The discharge activity monitoring presents another interesting insight into the process: it seems that the discharge activity does not have a self-amplifying pattern until the bearing's condition becomes sufficiently bad. After every change of speed the discharge activity first increased strongly and then slowly decayed to some level that seemed to be sustaining for as long as the rate at which fresh grease was supplied to the contact area was sufficient to overcome the degradation resulting in direct conductivity of the grease (so called resistive mode).

Further study is necessary to determine the chemical processes occurring in the grease under electrostatic discharge activity: So far it is unclear if the heat or the extreme electrical field density can restore the thickener soap to its original acid and how such acid would react with other components of this grease. It is also important to determine if other grease types (i.e. synthetic greases) suffer from similar transformations and how other additives may affect the process.

References

[1] Von Jouanne, A.; Enjeti, P.; Gray, W., "Application issues for PWM adjustable speed AC motor drives," Industry Applications Magazine, IEEE, vol. 2, no. 5, pp. 10-18, Sep./Oct. 1996, doi: 10.1109/2943.532149

[2] Chen, S.; Lipo, T.A.; Fitzgerald, D., "Source of induction motor bearing currents caused by PWM inverters," Energy Conversion, IEEE Transactions on, vol. 11, no. 1, pp. 25-32, Mar. 1996, doi: 10.1109/60.486572

[3] Chen, S.; Lipo, T.A.; Fitzgerald, D., "Modeling of motor bearing currents in PWM inverter drives," Industry Applications, IEEE Transactions on, vol. 32, no. 6, pp. 1365-1370, Nov./Dec. 1996, doi: 10.1109/28.556640.

[4] Tischmacher, H.; Gattermann, S., "Bearing currents in converter operation," Electrical Machines (ICEM), 2010 XIX Int. Conference on, pp. 1-8, 6-8 Sept. 2010, doi: 10.1109/ICELMACH.2010.5608126

[5] Boyanton, H.E.; Hodges, G., "Bearing fluting [motors]," Industry Applications Magazine, IEEE, vol. 8, no. 5, pp. 53-57, Sep./Oct. 2002 doi: 10.1109/MIA.2002.1028391.

[6] Yu, Z.-Q.; Yang, Z.-G., "Fatigue Failure Analysis of a Grease-Lubricated Roller Bearing from an Electric Motor," J. Fail. Anal. Prev., vol. 11, no. 2, pp. 158–166, 2010, doi: 10.1007/s11668-010-9422-z.

[7] Benbouzid, M.E.H., "Bibliography on induction motors faults detection and diagnosis," Energy Conversion, IEEE Transactions on , vol. 14, no. 4, pp. 1065-1074, Dec. 1999, doi: 10.1109/60.815029

[8] Link, P.J., "Minimizing electric bearing currents in ASD systems," Industry Applications Magazine, IEEE, vol. 5, no. 4, pp. 55-66, Jul/Aug 1999, doi: 10.1109/2943.771367.

[9] Schiferl, R.F.; Melfi, M.J., "Bearing current remediation options," Industry Applications Magazine, IEEE , vol. 10, no. 4, pp. 40-50, Jul./Aug. 2004, doi: 10.1109/MIA.2004.1311162.

[10] Muetze, A.; Binder, A., "Don't lose your bearings," Industry Applications Magazine, IEEE, vol. 12, no. 4, pp. 22-31, Jul./Aug. 2006, doi: 10.1109/MIA.2006.1678327.

[11] Muetze, A.; Binder, A., "Practical Rules for Assessment of Inverter-Induced Bearing Currents in Inverter-Fed AC Motors up to 500 kW," Industrial Electronics, IEEE Transactions on, vol. 54, no. 3, pp. 1614-1622, June 2007, doi: 10.1109/TIE.2007.894698.

[12] Prashad H., "Behaviour of lubricants in rolling-element bearings under the influence of electric current." in *Tribology in electrical environments,* 1st ed., Elsevier, 2006, ch. 3, pp. 25-69.

[13] Hurley, S., P.M. Cann, and H.A. Spikes. "Lubrication and reflow properties of thermally aged greases." *Tribology Transactions* 2000 : 221-228. Print.

[14] Cann, P.M.; Webster, M.N.; Doner, J.P.; Wikstrom, V.; Lugt, P., "Grease degradation in R0F bearing tests," Tribology Transactions, vol. 50, no. 2. pp. 187-197, 2007, doi: 10.1080/10402000701261003.

[15] Romanenko, A.; Ahola, J.; Muetze, A.; Niskanen, V., "Study of incipient bearing damage monitoring in variable-speed drive systems," Power Electronics and Applications (EPE'14-ECCE Europe), 2014 16th European Conference on, pp. 1-10, 26-28 Aug. 2014, doi: 10.1109/EPE.2014.6910992 .

[16] Bragg, W.H.; Bragg, W.L. (1913). "The reflexion of X-rays by crystals". Proc R. Soc. Lond. A 88 (605): 428–38. Bibcode:1913RSPSA..88..428B. doi:10.1098/rspa.1913.0040.

[17] Lüttschwager, N.O.B., "Raman spectroscopy of conformational rearrangementsat low temperatures folding and stretching of alkanesin supersonic jets," Ph.D. dissertation, Georg-August-University Göttingen, Germany, 2014.

[18] Coblentz Society, Inc., "Evaluated infrared reference spectra" in NIST Chemistry WebBook, NIST Standard Reference Database Number 69, Eds. P.J. Linstrom and W.G. Mallard, National Institute of Standards and Technology, Gaithersburg MD, 20899, http://webbook.nist.gov, (retrieved June 29, 2015).

[19] Yadav, L.D.S. "Infrared (IR) Spectroscopy" in *Organic Spectroscopy,* Springer, 2004, ch. 2, pp. 52-106.

[20] Gražulis, S., Daškevič, A., Merkys, A., Chateigner, D., Lutterotti, L., Quirós, M., Serebryanaya, N.R., Moeck, P., Downs, R.T. & LeBail, A. "Crystallography Open Database (COD): an open-access collection of crystal structures and platform for world-wide collaboration". *Nucleic Acids Research* 40, 2012, D420-D427.

[21] Grazulis, S., Chateigner, D., Downs, R. T., Yokochi, A. T., Quiros, M., Lutterotti, L., Manakova, E., Butkus, J., Moeck, P. & Le Bail, A. "Crystallography Open Database – an open-access collection of crystal structures". *J. Appl. Cryst.* 42, 2009, 726-729.

[22] Downs, R.T. & Hall-Wallace, M. "The American Mineralogist Crystal Structure Database". *American Mineralogist* 88, 2003, 247-250.

Publication IV

Romanenko A., Muetze A., and Ahola J.

Effects of Electrostatic Discharges on Bearing Grease Electric Properties

Reprinted from
2015 IEEE International Electric Machines Drives Conference (IEMDC)
2015, pp. 254-259

Effects of Electrostatic Discharges on Bearing Grease Electric Properties

Aleksei Romanenko[1], Annette Mütze[2], Jero Ahola[3]

***Abstract*–Bearing faults may significantly reduce the useful life of electric machines. With the advent of modern fast-switching frequency converters, electric currents induced by the high-frequency common-mode voltage of these converters have been recognized as additional, sometimes severe, contributors to bearing degradation. The degradation is understood to progress both by damaging bearing surfaces and by altering the chemical composition of lubrication greases, which can lead to ineffective lubrication and reduction in permissible mechanical bearing load. This paper studies the effect of grease degradation due to discharge currents on the grease electric properties of several greases typically used with electric drives.**

***Index Terms*–ball bearings, fault diagnosis, materials reliability, accelerated aging, electrostatic discharges, variable speed drives.**

I. Introduction

Bearing faults may significantly interfere with the reliability of electric machines. According to several studies, reviewed in [1], bearing failures cause between 13 % and 44 % of motor faults. The authors of [2] name mechanical breakage (70.53 % of reported bearing faults) and overheating (22.11 %) as the most frequent initiators for bearing damage, and high vibration (50.5 %), persistent overloading (22.77 %), and poor lubrication (12.87 %) as the most frequent contributors to eventual bearing failure.

The possibility of additional bearing damage caused by inverter-induced bearing currents in modern variable-speed drive systems has been well recognized. Different authors have described cause-and-effect chains for this potential damage, allowing selection of appropriate mitigation techniques (e.g. [3]–[10]). Understanding of the damage mechanism itself as it takes place inside the bearing is, however, still only very rudimentary. The degradation is generally understood to progress by the bearing currents (i) damaging the bearing surfaces [11] and (ii) altering the chemical composition of the grease [12]. The latter can lead to ineffective lubrication and reduction of the permissible mechanical bearing load.

This paper studies the effect of grease degradation due to discharge currents on the grease breakdown field strength of four different greases typically used with electric machines. We limit our discussion to electric discharge bearing currents that occur as discharges following voltage that has been built up across the bearing. The influence of further bearing grease and surface degradation that might occur due to (for a given time) continuous flow of current through a bearing following a breakdown, as it may be the case with high-frequency circulating bearing currents, is minimized in this setup, since the electrostatic discharge generator used is not able to provide significant long-term current output. Furthermore, the paper discusses correlations between grease chemical composition and rheological properties: the relationship between grease viscosity and shear rate.

II. Method

A. Test equipment

The influence of repetitive discharges on the grease breakdown field strength was analysed as follows. The equipment comprised a 1-axis micrometric screw modified by welding a bearing ball (17.5 mm diameter) to the shaft of the screw on one side and a copper-covered part of a 2.54 mm thick printed circuit board made of FR4 insulating material with copper outer layers on both sides (Fig. 1), an electrostatic discharge generator, and a portable oscilloscope.

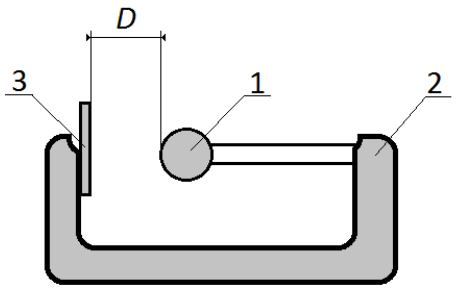

Fig. 1. Sketch of the experimental test setup. 1) 17.5 mm diameter bearing ball. 2) Modified 1-axis micrometric screw for exposure of bearing grease to electric discharges. 3) Printed circuit board fragment made of FR4 insulating material.

It should be noted that this setup only allows for analysis of discharges occurring in a static arrangement. However, this approach is justified because of the significantly shorter times of the discharges (discharge times between a few nano-

[1] A. Romanenko is with Lappeenranta University of Technology, Lappeenranta, Finland (e-mail: Aleksei.Romanenko@lut.fi).

[2] A. Muetze is with Graz University of Technology, Graz, Austria (e-mail Muetze@tugraz.at)

[3] J. Ahola is with Lappeenranta University of Technology, Lappeenranta, Finland (e-mail: Jero.Ahola @lut.fi).

and a few microseconds) than typical times between individual switching instances (at typical switching frequencies of a few kilohertz) and rotational speed of the bearings (of up to several hundreds of hertz).

The distance S_B travelled by the point on a surface of a bearing ball during a single spark event is estimated by

$$S_B = r_c F_S \left(1 - \frac{r_b^2}{r_c^2}\right) t\, \pi, \quad (1)$$

with the bearing ball radius r_b = 8.75 mm, bearing cage radius r_c = 36.25 mm, which are the dimensions of 6309ZZ bearing, a typical shaft rotational frequency of F_S = 25 Hz, and t = 1 us as an approximation of the duration of a single discharge spark. From this, we obtain S_B = 2.7 um. This value is in the same order of magnitude than the thickness of the grease lubricating film in rolling element bearings used with electric drives such as those motivating the work of this paper. Hence the shear rate, calculated by

$$\dot{\gamma} = \frac{v}{h}, \quad (2)$$

is in the range of (0.5…2) s^{-1}, assuming a film thickness h of (1…4) um and a bearing surface velocity v of 2 um/s. However, this typical film thickness is much smaller than the plate-to-ball distance of the test set up used in this investigation. Possible scaling effects will need to be included in the further analysis of the results obtained.

B. Viscosity measurements

The rheometry of grease samples was performed using an Anton Paar MCR 302 rheometer for three temperatures: 25, 40, and 60 °C. Three sets of 20 measurements were performed for each of the greases. Each set corresponds to one of the three temperatures and shear rates from 0.1 to 10 s^{-1} with logarithmic steps.

C. Breakdown voltage measurements

The measurements were performed on four different types of grease, "grease A" to "grease D", at a plate-to-ball distance of D = 100 um. Table *I* gives an overview of the base oil, thickener types, and additives of the four investigated greases.

For each type of grease investigated, 10 samples were investigated consecutively. Prior to each measurement of an individual sample, the space between the ball and the plate was cleaned. Then, the new grease sample was added with the ball at approximately 5 mm from the plate, and the distance between the ball and the plate was then reduced to the desired distance by one-directional movement. After initial positioning, the electrostatic discharge was initiated as follows: The maximal test voltage was set to 5 kV. The trigger of the oscilloscope was set to the falling edge of the input signal (single measurement mode). Voltage was applied until a discharge was detected by the oscilloscope. Then, the maximum voltage occurring within 0.1 us before this discharge was recorded, and the procedure was repeated again to obtain the next discharge measurement.

For each investigated sample, this procedure was repeated until one of the following two conditions was met: (a) the sample became conductive (the ball-plate system no longer showed capacitive behaviour, preventing any further voltage building across the bearing, no discharges were detected using the wireless detection method described in [13]), or (b) 70 measurements were performed.

TABLE I
BASE OIL AND THICKENER TYPES OF INVESTIGATED GREASES

Grease	Base oil type	Thickener type	Additive
A	mineral oil	multi-soap complex	--
B	mineral oil	aluminum complex	--
C	synthetic (silicone)	silicone based	--
D	synthetic (poly-alpha-olefins)	lithium complex	Extreme pressure and polytetrafluoroethylene

III. RESULTS

A. Viscosity analysis

Fig. 2 shows the results of the rheometry of the investigated grease samples. Some points in the plot seem to be kneeing at lower shear rates, which may be explained by excessive viscosity of these samples affecting the measurements. Thus, the points below 1 s^{-1} shear rate were excluded from all sets.

For each of the sets, and for each of the three temperatures measured, curve fitting was applied to the remaining points to obtain the viscosity of the grease as a function of the shear rate: The measured viscosities were fit to the so-called Power Law [14]

$$\eta = K\dot{\gamma}^{n-1} \quad (3)$$

where η is the viscosity, $\dot{\gamma}$ is the shear rate, n is the power law index defined by the properties of the material, and K is the material dependent proportional coefficient. The proportional coefficients were approximated by a linear function of temperature

$$K(T) = K_0 + kT \quad (4)$$

where T is the temperature, K_0 is the proportional coefficient at T = 0 °C, and k is a temperature dependent coefficient. The results of this curve fitting process are shown in Table *II* overleaf.

B. Breakdown voltage analysis

The statistical analysis of the sampled data was performed to determine the nature of the data distribution. First, Pearson's chi-squared test [15] was evaluated for each full data set to confirm that the initial variations in the measured data were significant. The test provided the probability p with

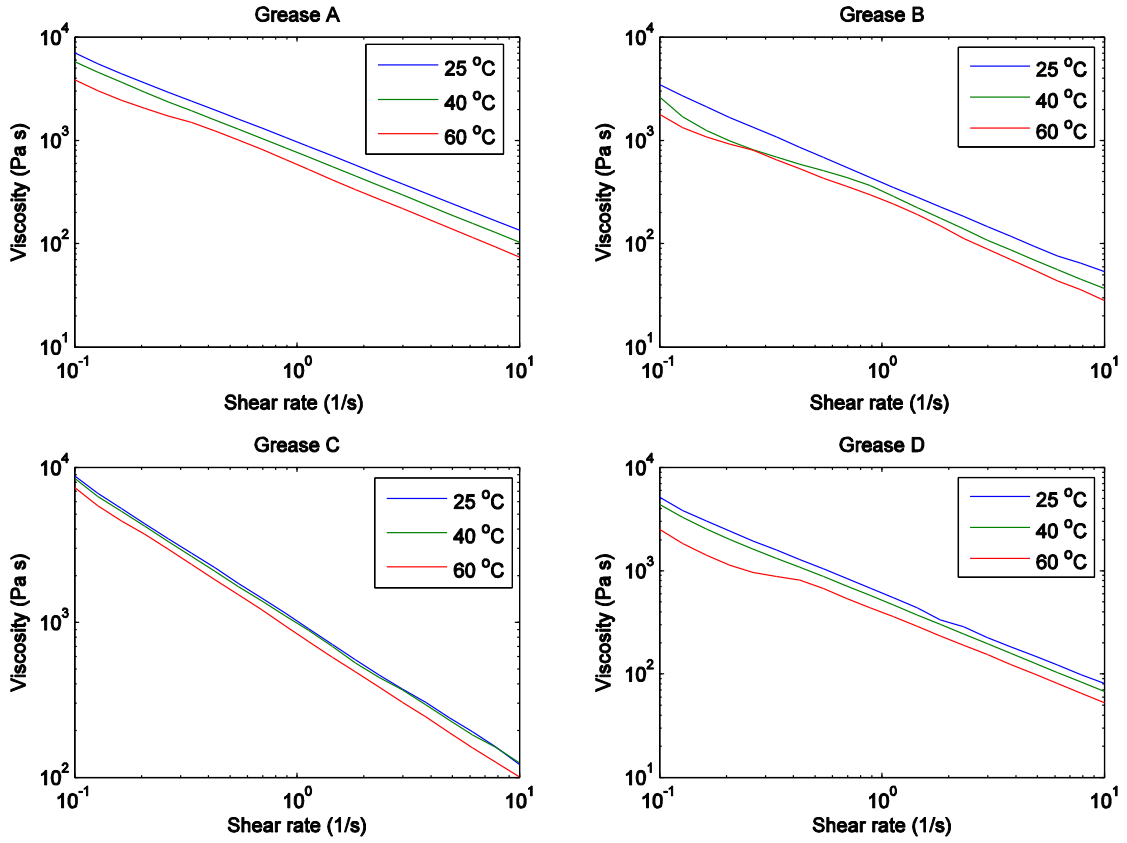

Fig. 2. Grease samples rheometry results.

which the tested data sets might belong to a normal distribution. The results are shown in Table *III*. Some samples became conductive too fast and thus were too short to be analysed with the chi-squared test. The samples for which the null-hypothesis significance strength is less than 0.05 were analysed further.

Each set of measured results was analysed as follows: For each of the four greases investigated, the data sets were grouped so that the first measurements of each set are in group 1, the second measurements of each set in group 2, the third measurements of each set in group 3, and so on. For each group the minimal, average, and maximal breakdown voltages were calculated. These values are presented in Fig. 3. For all sets of each grease, the average decline of the voltage over the first three measurements, K_{VD}, was calculated by

$$K_{VD} = (1 - U_{avg,3}/U_{avg,1})\ 100\,\% \qquad (5)$$

where $U_{avg,i}$ is the average breakdown voltage of the i^{th} group. The average variation K_{AVG} was calculated as

$$K_{AVG} = \frac{\Sigma_{i=1}^{69}\Sigma_{j=1}^{10} k_{rel,i,j}}{N_{nonDC}-10}, \qquad (6)$$

where N_{nonDC} is the total number of measurements over all sets of data of one type of grease before the corresponding

TABLE II
OVERVIEW OF EXPERIMENTAL TESTS

Grease	Temperature [°C]	Power Law index *n*	Proportional coefficient *K*	Proportional coefficient K_0 at 0 °C [s^{-1}]	Temperature dependent coefficient *k* [Pa s/°C]
A	25	0.1443	966.4326		
A	40	0.1289	767.5365	1230.2	-11.036
A	60	0.1109	577.1500		
B	25	0.1276	384.0011		
B	40	0.0564	312.5129	457.7	-3.272
B	60	0.0124	267.4456		
C	25	0.0913	1007.8		
C	40	0.1064	964.4926	1145	-5.024
C	60	0.0789	834.8803		
D	25	0.1303	591.2107		
D	40	0.1157	516.3991	731.0	-5.483
D	60	0.1210	399.9867		

TABLE III
CHI-SQUARED TEST OF MEASURED SAMPLES: NULL HYPOTHESIS STRENGTH, PROBABILITY *P* THE TESTED DATA SETS BELONG TO A NORMAL DISTRIBUTION

Sample	Grease A	Grease B	Grease C	Grease D
1	0.00544	0.06062	1.32E-06	8.78E-05
2	0.038897	0.069667	4.27E-11	0.000184
3	0.001061	0.000181	1.77E-07	0.001815
4	0.033019	0.635161	-	8.05E-07
5	0.072616	-	-	3.81E-07
6	0.107985	0.000464	0.00603	0.007107
7	0.05267	-	9.39E-07	0.057971
8	0.009139	-	0.016195	2.45E-07
9	0.030844	5.55E-05	0.369496	0.080343
10	0.021462	0.147534	1.95E-06	0.092969

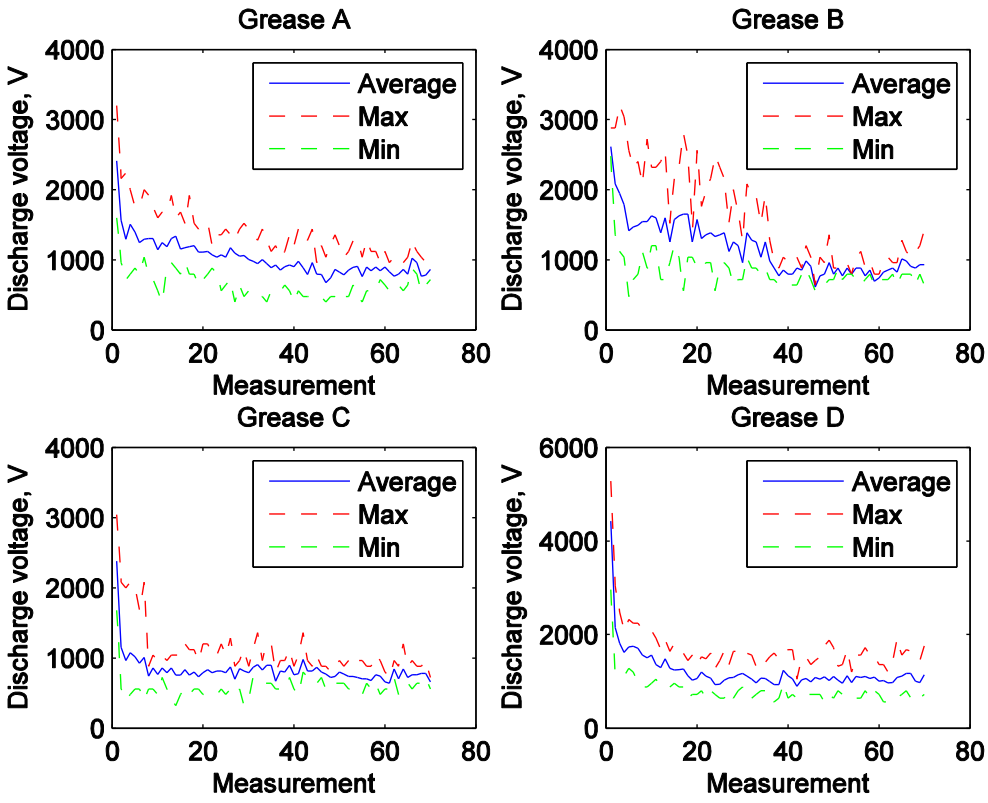

Fig. 3. Measured breakdown voltages.

grease sample became conductive. The coefficient $k_{rel,i,j}$ was calculated for all the measurements before the grease became conductive as the relative change of the breakdown voltage between two consecutive readings

$$k_{rel,\mathrm{i,j}} = \left| \frac{(Uj,\mathrm{i}+1 - Uj,\mathrm{i})}{(Uj,\mathrm{i}+1 + Uj,\mathrm{i})} \right| \cdot 100\ \%, \qquad (7)$$

where $U_{j,\mathrm{i}}$ is the i^{th} voltage measured in the j^{th} series. The coefficient $k_{rel,\mathrm{i,j}}$ is defined as 0 for all samples after the grease has become conductive. Table *IV* shows the measured breakdown voltages.

Samples C and D feature rapid (59.62 % and 58.97 %) drops of the initial breakdown voltage while samples A and B demonstrate much less rapid decreases of only 25.51 % and 46.45 % respectively. The individual sets of samples show from 10.99 to 11.47 % variation between the consecutive measurements. The difference between the smallest and the largest value is, however, only 0.48 %, which is very small when compared to the absolute values of the average variation K_{AVG}.

TABLE IV
MEASURED BREAKDOWN VOLTAGES

Grease	Decline of average voltage during the first three measurements	K_{AVG}	N_{nonDC}
A	46.45 %	10.99%	379
B	25.51 %	11.02%	178
C	59.62 %	11.16%	315
D	58.97 %	11.47%	421

IV. DISCUSSION

The results show that different types of grease may have different abilities to sustain their initial dielectric properties after a discharge has happened.

With the samples that became conductive, only a few hundreds of volts built up across the gap, and the values were lower than those that material with the dielectric strength of air (3 kV per 1 mm of thickness) would be able to sustain. Such behaviour has previously been reported in [16] and is considered to be caused by local film thickening, leading to metal-to-metal contact formation. In the work presented in this paper it was, however, not possible for the metallic parts to come into contact, which suggests that the grease became locally saturated with ionized particles conducting electric charge.

The results demonstrate the consequent reduction in dielectric strength of the grease samples as a result of the electric discharges. This can be explained by electrostatic discharge imbued oxidation and thermal decomposition of grease components, which may generate particles with dielectric strengths smaller than those of the initial components, thus reducing the grease's overall dielectric strength and increasing its dispersion. It is also possible that the conductive elements inside the grease cause the decline in apparent breakdown voltage as some parts of the grease conduct the potential through some parts of the gap. The decline in

breakdown strength might cause the decline in apparent discharge activity over time in an electric machine as the grease goes into resistive mode, reducing the voltage load between the shaft and frame of the machine. This is in line with the observed decline of peak discharge activity over time for different shaft rotational speeds and the change of the rotational speed at which this maximum occurs at [17].

The grease sample D demonstrated the best long-term resistance to degradation which may be explained by its synthetic base oil, composed of poly-alpha-olefins which are known for their resistance to thermal oxidation processes. Mineral oil samples A and B feature less rapid initial degradation of dielectric strength than the synthetic ones. The sample labelled B features very slow initial degradation, which might be contributed to its low viscosity: The particles damaged by discharge might have a chance to be replaced with fresh grease due to intensive molecular movement during heat dissipation processes. This is also in line with the analysis performed in [17], which suggests that a higher temperature of bearing results in the rise of discharge activity. Their findings can be explained if we consider that higher temperatures result in lower grease viscosity which in turn improves the rate at which the damaged grease is washed out.

The breakdown field strengths observed in the experiment reported on in this paper varied between 20-50 V/um at the initial discharges for each sample and 4-20 V/um when the greases' electric properties had been altered by discharges already. This is in the line with the observed typical discharge field strength of 15 V/um for rolling element bearings installed in variable speed drives in the field [18].

The test setup comprises a scaled (approx. 1:100) real life case with the assumption that the rotational speed does not affect the process during a single electrostatic discharge. Thus, when interpreting the findings in the context of rolling element bearings used with variable speed drives, some absolute values measured will need to be scaled: The maximum test voltage of the electrostatic discharge generator, 5 kV, corresponds to approximately 50 V occurring across the bearing, which is a realistic value for electric machines of variable speed drives installed in the field. Furthermore, the discharge generator provided a constant voltage in contrast to the higher harmonics contained in the voltage bearings of variable speed drive systems are submitted to. However, the discharges typically happen during times of constant voltage across the bearings, and the harmonics are considered low enough to not affect the dielectric constant of the material.

The exact energy dispatched into the system is not controlled, which might lead to a rather large variability of long-term results. This variability might be explained by the oscillations in the generator-bearing capacitance circuit happening after the discharge. Organic oil and wax molecules are dipoles and are susceptible to the effect of molecular polarization [19] which might persist even if the field is removed. Hence these oscillations might polarize the molecules of grease in either positive or negative polarization with respect to the applied voltage increasing or decreasing the relative permittivity for the following discharge. Furthermore, significant uncertainty comes from the potential presence of air bubbles in the shortest path of the current decreasing the effective dielectric strength. In the investigation, this effect was minimized by the high number of tests carried out for each of the configurations analysed.

While such uncertainties may challenge the analysis of the results, they are in line with the situation with real life applications, where the voltage across the bearings changes along with the variability of the individual switching incidences, and where air might be included within the grease, what might even be a function of the greases' rheological properties.

Further research on the characteristics of the grease conductivity is required, as the findings observed need to be understood in the context of those reported on in other studies: Increased surface roughness due to surface melting was suggested to reduce the distance between the bearing's ball and running surfaces, decreasing the resistance of the grease layer [17]. In [20], a hypothetical possibility of ball and ring surfaces melting together due to short-term local melting of surfaces at the moment an electrostatic discharge occurs is mentioned. Such melting would create a direct conducting path turning the bearing into resistive mode. Furthermore, the findings on the modification of the grease dielectric properties complement those on the effect of the energy introduced into the system by the discharges on the bearing surface, resulting either in melting or vaporization of the surface [11], and the possibility of further flattening of the small craters that has been cited to not affect the bearing life [21].

REFERENCES

[1] M.E.H. Benbouzid, "Bibliography on induction motors faults detection and diagnosis," *IEEE Trans. Energy Conversion*, vol. 4, no. 4, pp. 1065-1074, Dec. 1999.

[2] O.V. Thorsen and M. Dalva, "A survey of faults on induction motors in offshore oil industry, petrochemical industry, gas terminals, and oil refineries," *IEEE Trans. Ind. Appl.*, vol. 31, no. 5, pp. 1186-1196, 1995.

[3] S. Chen, T.A. Lipo, and D. Fitzgerald, "Modeling of bearing currents in inverter drives," *IEEE Trans. Ind. App.*, vol. 32, no. 6, pp. 1365-1370, Sep./Oct. 1996.

[4] S. Chen and T.A. Lipo, "Source of induction motor bearing currents caused by PWM inverters," *IEEE Trans. En. Conv.*, vol. 11, no. 1, pp. 25-32, Jan./Feb. 1996.

[5] P. Link, "Minimizing electric bearing currents in ASD systems," *IEEE Ind. Appl. Mag.*, vol. 5, no. 4, pp. 55-66, Jul./Aug. 1999.

[6] H.E. Boyanton and G. Hodges, "Bearing fluting," *IEEE Ind. Appl. Mag.*, vol. 8, no. 5, pp. 53-57, Sep./Oct. 2002.

[7] R.F. Schiferl and M.J. Melfi, "Bearing current remediation options," *IEEE Ind. Appl. Mag.*, vol. 10, no. 4, pp. 40-50, Jul./Aug. 2004.

[8] A. Muetze and A. Binder, "Don't lose your bearings - mitigation techniques for bearing currents in inverter-supplied drive systems," *IEEE Mag. Ind. Appl.*, vol. 12, no. 4, pp. 22-31, Jul./Aug. 2006.

[9] A. Muetze and A. Binder, "Practical rules for assessment of inverter-induced bearing currents in inverter-fed AC motors up to 500 kW," *IEEE Trans. Ind. Electron.*, vol. 54, no. 3. pp. 1614-1622, June 2007.

[10] A. Binder and A. Muetze, "Scaling effects of inverter-induced bearing currents in ac machines," *IEEE Trans. Ind. App.*, vol. 44, no. 3, pp. 769-776, May/Jun. 2008.

[11] H. Tischmacher and S. Gattermann, "Bearing currents in converter operation," in *The XIX Int. Conf. on Electrical Machines - ICEM 2010*, 2010, pp. 1-8.

[12] P.M. Cann, M.N. Webster, J.P. Doner, V. Wikstrom, and P. Lugt, "Grease Degradation in R0F Bearing Tests," *Tribol. Trans.*, vol. 50, no. 2, pp. 187-197, Apr. 2007.

[13] J. Ahola, V. Niskanen, J. Tamminen, and T. Ahonen, "Performance evaluation of radio frequency based EDM bearing current detection method" *8th International Conference on Condition Monitoring and Machinery Failure Prevention Technologies 2011* (CM 2011/MFPT 2011), pp. 473-481, 2011.

[14] W. Ostwald, "Ueber die rechnerische Darstellung des Strukturgebietes der Viskosität", *Kolloid-Zeitschrift*, vol. 47, no. 2, Feb. 1929, pp. 176-187.

[15] K. Pearson, "On the criterion that a given system of deviations from the probable in the case of a correlated system of variables is such that it can be reasonably supposed to have arisen from random sampling". *Philosophical Magazine Series 5* 50 (302): 157–175.

[16] A. Romanenko, J. Ahola, A. Muetze, and V. Niskanen, "Study of incipient bearing damage monitoring in variable-speed drive systems," *Power Electronics and Applications (EPE'14-ECCE Europe), 2014 16th European Conf. on*, 10 pages, Aug. 2014

[17] A. Muetze; J. Tamminen, and J. Ahola, "Influence of motor operating parameters on discharge bearing current activity," *IEEE Trans. Ind. App.*, vol. 47, no. 4, pp. 1767-1777, Jul./Aug. 2011.

[18] D.F. Busse, J.M. Erdman, R.J. Kerkman, D.W. Schlegel, and G.L. Skibinski, "The effects of PWM voltage source inverters on the mechanical performance of rolling bearings," *IEEE Trans. Ind. App.* vol. 33, no. 2, pp. 567-576, Mar./Apr. 1997

[19] R.E. Hummel, *Electronic Properties of Materials*. Springer Berlin Heidelberg, 2001, pp 166-193.

[20] W. Liu, "The prevalent motor bearing premature failures due to the high frequency electric current passage," *Eng. Fail. Anal.*, vol. 45, pp. 118-127, Oct. 2014.

[21] M. Kriese, E. Wittek, S. Gattermann, H. Tischmacher, G. Poll, and B. Ponick, "Influence of bearing currents on the bearing lifetime for converter driven machines," *Electrical Machines (ICEM), 2012 XXth International Conference on*, pp. 1735-1739, 2-5 Sept. 2012

BIOGRAPHIES

Aleksei Romanenko received the B.Eng.Tech in electric engineering from the Saint Petersburg Electrotechnical University in 2011 and the M.Sc. from Lappeenranta University of Technology and Saint Petersburg Electrotechnical University in 2013.

In 2013, he joined the Department of Electrical Engineering, Lappeenranta University of Technology as a Research Assistant and became a doctoral student there in 2014. His current research mainly focusses on the maintenance of electric machines, embedded systems, and wireless diagnostics.

Annette Muetze (S'03-M'04-SM'09) is a full professor at Graz University of Technology, Austria, where she heads the Electric Drives and Machines Institute. She received the Dipl.-Ing. degree in electric engineering from Darmstadt University of Technology, Germany and the degree in general engineering from the Ecole Centrale de Lyon, France, both in 1999, and the Dr.-Ing. degree in electrical engineering from Darmstadt University of Technology in 2004.

Prior to joining Graz, she worked as an Assistant Professor at the Electrical and Computer Engineering Department, University of Wisconsin-Madison, Madison, US, and as an Associate Professor at the School of Engineering of the University of Warwick in the UK. Her research interests are the interplay of the different elements of electric drive systems, including parasitic effects, performance evaluation, design optimization, and decision making criteria.

Jero Ahola received the M.Sc. and D.Sc. degrees in electrical engineering from Lappeenranta University of Technology (LUT), Lappeenranta, in 1999 and 2003, respectively. He is currently a Professor of energy efficiency and preventive maintenance of electrical equipment with the Department of Electrical Engineering, LUT. His main research interests are diagnostics of electrical drive systems and power line communications.

Publication V

Romanenko A., Muetze A., and Ahola J.

Effects of Electrostatic Discharges on Bearing Grease Dielectric Strength and Composition

Reprinted from
IEEE Transactions on Industrial Applications
vol. 52, no. 6, pp. 4835-4842, 2016

Effects of Electrostatic Discharges on Bearing Grease Dielectric Strength and Composition

A. Romanenko, *Student Member, IEEE,* A. Muetze, *Fellow, IEEE,* J. Ahola

***Abstract*—Bearing faults may significantly reduce the useful life of electric machines. With the advent of modern fast-switching frequency converters, electric currents induced by the high-frequency common-mode voltage of these converters have been recognised as additional, sometimes severe, contributors to bearing degradation. The degradation is understood to progress both by damaging the bearing surfaces and by altering the chemical composition of the lubrication greases, which can lead to ineffective lubrication and reduction in permissible mechanical bearing load. This paper studies the effect of grease degradation due to discharge currents on the grease dielectric strength and chemical composition of several greases typically used with electric drives. From this, conclusions on the grease selection for variable speed drive applications are drawn.**

***Index Terms*—Ball bearings, fault diagnosis, materials reliability, accelerated aging, electrostatic discharges, variable speed drives.**

I. Introduction

BEARING faults may significantly interfere with the reliability of electric machines. According to several studies, reviewed in [1], bearing failures cause between 13 % and 44 % of motor faults. The authors of [2] name mechanical breakage (70.53 % of reported bearing faults) and over-heating (22.11 %) as the most frequent initiators for bearing damage, and high vibration (50.5 %), persistent over-loading (22.77 %), and poor lubrication (12.87 %) as the most frequent contributors to eventual bearing failure.

The possibility of additional bearing damage caused by inverter-induced bearing currents in modern variable-speed drive systems has been well recognised. Different authors have described cause-and-effect chains for this potential damage, allowing selection of appropriate mitigation techniques (e.g. [3], [4], [5], [6], [7], [8], [9], [10]). Understanding of the damage mechanism itself as it takes place inside the bearing is, however, still only very rudimentary. The degradation is generally understood to progress by the bearing currents (i) damaging the bearing surfaces [11] and (ii) altering the chemical composition of the grease [12]. The latter can lead to ineffective lubrication and reduction of the permissible mechanical bearing load.

Extending the preliminary results presented in [13], this paper studies the effect of grease degradation due to discharge currents on the grease breakdown field strength and chemical composition of four different greases typically used with electric machines. We limit our discussion to electric discharge bearing currents that occur as discharges following voltage that has been built up across the bearing. The influence of further bearing grease and surface degradation that might occur due to (for a given time) continuous flow of current through a bearing following a breakdown, as it may be the case with high-frequency circulating bearing currents, is minimised in this setup, since the electrostatic discharge generator used is not able to provide significant long-term current output. Furthermore, the paper discusses correlations between grease chemical composition and rheological properties: the relationship between grease viscosity and shear rate. From this, conclusions on the grease selection for variable speed drive applications are drawn.

A. Romanenko is with Lappeenranta University of Technology, Lappeenranta, Finland (e-mail: Aleksei.Romanenko@lut.fi).
A. Muetze is with Graz University of Technology, Graz, Austria (e-mail Muetze@tugraz.at)
J. Ahola is with Lappeenranta University of Technology, Lappeenranta, Finland (e-mail: Jero.Ahola@lut.fi).

II. METHOD

A. Test equipment

The influence of repetitive discharges on the grease breakdown field strength was analysed as follows. The equipment comprised a 1-axis micrometric screw modified by welding a bearing ball (17.5 mm diameter) to the shaft of the screw on one side and a copper-covered part of a 2.54 mm thick printed circuit board made of FR4 insulating material with copper outer layers on both sides (Fig. 1), an electrostatic discharge generator, and a portable oscilloscope. It should be noted that this setup only allows for analysis of discharges occurring in a static arrangement. However, this approach is justified because of the significantly shorter times of the discharges (discharge times between a few nano and a few microseconds) than typical times between individual switching instances (at typical switching frequencies of a few kilohertz) and rotational speed of the bearings (of up to several hundreds of hertz).

The distance S_B travelled by the point on a surface of a bearing ball during a single spark event is estimated by

$$S_\mathrm{B} = r_\mathrm{C} F_\mathrm{S} \left(1 - \frac{r_\mathrm{b}^2}{r_\mathrm{c}^2}\right) t\pi, \tag{1}$$

with the bearing ball radius r_b = 8.75 mm, bearing cage radius r_c = 36.25 mm, which are the dimensions of 6309ZZ bearing, a typical shaft rotational frequency of F_S = 25 Hz, and t = 1 µs as an approximation of the duration of a single discharge spark. From this, we obtain S_B = 2.7 µm. This value is in the same order of magnitude than the thickness of the grease lubricating film in rolling element bearings used with electric drives such as those motivating the work of this paper. Hence the shear rate, calculated by

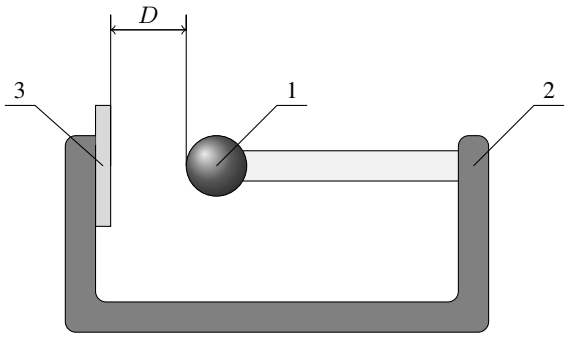

Fig. 1. Sketch of the experimental test setup. 1) 17.5 mm diameter bearing ball. 2) Modified 1-axis micrometric screw for exposure of bearing grease to electric discharges. 3) Printed circuit board fragment made of FR4 insulating material.

$$\dot{y} = \frac{v}{h'}, \tag{2}$$

is in the range of $(0.5 \ldots 2)\ \mathrm{s}^{-1}$, assuming a film thickness h of $(1 \ldots 4)$ µm and a bearing surface velocity v of 2 µm/s. However, this typical film thickness is much smaller than the plate-to-ball distance of the test set up used in this investigation. Possible scaling effects will need to be included in the further analysis of the results obtained.

B. Viscosity measurements

The rheometry of grease samples was performed using an Anton Paar MCR 302 rheometer for three temperatures: 25, 40, and 60 °C. Three sets of 20 measurements were performed for each of the greases. Each set corresponds to one of the three temperatures and shear rates from 0.1 to $10\,\mathrm{s}^{-1}$ with logarithmic steps.

C. Breakdown voltage measurements

The measurements were performed on four different types of grease, grease A to grease D, at a plate-to-ball distance of D = 100 µm. Table I gives an overview of the base oil, thickener types, and additives of the four investigated greases. For each type of grease investigated, 10 samples were investigated consecutively. Prior to each measurement of an individual sample, the space between the ball and the plate was cleaned. Then, the new grease sample was added with the ball at approximately 5 mm from the plate, and the distance between the ball and the plate was then reduced to the desired distance by one-directional movement. After initial positioning, the electrostatic discharge was initiated as follows: The maximal test voltage was set to 5 kV. The trigger of the oscilloscope was set to the falling edge of the input signal (single measurement mode). Voltage was applied until a discharge was detected by the oscilloscope. Then, the maximum voltage occurring within 0.1 µs before this discharge was recorded, and the procedure was repeated again to obtain the next discharge measurement.

For each investigated sample, this procedure was repeated until one of the following two conditions was met: (a) the sample became conductive (the ball-plate system no longer showed capacitive behaviour, preventing any further voltage building across the bearing, no discharges were detected using the wireless detection method described in [14]), or (b) 70 measurements were performed.

TABLE I
BASE OIL AND THICKENER TYPES OF INVESTIGATED GREASES

Grease	Base oil type	Thickener type	Additive
A	mineral oil	multi-soap complex	–
B	mineral oil	aluminium complex	–
C	synthetic silicone	silicone based	–
D	synthetic poly-alphaolefines	lithium complex	extreme pressure and polytetrafluoroethylene (PTFE)

D. Continuous discharging degradation

The test setup was reconfigured to provide continuous power supply via high-voltage DC rectifier (2.5 kV max. voltage, 3 W maximal power). With this power source the effects of discharging on grease composition and mechanical properties were further studied as follows.

For each tested grease a set of six degradation sequences were performed. At the beginning of each sequence the fresh grease was applied between the ball and the plate, while the distance between the two was 3 mm. Then, the voltage source was set to output 1350 V DC which was controlled using a FLUKE 87 True RMS multimeter. After applying the voltage the distance d was decreased with steps of 2 µm until the initial discharge happened (this distance is defined as d_{idp}). From that point the distance was increased in steps of 280 µm in order to increase the thickness of grease layer and prevent the grease from going into direct conductivity. After the increase the system was left to discharge continuously for 1 hour. Then, the damaged grease samples were obtained from the gap and the procedure was started from the beginning.

E. Fourier transform infrared spectroscopy

Fourier transform infrared spectroscopy (FTIR) was used to analyse the quantitative changes in the grease composition due the electrostatic discharges. The method, thoroughly described in [15], is commonly used in the analysis of organic compounds as it is sensitive to the presence of certain functional groups in organic molecules. Each functional group has one or multiple frequency bands in the infrared range at which it absorbs energy due to natural frequencies of its stretching, bending or other types of movements relative to the other atoms in the molecule. These resonance frequencies vary slightly with changes in the rest of the molecule (apart from the functional group they are specific to) and can overlap with resonances of other groups present in molecules of the compound. The absorption rate relates to the number of molecules in the compound as

$$T = e^{-\mu \ell}, \tag{3}$$

where μ is the Napierian attenuation coefficient - constant for material under similar external conditions and ℓ defines thickness of the material layer. Eq. (3) is known as Beer–Lambert–Bouguer law [15] and can be used to track changes in proportions of molecules in compounds.

F. X-Ray diffractometry

During X-Ray diffractometry (XRD) the electrons of certain wavelength are projected onto the sample from different angles to find such angles at which, due to diffraction in crystalline structures, the electrons are reflected into the detector with amplified magnitude. The angle at which diffraction peak is observed is related to the intermolecular space in the crystal structure according to Bragg's law

$$n\lambda = 2d\sin(\theta) \tag{4}$$

where n is the peak order, λ is the electron wavelength, d is the intermolecular distance, θ is half the diffraction angle. The measurements were performed using CuK$_\alpha$ emission with λ = 1.5444260 Å.

III. RESULTS

A. Viscosity analysis

Fig. 2 shows the results of the rheometry of the investigated grease samples. Some points in the plot seem to be kneeing at lower shear rates, which may be explained by excessive viscosity of these samples affecting the measurements. Thus, the points below 1 s^{-1} shear rate were excluded from all sets.

For each of the sets, and for each of the three temperatures measured, curve fitting was applied to the remaining points to obtain the viscosity of the grease as a function of the shear rate: The measured viscosities were fit to the so-called Power Law [16]

$$\eta = K\dot{y}^{\text{n-1}} \tag{5}$$

where η is the viscosity, $\dot{y}$ is the shear rate, n is the power law index defined by the properties of the material, and K is the material dependent proportional coefficient.The proportional coefficients were approximated by a linear function of temperature

$$K(T) = K_0 + kT \tag{6}$$

where T is the temperature, K_0 is the proportional coefficient at $T = 0\,^\circ$C, and k is a temperature dependent coefficient. The results of this curve fitting process are shown in Table II.

B. Breakdown voltage analysis

The statistical analysis of the sampled data was performed to determine the nature of the data distribution. First, Pearson's chi-squared test [17] was evaluated for each full data set to confirm that the initial variations in the measured data were significant. The test provided the probability p with which the tested data sets might belong to a normal distribution. The results are shown in Table III. Some samples became conductive too fast and thus were too short to be analysed with the chi-squared test. The samples for which the null-hypothesis significance strength is less than 0.05 were analysed further.

Each set of measured results was analysed as follows: For each of the four greases investigated, the data sets were grouped so that the first measurements of each set are in group 1, the second measurements of each set in group 2, the third measurements of each set in group 3, and so on. For each

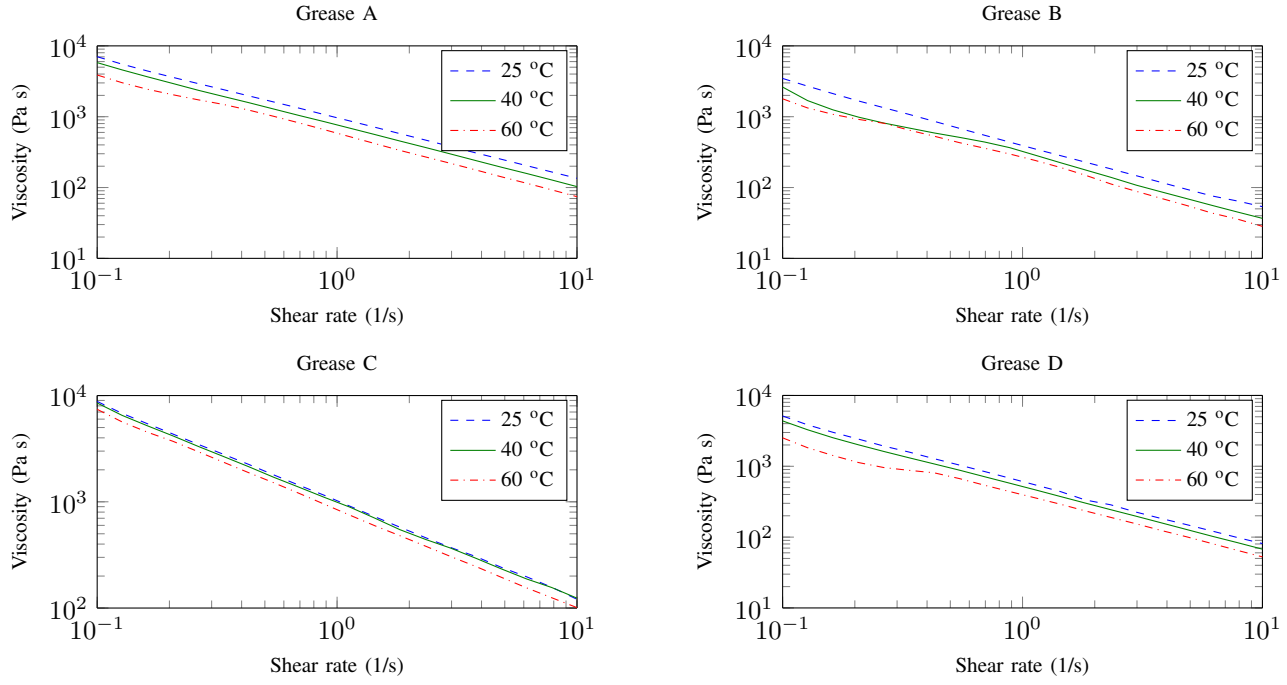

Fig. 2. Grease samples rheometry results.

TABLE II
OVERVIEW OF VISCOSITY MEASUREMENTS

Grease	Temperature [°C]	Power law index n	Proportional coefficient K	Proportional coefficient K_0 at 0 °C[s^{-1}]	Temperature dependent coefficient h [Pa s/°C]
A	25	0.1443	966.4326		
A	40	0.1289	767.5365	1230.2	-11.036
A	60	0.1109	577.1500		
B	25	0.1270	384.0011		
B	40	0.0564	312.5129	457.7	-3.272
B	60	0.0124	267.4456		
C	25	0.0913	1007.8		
C	40	0.1064	964.4926	1145	-5.024
C	60	0.0789	834.8803		
D	25	0.01303	591.2107		
D	40	0.1157	516.3991	731.0	-5.483
D	60	0.1210	399.9867		

group the minimal, average, and maximal breakdown voltages were calculated. These values are presented in Fig. 3. For all sets of each grease, the average decline of the voltage over the first three measurements, K_{VD}, was calculated by

$$K_{\mathrm{VD}} = \frac{1 - U_{\mathrm{avg3}}}{U_{\mathrm{avg1}}} 100\,\%, \tag{7}$$

where U_{avg},i is the average breakdown voltage of the i^{th} group. The average variation K_{AVG} was calculated as

$$K_{\mathrm{AVG}} = \frac{\sum_{\mathrm{i=1}}^{69} \sum_{\mathrm{j=1}}^{10} k_{\mathrm{rel,i,j}}}{N_{\mathrm{nonDC}} - 10}, \tag{8}$$

where N_{nonDC} is the total number of measurements over all sets of data of one type of grease before the corresponding grease sample became conductive. The coefficient $k_{\mathrm{rel,i,j}}$ was calculated for all the measurements before the grease became conductive as the relative change of the breakdown voltage between two consecutive readings

$$k_{\mathrm{rel,i,j}} = \left| \frac{U_{\mathrm{i+1,j}} - U_{\mathrm{i,j}}}{U_{\mathrm{i+1,j}} + U_{\mathrm{i,j}}} \right| 100\,\%, \tag{9}$$

where $U_{\mathrm{j,i}}$ is the i^{th} voltage measured in the j^{th} series. The coefficient $k_{\mathrm{rel,i,j}}$ is defined as 0 for all samples after the grease has become conductive. Table IV shows the measured breakdown voltages.

Samples C and D feature rapid (59.62 % and 58.97 %) drops of the initial breakdown voltage while samples A and B demonstrate much less rapid decreases of only 25.51 % and 46.45 % respectively. The individual sets of samples show from 10.99 to 11.47 % variation between the consecutive measurements. The difference between the smallest and the largest value is, however, only 0.48 %, which is very small when compared to the absolute values of the average variation K_{AVG}.

C. Grease composition analysis

1) FTIR: The FTIR spectra of the damaged and the new grease samples were compared. The results are presented in Fig. 4. The measurements for greases A, B and D were scaled using the peak value of 2800 - 3000 cm^{-1} band to compensate

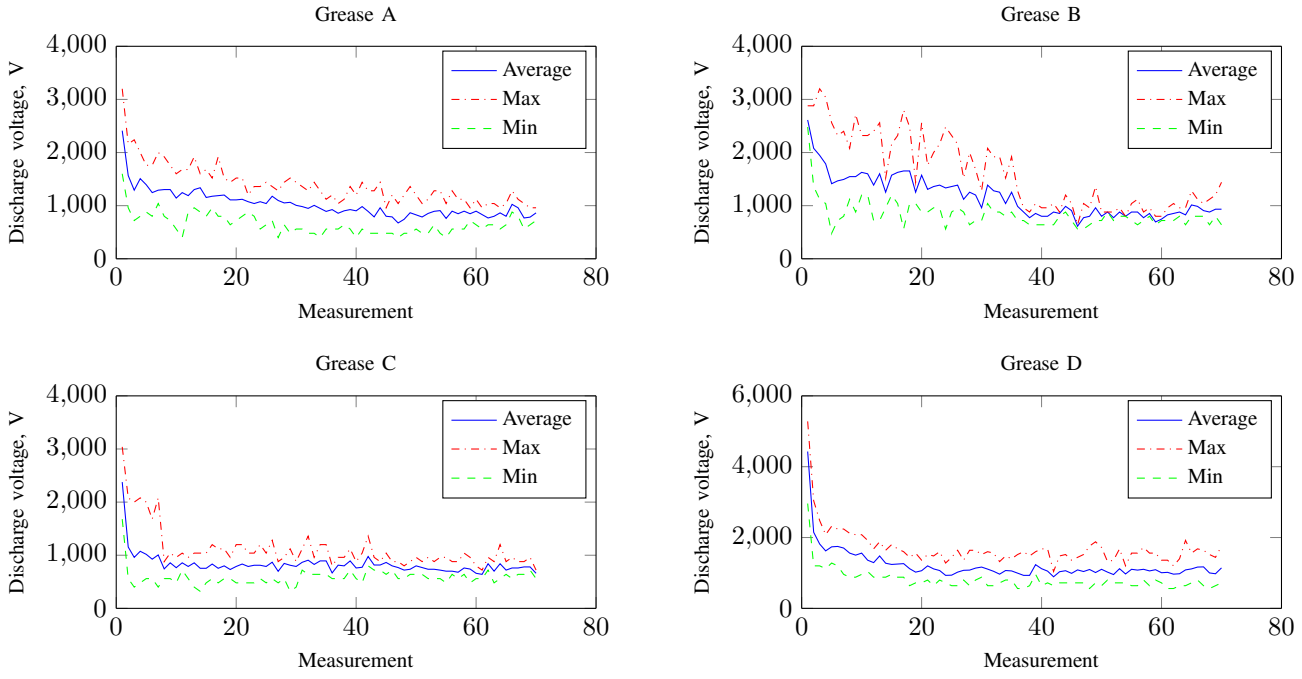

Fig. 3. Measured breakdown voltage.

TABLE III
CHI-SQUARED TEST OF MEASURED SAMPLES: NULL HYPOTHESIS STRENGTH, PROBABILITY P THE TESTED DATA SETS BELONG TO A NORMAL DISTRIBUTION

Samples	GreaseA	GreaseB	GreaseC	GreaseD
1	0.00544	0.06002	1.32E-06	B.78E-05
2	0.038897	0.069667	4.27E-11	0.000184
3	0.001061	0.000181	1.77E-07	0.001815
4	0.033019	0.635161	–	8.05E-07
5	0.072616	–	–	3.81E-07
6	0.107985	0.000464	0.00603	0.007107
7	0.05267	–	9-39E-07	0.057971
8	0.009139	–	0.016195	2.45E-07
9	0.030844	5.55E-05	0.369496	0.080343
10	0.021462	0.147534	1.95E-06	0.092969

TABLE IV
MEASURED BREAKDOWN VOLTAGES

Grease	Decline of average voltage during the first three measurements	K_{AVG}	N_{nonDC}
A	46.45 %	10.99 %	379
B	25.51 %	11.02 %	178
C	59.62 %	11.16 %	315
D	58.97 %	11.47 %	421

for possible variations in sample size. The measurements of grease C was scaled using peak value around wavenumber 700 cm^{-1}.

The analysis of silicone-based grease presented only minor variations in spectral composition. This is possible due to the main component of the grease not containing molecules with functional groups observable with FTIR.

Both natural and synthetic non-silicone greases present a significant decrease in the absorption rate of peaks with wavenumbers from 400 to 1700 cm^{-1}. I.e. Lithium stearate (lithium soap), which is used as a thickener in some of the tested greases, has absorption peaks next to wavenumbers 710 - 715, 1440 - 1470 and 1570 - 1590 cm^{-1} 1 [18]. This indicates a notable decline in the amount of all functional groups with respect to variations of the CH bond stretching band (at wavenumbers 2800 - 3000 cm^{-1}) which is common to alkanes and most other organic molecules. Such decline suggests that the grease composition was significantly altered by decrease in additives and thickeners. The composition of grease A seems to be less affected by the discharging than the composition of the other non-silicone greases.

2) XRD: The results of the XRD analysis are presented in Fig. 5. The results were scaled and shifted using the highest peak magnitude and background level to compensate for variations in sample size. The following observations and conclusions can be drawn from this measurement:

- Grease A contains multiple peaks related to the presence of calcite [18].
- Greases B and C present wide and weak diffraction peaks that can be explained be diffraction in amorphous compounds of grease. Hence the variation in relative peak strength indicates changes in the composition.

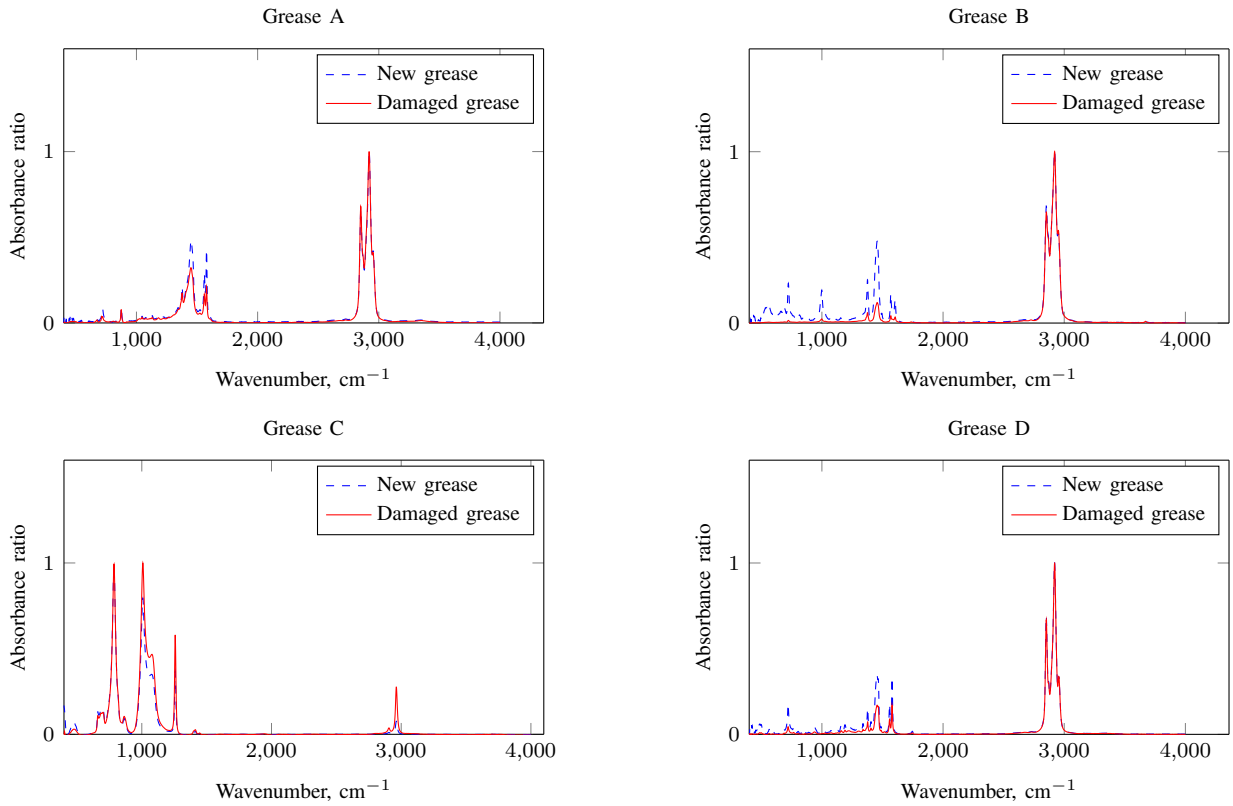

Fig. 4. Changes in FTIR spectra.

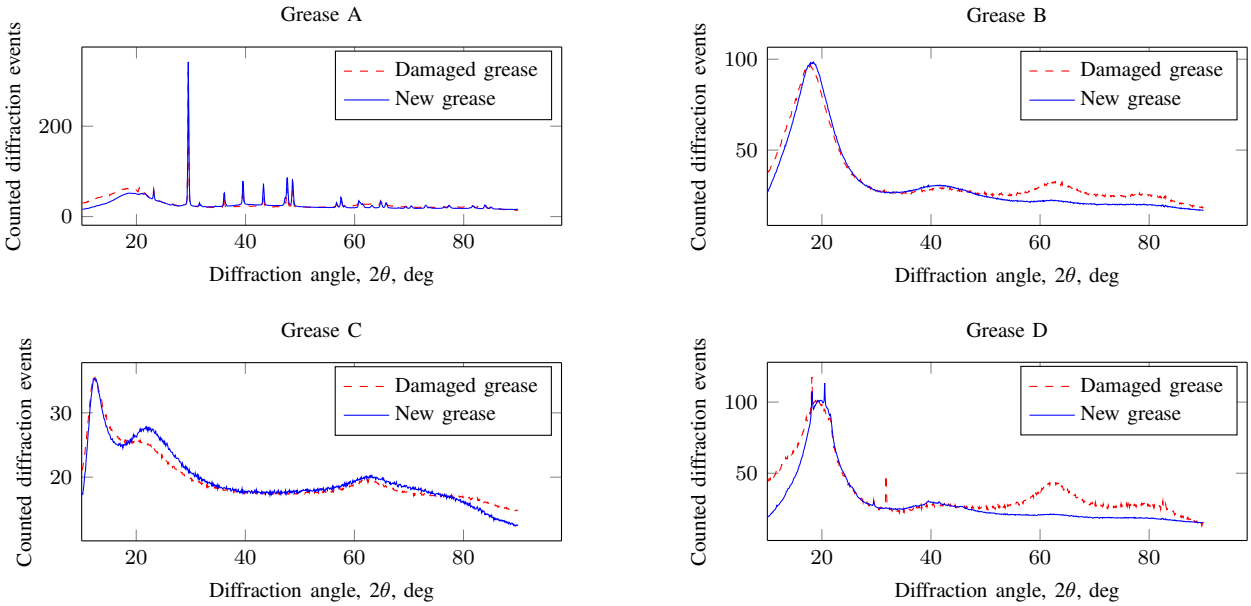

Fig. 5. Changes in X-Ray difractometry measurements.

- Grease D indicates three single narrow peaks which might be related to polytetrafluoroethylene (PTFE) used as additive in this grease. The peak shift of peak location might be explained by changes in the structure of PTFE crystals due to discharges. Another possibility is that some thickener molecules produced metal atoms (i.e. Lithium) which then formed crystal structures.

IV. DISCUSSION

A. Grease dielectric properties

The results show that different types of grease may have different abilities to sustain their initial dielectric properties after a discharge has happened.

With the samples that became conductive, only a few hundreds of volts built up across the gap, and the values were lower than those that material with the dielectric strength of air (3 kV per 1 mm of thickness) would be able to sustain. Such behaviour has previously been reported in [19] and is considered to be caused by local film thickening, leading to metal-to-metal contact formation. In the work presented in this paper it was, however, not possible for the metallic parts to come into contact, which suggests that the grease became locally saturated with ionised particles conducting electric charge

The results demonstrate the consequent reduction in dielectric strength of the grease samples as a result of the electric discharges. This can be explained by electrostatic discharge imbued oxidation and thermal decomposition of grease components, which may generate particles with dielectric strengths smaller than those of the initial components, thus reducing the grease's overall dielectric strength and increasing its dispersion. It is also possible that the conductive elements inside the grease cause the decline in apparent breakdown voltage as some parts of the grease conduct the potential through some parts of the gap. The decline in breakdown strength might cause the decline in apparent discharge activity over time in an electric machine as the grease goes into resistive mode, reducing the voltage load between the shaft and frame of the machine. This is in line with the observed decline of peak discharge activity over time for different shaft rotational speeds and the change of the rotational speed at which this maximum occurs at [20].

The grease sample D demonstrated the best long-term resistance to degradation which may be explained by its synthetic base oil, composed of poly-alpha-olefines which are known for their resistance to thermal oxidation processes. Mineral oil samples A and B feature less rapid initial degradation of dielectric strength than the synthetic ones. The sample labelled B features very slow initial degradation, which might be contributed to its low viscosity: The particles damaged by discharge might have a chance to be replaced with fresh grease due to intensive molecular movement during heat dissipation processes. This is also in line with the analysis performed in [20], which suggests that a higher temperature of bearing results in the rise of discharge activity. Their findings can be explained if we consider that higher temperatures result in lower grease viscosity which in turn improves the rate at which the damaged grease is washed out.

The breakdown field strengths observed in the experiment reported on in this paper varied between 20 - 50 V/µm at the initial discharges for each sample and 4 - 20 V/µm when the greases' electric properties had been altered by discharges already. This is in line with the observed typical discharge field strength of 15 V/µm for rolling element bearings installed in variable speed drives in the field [21].

B. Grease composition

A notable decline in the absorption of IR waves in the bands that are related to additives and thickeners was observed. The changes are expected due the organic nature of the greases, high applied electric field densities and high local increases in temperature which provide energy for chemical reactions or catalyse them. The results of XRD indicate no appearance of melted metal particles (from melted copper or steel surfaces) in the grease samples. Such particles are common in the grease samples obtained from damaged bearings. The absence of such particles in this study is explained by the lack of mechanical contact between electrodes and significant movement of the tested grease samples. The analysis of grease sample D, however, featured disappearance of one resonance peak and appearance of a new one, which can be explained by the changes in the structure of the PTFE additive. The lack of metal particles in the grease composition suggests another explanation of grease conductivity phenomenon during continuous discharging.

At large, such changes in grease composition will reduce the viscosity of the grease, which is supported by thickener components. The decrease of viscosity means that the thickness of the grease film will decrease, potentially subjecting rolling surfaces to additional mechanical friction. Hence, such change in grease composition can potentially affect the lifetime of the bearing subject to the electrostatic discharges due to the bearing currents. Note that the alternative scenario where changes in grease composition result in higher thickness would also be potentially harmful as thicker grease would have limited ability to spread and mix inside the bearing.

Additionally, both the high electric field density prior to the discharge and the high temperatures resulting from it might become a source of hydrogen ions and molecules. Such molecules are theorised to be one of the causes of white etching cracks (WEC) on bearing rolling surfaces [22]. WEC eventually lead to bearing mechanical destruction. The hypothesis on the formation of ionised particles is also supported by the drop in breakdown voltage and potential direct conductivity achieved by the grease samples under the conditions of continuous application of electrical field.

C. Research applicability and limitations

The test setup comprises a scaled (approx. 1:100) real life case with the assumption that the rotational speed does not affect the process during a single electrostatic discharge. Thus, when interpreting the findings in the context of rolling element bearings used with variable speed drives, some absolute values measured will need to be scaled: The maximum test voltage of the electrostatic discharge generator, 5 kV, corresponds to approximately 50 V occurring across the bearing, which is a realistic value for electric machines of variable speed drives installed in the field. Furthermore, the discharge generator provided a constant voltage in contrast to the higher harmonics contained in the voltage bearings of variable speed drive systems are submitted to. However, the discharges typically happen during times of constant voltage across the bearings, and the harmonics are considered low enough to not affect the dielectric constant of the material.

The exact energy dispatched into the system is not controlled, which might lead to a rather large variability of long-term results. This variability might be explained by the oscillations in the generator-bearing capacitance circuit happening after the discharge. Organic oil and wax molecules are dipoles and are susceptible to the effect of molecular polarisation [23] which might persist even if the field is removed. Hence these oscillations might polarise the molecules of grease in either positive or negative polarisation with respect to the applied voltage increasing or decreasing the relative permittivity for the following discharge. Furthermore, significant uncertainty comes from the potential presence of air bubbles in the shortest path of the current decreasing the effective dielectric strength. In the investigation, this effect was minimised by the high number of tests carried out for each of the configurations analysed.

While such uncertainties may challenge the analysis of the results, they are in line with the situation with real life applications, where the voltage across the bearings changes along with the variability of the individual switching incidences, and where air might be included within the grease, what might even be a function of the greases' rheological properties.

D. Summary and further study

Continuous electrostatic discharging through the lubricating greases investigated has shown to lead to significant degradation of the greases' dielectric properties: the results of this study suggest formation of a conducting channel consisting of ionised particles that result from chemical decomposition of original grease components: mainly additives and thickeners. Such change in grease composition can potentially cause bearing mechanical overloading and corrosive effects on bearing rolling surfaces. This aspect should be carefully considered in the grease selection for VSD applications, notably with respect to the bearing load capacity, as the grease composition (and its change) do affect the greases' rheological properties. Furthermore, a certain temperature margin should be provided, to account for the local heating due to the electrostatic discharges.

Further research on the characteristics of the grease conductivity and composition changes is required, as the findings observed need to be understood in the context of those reported on in other studies: Increased surface roughness due to surface melting was suggested to reduce the distance between the bearing's ball and running surfaces, decreasing the resistance of the grease layer [20]. In [24], a hypothetical possibility of ball and ring surfaces melting together due to short-term local melting of surfaces at the moment an electrostatic discharge occurs is mentioned. Such melting would create a direct conducting path turning the bearing into resistive mode. Furthermore, the findings on the modification of the grease dielectric properties complement those on the effect of the energy introduced into the system by the discharges on the bearing surface, resulting either in melting or vaporisation of the surface [11], and the possibility of further flattening of the small craters that has been cited to not affect the bearing life [25].

REFERENCES

[1] M. E. H. Benbouzid, "Bibliography on induction motors faults detection and diagnosis," *IEEE Transactions on Energy Conversion*, vol. 14, no. 4, pp. 1065–1074, 1999.

[2] O. Thorsen and M. Dalva, "A survey of faults on induction motors in offshore oil industry, petrochemical industry, gas terminals, and oil refineries," *IEEE Transactions on Industry Applications*, vol. 31, no. 5, pp. 1186–1196, 1995. [Online]. Available: http://www.scopus.com/inward/record.url?eid=2-s2.0-0029374064&partnerID=tZOtx3y1

[3] S. Chen, T. A. Lipo, and D. Fitzgerald, "Modeling of motor bearing currents in PWM inverter drives," *IEEE Transactions on Industry Applications*, vol. 32, pp. 1365–1370, 1996.

[4] ——, "Source of induction motor bearing currents caused by pwm inverters," *IEEE Transactions on Energy Conversion*, vol. 11, no. 1, pp. 25–32, Mar 1996.

[5] P. J. Link, "Minimizing electric bearing currents in asd systems," *IEEE Industry Applications Magazine*, vol. 5, no. 4, pp. 55–66, Jul 1999.

[6] H. E. Boyanton and G. Hodges, "Bearing fluting [motors]," *IEEE Industry Applications Magazine*, vol. 8, no. 5, pp. 53–57, Sep 2002.

[7] R. F. Schiferl and M. J. Melfi, "Bearing current remediation options," *Industry Applications Magazine, IEEE*, vol. 10, pp. 40–50, 2004.

[8] A. Muetze and A. Binder, "Don't lose your bearings," *IEEE Industry Applications Magazine*, vol. 12, no. 4, pp. 22–31, July 2006.

[9] ——, "Practical rules for assessment of inverter-induced bearing currents in inverter-fed AC motors up to 500 kW," *IEEE Transactions on Industrial Electronics*, vol. 54, pp. 1614–1622, 2007.

[10] A. Binder and A. Muetze, "Scaling effects of inverter-induced bearing currents in AC machines," *IEEE Transactions on Industry Applications*, vol. 44, no. 3, pp. 769–776, 2008.

[11] H. Tischmacher and S. Gattermann, "Bearing currents in converter operation," in *The XIX International Conference on Electrical Machines - ICEM 2010*. IEEE, Sep. 2010, pp. 1–8. [Online]. Available: http://www.scopus.com/inward/record.url?eid=2-s2.0-78649586950&partnerID=tZOtx3y1

[12] P. M. Cann, M. N. Webster, J. P. Doner, V. Wikstrom, and P. Lugt, "Grease Degradation in R0F Bearing Tests," *Tribology Transactions*, vol. 50, no. 2, pp. 187–197, apr 2007. [Online]. Available: http://www.scopus.com/inward/record.url?eid=2-s2.0-34249047016&partnerID=tZOtx3y1

[13] A. Romanenko, A. Mütze, and J. Ahola, "Effects of electrostatic discharges on bearing grease electric properties," in *2015 IEEE International Electric Machines Drives Conference (IEMDC)*, May 2015, pp. 254–259.

[14] J. Ahola, V. Niskanen, J. Tamminen, and T. Ahonen, "Performance evaluation of radio frequency based edm bearing current detection method," vol. 1, 2011, pp. 473–481, cited By 0.

[15] P. R. Griffiths and J. A. de Haseth, *Introduction to Vibrational Spectroscopy*. John Wiley & Sons, Inc., 2006, pp. 1–18. [Online]. Available: http://dx.doi.org/10.1002/9780470106310.ch1

[16] W. Ostwald, "Ueber die rechnerische darstellung des strukturgebietes der viskosität," *Kolloid-Zeitschrift*, vol. 47, no. 2, pp. 176–187, 1929. [Online]. Available: http://dx.doi.org/10.1007/BF01496959

[17] K. Pearson, "X. on the criterion that a given system of deviations from the probable in the case of a correlated system of variables is such that it can be reasonably supposed to have arisen from random sampling," *Philosophical Magazine Series 5*, vol. 50, no. 302, pp. 157–175, 1900.

[18] C. S. Inc., *Evaluated infrared spectra*. National Institute of Standards and Technology, Gaithersburg MD. [Online]. Available: http://webbook.nist.gov

[19] A. Romanenko, J. Ahola, A. Muetze, and V. Niskanen, "Study of incipient bearing damage monitoring in variable-speed drive systems," in *Power Electronics and Applications (EPE'14-ECCE Europe), 2014 16th European Conference on*, Aug 2014, pp. 1–10.

[20] A. Muetze, J. Tamminen, and J. Ahola, "Influence of motor operating parameters on discharge bearing current activity," *IEEE Transactions on Industry Applications*, vol. 47, no. 4, pp. 1767–1777, July 2011.

[21] D. F. Busse, J. M. Erdman, R. J. Kerkman, D. W. Schlegel, and G. L. Skibinski, "The effects of pwm voltage source inverters on the mechanical performance of rolling bearings," *IEEE Transactions on Industry Applications*, vol. 33, no. 2, pp. 567–576, Mar 1997.

[22] W. Holweger, M. Wolf, D. Merk, T. Blass, M. Goss, J. Loos, S. Barteldes, and A. Jakovics, "White etching crack root cause investigations," *Tribology Transactions*, vol. 58, no. 1, pp. 59–69, 2015.

[23] R. E. Hummel, *Electronic Properties of Materials*. Springer Berlin Heidelberg, 2001. [Online]. Available: http://link.springer.com/chapter/10.1007%2F978-3-642-86538-1_9#page-1

[24] W. Liu, "The prevalent motor bearing premature failures due to the high frequency electric current passage," *Engineering Failure Analysis*, vol. 45, pp. 118–127, 2014.

[25] M. Kriese, E. Wittek, S. Gattermann, H. Tischmacher, G. Poll, and B. Ponick, "Influence of bearing currents on the bearing lifetime for converter driven machines," in *Proceedings - 2012 20th International Conference on Electrical Machines, ICEM 2012*, 2012, pp. 1735–1739.

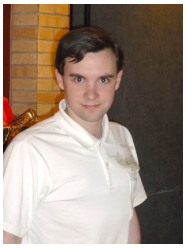

Aleksei Romanenko (S'11-16) received the B.Eng.Tech in electric engineering from the Saint Petersburg Electrotechnical University in 2011 and the dual-degree M.Sc. from Lappeenranta University of Technology and Saint Petersburg Electrotechnical University in 2013.

In 2013, he joined the Department of Electrical Engineering, Lappeenranta University of Technology as a Research Assistant and became a doctoral student there in 2014. His current research mainly focuses on the maintenance of electric machines, embedded systems, and non-intrusive diagnostics.

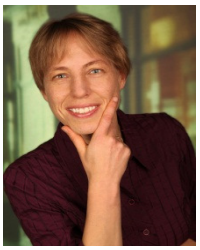

Annette Muetze (S'03-M'04-SM'09-F'16) is a full professor at Graz University of Technology, Austria, where she heads the Electric Drives and Machines Institute. She received the Dipl.Ing. degree in electric engineering from Darmstadt University of Technology, Germany and the degree in general engineering from the Ecole Centrale de Lyon, France, both in 1999, and the Dr.Ing. degree in electrical engineering from Darmstadt University of Technology in 2004.

Prior to joining Graz, she worked as an Assistant Professor at the Electrical and Computer Engineering Department, University of Wisconsin-Madison, Madison, US, and as an Associate Professor at the School of Engineering of the University of Warwick in the UK. Her research interests are the interplay of the different elements of electric drive systems, including parasitic effects, performance evaluation, design optimization, and decision making criteria.

Jero Ahola received the M.Sc. and D.Sc. degrees in electrical engineering from Lappeenranta University of Technology (LUT), Lappeenranta, in 1999 and 2003, respectively. He is currently a Professor of energy efficiency and preventive maintenance of electrical equipment with the Department of Electrical Engineering, LUT. His main research interests are diagnostics of electrical drive systems and power line communications.

Publication VI

Romanenko A., Muetze A., and Ahola J.
Incipient Bearing Damage Monitoring of 940-Hour Variable Speed Drive System Operation

Reprinted from
IEEE Transactions on Energy Conversion
vol. 32, no. 99, p. 99-110, 2017

Incipient Bearing Damage Monitoring of 940-Hour Variable Speed Drive System Operation

A. Romanenko, *Student Member, IEEE,* A. Muetze, *Fellow, IEEE,* J. Ahola

***Abstract*—Inverter-induced high-frequency bearing currents are a recognised cause of bearing failure in frequency converter-fed electric machines. Mechanical bearing faults are generally identified by vibration measurements. In our work, we submit bearings to electric discharge machining bearing currents, measure the electrical stress placed on the bearings, the resulting vibration signal and operating temperature, and apply time and frequency domain signal processing techniques for feature extraction. Experiments are run for 940 hours of operation, so as to study the incipient bearing failure behaviour. After the end of the test run the bearing surfaces are inspected using scanning electron microscopy.**

***Index Terms*—Ball bearings, converter machine interactions, diagnostics, induction machine, wireless sensors.**

I. Introduction

IT has been well recognised that modern variable-speed drives that use fast-switching inverters can engender a variety of parasitic phenomena. Among these phenomena are inverter-induced bearing currents that can cause significant harm and eventually lead to the failure of the motor and generator bearings (and also adjacent gears and gear bearings within such drive systems).

Several types of inverter-induced bearing currents have been identified, such as capacitive displacement, electric discharge machining (EDM), high-frequency circulating, and rotor-to-ground currents. With EDM currents, that are in the focus of this work, electric discharges occur statistically distributed between the raceways of the inner and outer ring and the rolling elements of a bearing. While the exact mechanism of bearing failure due to such bearing currents is not understood, it has been well established that such currents can be a starting point for bearing damage.

This paper investigates the development of EDM-type inverter-induced bearing damage during a laboratory test run with a specially modified motor setup using vibration analysis, non-intrusive discharge activity monitoring and temperature monitoring techniques. From this, conclusions are drawn on the process of pitting damage progression and on the vibration criteria selection for prediction of this type of damage.

Followed by a brief review of bearing damage modelling, damage mitigation and monitoring techniques, the paper first describes the approach used and explains the selection of the different motor operating modes. The methodology used for the data processing is then presented. In the second part, the results of different types of analysis are discussed and correlations identified. From these results, hypotheses for fault development are derived.

A. Romanenko is with Lappeenranta University of Technology, Lappeenranta, Finland (e-mail: Aleksei.Romanenko@lut.fi).
A. Muetze is with Graz University of Technology, Graz, Austria (e-mail: Muetze@tugraz.at)
J. Ahola is with Lappeenranta University of Technology, Lappeenranta, Finland (e-mail: Jero.Ahola@lut.fi).

II. State of the art review

A. Bearing damage modelling and damage mitigation

Different authors have described the cause-and-effect chains of inverter induced bearing damage, allowing the selection of appropriate mitigation techniques. The works on modelling of the bearing current phenomenon started by the authors of [1], who first presented lumped-parameter model of electrical machine structural elements, and [2], who proposed a hypothesis explaining the origination of high-frequency bearing currents in systems with PWM drives and investigates the influence of machine dimensions and operation parameters on the phenomenon. Several years later [3] assembled and reviewed the hypotheses regarding the possible damage causes.

Several approaches for current prevention and damage mitigation several studies have emerged in the recent years. For example, in [4]–[6] electrostatic shielding of motor was investigated and bearing life-time dependency of average current density was presented. [3] suggested ground level equalisation between components of the system, insulated bearings, reduction of PWM switching frequency and $\frac{dV}{dt}$ rate using common mode chokes and reactors as bearing current mitigation techniques. The same study also suggested the use of a Faraday cage as a mitigation technique. In [7] a case study of fluting in a paper mill was presented. Different mitigation techniques were studied and rejected by the authors. The solution proposed was to connect rotating and stationary parts with low impedance path which was a newly proposed technique. [8] suggested the use of inductive filters to reduce high-frequency components in PWM drives. In [9] cable shielding and bearing insulation effect on bearing currents in machines of different sizes was studied. The paper also suggested the use of hybrid bearings with ceramic balls to suppress the bearing currents. A summarising review of damage mitigation techniques and comparison their efficiency is presented in [10].

B. Damage monitoring techniques

One of the earliest proposals of bearing damage monitoring using methods based on frequency composition of vibration signal measured or estimated from stator currents was presented in [11]. The technique was initially proposed as a sensorless monitoring of RMS vibration levels of different frequencies. The substitution is possible as the stator current

is an effective measure of torque which in its turn correlates to RMS vibration levels as it takes additional torque to overcome defects that cause the vibration increase. The approach was later developed by different authors. I.e. [12] presents the detection of macroscopic damages such as race crack, hole or seal displacement using frequency components of stator current. Different authors also attempted the application of such techniques to detection of fluting pattern and pitting race resulting from bearing currents.

According to [13], EDM currents first lead to pitting of the outer or inner ring and in later stages to an increase in wide-band vibration. The authors of [14] explain that the usability of vibration monitoring for predictive maintenance of inverter-induced bearing failures is rather limited, mainly because of lack of knowledge of the damage evolution within the bearing, from incipient damage, at which stage countermeasures can be applied and operational continued, to severe damage preventing further operation. A general approach for application of vibration based condition monitoring for evaluation of bearing remaining useful life (RUL) in the presence of inverter-induced bearing currents is described in [15]. Another study [16] suggests RUL estimation using a Kalman filter technique applied to vibration measurements.

The direct vibration monitoring was selected to be the main technique for this study as stator current monitoring was considered to be mainly the derivative of vibration monitoring and thereof containing less information.

III. Equipment and Methods

A. Laboratory setup

The test rig comprises a low-voltage off-the shelf squirrel cage induction motor (3-phase, 15 kW, 4-pole) and a load machine of similar type coupled with an insulating coupler (Figs. 1,2). The test motor has 6309 deep groove ball bearings with a clearance of C3, greased with an off the shelf lithium-soap-based grease. Both bearings of the test motor are electrically insulated towards the frame by polyethylene sleeves. The drive-end (DE) bearing insulation is short-circuited by a short wire, enabling intrusive bearing current measurement (R&S ZC-20, DC-100MHz) and allowing the bearing current to influence the bearing's state. Thus, with the exception of a negligible fraction flowing through the two capacitances between the bearing outer ring and the stator frame and between the rotor and the stator frame, the bearing current will always flow through the DE bearing. To generate the discharge currents, voltage is supplied to the motor non-drive end (NDE) between the motor shaft and the frame with a signal generator (Phillips PM5135) connected to a galvanically isolating transformer with a 2:1 winding ratio. The out-put signal from the transformer is supplied to the rotor by means of an electric slip ring (Mercotac 110, contact resistance $R_{\text{contact}} < 1m\Omega$, max. current $I_{\text{max}} = 10A$, max. frequency F_{max} = 200 MHz). The bearing voltage is measured with a high impedance differential probe (R&S ZT-01 DC-100MHz) from the terminals of the coupler. The measurement equipment further comprises a piezoelectric vibration measurement sensor (Kistler 8\712A5M1, ±5g, BW = 0.5-8000 Hz) supplied by a Kistler type 5114 voltage source, four temperature sensors (EPCOS - B57560G104F 100 kOhm thermistors): three for measurement of the bearing outer ring temperature and one for the measurement of the load machine stator frame temperature, as well as a radio-frequency (RF) measurement setup for the counting of pulses originating from the bearing discharges [17], [18], thereby providing the so-called "discharge activity" (DA). The RF measurement equipment includes an antenna (EMCO 93148), an oscilloscope (R&S RTO1014) and a digital pulse counter. The SEM pictures are taken with a Hitachi SU3500 scanning electron microscope.

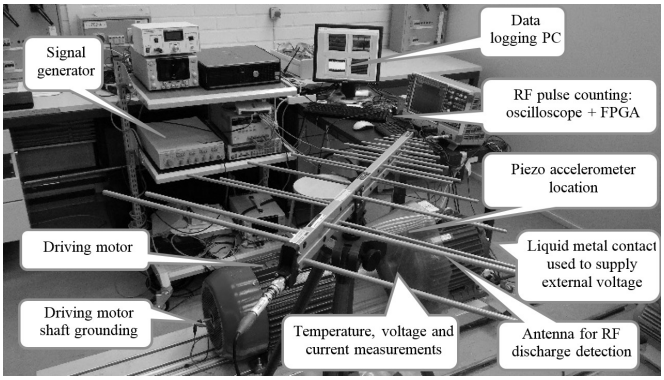

Fig. 1. Photo of the laboratory test setup.

B. Test program

Fig.3 illustrates the test program conducted with the test setup. The bearings were submitted to electric stress by a sinusoidal voltage generator with 60 V_{pp} open-loop peak-to-peak voltage and 300 kHz frequency, as described above. The EDM DA was monitored with a non-intrusive RF-based bearing current detection method [17] and additional recording of the bearing temperature. The state of health of the bearing was monitored by vibration measurement to make it possible to establish the relation of any incipient failure within the bearing to the electric stress the bearing had been subjected to. The sampling of bearing temperatures, vibration and discharges, as described below, was started and the motor was run for a total of 940 hours. The bearings were then inspected visually and with an electron microscope to assess their state of health and correlate it with the results of the vibration measurements.

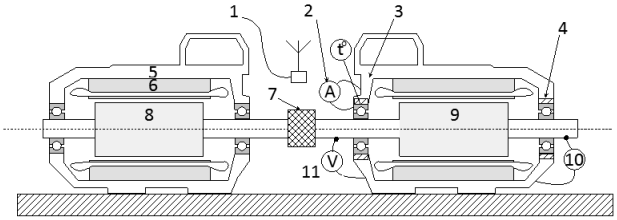

Fig. 2. Schematic of laboratory test setup. 1) RF measurement equipment; 2) Current measurements; 3) Piezo-electric accelerometer installed in the same plane as DE bearing; 4) Bearing insulation; 5) Frame; 6) Stator; 7) Insulating coupler; 8) Driving motor; 9) Test motor; 10) Adjustable voltage source; 11) Shaft voltage measurements.

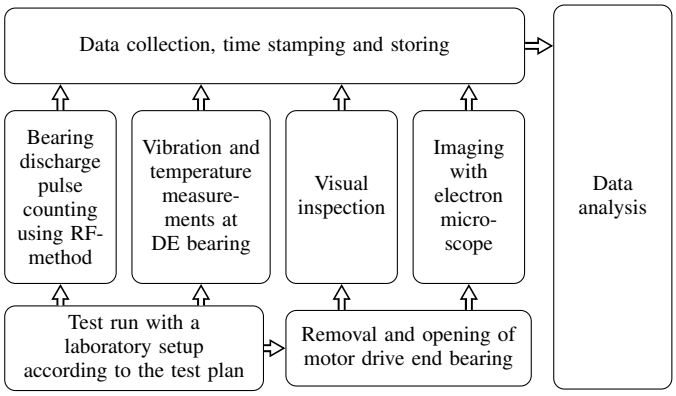

Fig. 3. Test program conducted with the laboratory test setup.

TABLE I
ROTATING FIELD FREQUENCY SELECTION

Interval no.	t_{start}, hours	Duration, hours	F_{F}, Hz
0	0	125.5	50
1	125.5	40.2	50
2	166.7	28.8	0*
3	195.5	67.3	13
4	262.8	23	30
5	285.8	27.8	13
6	313.6	3.8	20
7	317.4	114	varying, eq. (1)
8	431.4	52.4	50
9	483.8	66.9	20
10	550.7	389.5	50

* The drive had to be stopped for 30 hours for maintenance on the measurement equipment to be performed.

C. Test sequence speed selection

The rotational speed of the motor shaft was varied over the course of the test run to facilitate bearing grease degradation and bearing wear. The time intervals were selecting following the monitoring of the DA. When DA levels were low (less than 30 discharges per second) for continuous period of time (longer than 2 hours) the operation mode was changed. At the beginning of each time interval speed between 0 and 1500 rpm that provided the maximal amount of detected discharges was chosen. This selection is possible due to the dependence of DA intensity on grease thickness and temperature which are in turn vary with shaft rotation speed. The new point of maximum DA was selected 10 times until the maximal DA activity point stabilised at 1500 rpm. The complete sequence of speed changes is presented in Table I. The bearing was initially run at a supply of frequency FF of 50 Hz (n = 1500 rpm) for 125.5 hours without any voltage applied to the shaft of the machine. The external voltage source was then turned on. After 317.6 hours the frequency at which the maximum of discharge activity was observed shifted close to 50 Hz and the speed was selected to vary between 45 Hz and 50 Hz according to:

$$f(t) = 2.5\sin(0.1\pi t) + 45, \tag{1}$$

where t is the time in seconds from the beginning of the varying speed mode. For 114 hours, the machine was operated sequentially in varying speed mode for 4 minutes and at constant speed (50 Hz/1500 rpm) for 1 minute for the vibration measurements to be taken under constant and well-defined conditions. At t = 431.4 hours constant speed operation continued.

D. Discharge activity monitoring

The antenna was directed to the DE of the test motor, at approximately 1 m distance (Fig. 1). The RF pulses were measured with an oscilloscope over a 50 ohms termination. The triggering voltage to detect RF pulses was adjusted to 5 mV, detecting the rising edge crossing. The DA was determined from the number of counted crosses sampled over time windows of 30 s. This number is understood to be proportional to the number of electrostatic discharges occurring in the bearing [19].

E. Vibration monitoring

The vibration signal from the motor DE (20 kSamples/s, 400 kSamples record length, 16 bit samples with 0.305 mV [3.05 mm/s^2] resolution), the bearing temperature, and the detected RF signals were measured and periodically stored using a general purpose data acquisition system. (Period times of 30 seconds for the temperature and RF signal, 5 minutes for the vibration measurements respectively.)

The output of the acceleration sensor is independent of its supply voltage level. The main error in the acceleration measurements is due to the sensitivity error, which is maximum 5 %, and a long term stability error, which is 1 % in the worst case. Thus, the maximum error of the acceleration measurements is 6 % of the absolute readings.

Spectral analysis was selected to analyse the measured vibrations because it allows a good trade-off between computational effort (allowing processing of significant amounts of data) and insight into the degradation process. The sampled data was processed with the Cooley-Tukey fast Fourier transform algorithm [20]. This algorithm computes the discrete Fourier transform for an input vector of size N according to:

$$X(k) = \sum_{\text{j=1}}^{N} x(j)\omega_{\text{N}}^{(j-1)(k-1)}, \tag{2}$$

$$\omega_{\text{N}} = e^{(-2\pi i)/N}, \tag{3}$$

where $k = 1 \ldots N, j = 1 \ldots N, x(j)$ is the j$^{\text{th}}$ element of the input vector, $X(k)$ is the k^{th} element of the transformation result vector, ω_{N} is the Nth root of unity. The transformation was applied to each set of 400000 samples of voltage recorded by the digital acquisition platform, after which the transformed signal was down sampled to a resolution of 1 Hz by the averaging magnitudes of consecutive frequency components. The acceleration sensitivity of the sensor is 1 V per 9.8 m/s^2. The result of the transformation is a vector containing frequency components from 0.05 Hz to 10 kHz. The magnitudes of the vector components were then summed up for each 1 Hz band.

The resulting plots were combined into a continuous surface plot representing the magnitude of the signal in each band over the duration of the experiment.

F. Temperature measurements

The temperatures were measured from three sensors located approximately 1 cm away from the DE bearing, denominated bearing probes A, B and C, and a sensor located next to the coil stack on the upper quarter of the stator approximately 30 cm from the DE bearing. Each reading was taken as an average value of 30000 samples sampled at 1 kHz.

The worst case error of the temperatures measured with a single probe is 0.52 K $\pm$ 0.5 % of the respective value.

G. Scanning electron microscope imaging

The accelerating field voltage of the scanning microscope was varied between 5 and 15 kV. The lower energy scan of 5 kV is typically used to examine the surface without penetrating it. Higher energy (here 15 kV) is used to reduce noise at high magnification images. Higher energy however causes deeper electron penetration of the surface and thus comes at the price of reduced sensitivity to phenomena at the material's surface.

IV. Results of Experimental Investigations

A. Visual inspection

For the visual inspection, both bearings were cut into segments. The segments of the inner and outer rings of the NDE bearing (that had not been subjected to discharge bearing currents) showed no signs of pitting or other damage. The DE's rings had a visible grey trace of 2-3 mm width. The width and intensity of the trace on the outer ring varied, with maximum width and intensity at the point that had been located at the bottom during operation. The inner ring's trace was uniformly coloured.

B. Scanning electron microscope imaging

Figs. 4 and 5 respectively show the DE used bearing surface (back-scattering electron topographic mode, BSE-TOPO) as if illuminated by direct light from its top-left corner at 45 degrees and the relative mass of the chemical elements (back-scattering electron composition mode, BSE-COMP): lighter areas are heavier elements (metals) and darker areas are lighter elements (organics). The accumulations formed by grease residues and metal areas are observable from comparison of both plots. Based on the BSE-COMP and BSE-TOPO plots, these accumulations comprise two types of features:

- Type A: craters (which seem to have mechanical origin) of different sizes (up to 5 µm) and shapes filled with organic elements.

- Type B: small (<1.5 µm in diameter) round-shaped "droplets" of non-organic elements surrounded by organic elements. The formation of these droplets is understood to be due to cohesive forces pulling molten steel together while it is suspended in the grease "basin". The droplets then cool down and freeze.

Polishing traces are clearly visible in areas of the bearing that have not been subjected to discharges. The NDE surfaces contained only type A features while the DE bearing shows type B features in the grey trace areas. The lighter trace areas seem to have fewer type B features. This behaviour suggests that darkening of the surface happens due to the appearance of type B features. Such behaviour can be expected as the dimensions of such features are similar to the wavelength of visible light: 0.38 µm to 0.72 µm. The smooth transition in colour from light to dark suggests that the process is continuous and not self-healing as the initial polishing traces never get restored.

C. Bearing temperature during running time

Fig. 6 presents the four measured temperatures. During the experiment, the temperature measured around the bearing seat varied between 27.5 and 35.5 degrees Celsius, with notable changes in average value shortly after changes of speed. The temperatures within the same speed settings had no clear long-term pattern of trends. However, during the last period of measurements (after t = 550.7 hours) rapid variations of temperatures were observed, despite the fact that the speed was kept constant. Such variations likely originate directly from within the bearing. On the limited data available such behaviour could be attributed to variations in grease properties in the surface contact area (including but not limited to the discharge area).

The noise of the environment and the power source resulted in a standard deviation of a single sample below 0.25 degrees Celsius. However, at some time intervals the noise of the test environment became significantly higher, up to 1 degrees Celsius.

D. RF discharges count

Fig. 7 shows the measured DA over the duration of the experiment, which changes over time, as reported in [19]. The measured DA over the first 125.5 hours mainly consisted of the background noise level of the test laboratory.

Initially, several changes of the speed were performed (described in Section II.C) that resulted in sharp short-term rises of DA followed by gradual decreases of the DA. Such changes were done to obtain again a new point of maximum DA. When such method of increasing the discharge activity was recognised as inefficient (the decays became too rapid) the varying motor speed pattern was introduced. In this mode of operation the DA increased until it reached its maximum ($3.27{\cdot}10^5$ discharges per second, at 411.3 hours running time) and then the short-term maxima of discharge activity began to decay. Subsequent changes of the speed reference to 20 and 50 Hz did not increase the DA further, and the DA dropped rapidly below the levels observed before the variable speed operation mode. Finally, the DA stayed at levels lower than 104 discharges per second for the last 450 hours of the experiment. This decaying behaviour is in line with findings of [19]. The increase in DA during the variable speed operation could be explained by increased intensity of regreasing of the contact area.

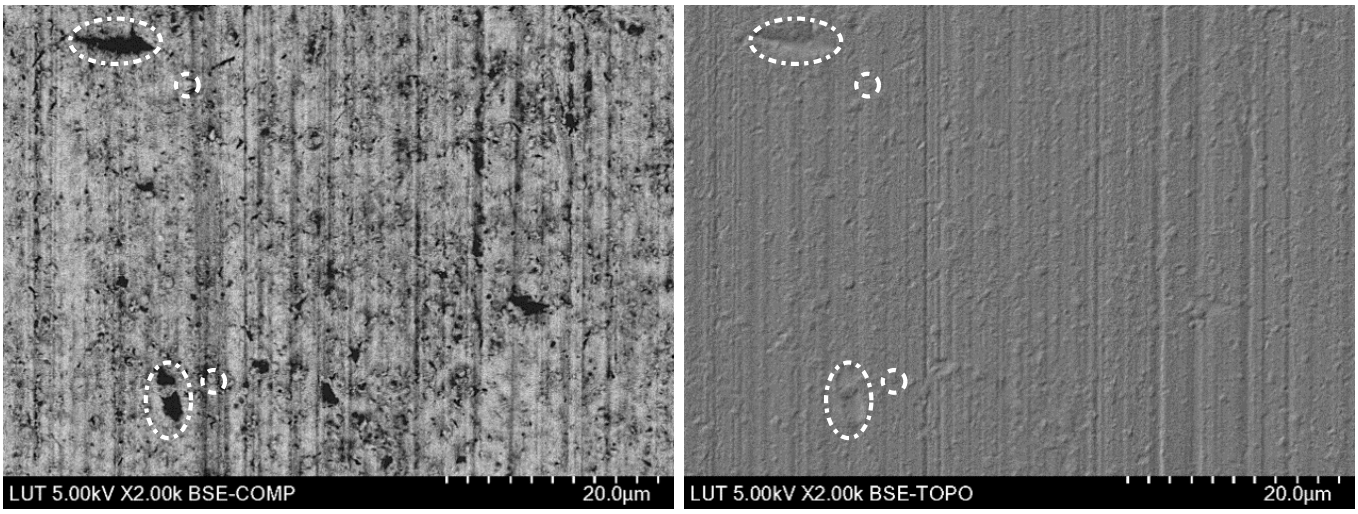

Fig. 4. Electron microscope images of the light trace area of the used DE bearing's outer ring topology (left) and surface material composition (right). Dash-dotted ellipses depict the locations of some "type A" features. Dashed circles depict the locations of some of the largest "type B" features.

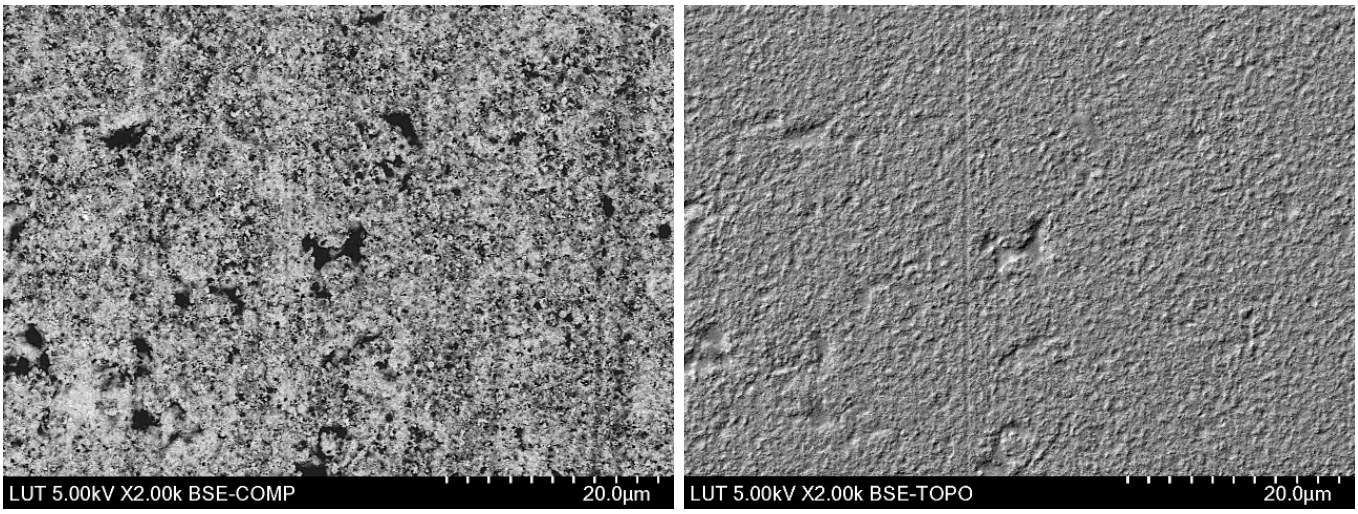

Fig. 5. Electron microscope images of the trace area of used DE bearing's inner ring topology (left) and surface material composition (right).

Fig. 8 presents the total number of discharges counted from the beginning of the experiment. The total number of detected discharges over the duration of the experiment is $6.64 \cdot 10^9$. 41.45 % of these discharges occurred between 125.4 and 166.6 hours. This period is related to the initial DA of new grease. Another 55.27 % occurred between 240 and 550 hours while the system was mostly operated in variable speed mode.

V. Analysis

A. Analysis of vibration measurements

Selected results of vibration sampling are shown in Figs. 9 and 10: samples of the undamaged bearing system (during the pre-run period) and after the bearing started to show significant increase in vibration intensity. The raw data samples suggest an increased frequency of occurrence of high acceleration spikes in the latter set of samples. In addition, the vibration magnitudes seem to have increased. Such changes would suggest an increase in roughness of the bearing surface, lubricating grease degradation or other mechanical damage.

The intervals with F_F different from 50 Hz were excluded from the interpretation as the speed not only affects the base harmonic frequency but also the intensity of friction and temperature of operation, as can be seen from Fig. 6.

For electric machines operating with rolling element bearings, changes in vibration levels are mainly expected at three different frequencies [21]:

Outer ring pass frequency:

$$F_\mathrm{BPO} = \frac{N_\mathrm{B}}{2} F_\mathrm{S}(1 - \frac{D_\mathrm{b}}{D_\mathrm{c}}) \tag{4}$$

Inner ring pass frequency:

$$F_\mathrm{BPI} = \frac{N_\mathrm{B}}{2} F_\mathrm{S}(1 + \frac{D_\mathrm{b}}{D_\mathrm{c}}) \tag{5}$$

Ball rotation frequency:

$$F_\mathrm{B} = \frac{D_\mathrm{c}}{2D_\mathrm{b}} F_\mathrm{S}(1 - \frac{{D_\mathrm{b}}^2}{{D_\mathrm{c}}^2}) \tag{6}$$

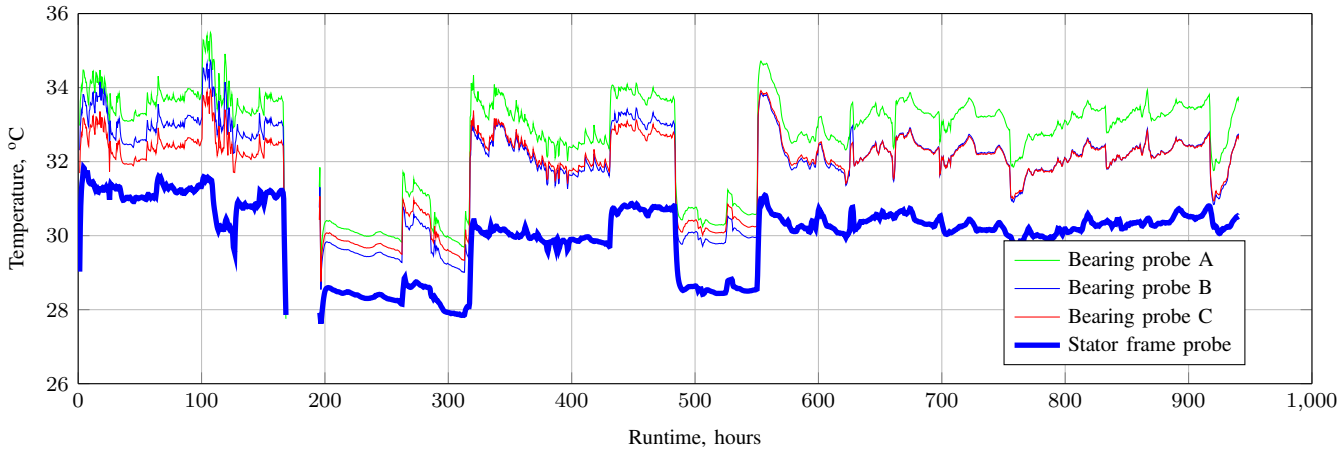

Fig. 6. Measured bearing temperature over time.

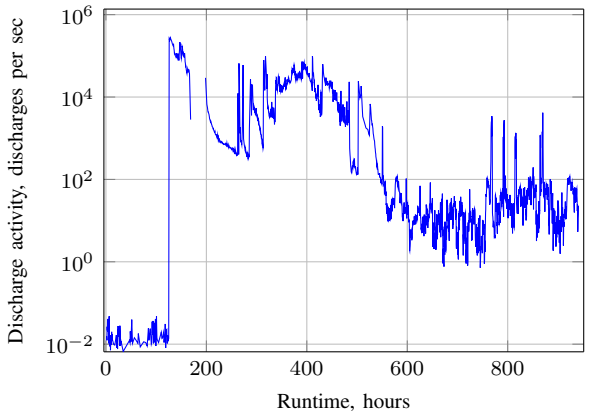

Fig. 7. Discharge activity evolution.

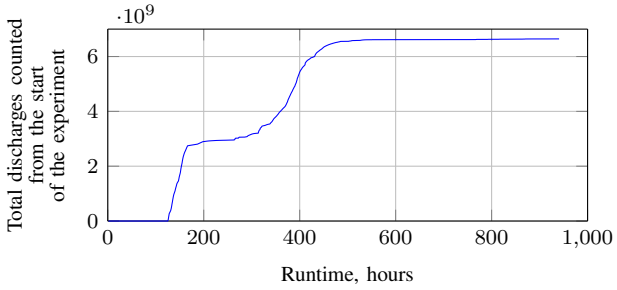

Fig. 8. Total discharges counted since the beginning of experiment

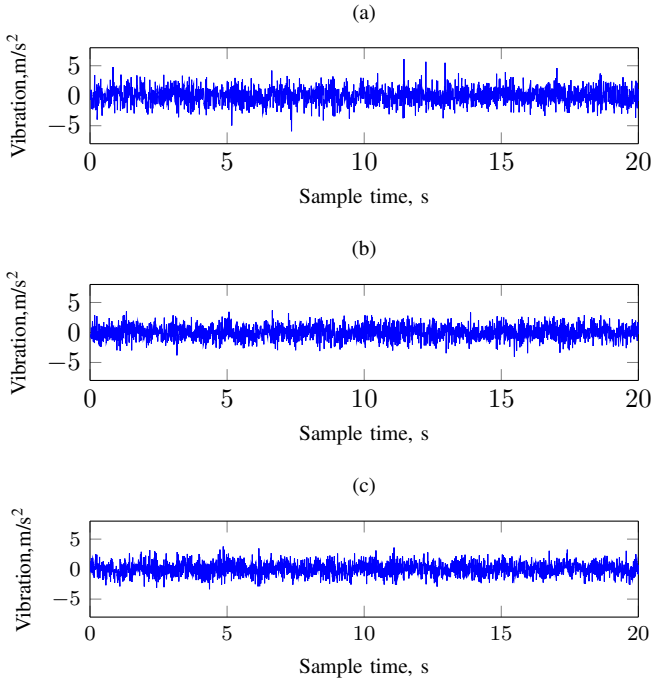

Fig. 9. Vibration samples taken during the pre-run period of measurements at t equal 0 (a), 60 (b) and 120 (c) hours.

where D_b and D_c are the bearing ball and cage diameters respectively, N_B - number of balls and F_S is the shaft rotational frequency. For the test setup, the corresponding values are D_b = 17.5 mm, D_c = 72.5 mm, N_B = 8 and F_S = 25 Hz, giving F_{BPO} = 75.86 Hz, and F_B = 48.77 Hz, F_{BPI} = 124.14 Hz.

The frequency domain representation of the vibration at the end of the experiment (t = 940 hours) is shown in Fig. 11. The response contains several strong components which are:

- multiples of the shaft speed of rotation (25 Hz);

- harmonics, related to the mechanics of bearing components are present, notably F_B and its harmonics, F_{BPO}, F_{BPI};

- high-frequency components which can be attributed to the natural mechanical resonances present in the system. These components are present in two bands. The first band spans from 2 to 3 kHz, the second from 7 to 10 kHz.

The evolution of the characteristic frequency components F_B, F_{BPO}, and F_{BPI} over time is presented in Fig. 12. The vibration magnitude at F_B seems to have a positive trend after the system has been run at lower than nominal rotation speeds for 120 hours. There is a period of significant vibration (>0.8 m/s^2) at the F_{BPO} frequency which corresponds to the period of variable rotation speed. Based on the data available such increase would seem to be caused by either additional mechanical stress during the variable speed operation, high-intensity prolonged DA or both at the same time. The magnitudes of the

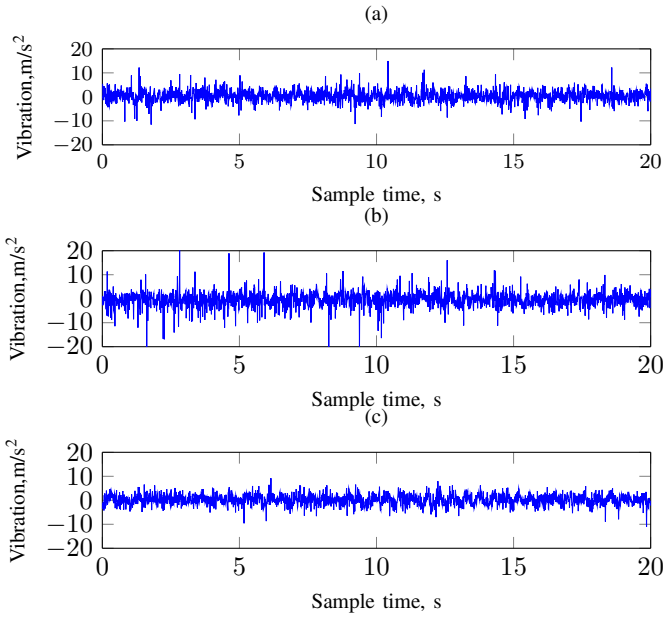

Fig. 10. Vibration samples taken during the last period of measurements at t equal 640 (a), 790 (b) and 940 (c) hours.

F_{BPI} components would seem to be affected by the variable-speed operation mode in the same way as F_{BPO}, though to a smaller extent.

The evolution of the vibration signal spectral composition over time is shown in Fig. 13. There seems to be a steady increase in vibration magnitude in the 2.3-2.7 kHz band over the duration of the experiment. Another notable observation is the pulsing increases of the magnitudes of the 4.5-5 kHz and 7-10 kHz bands. This behaviour would seem to be triggered by some event that happened between the end of the variable speed mode of operation and t = 570 hours, when the system was set to constant speed operation mode for the last time.

In order to analyse the effect of bearing surface roughness and local elevations a 3-5 kHz band envelope spectrum (as described in [22]) was computed. The envelope was obtained as an absolute value of the timed-domain representation of the filtered signal. The filtering was performed by zeroing frequency components outside of this band in the fast Fourier transform of the original signal and computing the inverse transform for the resulting frequency domain representation. The results of the transform are presented as spectrograms of per band vibration intensity versus time in Fig. 14. The increase over time of the magnitudes is clearly visible. The frequencies related to F_{BPO} and its harmonics appear in the spectrum when the system is suffering the most significant DA. Notably, at the same time, the normal spectrum indicates a very small intensity of vibration in the 3-5 kHz band apart from a floating frequency that drifts from 3.4 to 3.8 kHz over the duration of 180 hours during the variable speed operation. Later (t >550 h), when the system is run at constant nominal speed other multiples of the rotational frequency (25 Hz) appear in the spectrum. The data seem to suggest that some mechanical degradation occurred first in the bearing outer ring, which caused further bearing deterioration. This observation is in line with the results reported in [13] suggesting that fluting damage first occurs as surface deterioration of the outer ring and then progresses to the inner ring.

B. Vibration spectral composition modelling

1) Model description: The shaft displacing forces were modelled to evaluate the expected changes in the vibration signal frequency composition of a multipoint damage, normally distributed around single central point, from the case of a single point damaged described by eqs. (4)-(6).

The 2-dimensional model presents a single axial section of a ball bearing. The model was developed assuming tight non-lubricated contact between outer ring, inner ring and balls. The local increments in rolling surface height were modelled as sinusoidal-shaped bumps according to equation

$$h_{\text{bump}}(\alpha) = l_{\text{bump}} \left[\cos\left(\frac{\frac{\pi}{6}(\alpha - \alpha_{\text{centre}})}{\frac{l_{\text{bump}}}{2\pi R_{\text{surf}}}} \right) - \cos(\frac{\pi}{6}) \right], \quad (7)$$

where l_{bump} is the modelled bump length, R_{surf} - nominal radius of a rolling surface.

The force exerted by the bump on the shaft is estimated with the simplified Hertzian contact equation

$$F(R) = \tfrac{4}{3} E^* R^{1/2} d^{3/2} \quad (8)$$

where R is the contact sphere radius, d is contact depth and equivalent elastic modulus

$$\frac{1}{E^*} = \frac{1-\nu_1^2}{E_1} + \frac{1-\nu_2^2}{E_2} \quad (9)$$

where $E_1 = E_2$ and assumed to be equal to elastic modulus of stainless steel ($180 \cdot 10^9$ Nm^2) and $\nu_1 = \nu_2$ are assumed to be Poisson's ratios of stainless steel and equal to 0.3. The total force exerted on the shaft is computed as vector sum of individual forces produced by bearings. The direction of the applied force is assumed to be aligned with ball centre to the shaft centre radius.

$$F_i(\alpha) = F(h_{\text{outer}}(\alpha_i) + h_{\text{inner}}(\beta_i)) \quad (10)$$

where h_{outer} and h_{inner} are the corresponding cumulative height of the outer and inner bearing ring at the point of ball to ring contact and angles

$$\alpha_i(t) = \theta_i + 2\pi F_{\text{cage}} t \quad (11)$$

$$\beta_i(t) = \theta_i + 2\pi F_{\text{shaft}} t - 2\pi F_{\text{cage}} t \quad (12)$$

define the variation of that contact point in time, t. The angles θ_i define the initial shift of each ball in cage and are equal to $\frac{2\pi}{N}, \frac{4\pi}{N}, \ldots, 2\pi$. The rotation frequencies are

$$F_{\text{cage}} = F_{\text{shaft}} \frac{R_{\text{inner}}}{R_{\text{inner}} + R_{\text{outer}}} \quad (13)$$

and F_{shaft}, which is the shaft rotation speed and assumed to be 25 Hz. R_{inner} = 27.5 mm and R_{outer} = 45 mm are the bearing inner and outer race radii.

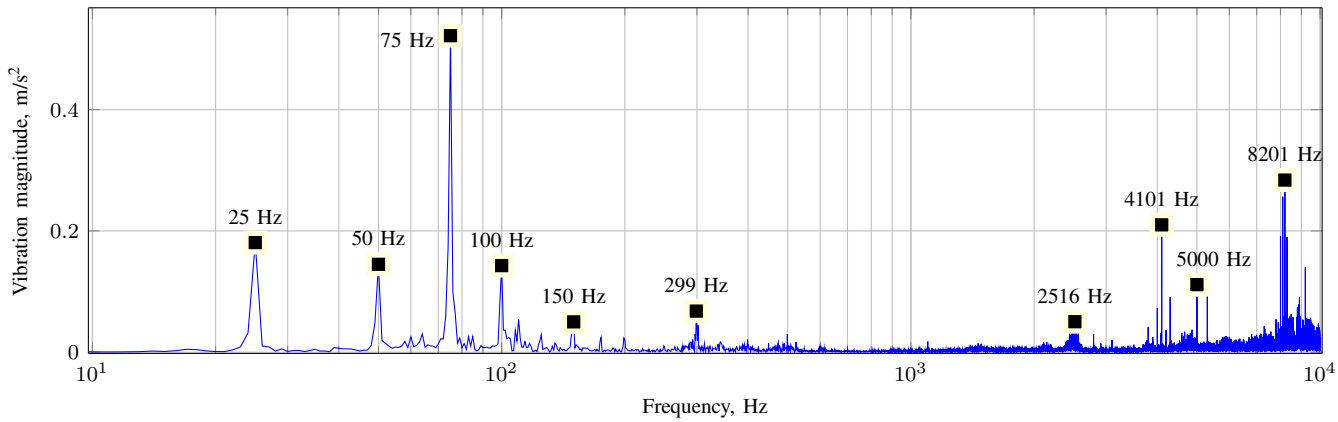

Fig. 11. Frequency composition of the vibration signal at the end of the experiment.

The outer ring defect due to pitting was modelled as a set of single point damages normally distributed around the centre angle mean value α_c of $\frac{\pi}{2}$ (corresponding to the bottom of the bearing) with 95 % of points distributed over an area with length of $6\sigma_{dd}$. The size of each damage was fixed as l_{bump} = 10 µm.

2) Results of vibration spectral composition modelling: First, the total number of defects was fixed at 500 while the deviation of the distribution was increased from 0.01 rad to 0.2 rad with a step of 0.01 rad. For each value 100 model runs with different sets of damage points were performed. The results are presented in Fig. 15. The figure features the mean values of the magnitudes over 100 test runs and 3σ interval around the mean value based on the standard deviation in each set of 100 model results. The modelling shows that the magnitudes of the harmonics from the first to the eighth decreased rapidly as the damage spread increased from 0.01 to 0.1 rad. After that point the harmonic variation is insignificant when compared to the magnitude variation between the samples due to the probabilistic nature of damage distribution. This observation suggests that for a given bearing damage the vibration magnitude at a single frequency might be affected significantly by the layout of the damage. Hence, the damages that were caused by discharge currents with similar energies might not cause the same vibration characteristics, even if all other parameters, except for the distribution of the

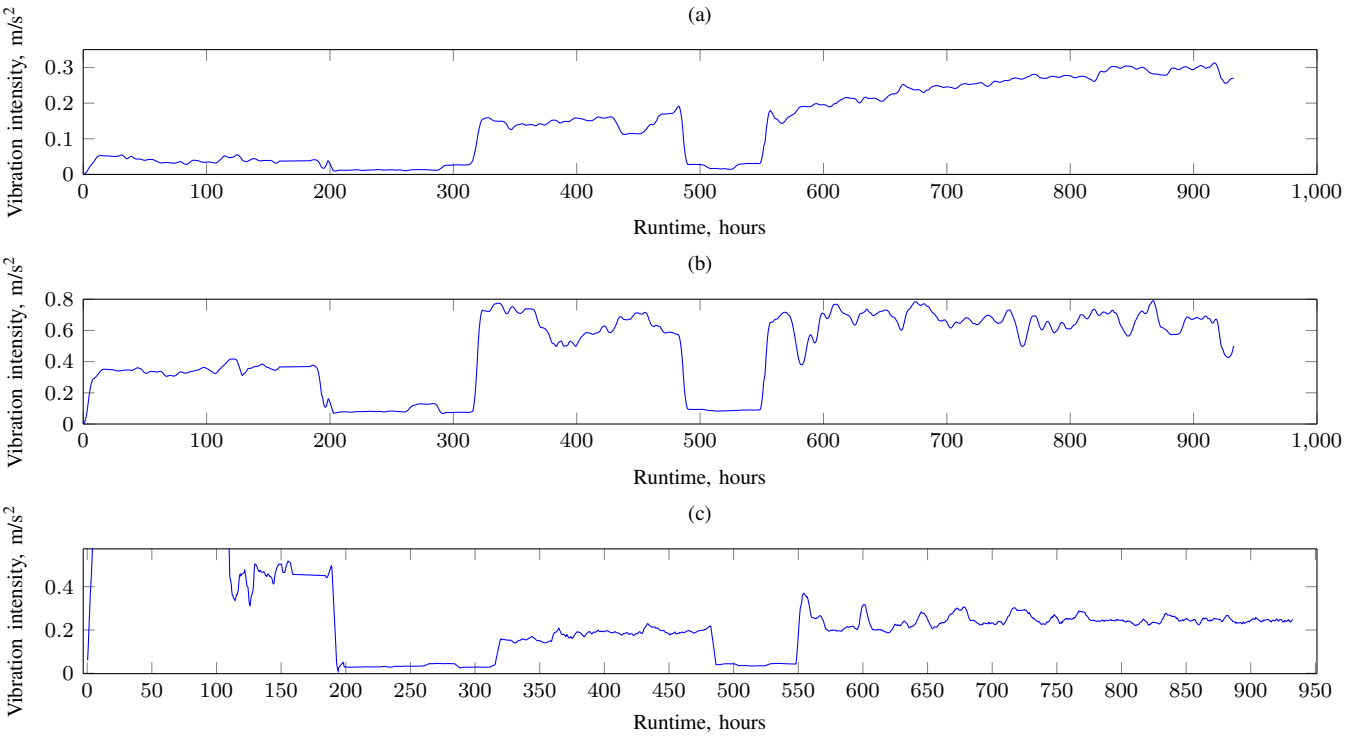

Fig. 12. Vibrations in 1 Hz bands around the characteristic frequency components F_B (a), F_{BPO}(b) and F_{BPI} (c) of a normal spectrum. The data on the F_{BPI} plot is clipped during the pre-run period.

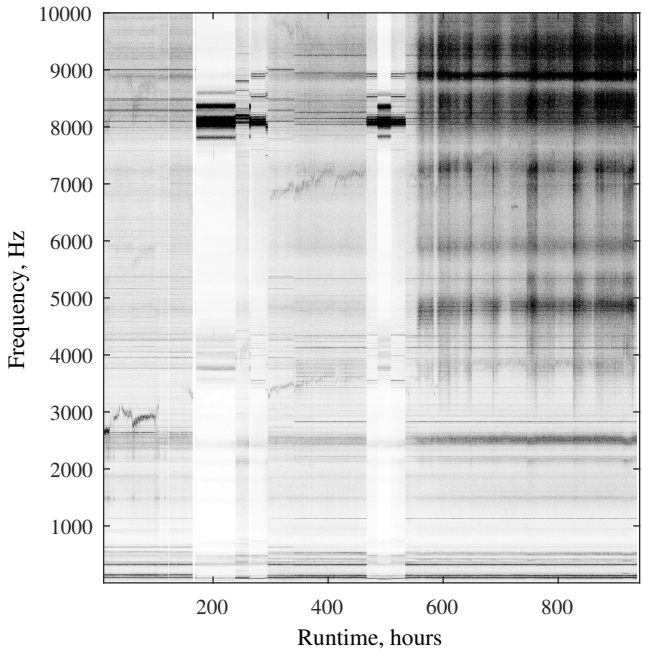

Fig. 13. Evolution of vibration signal spectral composition. [m/s^2]

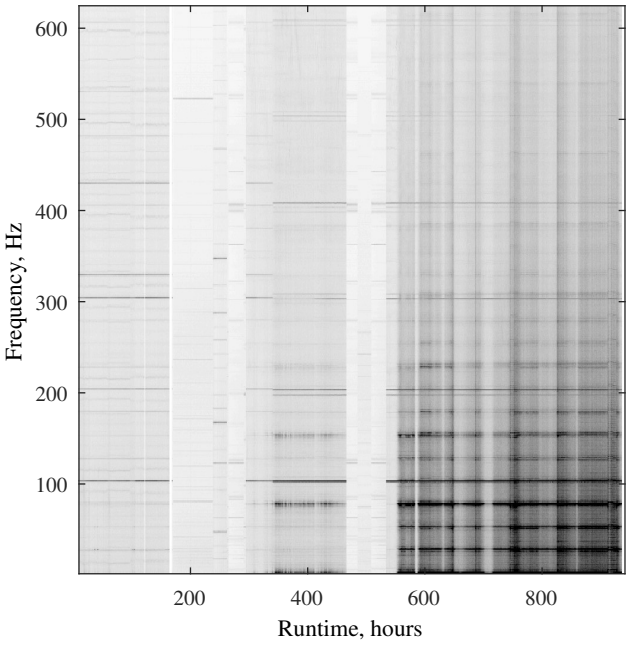

Fig. 14. Evolution of 3-5 kHz band envelope spectral composition. [m/s^2]

damage, might be the same. The higher order harmonics seem to be less affected be the increase in damage spread then the lower order harmonics.

In a second step the increase of vibration magnitudes with the increase of the damage is modelled. The results are shown in Fig. 16. The spread of the damage was fixed as 0.2 radians while the number of damage points varied from 100 to 2000 points in steps of 100 points. The figure features high-order harmonics of vibration signal in the band from 2 to 3.5 kHz. The harmonics behave similarly show slight increase in magnitude as the damage increases. However, the rate at which the standard deviation of the magnitudes grows is higher than that of their mean value.

This confirms that single frequency components are not suitable for the monitoring of bearing damage due to discharge bearing currents. Fig. 17 presents the result of aggregation of all high-frequency components in the 2 to 5 kHz band. The aggregated value grows with the increase in the number of damage points the same way as the mean value of the high frequency harmonics. However, due to the averaging of multiple frequencies the standard deviation values are much lower than those of the single frequency components. This suggests the use of sums of high frequency harmonics as an efficient vibration-based damage criteria for pitting damage. For example Fig. 13 shows a vibration increase in bands above 1 kHz while the low-frequency bands and primary harmonic for outer ring damage (Fig. 12) show no observable variation.

C. Discharge energy analysis

For completion, the total energy introduced into the DE bearing during the test run is established. In [23] the total of capacitances across bearings (the bearing capacitance itself combined with the rotor-to-stator capacitance) of the same type, operating in the same machine were determined. This capacitance was computed to 0.36 nF at 23 °C and 0.89 nF at 37 °C. Assuming a linear relationship, the capacitance as a function of temperature is interpolated by

$$C_{\text{tot}} = 0.0379(T - 23) + 0.36, \tag{14}$$

where T is the machine frame temperature in degrees Celsius. The average temperature during the experiment varied between 25.5 and 35.5 degrees Celsius. From this interpolation the capacitance is estimated to vary between 0.46 nF (25.5 °C value) and 0.83 nF (33 °C value). The order of magnitude of these values is in agreement with published capacitance values, such as the results presented in [24].

The larger value (at 35.5 °C) was used to estimate the upper bound of energy released from within the bearing onto the bearing surface during a discharge:

$$E = \frac{C_{\text{tot}}\, U^2}{2}, \tag{15}$$

where C_{tot} is the estimated worst-case capacitance and U is the maximum shaft voltage. For the chosen supply voltage of 60 V_{pp}, the energy of a single discharge is E = 373.5 nJ. Note that the true upper bound of energy released into the bearing could be even higher, as additional energy might be released from the rotor-to-frame capacitance. However, according to [14], such energy level would be sufficient to vaporise craters with radii up to 1.38 μm and melt craters with radii up to 2.57 μm while the electron microscope analysis shows features with diameters between 0.5 and 1.5 μm. The formation of such features corresponds to the discharges happening in a 0.83 nF capacitance at voltages around 10 V. It was observed

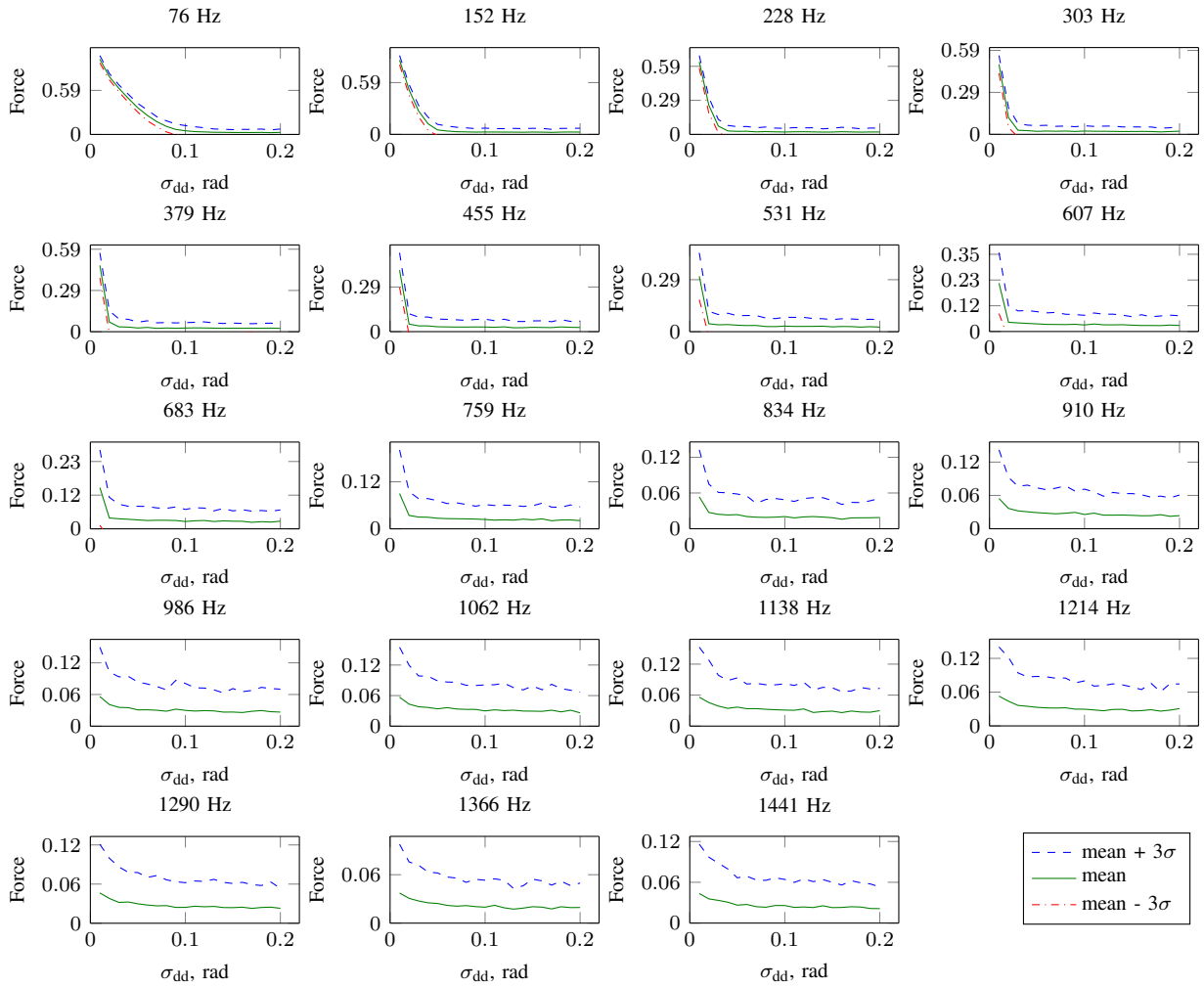

Fig. 15. F_{BPO} harmonics change with the spread of damage.

that the discharges mostly happen before the shaft voltage has reached the peak value of the applied shaft voltage. Such behaviour can prevent the shaft voltage from reaching higher values as the bearing temporarily goes into resistive mode [23]. Furthermore, it is possible that some of the energy dissipated during the discharge is dissipated into the grease film, contributing to its degeneration.

Assuming discharges occurring at 10 V and given the calculations above, we estimate the energy introduced into the bearing by the discharges as 275.6 J or 85 µW of average discharge power over the duration of the experiment. This amount of energy introduced into the DE bearing led to the detectable vibration changes. This estimate is considered to be important for further research and comparison with other future works as a measure of damage.

VI. Summary

In this paper the development of EDM-type inverter-induced bearing damage was investigated in a 940-hours long run of a specially modified test setup. The test system was operated in conditions that simulated a 60 V_{pp} 300 kHz voltage occurring between the test motor shaft and the stator frame eventually causing discharges in the DE bearing. Based on detailed monitoring and analysis of multiple parameters the following observations were made:

- Visual inspection showed grey traces on the surfaces of the bearing subjected to discharges that are absent on the surfaces of bearing that was subjected only to mechanical wear. This complements the observations made in [25], in which the bearing in the state of initial formation of a similar trace under conditions of lower peak to peak voltage applied and less total discharge activity observed.

- The scanning electron microscope picturing reveals that the surface has been damaged with two distinct types of damage: formation of craters (features of complex shape with sizes from 2 to 10 micrometres in longest dimension) and, in the contrast to frequently reported pitting craters, small (<1.5 µm) elevations.

- The DA gradually decayed after each sharp rise that followed a step change of speed as already reported on in [19]. However, after the speed mode was set to variable the DA only increased for the first 90 hours and then decayed to a level where it was no longer significantly affected by any changes in the speed of the motor shaft.

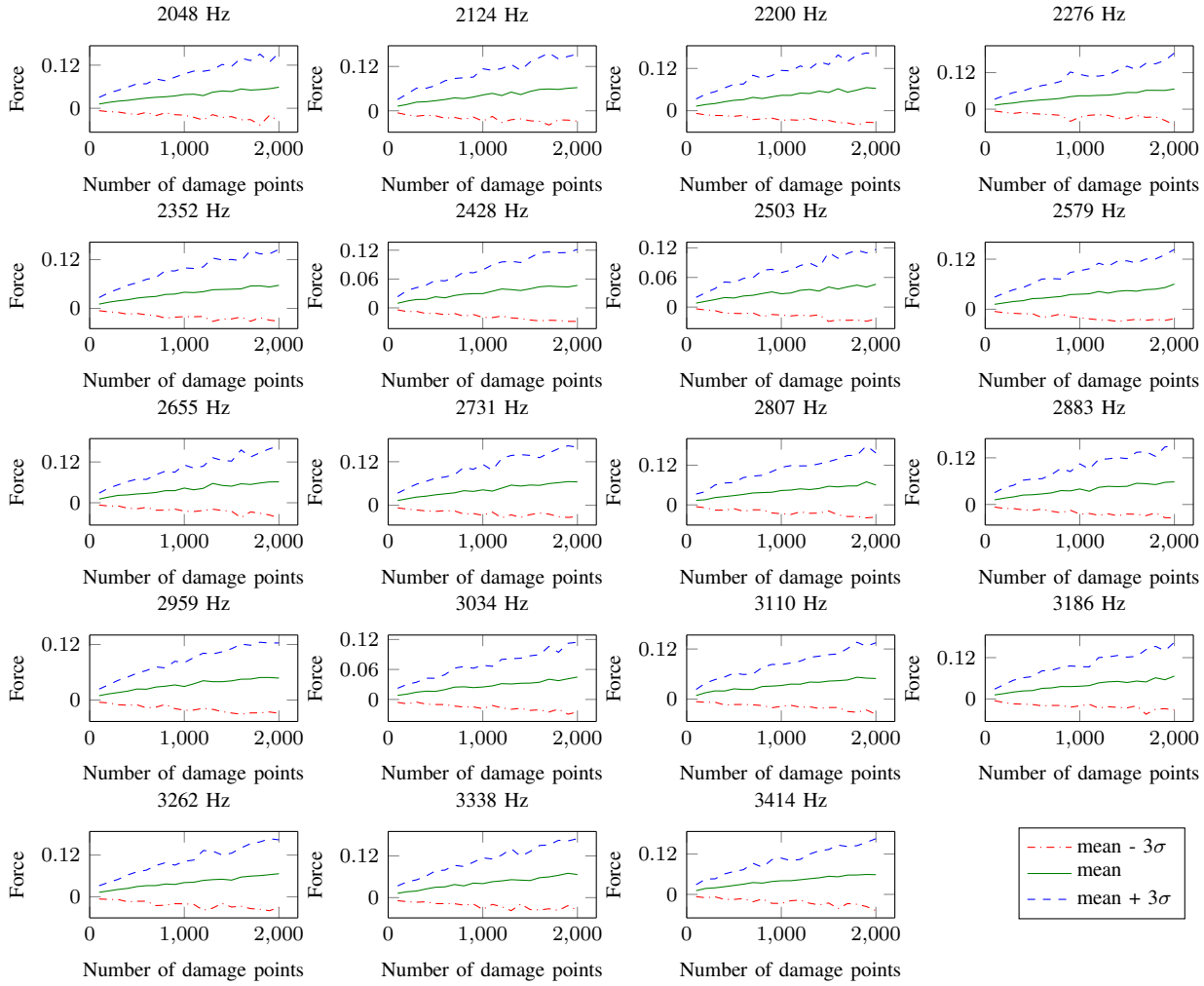

Fig. 16. F_{BPO} harmonics change with the number of damage points - the increase in average magnitude is mostly negated by the increase in standard deviation.

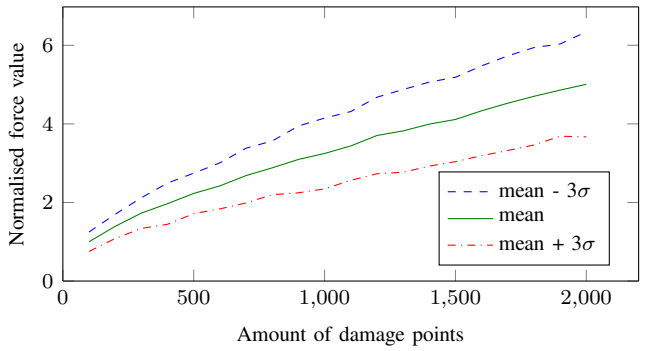

Fig. 17. Variation of 2-5 kHz band signal with the increase in number of single point damages.

- Vibration analysis showed a more than three times increase in the peak value of vibrations over 20 seconds by the end of experiment in comparison to the levels at the beginning of experiment. This increase as well as the absence of a significant increase in the base frequencies for outer and inner ring damage corresponds to the predictions of modelling presented in Subsection V.B of this paper as well as to observations reported in [13]

- The findings suggest that the monitoring of a single frequency is not suitable for detection of outer/inner ring damage due to EDM currents. The simultaneous monitoring of multiple high-frequency components of vibration is proposed because it allows to alleviate the influence of distribution variations of the damage points and increases the confidence level of vibration monitoring measurements.

The increase detected through vibration monitoring in the F_{BPO} component at early stages of the test run (300-500 hours) suggested a defect in the outer ring of a bearing. According to further analysis of the vibration monitoring data and vibration modelling it is likely that this defect first occurred as a single point damage on the outer surface of the DE bearing. As the duration of the experiment was short compared to the expected lifetime of this bearing under this loading scenario it appears that the main degradation caused to the bearing occurred because of the DA. Based on information obtained from the RF monitoring system it seems that the DA was reduced by the increased vibration because most of the accumulated

energy introduced into the bearing by the discharges had been released before the significant increase in vibration appeared. In the presence of vibrations, the capacitance might discharge at lower voltage levels already, possibly under the influence of metal particles in the grease passing the rolling element and/or surface more closely. Hence, the latter damage would seem to be caused mostly by mechanical overloading of both the DE and the NDE bearings. This explanation is supported by the appearance of mechanical degradation in both bearings seen in the SEM imaging. On the data available it would seem that the damaged caused to bearing was not self-healing although not yet destructive.

REFERENCES

[1] S. Chen, T. Lipo, and D. Fitzgerald, "Modeling of motor bearing currents in PWM inverter drives," *IEEE Transactions on Industry Applications*, vol. 32, pp. 1365–1370, 1996.

[2] J. Erdman, R. Kerkman, D. Schlegel, and G. Skibinski, "Effect of PWM inverters on AC motor bearing currents and shaft voltages," *IEEE Transactions on Industry Applications*, vol. 32, pp. 250–259, 1996.

[3] P. J. Link, "Minimizing electric bearing currents in asd systems," *IEEE Industry Applications Magazine*, vol. 5, no. 4, pp. 55–66, Jul 1999.

[4] D. Busse, J. Erdman, R. Kerkman, D. Schlegel, and G. Skibinski, "Bearing currents and their relationship to PWM drives," *IEEE Transactions on Power Electronics*, vol. 12, pp. 243–252, 1997.

[5] D. Busse and J. Erdman, "System electrical parameters and their effects on bearing currents," *IEEE Transactions on Industry Applications*, vol. 33, pp. 577–584, 1997.

[6] D. Busse, J. Erdman, R. Kerkman, D. Schlegel, and G. Skibinski, "Characteristics of shaft voltage and bearing currents," *IEEE Industry Applications Magazine*, vol. 3, no. 6, pp. 21–32, Nov 1997.

[7] H. E. Boyanton and G. Hodges, "Bearing fluting [motors]," *IEEE Industry Applications Magazine*, vol. 8, no. 5, pp. 53–57, Sep 2002.

[8] H. Akagi and T. Doumoto, "An approach to eliminating high-frequency shaft voltage and ground leakage current from an inverter-driven motor," *IEEE Transactions on Industry Applications*, vol. 40, pp. 1162–1169, 2004.

[9] A. Muetze and A. Binder, "Don't lose your bearings," *IEEE Industry Applications Magazine*, vol. 12, no. 4, pp. 22–31, July 2006.

[10] R. Schiferl and M. Melfi, "Bearing current remediation options," *Industry Applications Magazine, IEEE*, vol. 10, pp. 40–50, 2004.

[11] R. R. Schoen, T. G. Habetler, F. Kamran, and R. G. Bartfield, "Motor bearing damage detection using stator current monitoring," *IEEE Transactions on Industry Applications*, vol. 31, no. 6, pp. 1274–1279, Nov 1995.

[12] L. Frosini and E. Bassi, "Stator current and motor efficiency as indicators for different types of bearing faults in induction motors," *IEEE Transactions on Industrial Electronics*, vol. 57, no. 1, pp. 244–251, Jan 2010.

[13] H. Tischmacher and S. Gattermann, "Multiple signature analysis for the detection of bearing currents and the assessment of the resulting bearing wear," in *Power Electronics, Electrical Drives, Automation and Motion (SPEEDAM), 2012 International Symposium on*, June 2012, pp. 1354–1359.

[14] M. Kriese, E. Wittek, S. Gattermann, H. Tischmacher, G. Poll, and B. Ponick, "Influence of bearing currents on the bearing lifetime for converter driven machines," in *Proceedings - 2012 20th International Conference on Electrical Machines, ICEM 2012*, 2012, pp. 1735–1739.

[15] A. Muetze and E. G. Strangas, "On inverter induced bearing currents, bearing maintenance scheduling, and prognosis," in *Electrical Machines (ICEM), 2014 International Conference on*, Sept 2014, pp. 1915–1921.

[16] R. Singleton, E. Strangas, and S. Aviyente, "Extended kalman filtering for remaining-useful-life estimation of bearings," *IEEE Transactions on Industrial Electronics*, vol. 62, pp. 1781–1790, 2015.

[17] V. Niskanen, A. Muetze, and J. Ahola, "On the role of the shaft end and the influence of frame size and load coupling on the rf emission characteristics of induction motors," *EPE Journal (European Power Electronics and Drives Journal)*, vol. 23, no. 4, pp. 42–50, 2013. [Online]. Available: www.scopus.com

[18] V. Sarkimaki, "Radio frequency method for detecting bearing currents in induction motor," Ph.D. dissertation, Lappeenranta University of Technology, Finland, 2009.

[19] A. Muetze, J. Tamminen, and J. Ahola, "Influence of motor operating parameters on discharge bearing current activity," *IEEE Transactions on Industry Applications*, vol. 47, no. 4, pp. 1767–1777, July 2011.

[20] J. Cooley and J. Tukey, "An algorithm for the machine calculation of complex fourier series," *Math. Comput.*, vol. 19, pp. 297–301, 1965.

[21] B. Li, M. Y. Chow, Y. Tipsuwan, and J. C. Hung, "Neural-network-based motor rolling bearing fault diagnosis," *IEEE Transactions on Industrial Electronics*, vol. 47, pp. 1060–1069, 2000.

[22] F. Immovilli, A. Bellini, R. Rubini, and C. Tassoni, "Diagnosis of bearing faults in induction machines by vibration or current signals: A critical comparison," *IEEE Transactions on Industry Applications*, vol. 46, pp. 1350–1359, 2010.

[23] V. Niskanen, A. Muetze, and J. Ahola, "Study on bearing impedance properties at several hundred kilohertz for different electric machine operating parameters," *IEEE Transactions on Industry Applications*, vol. 50, pp. 3438–3447, 2014.

[24] E. Wittek, M. Kriese, H. Tischmacher, S. Gattermann, B. Ponick, and G. Poll, "Capacitance of bearings for electric motors at variable mechanical loads," in *Electrical Machines (ICEM), 2012 XXth International Conference on*, Sept 2012, pp. 1602–1607.

[25] A. Romanenko, J. Ahola, A. Muetze, and V. Niskanen, "Study of incipient bearing damage monitoring in variable-speed drive systems," in *Power Electronics and Applications (EPE'14-ECCE Europe), 2014 16th European Conference on*, Aug 2014, pp. 1–10.

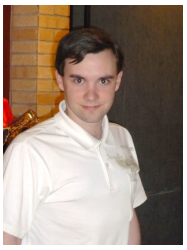

Aleksei Romanenko (S'11-16) received the B.Eng.Tech in electric engineering from the Saint Petersburg Electrotechnical University in 2011 and the dual-degree M.Sc. from Lappeenranta University of Technology and Saint Petersburg Electrotechnical University in 2013.

In 2013, he joined the Department of Electrical Engineering, Lappeenranta University of Technology as a Research Assistant and became a doctoral student there in 2014. His current research mainly focuses on the maintenance of electric machines, embedded systems, and non-intrusive diagnostics.

Annette Muetze (S'03-M'04-SM'09-F'16) is a full professor at Graz University of Technology, Austria, where she heads the Electric Drives and Machines Institute. She received the dual Dipl.Ing. degree in electrical engineering from Darmstadt University of Technology, Darmstadt, Germany, and general engineering from the Ecole Centrale de Lyon, Ecully, France, in 1999, and the Dr.Ing. degree in electrical engineering from Darmstadt University of Technology in 2004.

Prior to joining Graz, she worked as an Assistant Professor at the Electrical and Computer Engineering Department, University of Wisconsin-Madison, Madison, US, and as an Associate Professor at the School of Engineering of the University of Warwick in the UK. Her research interests are the interplay of the different elements of electric drive systems, including parasitic effects, performance evaluation, design optimization, and decision making criteria.

Jero Ahola received the M.Sc. and D.Sc. degrees in electrical engineering from Lappeenranta University of Technology (LUT), Lappeenranta, in 1999 and 2003, respectively. He is currently a Professor of energy efficiency and preventive maintenance of electrical equipment with the Department of Electrical Engineering, LUT. His main research interests are diagnostics of electrical drive systems and power line communications.

ACTA UNIVERSITATIS LAPPEENRANTAENSIS

742. LAYUS, PAVEL. Usability of the submerged arc welding (SAW) process for thick high strength steel plates for Arctic shipbuilding applications. 2017. Diss.

743. KHAN, RAKHSHANDA. The contribution of socially driven businesses and innovations to social sustainability. 2017. Diss.

744. BIBOV, ALEKSANDER. Low-memory filtering for large-scale data assimilation. 2017. Diss.

745. ROTICH, NICOLUS KIBET. Development and application of coupled discrete and continuum models in solid particles classification. 2017. Diss.

746. GAST, JOHANNA. The coopetition-innovation nexus: Investigating the role of coopetition for innovation in SMEs. 2017. Diss.

747. KAPOOR, RAHUL. Competition and disputes in the patent life cycle. 2017. Diss.

748. ALI-MARTTILA, MAAREN. Towards successful maintenance service networks – capturing different value creation strategies. 2017. Diss.

749. KASHANI, HAMED TASALLOTI. On dissimilar welding: a new approach for enhanced decision-making. 2017. Diss.

750. MVOLA BELINGA, ERIC MARTIAL. Effects of adaptive GMAW processes: performance and dissimilar weld quality. 2017. Diss.

751. KARTTUNEN, JUSSI. Current harmonic compensation in dual three-phase permanent magnet synchronous machines. 2017. Diss.

752. SHI, SHANSHUANG. Development of the EAST articulated maintenance arm and an algorithm study of deflection prediction and error compensation. 2017. Diss.

753. CHEN, JIE. Institutions, social entrepreneurship, and internationalization. 2017. Diss.

754. HUOTARI, PONTUS. Strategic interaction in platform-based markets: An agent-based simulation approach. 2017. Diss.

755. QU, BIN. Water chemistry and greenhouse gases emissions in the rivers of the "Third Pole" / Water Tower of Asia". 2017. Diss.

756. KARHU, PÄIVI. Cognitive ambidexterity: Examination of the cognitive dimension in decision-making dualities. 2017. Diss.

757. AGAFONOVA, OXANA. A numerical study of forest influences on the atmospheric boundary layer and wind turbines. 2017. Diss.

758. AZAM, RAHAMATHUNNISA MUHAMMAD. The study of chromium nitride coating by asymmetric bipolar pulsed DC reactive magnetron sputtering. 2017. Diss.

759. AHI, MOHAMADALI. Foreign market entry mode decision-making: Insights from real options reasoning. 2017. Diss.

760. AL HAMDI, ABDULLAH. Synthesis and comparison of the photocatalytic activities of antimony, iodide and rare earth metals on SnO2 for the photodegradation of phenol and its intermediates under UV, solar and visible light irradiations. 2017. Diss.

761. KAUTTO, JESSE. Evaluation of two pulping-based biorefinery concepts. 2017. Diss.

762. AFZALIFAR, ALI. Modelling nucleating flows of steam. 2017. Diss.

763. VANNINEN, HEINI. Micromultinationals - antecedents, processes and outcomes of the multinationalization of small- and medium-sized firms. 2017. Diss.

764. DEVIATKIN, IVAN. The role of waste pretreatment on the environmental sustainability of waste management. 2017. Diss.

765. TOGHYANI, AMIR. Effect of temperature on the shaping process of an extruded wood-plastic composite (WPC) profile in a novel post-production process. 2017. Diss.

766. LAAKKONEN, JUSSI. An approach for distinct information privacy risk assessment. 2017. Diss.

767. KASURINEN, HELI. Identifying the opportunities to develop holistically sustainable bioenergy business. 2017. Diss.

768. KESKISAARI, ANNA. The impact of recycled raw materials on the properties of wood-plastic composites. 2017. Diss.

769. JUKKA, MINNA. Perceptions of international buyer-supplier relational exchange. 2017. Diss.

770. BAYGILDINA, ELVIRA. Thermal load analysis and monitoring of doubly-fed wind power converters in low wind speed conditions. 2017. Diss.

771. STADE, SAM. Examination of the compaction of ultrafiltration membranes with ultrasonic time-domain reflectometry. 2017. Diss.

772. KOZLOVA, MARIIA. Analyzing the effects of a renewable energy support mechanism on investments under uncertainty: case of Russia. 2017. Diss.

773. KURAMA, ONESFOLE. Similarity based classification methods with different aggregation operators. 2017. Diss.

774. LYYTIKÄINEN, KATJA. Removal of xylan from birch kraft pulps and the effect of its removal on fiber properties, colloidal interactions and retention in papermaking. 2017. Diss.

775. GAFUROV, SALIMZHAN. Theoretical and experimental analysis of dynamic loading of a two-stage aircraft engine fuel pump and methods for its decreasing. 2017. Diss.

776. KULESHOV, DMITRII. Modelling the operation of short-term electricity market in Russia. 2017. Diss.

777. SAARI, JUSSI. Improving the effectiveness and profitability of thermal conversion of biomass. 2017. Diss.

778. ZHAO, FEIPING. Cross-linked chitosan and β-cyclodextrin as functional adsorbents in water treatment. 2017. Diss.

779. KORHONEN, ILKKA. Mobile sensor for measurements inside combustion chamber – preliminary study. 2017. Diss.

780. SIKIÖ, PÄIVI. Dynamical tree models for high Reynolds number turbulence applied in fluid-solid systems of 1D-space and time. 2017. Diss.